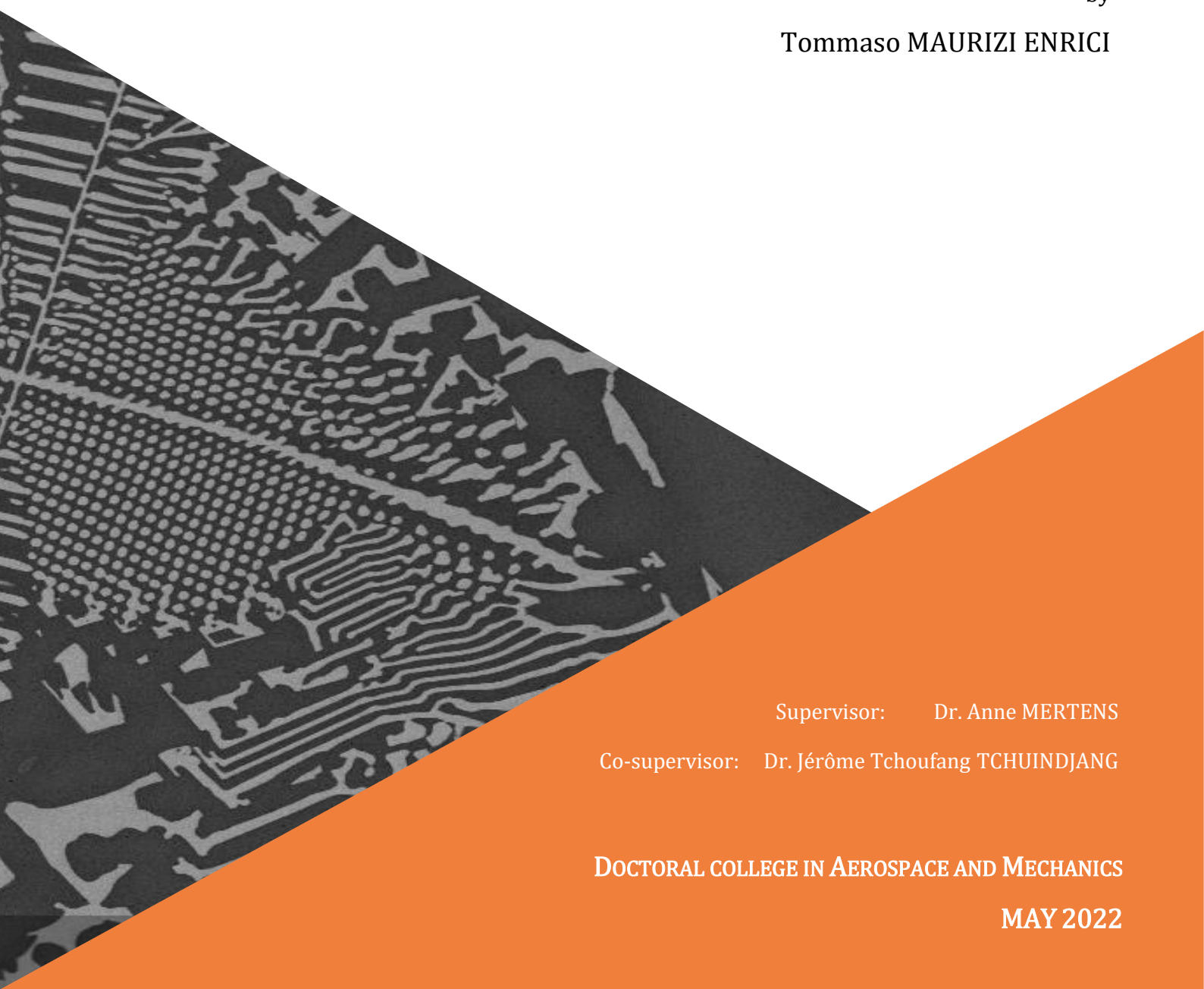


# **Development, metallurgical and tribological characterization of complex alloys and metal matrix composites obtained from manufacturing processes under non-equilibrium conditions**

A thesis submitted in partial fulfillment of the requirements  
for the degree of Doctor of Philosophy (Phd) in Engineering Science

by

**Tommaso MAURIZI ENRICI**



Supervisor: Dr. Anne MERTENS

Co-supervisor: Dr. Jérôme Tchoufang TCHUINDJANG

**DOCTORAL COLLEGE IN AEROSPACE AND MECHANICS**

**MAY 2022**

---

---

***Examination committee:***

Prof. **P. Duysinx** (President)

University of Liège, Belgium

Prof. **A. Mertens** (Supervisor)

University of Liège, Belgium

Dr **J.T. Tchuindjang** (Co-Supervisor)

University of Liège, Belgium

Dr **F. Boschini**

University of Liège, Belgium

Prof. **S. Castagne**

KULeuven, Belgium

Prof. **M. Pellizzari**

University of Trento, Italy

Prof. **A. Sinatora**

Instituto Tecnológico Vale, Ouro Preto, Brazil

---

© ULiège - Faculty of Applied Sciences - Quartier Polytech 1, Allée de la Découverte, 12 - B-4000 Liège (Belgium)

*All rights reserved. No part of the publication may be reproduced in any form by print, photoprint, microfilm or any other means without written permission from the publisher.*


*Tous droits réservés. Aucun extrait de cet ouvrage ne peut être reproduit, ni saisi dans une banque de données, ni communiqué au public, sous quelque forme que ce soit, électronique, mécanique, par photocopie, film ou autre, sans le consentement écrit et préalable de l'éditeur.*



---

"Who cares if one more light goes out?"

Well, I do"

Chester Bennington 



---

---

## Table of contents

Acknowledgements.....	9
Abstract.....	11
Resumé .....	13
1. Introduction and context .....	15
1.1. Concept and brief history of Additive Manufacturing processes.....	15
1.2. Feedstock for AM .....	17
1.3. Materials for AM vs materials by AM.....	18
1.4. Purpose of the work .....	20
References section 1 .....	23
2. State of the art .....	27
2.1. Advanced materials fabricated by AM .....	27
2.1.1. Composites materials via LC.....	28
2.1.2. Modified alloys via LC.....	30
2.2. Metals fabricated under high cooling rates .....	31
2.2.1. Microstructures after centrifugal casting .....	31
2.2.2. AM microstructures .....	34
2.3. Properties of AM alloys .....	38
2.3.1. Wear performance of 316L and its MMC.....	39
References section 2 .....	41
3. Fabrication and characterization of alloys and MMC fabricated by LC.....	51
3.1. Powder handling and preparation.....	51
3.1.1. Separate handling of the powders .....	51
3.1.2. Powder preparation.....	52
3.2. Fabrication .....	54
3.2.1. Process parameters.....	54
3.2.2. Interactions between reinforcements and molten metal.....	55
3.3. Macroscopic characterization.....	59
3.3.1. Detection of microstructural variations .....	59
3.3.2. Microstructural variation due to heat accumulation .....	61
3.3.3. Evolution of the macrohardness .....	64
3.4. Characterization of complex microstructures .....	67
3.4.1. Metastable carbides in centrifugal casting.....	69
3.4.2. Out-of-equilibrium microstructures in AM .....	71
3.5. Characterization of the properties .....	74
3.5.1. Strengthening of the matrix .....	74
3.5.2. Wear behaviour and performances .....	75
References section 3 .....	79

---

---

4. Conclusions.....	87
5. Perspectives.....	91
Appendix .....	93
Article #1 : Elucidation of the solidification sequence of a complex graphitic HSS alloy under a combined approach of DTA and EBSD analyses .....	95
Article #2 : Microstructural and Thermal Characterization of 316L+WC Composite Coatings obtained by Laser Cladding .....	111
Article #3 : Heat accumulation in multiple-layer 316L+WC composite deposit fabricated by directed energy deposition: Influence on local microstructure and hardness .....	123
Article #4 : Wear behaviour of laser clad 316L + WC composite against alumina .....	147
Article #5 : On the microstructures and strengthening mechanisms of new high-silicon austenitic stainless steels obtained by Laser Cladding.....	175
Curriculum Vitae .....	205

---

---

## Acknowledgements

It seems that it is done. I write these acknowledgements after this page has already been turned and months and months stepped away, but I still have crystal clear in my mind all the people that I met and what they have done for me.

I would like to start with prof. Jacqueline Lecomte-Beckers, who has “guilt” of my presence at the University of Liège and who, even if in a relatively short time together, transmitted me a lot of her experience and work discipline. I would like to also thank prof. Anne Mertens, who supervised my work after prof. Lecomte-Beckers and let me propose my ideas, accepting the topic of this PhD. Nevertheless, the two professors won’t blame me if I highlight the importance of my mentor Dr Jérôme Tchoufang Tchoundjang. Over these years, from my master thesis to the end of the PhD thesis, he made me a better person and a better scientist, being himself an example. I hope that I’ve honoured his example of undefeatable love for research. I’ll always remember the long discussions in front of one or two coffees until dark.

I would like to thank my clad-buddies Hakan Paydas and Olivier Dedry for their friendship during these years and, of course, for their practical support and their professionalism. Of course, I want to acknowledge the other members of the Metallic Material Science (MMS) team, Sylvie Salieri, Rosine Pirson, Sylvie Reginster, Neda Hashemi, Henry-Michael Montrieux for the moral support that they offered me and for making me feel like in a very multicultural family.

In these years, I had the honour to supervise few young engineers during their master theses and thus I would like to thank Daniele Mario, Enrico Saggionetto, Elena Mancini, Mattia Nordera, Iñigo Serrano, Chiara Corongiu and Tobia Niccolini for their work and enthusiasm. Hope to have left something good.

I would like to acknowledge also Prof. Duysinx for his kindness since my first day, Dr Boschini for his interest in my research, Prof. Ertugrul for his stubbornness, Vincent Delaval for his patience, Samuel Rondia for his professionalism and Julien Magnien and Raoul Carrus for their precious help with the laser cladding.

A special thanks to Laura Zorzetto and my all lifelong friends Fabio Barbisan, Luca Ortali and Antonio Ferrandino for always being there when I needed them. It doesn’t matter how far we are from each other.

I would like to also thank Jonathan Velasco, Joao Ferreira and Andreea Bela for their friendship in difficult times and for their strength in facing life. You are an example for me.

A très grande merci to my French family, Etienne Boulier, Klara Weck, Brian Traquet and Margaux Tornare for all the good time that we spent together in rue de 22, for all the discussions together, for

---

---

being the only ones on my side in very difficult moments and for the “addiction” to board games. I’ll miss these moments spent with you.

Of course, I should give gratitude to all the people that shared my path during these years in Belgium: Radomir Jasic, Pablo Morato, Lucas Marquez, Antonio Gamba, Nikola Tatar, Paola Genevini, Marina D’Antimo, Sara Echeverry and Ruben Jardin. Thank you for having shared your journey with me.

I want also to thank my friends Beatrice Pezzutto, Chiara Zanusso, Roberta Pietri, Elena Briasco, Anett Laukova, Marco De Lazzari, Nicola Mestriner and Riccardo De Gobbi for always being there for a good word or for really bad ones when it was necessary.

With all my heart, I want to thank my family and my Spanish family for supporting me in this adventure and always encouraging me in difficult moments. In particular, thanks to my parents and my brother, I could blossom over the years and embrace my curiosity for science.

Last but really not the least, I want to thank with all the cells of my body my love Ana for who she is and for what she did for me in these years of waiting, growing together and even learning about life together.

---

---

## Abstract

Additive manufacturing (AM) has experienced significant growth over the past 25 years in several areas, ranging from the conception of new machines to the number and complexity of parts produced.

Currently, a particularly interesting research field is the development of alloys and composite materials which are only accessible due to the particularities of AM processing. The improvement or modification of existing alloys by AM is a further step to open new possibilities for the industries. Such modification of the existing alloys can be achieved by combining available raw materials to adapt their compositions or create metal matrix composites. The fabrication of these materials can be carried out via powder-bed fusion processes (mostly known as selective laser melting) with prior mixing of the powders or via powder feeding techniques as laser cladding (LC) with powder mixing during the process. This is the context of the present PhD research, focused on understanding the underlying metallurgy of materials composed of 316L stainless steel and hard carbides fabricated by LC.

By considering three different reinforcements, a deeper understanding is gained of the interactions between ceramic powders and molten metal during LC. Indeed, depending on the nature of the reinforcement, partial or total dissolution of the particles occurs and the dissolved elements enrich the composition of the parent 316L matrix. This modification of the composition and the variation of the process conditions during deposition were considered in order to understand the resulting microstructures and mechanical properties.

In order to elucidate the new solidification routes of these complex materials, a novel methodology was first implemented on a complex graphitic high speed steel fabricated by centrifugal casting, and then its application was extended towards microstructures obtained after AM. This so-called “reverse analysis” is based on the backwards consideration of the differential thermal analysis heating curve and the features of the phases in the microstructures.

Macro-hardness, nano-hardness and wear resistance of the materials were evaluated to correlate the microstructures to the mechanical properties. Results highlight a remarkable improvement in all the considered mechanical properties compared to the parent 316L. Interestingly, a variation of these properties was observed, depending on the thickness of the coating, the volume percentage and the nature of the reinforcements. Pin-on-disc tests gave a good estimation of the improvement of the wear resistance and different wear behaviours. In particular, the novel approach of the interrupted tests is found efficient in order to elucidate both the wear mechanisms and the wear sequence.

In conclusion, this work highlights the possibility to tailor the microstructure of complex AM materials depending on the needs of the application.

---

Keywords: Laser cladding, metal matrix composite, cooling rates, carbide, reinforcements, powder handling, solidification, heat accumulation, DTA, hardness, nanoindentation, wear.

---

---

## Resumé

La fabrication additive (FA) a connu une croissance importante au cours des 25 dernières années dans plusieurs domaines, allant de la conception de nouvelles machines à la complexité des pièces produites.

Actuellement, un domaine de recherche particulièrement intéressant est le développement d'alliages et de matériaux composites via le procédé de FA, étant donné que les techniques de coulée conventionnelles ne le permettent pas. L'amélioration ou la modification des alliages existants par FA est une étape supplémentaire pour ouvrir de nouvelles possibilités aux industries. Cette modification des alliages peut se faire soit en combinant les poudres pour former par fusion complète de nouveaux alliages, soit en créant des composites à matrice métallique si on a seulement fusion partielle d'une des poudres. La fabrication de ces matériaux peut être réalisée par des procédés de fusion en lit de poudre (plus connus sous le nom de selective laser melting) avec mélange préalable des poudres ou par laser cladding (LC) avec mélange des poudres pendant le processus. C'est dans ce contexte que s'inscrit la présente recherche, qui vise à comprendre la métallurgie sous-jacente des matériaux composés par des mélanges d'acier inoxydable 316L et de carbures durs fabriqués par LC.

La prise en compte de types de carbures différents permet de mieux comprendre les interactions entre ces carbures et le métal fondu pendant le processus de déposition. En effet, le caractère partiel ou complet de la dissolution du carbure influence plus ou moins fortement la composition de la structure, que ce soit vis-à-vis des nouveaux carbures in situ ou de la composition de la matrice. Ces modifications elles-mêmes influencées par les paramètres du procédé qui peuvent varier en cours de fabrication sont considérées afin de comprendre les microstructures et les propriétés mécaniques associées.

Le schéma de solidification de tels matériaux composites élaborés par LC est déjà très complexe, avec l'existence de phases hautement hors équilibre. Une approche nouvelle est développée pour permettre d'étudier le schéma de solidification dans de tels matériaux. Pour ce faire, la nouvelle méthodologie est d'abord mise en œuvre sur un acier à outils graphitique fabriqué par coulée centrifuge, avant d'être étendue aux microstructures obtenues après FA. Cette approche dite " analyse inverse" est basée sur la prise en compte à rebours de la courbe de chauffage en analyse thermique différentielle, associée à une approche de caractérisation de phases hors équilibre via l'analyse EBSD.

La macro-dureté, la nanodureté et la résistance à l'usure des matériaux ont été évaluées afin de corrélérer les microstructures aux propriétés mécaniques. Les résultats mettent en évidence une amélioration remarquable de toutes les propriétés mécaniques considérées par rapport au 316L. Il est intéressant de noter qu'une variation de ces propriétés a été observée en fonction de la profondeur du dépôt, du pourcentage volumique et de la nature des carbures. Les tests de glissement sec par pion sur disque ont donné une bonne estimation de l'amélioration de la résistance à l'usure, tout en permettant

---

d'identifier les mécanismes d'usure, en considérant notamment une approche via des tests d'usure interrompus.

En conclusion, ce travail met en évidence la possibilité d'adapter la microstructure de matériaux AM complexes en fonction des besoins de l'application.

Mots-clés : Revêtement laser, composite à matrice métallique, vitesses de refroidissement, carbure, renforts, manipulation de poudre, solidification, accumulation de chaleur, DTA, dureté, nanoindentation, usure.

## 1. Introduction and context

### 1.1. Concept and brief history of Additive Manufacturing processes

Additive manufacturing (AM), commonly known as three-dimensional (3D) printing, has grown and changed tremendously in the past 30 years. The main difference between AM and classical manufacturing processes lies in the building concept. Indeed, classical manufacturing approach is composed of near-net-shape processes (i.e. forging, casting etc.) and subtractive processes (i.e. CNC machining, electrical discharge machining (EDM) etc.), where material is removed from a simple-design blank in order to obtain the final part (Fig. 1-1). The advantages of this approach are the great dimensional accuracy and the large choice of material, including wood, metal and polymers. The obvious downfall is the large waste created during the process (Thompson, 2015; Wei, 2020).

On the other hand, AM processes build or add material layer by layer in order to fabricate the targeted object (Fig. 1-1), using powders, wire or other feedstock (DebRoy, 2018; Martin, 2017; Sames, 2016; Todd, 2017). The major benefit of AM consists in achieving near-net-shape parts of complex design with reduced waste of material over the whole process.

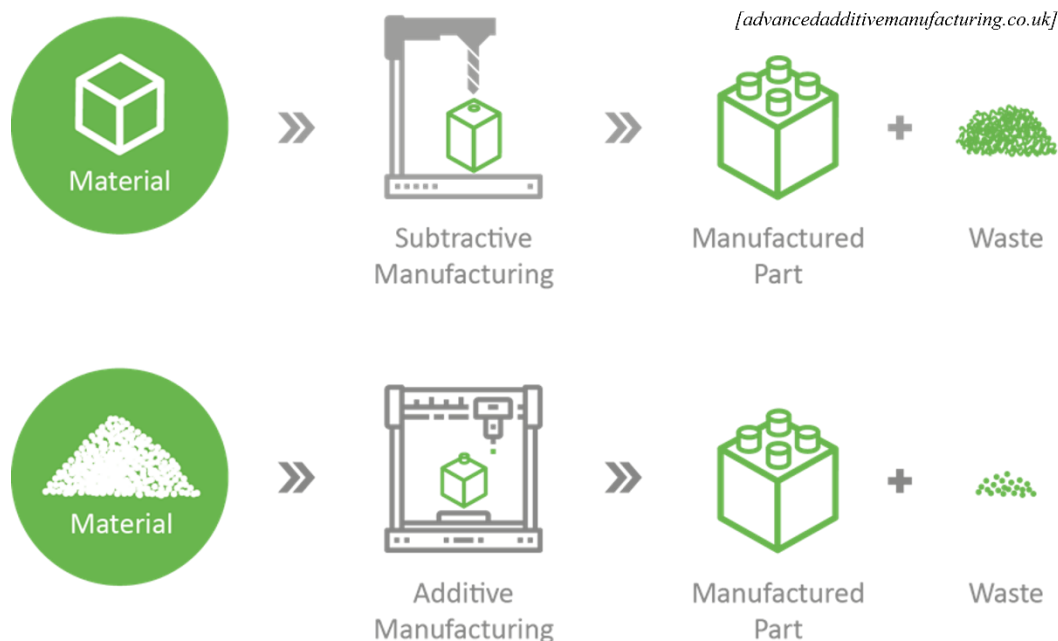
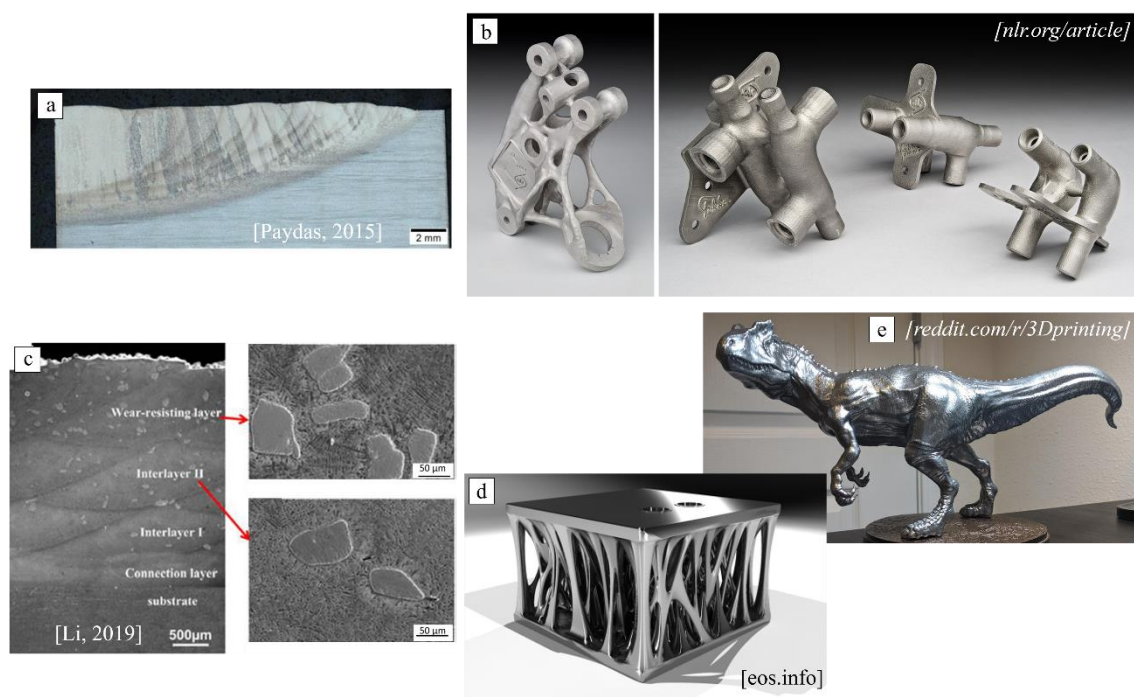


Fig. 1-1: Schematic illustration of the differences between subtractive (conventional) manufacturing processes and additive manufacturing processes.

The first commercialized AM technologies have been available since the late 80s, which are the Stereolithography (SLA) and the Selective Laser Sintering (SLS), where polymer feedstock solidifies under laser radiation. These technologies are still used today in prototyping applications (AMpower, 2019; Sames, 2016).

The first experiments relevant to metal AM started by adapting technologies already applied to polymers. The first reported metallic ‘3D printed’ object was fabricated in an adapted SLS machine in 1990 using metal powders (copper, tin and Pb-Sn solder). The first commercial SLS for metal was introduced by EOS system in 1994 (*AMpower, 2019*). Only in 1999 FOCKELE & SCHWARZE introduced the first Selective Laser Melting (SLM) system, after the development within the early 90s of high energy fiber lasers able to directly melt metal alloys. The term SLM generally refers to all the metal powder-bed fusion (PBF) processes with a laser as a heat source and where complete melting of the metal powders is achieved (*Sames, 2016*). The key feature of this technology is the capability to achieve complex geometries, although with limited size and often with porosities or other printing defects (Fig. 1-2b, d and e).



*Fig. 1-2: Few examples of the potential of AM. Researchers in academia are investigating new possibilities and materials (a and c). The continuous improvement of the devices (d) and the materials (c) is attracting increasing attention from the industry (b) and the general public (e).*

Another important class of devices, which use a laser as a heat source, is known as Laser Cladding (LC) or Directed Energy Deposition (DED). It allows to handle two or more different powders that are fed into a focused laser beam while being scanned across a substrate, thus leaving behind a coating or an object. This technology is fed by powders as well as wires and traces its history to welding technologies. It was developed as AM technology by Sandia National Laboratories in 1995, applying a laser heat source (*Sames, 2016*). Then in 1998, OPTOMECH sold the first commercial LC machine and other companies followed over the next two decades (*AMpower, 2019*). LC is considered an underdog among the various AM technology mainly because it does not build complex geometries. Nevertheless, it has the capacity of producing high-strength, multi-materials parts and most of all, it is

versatile. It can build parts from scratch, add features to existing parts, or repair damaged or worn objects, reaching a full metallurgical bond (Fig. 1-2a and c) (Lang, 2020).

At the beginning of this century, many companies discontinued their engagement in these technologies due to limited market size, low prospects in machine sales, high costs and low reproducibility of the produced parts. The commercial and scientific turning point of these technologies occurred in 2013 with the expiration of the patents from Fused Deposition Modelling (FDM), a polymer-based AM technology, which pushed low-cost PBF machines into the consumer market (AMpower, 2019; Sames, 2016). Following this change, news coverage of AM increased significantly, presenting AM as the ultimate future in manufacturing. Stock prices of AM companies skyrocketed. PBF machines in particular were sold to many curious industrial users and R&D departments. For the following five years, PBF system suppliers achieved a continuous increase in sales as many adopted the technology. The typical applications were part repairs (Fig. 1-2a), biomedical implants, aerospace structures (Fig. 1-2b) and high-temperature components (Martin, 2017).

Early in 2015, stock prices of traded AM companies declined significantly due to the difficulties to replace completely the classical manufacturing processes at the industrial scale (Sculpteo, 2020). Nevertheless, the sales in PBF systems kept steady as a great number of industries, such as aerospace, energy and gas & oil were adopting the technology.

Indeed, recent years have seen consistent media, academic and industry interest in AM, fuelled by reports of high growth rates and publicity around exciting new case studies. A damaging consequence of this attention is the lack of realistic approaches to understand the sector and the degree to which it can ever be as transformative as pundits would lead the general public to believe. Nowadays, the emerging two approaches are the hybrid Additive Manufacturing, where powder bed AM and LC are combined with classical manufacturing processes and the research of new materials for AM (Dávila, 2020; Johns, 2020; Sames, 2016; Sculpteo, 2020; Wei, 2020). This PhD thesis by articles has as aim to contribute to the development of new solution for AM. In particular, the research of new alloys or composite will be further discussed in section 1.3.

## 1.2. Feedstock for AM

Metal AM feedstock has unique requirements. For the most part, it is in the form of metallic powders. As a matter of fact, metal AM is considered as part of a larger and earlier world called powder metallurgy (PM), where a large variety of powders are used in many industries (Al-Mangour, 2015; Dawes, 2015; Kingsbury, 2019). AM is considered a recent and expensive niche of PM since its volume market is still very small. Metal powder production, in general, is inefficient without

sufficient manufacture scale and thus if the demand is variable, the market pricing remains fluid and inflated as a result (*Kingsbury, 2019*).

In recent years, there has been an emphasis on the development of atomising equipment to produce dedicated AM powders in order to meet stringent customer requirements around morphology, purity and particle size distribution. Indeed, in order to assure high quality of the final parts, powders must exhibit specific characteristics, such as spherical or globular shape to ensure good flowability, tailored particle size distribution for the specific machine and high purity without presence of oxidation (*Aboulkhair, 2019; Dawes, 2015*).

Most of the AM machines users that do not have a PM or metallurgical background think that many of the defects occurring during printing (i.e. porosities, cracking, laser spatter and shape distortion) are only due to the process parameters or to the limited capacities of the machine. In contrast, in most cases, these problems are mainly due to poor handling of the powders or to the use of materials that were not designed for AM (*Aboulkhair, 2019; Gingell, 2019; Sames, 2016*).

When AM technologies first appeared (section 1.1), companies and researchers have applied weldable alloys available in the PM market to the layer-by-layer process. Indeed, at that stage, the interest was in the development of the machines since the technology was still in its infancy (*AMpower, 2019; Sames, 2016; Sculpteo, 2020*). On the contrary, in recent years, machines have achieved good performances and their development is still proceeding. Nowadays particular attention is being focused on materials (*Aboulkhair, 2019; Gingell, 2019; Johns, 2020; Kingsbury, 2019*). The rapid rise of AM system sales since 2013 has been met by a corresponding rise in the demand for AM-specific metal powders. Materials companies are targeting this high-growth and high-margin market, first investing in AM powder capacity and then enlarging their portfolio with known alloys (*Gingell, 2019; Kingsbury, 2019; N. Li, 2019*).

The effect of these large investments on AM powder production is evidenced by decreasing AM powder prices observed over the past five years (*AMpower, 2019; Johns, 2020*). This reduction is positive for the industry since it leads to lower part cost and it also puts significant pressure on powder manufacturers to remain competitive (*Johns, 2020*).

### 1.3. Materials for AM vs materials by AM

As mentioned in section 1.2, with AM on the rise, customers and producers alike are shifting their focus toward the materials that are commercially available for this technology. Indeed, the most crucial barrier for the widespread adoption in AM nowadays is considered to be the low number of alloys usable as standard material for AM parts. Compared to conventional processes, only 50 out of almost 5500 alloys are available for AM (*Beckers, 2019; Martin, 2017*).

Therefore, a novel trend is emerging, considering the design of a new generation of alloys for AM and by AM. Indeed, for 5000 years, whenever a new manufacturing method was invented, new materials and alloys have never been far behind (Gingell, 2019). As also shown in Fig. 1-3, the performance of components has been higher when they are made from alloys that have been tailored for a specific manufacturing process. AM is not likely to be any different. Indeed, powder producers and developer as Aubert&Duval and OxMet are working with metallurgists in order to improve the printability, by improving the weldability and decreasing the crack susceptibility. Furthermore, a further target is to exploit the refined microstructures formed at extremely high cooling rates in AM technologies, thus improving component performances (N. Li, 2019; Tang, 2020).

Besides, the fabrication of composite materials by AM has been investigated in recent years, leading to microstructures and properties hard to obtain with PM or other conventional manufacturing processes (Deschuyteneer, 2015; N. Li, 2019; A. I. Mertens, 2016). In particular, LC has shown large possibilities in that respect as it allows to handle two or more powders, while varying their amount at the same time. Therefore, structures can be added onto work pieces, including functionally graded material (FGM). Such addition can then deliver specific and beneficial properties (i.e. improved corrosion or wear resistance) at localised parts of a component (Lang, 2020; N. Li, 2019).

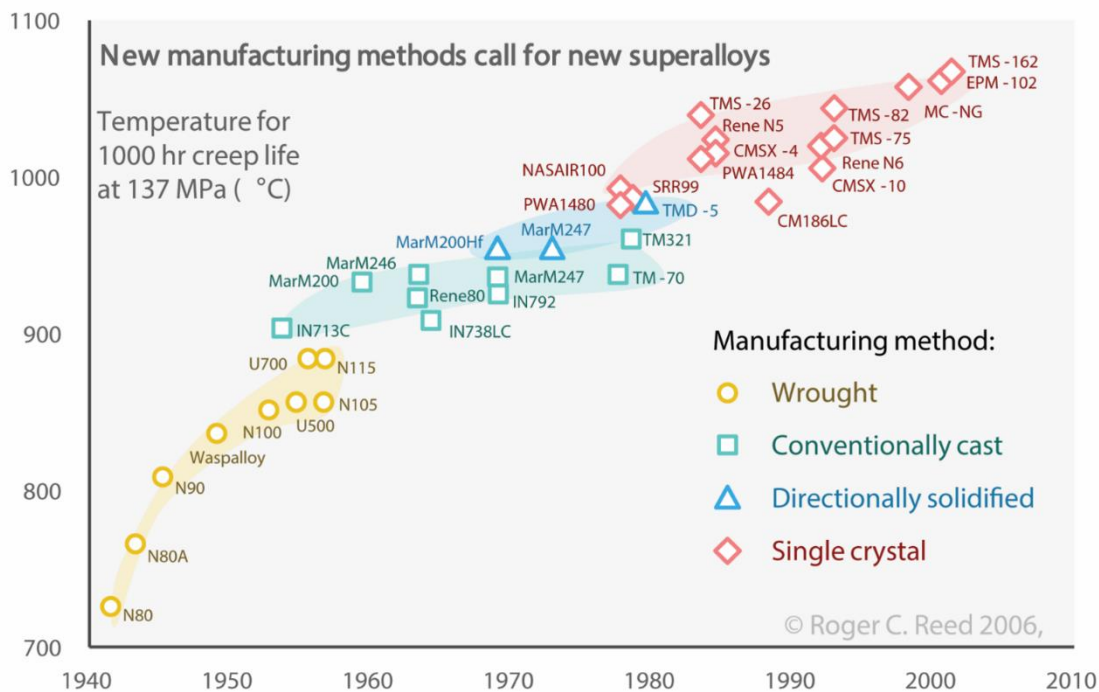


Fig. 1-3: Example of the evolution of the performance through the years with the development of new processes and thus new alloys (Gingell, 2019).

Moreover, LC can be quite performant for materials development since the quantity of powders needed is small in comparison to PBF and since this process is able to quickly build deposit with a 100% dense, metallurgically bonded and tailored material (Aboulkhair, 2019; Lang, 2020; N. Li, 2019; Sames, 2016).

#### 1.4. Purpose of the work

LC was used in this work in order to modify the 316L stainless steel, a work-horse material, applied where the corrosion resistance is a paramount requirement, but with poor wear resistance (*Todd, 2017; Wang, 2018*). To overcome this weakness and evaluate possible modifications of this common alloy, the introduction of harder reinforcement or reactants during LC could be considered, creating either a Metal Matrix Composite (MMC) coating or a modified alloy upon a 316L substrate. MMC refer to a class of materials in which two or more materials are combined by some means in order to achieve improvements in specific responses. Often, hard and brittle ceramic reinforcements are embedded into ductile alloy matrix, aiming to combine the good properties of both, thus paving ways for better design options and solutions.

316L was chosen as the hosting matrix due to the large number of studies focused on its application in AM and due to its high Ni and Mn contents, which assures the stabilisation of an austenitic matrix (*Feenstra, 2020; J. Li, 2019; Todd, 2017; Wang, 2018*). Indeed, alloys exhibiting displacive phase transformation (i.e. bainitic and martensitic transformation) were avoided, to focus on the interactions between reinforcement and hosting matrix.

WC and SiC were chosen as reinforcements due to their high hardness, chemical affinity with Fe-based alloys, theoretical high melting point and easy availability in the market (*Pierson, 1996; Thawari, 2003*). WC is often selected as reinforcement in Ni-based alloys for applications above 600°C and Fe-based alloys for applications up to 400°C (*Deschuyteneer, 2015; Domitner, 2019; Lu, 2019*). On the other hand, although SiC has been widely considered as reinforcement in several alloys in PM applications, there are discrepancies regarding its effect and performances when processed by AM (*Brytan, 2011; Dutta Majumdar, 2009; Lian, 2020; A. Mertens, 2017; Patankar, 2000; Yip, 2015*).

This PhD research aims to understand the metallurgy behind materials composed of 316L and hard carbides fabricated by AM. Additional attention is given to the insights that this work may deliver on the design of future alloys for AM. For this purpose, the characterization of out-of-equilibrium microstructures is presented within Article #1 and #2. The interactions between reinforcements and the molten metal at high temperature and the influence of the deposition conditions are considered in Article #2, #3 and #5, and finally, the mechanical properties are evaluated in Article #3, #4 and #5. Table 1-1 summarizes the main articles that will be considered for this thesis.

Moreover, prior to the study of structures generated by LC, the microstructure of a complex High Speed Steel (HSS) manufactured by centrifugal casting, was considered to set an efficient and relevant characterization method for out-of-equilibrium microstructures (*Boccalini Jr, 2001; Lecomte-Beckers, 2009*). Although it is considered a conventional manufacturing process, centrifugal casting is

characterized by fast cooling rates (albeit lower than for AM), thus leading to the occurrence of metastable phases during solidification stage (Hashimoto, 2004; Tchuindjang, 2011). This complex microstructure rich with hard carbides is considered here to provide the link between the conventional microstructures under equilibrium conditions and the out-of-equilibrium microstructures typical of AM processes.

Table 1-1: List of the five main contributions of this PhD research. The original versions of the five articles are given in Appendix following the chronological order of publication/submission.

Article	Complete title [status]
1	Maurizi Enrici, T., Mertens, A., Sinnaeve, M., & Tchuindjang, J. T. (2019). "Elucidation of the solidification sequence of a complex graphitic HSS alloy under a combined approach of DTA and EBSD analyses." <i>Journal of Thermal Analysis and Calorimetry</i> , 1–15. <a href="https://doi.org/10.1007/s10973-019-09093-9">https://doi.org/10.1007/s10973-019-09093-9</a>
2	Maurizi Enrici, T., Dedry, O., Boschini, F., Tchuindjang, J. T., & Mertens, A. (2020). "Microstructural and Thermal Characterization of 316L+WC Composite Coatings obtained by Laser Cladding." <i>Advanced Engineering Materials</i> , 13, 1–12. <a href="https://doi.org/10.1002/adem.202000291">https://doi.org/10.1002/adem.202000291</a>
3	Maurizi Enrici, T., Dedry, O., Mario, D., Paydas, H., Tchoufang, J., & Mertens, A. (n.d.). "Heat accumulation in multiple layers 316L + WC composite fabricated by DED: influence on local microstructure and hardness" [Submitted to Additive Manufacturing].
4	Maurizi Enrici, T., Mario, D., Dedry, O., Castagne, S., Tchuindjang, J. T., & Mertens, A. (n.d.). "Wear behaviour of laser clad 316L + WC composite against alumina." [Submitted to Additive Manufacturing.]
5	Maurizi Enrici, T., Saggionetto, E., Dedry, O., Ertugrul, O., Boschini, F., Tchuindjang, J. T., & Mertens, A. (n.d.). "On the microstructures and strengthening mechanisms of new high-silicon austenitic stainless steels obtained by Laser Cladding" [In preparation]

The structure of the thesis is as follows.

After the ongoing introduction and context (section 1), a brief state of the art (section 2) is followed by the main claims and contributions (section 3) of the five research manuscripts (Table 1-1). Every time, a reminder is made within the five articles regarding the related outcomes. Few additional results are presented to give a broader picture of the work (including results from several master theses connected to the PhD work over the past 4 years and papers published but not directly considered within the body of the thesis).

Regarding the body of the thesis in section 3, the general purpose of the work is cast into five specific sub-topics, which correspond to the necessary steps in the fabrication and characterization of a material manufactured by LC:

- **Powder handling and preparation**

The development of modified alloys and MMC is explored by combining different feedstock. Depending on the characteristics of each powder, correct powder handling and preparation are needed to fabricate a sound and homogeneous deposit via LC.

- **Fabrication**

The microstructures observed at room temperatures arise from the interactions at high temperatures between the melt pool and the reinforcements. In case of dissolution of the reinforcements, the modification of the original alloy composition leads to a variation of the solidification route.

- **Macroscopic characterization**

With the progress of the fabrication of thick deposits, heat accumulation leads to variations of the cooling rates and thus the residence time at high temperatures. These variations influence the solidification conditions and thus the final microstructures. Macrohardness measurements along the deposit height are considered to evaluate these variations.

- **Microstructure characterization of complex microstructures**

The phases formed at extremely high cooling rates are analysed with a novel characterization method, allowing the elucidation of complex out-of-equilibrium solidification routes.

- **Characterization of the properties**

The evaluation of the improved properties of the 316L+XC materials was carried out via nanoindentation and pin-on-disc tests in order to determine the influence of any given phase in the wear mechanisms and to highlight micro-macro correlations.

## References section 1

- Aboulkhair, N. T., Simonelli, M., Parry, L., Ashcroft, I., Tuck, C., & Hague, R. (2019). "3D printing of Aluminium alloys: Additive Manufacturing of Aluminium alloys using selective laser melting." *Progress in Materials Science*, 106(May), 100578. <https://doi.org/10.1016/j.pmatsci.2019.100578>
- Al-Mangour, B. (2015). "Powder metallurgy of stainless steel: State-of-the art, challenges, and development." In *Stainless Steel: Microstructure, Mechanical Properties and Methods of Application* (pp. 37–80).
- AMpower. (2019). *AMpower Report 2019*. Retrieved from <https://additive-manufacturing-report.com/technology/additive-manufacturing-history/>
- Beckers, D. (2019). "Rapid qualification of new alloys for Additive Manufacturing through a holistic process chain." *Metal Additive Manufacturing*, 5(2), 159–166.
- Boccalini Jr, M., & Goldenstein, H. (2001). "Solidification of high speed steels." *International Materials Reviews*, 46(2), 92–115. <https://doi.org/10.1179/095066001101528411>
- Brytan, Z., Dobrzański, L. a, & Pakieła, W. (2011). "Laser surface alloying of sintered stainless steels with SiC powder." *Journal of Achievements in Materials and Manufacturing Engineering*, 47(1), 42–56.
- Dávila, J. L., Neto, P. I., Noritomi, P. Y., Coelho, R. T., & da Silva, J. V. L. (2020). "Hybrid manufacturing: a review of the synergy between directed energy deposition and subtractive processes." *International Journal of Advanced Manufacturing Technology*, 110(11–12), 3377–3390. <https://doi.org/10.1007/s00170-020-06062-7>
- Dawes, J., Bowerman, R., & Trepleton, R. (2015). "Introduction to the additive manufacturing powder metallurgy supply chain." *Johnson Matthey Technology Review*, 59(3), 243–256. <https://doi.org/10.1595/205651315X688686>
- DebRoy, T., Wei, H. L., Zuback, J. S., Mukherjee, T., Elmer, J. W., Milewski, J. O., ... Zhang, W. (2018). "Additive manufacturing of metallic components – Process, structure and properties." *Progress in Materials Science*, 92, 112–224. <https://doi.org/10.1016/j.pmatsci.2017.10.001>
- Deschuyteneer, D., Petit, F., Gonon, M., & Cambier, F. (2015). "Processing and characterization of laser clad NiCrBSi/WC composite coatings - Influence of microstructure on hardness and wear." *Surface and Coatings Technology*, 283, 162–171. <https://doi.org/10.1016/j.surfcoat.2015.10.055>
- Domitner, J., Aigner, M., Stern, T., Paar, A., Sommitsch, C., & Elizondo, L. (2019). "Thermo-Mechanical Wear Testing of Metal Matrix Composite Cladding for Potential Application in Hot Rolling Mills." *Steel Research International*, 1900478. <https://doi.org/10.1002/srin.201900478>
- Dutta Majumdar, J., Kumar, A., & Li, L. (2009). "Direct laser cladding of SiC dispersed AISI 316L stainless steel." *Tribology International*, 42(5), 750–753. <https://doi.org/10.1016/j.triboint.2008.10.016>
- Feenstra, D. R., Cruz, V., Gao, X., Molotnikov, A., & Birbilis, N. (2020). "Effect of build height on the properties of large format stainless steel 316L fabricated via directed energy deposition." *Additive Manufacturing*, 34(April), 101205. <https://doi.org/10.1016/j.addma.2020.101205>
- Gingell, R. (2019). "Alloys by Design: The future of materials for Additive Manufacturing." *Metal Additive Manufacturing*, 5(4), 119–127.
- Hashimoto, M., Kubo, O., & Matsubara, Y. (2004). "Analysis of carbides in multi-component white cast iron for hot rolling mill rolls." *ISIJ International*, 44(2), 372–380. <https://doi.org/10.2355/isijinternational.44.372>

- Johns, J. (2020). "Current perspectives on metal AM: Hype , volume manufacturing and the geographies of production." *Metal Additive Manufacturing*, 6(1), 123–133.
- Kingsbury, A., & Horvath, D. T. (2019). "The evolving metal powder marketplace: Total solutions, vertical integrations and start-up innovations." *Metal Additive Manufacturing*, Vol. 5 No.(4), 109–116.
- Lang, M. (2020). "From aerospace engineering to AM: Melanie Lang on FormAlloy and the future of Directed Energy Deposition (DED)." *Metal Additive Manufacturing*, 6(3), 145–152.
- Lecomte-Beckers, J., & Tchuindjang, J. T. (2009). "Structural Investigations of Solidification and Heat Treatments Influence on High Alloyed Cast Irons Grades with Nb-V-Ti additions." *Defect and Diffusion Forum Series*, 289–292, 77–86. <https://doi.org/10.4028/www.scientific.net/DDF.289-292.77>
- Li, J., Zhao, Z., Bai, P., Qu, H., Liang, M., Liao, H., ... Huo, P. (2019). "Tribological behavior of TiC particles reinforced 316Lss composite fabricated using selective laser melting." *Materials*, 16(6). <https://doi.org/10.3390/ma12060950>
- Li, N., Huang, S., Zhang, G., Qin, R., Liu, W., Xiong, H., ... Blackburn, J. (2019). "Progress in additive manufacturing on new materials: A review." *Journal of Materials Science and Technology*. The editorial office of *Journal of Materials Science & Technology*. <https://doi.org/10.1016/j.jmst.2018.09.002>
- Lian, G., Zhao, C., Zhang, Y., Feng, M., & Jiang, J. (2020). "Investigation intomicro-hardness and wear resistance of 316L/SiC composite coating in laser cladding." *Applied Sciences (Switzerland)*, 10(9). <https://doi.org/10.3390/app10093167>
- Lu, J. Z., Cao, J., Lu, H. F., Zhang, L. Y., & Luo, K. Y. (2019). "Wear properties and microstructural analyses of Fe-based coatings with various WC contents on H13 die steel by laser cladding." *Surface and Coatings Technology*, 369(April), 228–237. <https://doi.org/10.1016/j.surfcoat.2019.04.063>
- Martin, J. H., Yahata, B. D., Hundley, J. M., Mayer, J. A., Schaedler, T. A., & Pollock, T. M. (2017). "3D printing of high-strength aluminium alloys." *Nature*, 549(7672), 365–369. <https://doi.org/10.1038/nature23894>
- Mertens, A. I., & Lecomte-Beckers, J. (2016). "On the Role of Interfacial Reactions , Dissolution and Secondary Precipitation During the Laser Additive Manufacturing of Metal Matrix Composites : A Review." In I. V Shishkovsky (Ed.), *New Trends in 3D Printing (I.V., pp. 187–213)*. Rijeka, Croatia: InTech. <https://doi.org/10.5772/63045>
- Mertens, A., L'Hoest, T., Magnien, J., Carrus, R., & Lecomte-Beckers, J. (2017). "On the Elaboration of Metal-Ceramic Composite Coatings by Laser Cladding." *Materials Science Forum*, 879(November 2016), 1288–1293. <https://doi.org/10.4028/www.scientific.net/MSF.879.1288>
- Patankar, S. N., & Tan, M. J. (2000). "Role of reinforcement in sintering of SiC/316L stainless steel composite." *Powder Metallurgy*, 43(4), 350–352. <https://doi.org/10.1179/003258900666078>
- Pierson, H. O. (1996). *HANDBOOK OF REFRACTORY CARBIDES & NITRIDES: Properties, Characteristics, Processing and Applications*. (W. Andrew, Ed.). Albuquerque, New Mexico: NOYES PUBLICATIONS, Westwood, New Jersey, U.S.A.
- Sames, W. J., List, F. A., Pannala, S., Dehoff, R. R., & Babu, S. S. (2016). "The metallurgy and processing science of metal additive manufacturing." *International Materials Reviews*, 61(5), 315–360. <https://doi.org/10.1080/09506608.2015.1116649>
- Sculpteo. (2020). The state of 3D printing 2020. Retrieved from <https://www.sculpteo.com/en/>

- Tang, Y. T., Panwisawas, C., Ghossoub, J. N., Gong, Y., Clark, J., Németh, A., ... Reed, R. C. (2020). "Alloys-By-Design: Application to New Superalloys for Additive Manufacturing." *Acta Materialia*, 202, 417–436. <https://doi.org/10.1016/j.actamat.2020.09.023>
- Tchuindjang, J. T., Sinnaeve, M., & Lecomte-Beckers, J. (2011). "Influence of High Temperature Heat Treatment on in situ Transformation of Mo-rich Eutectic Carbides in HSS and Semi-HSS Grades." In 4th Conference ABRASION (pp. 61–75).
- Thawari, G., Sundararajan, G., & Joshi, S. V. (2003). "Laser surface alloying of medium carbon steel with SiC(P)." *Thin Solid Films*, 423(1), 41–53. [https://doi.org/10.1016/S0040-6090\(02\)00974-4](https://doi.org/10.1016/S0040-6090(02)00974-4)
- Thompson, S. M., Bian, L., Shamsaei, N., & Yadollahi, A. (2015). "An overview of Direct Laser Deposition for additive manufacturing; Part I: Transport phenomena, modeling and diagnostics." *Additive Manufacturing*. Elsevier B.V. <https://doi.org/10.1016/j.addma.2015.07.001>
- Todd, I. (2017). "Metallurgy: Printing steels." *Nature Materials*, 17(1), 13–14. <https://doi.org/10.1038/nmat5042>
- Wang, Y. M., Voisin, T., McKeown, J. T., Ye, J., Calta, N. P., Li, Z., ... Zhu, T. (2018). "Additively manufactured hierarchical stainless steels with high strength and ductility." *Nature Materials*, 17(1), 63–70. <https://doi.org/10.1038/NMAT5021>
- Wei, H. L., Mukherjee, T., Zhang, W., Zuback, J. S., Knapp, G. L., De, A., & DebRoy, T. (2020). "Mechanistic models for additive manufacturing of metallic components." *Progress in Materials Science*, (May). <https://doi.org/10.1016/j.pmatsci.2020.100703>
- Yip, M. W., Barnes, S., & Sarhan, A. A. D. M. (2015). "Deposition of a silicon carbide reinforced metal matrix composite (P25) layer using CO2 laser." *Journal of Manufacturing Science and Engineering, Transactions of the ASME*, 137(3), 1–8. <https://doi.org/10.1115/1.4029831>



## 2. State of the art

Metals exhibit different microstructures and intermetallics with different morphologies depending on the manufacturing process and the elements partitioning during solidification. This section shows few examples of advanced materials fabricated by AM in the last two decades (section 2.1) and microstructures formed under out-of-equilibrium conditions during centrifugal casting (section 2.2.1) and AM (section 2.2.2), focusing especially on classical Fe-based alloys. Moreover, a short comparison between the mechanical properties of metals fabricated by conventional and AM processes will be presented in section 2.3, with a particular focus on the wear properties of the 316L and its MMC.

### 2.1. Advanced materials fabricated by AM

AM is capable to fabricate a large range of materials, but the actual number of AM alloys is limited. Depending on the technology, stainless steels, Al-alloys, Ni-alloys, Ti-alloys can be printed. As also mentioned in section 1.3, from the rise of the metal AM, researchers have investigated the possibility to fabricate new MMC and later modified alloys by AM in order to enlarge the AM application range and to improve the properties of the limited number of available alloys. Traditionally, most of the classical manufacturing processes are not suitable for the production of MMC due to segregations issues, although molten stir casting techniques could overcome the problem to varying degrees (*Behera, 2020*). In contrast, powder metallurgy is employed efficiently for processing such materials with better control of the dispersion of the reinforcements. However, this method suffers from limitations such as the fabrication of complex shapes and the densification of the final parts. Therefore, the interest of the MMC fabrication by AM lies in the higher densification compared to powder metallurgy-based methods due to the higher capillary forces for the liquid flow and the higher wettability of the hosting matrix to the reinforcements (*Behera, 2020; Su, 2020*).

Fig. 2-1 shows few examples of the strengthening mechanisms that may be obtained in MMC fabricated via SLM or PBF technologies. MMC fabricated by LC will be presented separately in section 2.1.1. Indeed, depending on the relative feedstock of the techniques and the process itself, different MMC are obtained. In addition to the characteristics mentioned in section 1.1, for MMC fabrication, the SLM limitations are mainly the size of the reinforcements, the obligation to use pre-mixed powders and the difficulties to keep a homogeneous composition with the increase of the percentage of reinforcements (*AlMangour, 2017; N. Li, 2019*).

Prior to the SLM fabrication, particles of the reinforcement and of the matrix must be mixed in order to obtain the feedstock for the AM machine. For this purpose, mechanical alloying is widely applied, where the two powders and larger balls (with radius ~ mm or cm) are mixed in a bowl in order to attach the smaller reinforcements to the softer matrix particles (Fig. 2-1d) (*Arik, 2006; Muvvala, 2018; Sheikhzadeh, 2012*). In this manner, the host particles, with suitable size for SLM, carry the reinforcements during the process. Homogeneous powder mixtures could also be obtained with

alternative methods without deformation of the powders (i.e. electrostatic absorption dispersion (Y. Song, 2019), tumbling mixer (Aboulkhair, 2019) or even ball milling without balls. When these methods are not applied, the difference among the densities of the two powders lead to powder segregations and thus to a heterogeneous MMC.

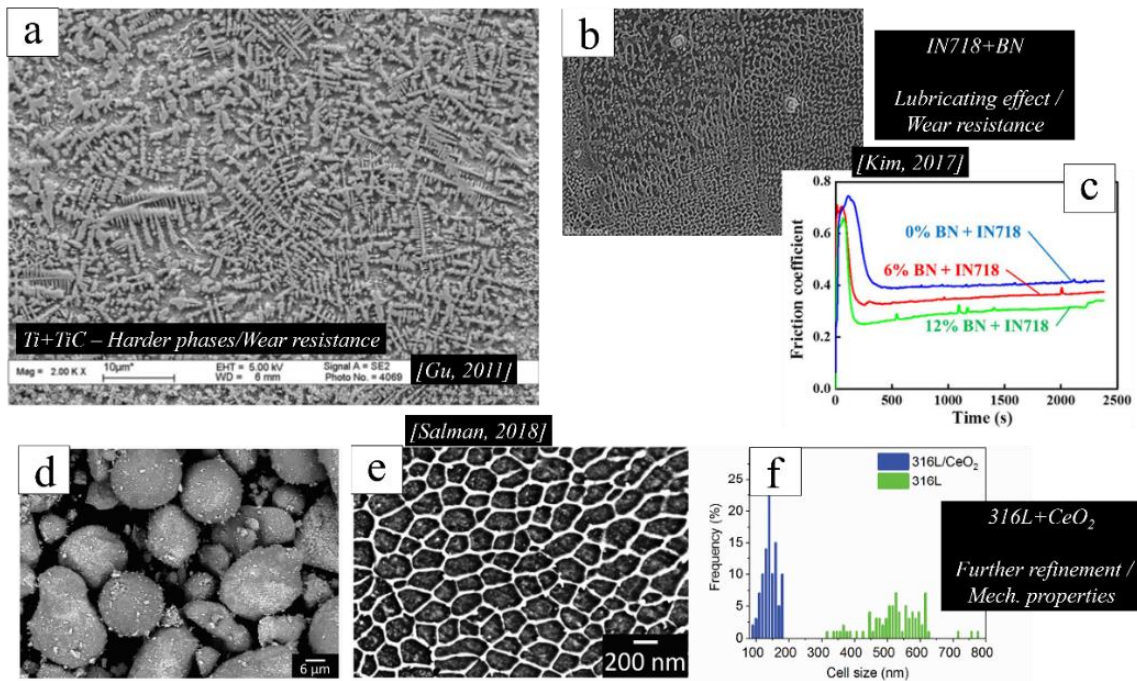


Fig. 2-1: (a) SLM-processed TiC/Ti nanocomposite microstructure (Gu, 2011). (b) Microstructure of IN718+6 vol.%BN composite and (c) the variation of the friction coefficient during wear test (Kim, 2017). (d) 316L/CeO<sub>2</sub> powder mixture ball milled for 2h, (e) 316L/CeO<sub>2</sub> microstructure and (f) the cell size of the parent 316L and the composite (Salman, 2018).

As shown in Fig. 2-1a, wear-resistant microstructure could be obtained from the dissolution of the initial reinforcements during the MMC fabrication and then the formation of harder solidification phases (Gu, 2011). Understanding the interactions between the two powders during fabrication and the dissolution of the initial reinforcements is a paramount need for the design and the fabrication of MMC. The total and partial dissolution or, on the contrary, the lack of dissolution are linked to the features of the powders. This will be considered in depth in section 3.2.2. Indeed, the original reinforcements can sometimes be maintained with lack of dissolution (Fig. 2-1b), obtaining self-lubricant properties (Fig. 2-1c) and thus the improvement of the wear resistance (Kim, 2017). Furthermore, an interesting approach is to obtain a grain refinement (Fig. 2-1f) with either the addition of reinforcements composed of high melting elements or low reactive reinforcements which act as nuclei for the heterogeneous nucleation (J. Hunter Martin, 2020; Salman, 2018).

### 2.1.1. Composites materials via LC

As mentioned in section 1.1, LC exhibits several advantages for MMC fabrication, linked to the possibility of handling two or more powders separately (Fig. 2-2), a larger range of acceptable powder size (Fig. 2-2d) compared to SLM and the possibility to vary the reinforcement/matrix ratio during the

deposition (Fig. 2-2b). LC main limitation is linked to the characteristics of the process allowing only for building simple geometries. Indeed, the main application of LC is the deposition of MMC coatings. As an example, Fig. 2-2 represents the large use of WC as reinforcement in Ni-based. Depending on the hosting matrix, a part of each particle is dissolved and this dissolution increases with the decrease of the particle size (Fig. 2-2d). Fig. 2-2a and c show the reinforced microstructures around the WC.

As in PBF technologies, the large variability of LC in raw materials (Fig. 2-3) allows to obtain MMC with lubricating properties (X. B. Liu, 2014; Torres, 2018), rather than simply add hard phases in the microstructures (Fig. 2-3a and c) (Akinlabi, 2019). Furthermore, mechanical alloying could also be applied in order to obtain a homogeneous powder mixture with a well-tailored high percentage of reinforcements prior to the LC (Candel, 2010; Muvvala, 2018). This approach enlarges even more the available choice of powders for LC since small reinforcements (1-20  $\mu\text{m}$ ) could be carried by the hosting powders (range of particle size = 50-200  $\mu\text{m}$ ).

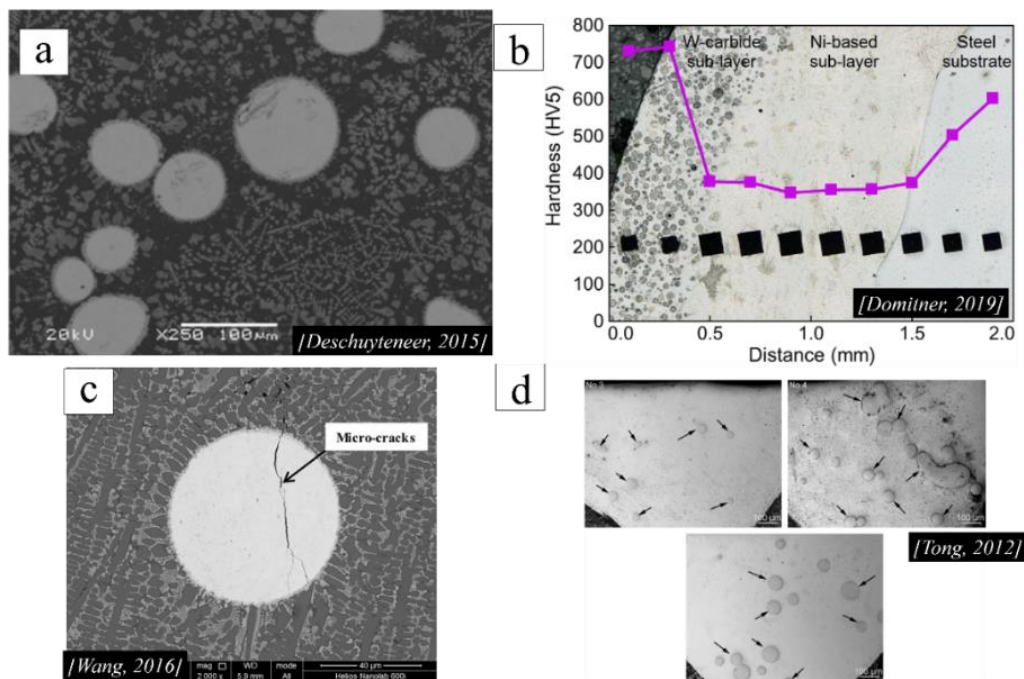


Fig. 2-2: (a) Microstructure of NiCrBSi/WC composite with 30 vol.% WC (Deschuyteneer, 2015). (b) Hardness profile at the cross-section of the clad FGM (Domitner, 2019). (c) Microstructure of 316L+WC composite with a micro-crack across the WC reinforcement (J. Wang, 2016). (d) Three tracks deposited with the same volume percentage, but with different WC size distribution. Dissolution of the WC is enhanced with the decrease of the reinforcement size (Tong, 2012).

Nevertheless, by enhancing the dissolution of the reinforcements, the high energies and temperature enforced during LC imposes that particular attention must be given to the design and match between host powders and reinforcements. Indeed, the application of SiC or  $\text{Al}_2\text{O}_3$ , that are theoretically considered as good reinforcement for PM, gives way to discrepancies in the literature about their interactions with Fe-based alloys during AM processes (Dutta Majumdar, 2009; Lian, 2020; Patankar, 2000; Stefanescu, 1990; Xu, 2014; Yip, 2015).

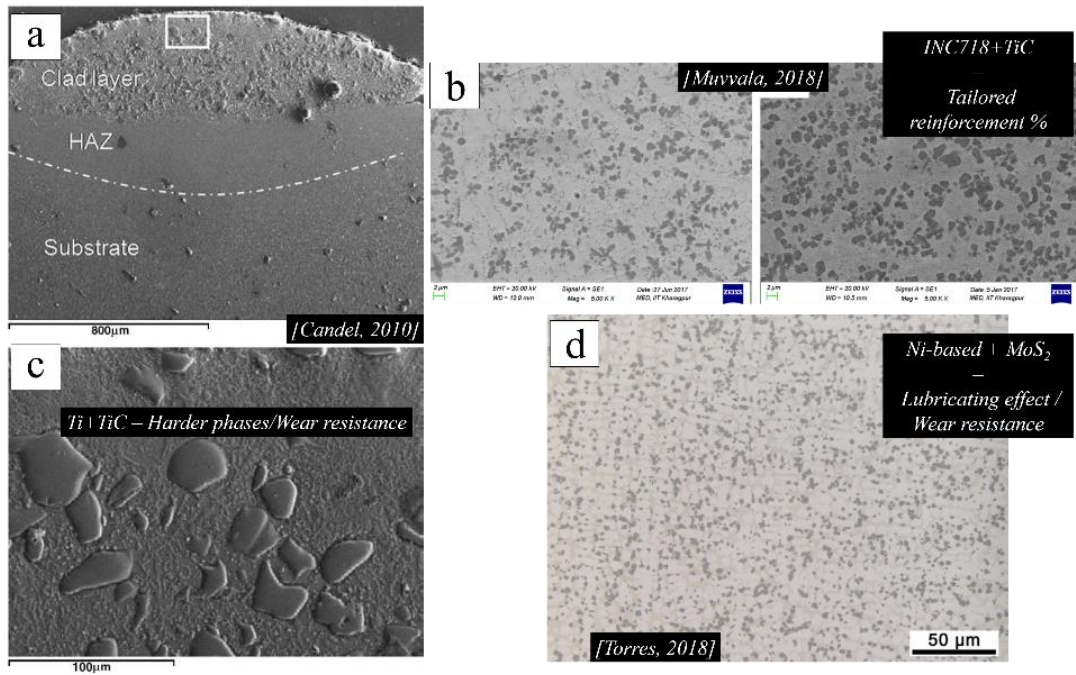


Fig. 2-3: (a and c) Cross-section of the Ti/TiC composite with 30 vol.% TiC (Candel, 2010). (b) Microstructure of INC718/TiC composite with respectively 20 and 30 vol.% TiC (Muvvala, 2018). (d) Microstructure of the Ni/MoS<sub>2</sub> with the 10 wt.% MoS<sub>2</sub>.

### 2.1.2. Modified alloys via LC

In micro-alloying or surface modification, tailored powder mixture and the enhanced dissolution characteristic of LC are used to completely dissolve the reinforcements, here used as reactants, and thus to form modified alloys (C. Li, 2019; Lian, 2020; Z. Zhang, 2016). The modification of the initial composition of commercial alloys may lead to a further refinement of the microstructure and contribute to the improvement of corrosion resistance and creep properties (B. C. Li, 2020; Z. Zhang, 2016). Depending on the hosting matrix and on the targeted improvement, the reactants may be introduced as either pure elements (e.g. Nb, Mo or Si) or as intermetallic (e.g. TiC or SiC). On one hand, pure elements are often used to stabilize specific phases in the microstructure or achieve an improvement of the corrosion resistance (B. C. Li, 2020; Vrancken, 2014; Wu, 2019; Y. L. Zhang, 2020; Z. Zhang, 2016). On the other hand, intermetallics are introduced when among the targeted improvements, the wear resistance is aimed (Krakhmalev, 2014; C. Li, 2019; Lian, 2020).

## 2.2. Metals fabricated under high cooling rates

### 2.2.1. Microstructures after centrifugal casting

Centrifugal casting is a process commonly applied to manufacture rolls for hot strip mills (Rajan, 2010), where the chosen material is poured in a turning mould before being melted in an arc furnace (Maurizi Enrici, 2015). High-speed steels (HSSs), high-alloyed cast irons (HACIs) and other complex materials (MMC or FGM) could be produced through this manufacturing process (Lecomte-Beckers, 2007; Luan, 2010; Rajan, 2010). In particular, among these materials, HSS has received great attention due to its versatility and its relatively wide range of chemical compositions.

In HSS, C content ranges between 0.3 and 2 wt.%, with the presence of strong carbide-forming elements such as V, Nb, Ta, Ti, W or Mo which lead to the formation of hard solidification carbides in a martensitic or bainitic matrix (Chen, 2016; Hashimoto, 2004; Lecomte-Beckers, 2012). The carbides content and distribution influence the mechanical properties of HSS, such as their strength, hot hardness, wear resistance or fracture toughness (Coronado, 2009; Delaunois, 2018; Luan, 2010; Tchuindjang, 2015). The nature, morphology and composition of the carbides depend on the alloy chemical composition and on the cooling rate during solidification (Boccalini Jr, 1999).

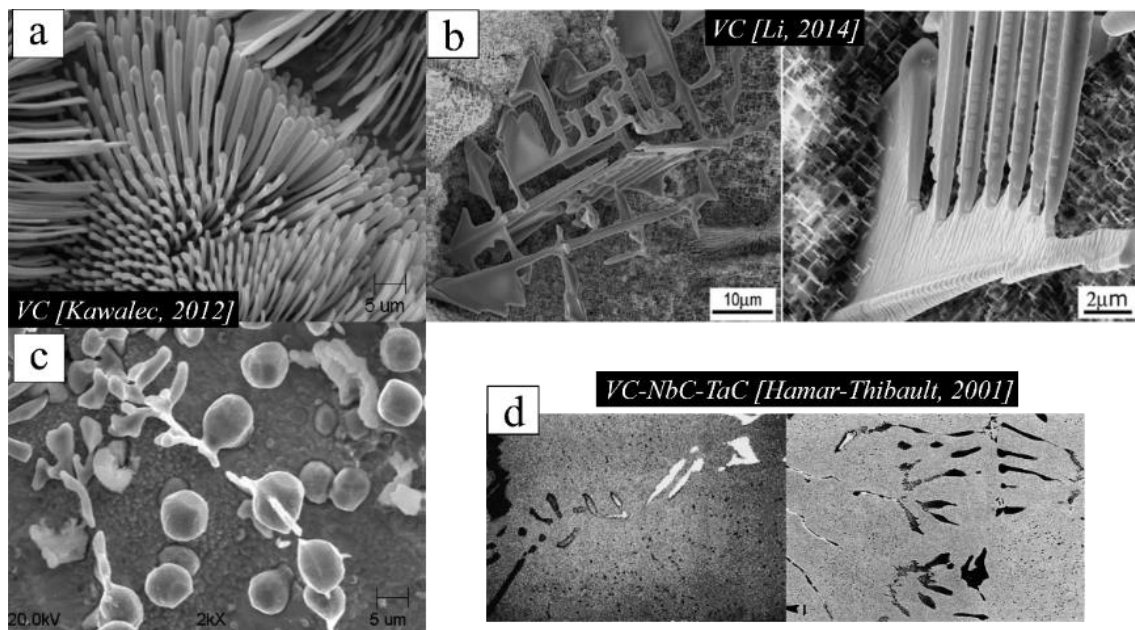


Fig. 2-4: SEM micrographs show (a and b) coral-like and (c) globular VC carbides (Kawalec, 2012); (d) Different contrasts (BSE mode) into branched (V, Nb, Ta)C carbides (Hamar-Thibault, 2001) correspond to a variation of the composition during solidification.

Depending on the moment of their formation during the casting process, carbides can be of various types, i.e. primary carbides, pseudo-primary carbides, eutectic and secondary carbides. Primary carbides (PCs) precipitate from the liquid and correspond to the liquidus temperature (Tchuindjang & Lecomte-Beckers, 2011). Pseudo-primary carbides (PPCs) forms by a process of cooperative growth with the austenitic matrix, where a gradient of composition from the core to the boundary of the cell is

observed (X. W. Li, 2014). Eutectic carbides (ECs) are formed at the end of the solidification and set the solidus temperature. They are located at the cell or grain boundaries. Finally, secondary carbides (SCs) precipitate in the solid-state and are mostly located inside cells or grains (Tchuindjang & Lecomte-Beckers, 2011; Yikun, 2010).

Hereafter, the most common carbides are described. Every refractory metal exhibits specific tendencies when combined with C. Therefore, based on these tendencies, carbides formed from direct solidification from the liquid could be distinguished: MC carbides where “M” is one high melting temperature element (V, Ti, Ta, Nb, Hf and Zr), Mo-W carbides and Cr-Fe carbides. The influence of secondary elements and of the cooling rates is considered as well.

V, Ti, Ta, Nb, Hf and Zr tend to form MC carbide in various morphologies (Hamar-Thibault, 2001; Lecomte-Beckers, 2009; Samsonov, 2008). Depending on their temperature of precipitation, these carbides exhibit divorced or irregular morphology as PCs (Fig. 2-4c), coral-like as PPCs (Fig. 2-4a and b) and branched petal-like as ECs (Fig. 2-4d). Divorced or globular morphology is also observed in SCs. High contents of these strong MC carbides formers enhance the PCs precipitation from the liquid phase, sometimes allowing the suppression of MC ECs. In addition, the higher the cooling rates, the higher is the tendency to form PCs rather than ECs (Boccalini Jr & Goldenstein, 2001). The crystal order is FCC and in particular, PCs and PPCs exhibit lattice parameters close to the ones of austenite since the carbides act as heterogeneous nuclei (Kawalec, 2012; X. W. Li, 2014). The composition of primary and pseudo-primary MC carbides shows variation from the centre outward, owing to their growth from a melt whose composition is continuously changing during solidification (Fig. 2-4d) (Boccalini Jr & Goldenstein, 2001; Kawalec, 2010). They are characterized by a high hardness both at room and high temperatures.

In contrast, W and Mo are exceptions among the refractory elements since during solidification from liquid, their most thermodynamically stable carbides are  $M_2C$  and  $M_6C$  ECs (Boccalini Jr & Goldenstein, 2001; Fischmeister, 1989). WC and MoC carbides may be synthesized from other conditions (Weimer, 2012). From the liquid, W favours, in particular, the formation of the  $M_6C$  carbides (Fig. 2-5c and d). This carbide is characterized by a three-dimensional morphology with a central platelet from which secondary platelets arise horizontally, showing a fishbone or skeletal morphology in the cross-section (Okane, 2001). This morphology is not influenced by chemical composition and it can exhibit Mo, Fe, V and Cr amounts. Furthermore, the  $M_6C$  formation is favoured by the minor presence of Si and Nb (Jiang, 2016; Pan, 2004).  $M_6C$  carbides exhibit a complex FCC crystal lattice (Hashimoto, 2004).

On the other hand, the formation of the  $M_2C$  carbides is favoured compared to the  $M_6C$  carbides with high cooling rates and with the increase of the Mo, V and C amounts (Boccalini Jr & Goldenstein, 2001; Hashimoto, 2004). Indeed, the  $M_2C$  carbides are commonly associated with Mo and they exhibit

an irregular or regular morphology (Fig. 2-5a and b) depending on the cooling rates and the chemical composition (Zhou, 2012). The irregular morphology is favoured at relatively lower cooling rates and high V content (Yikun, 2010). In contrast, the regular morphology is favoured at higher cooling rates and low V content.  $M_2C$  carbides exhibit a hexagonal crystal lattice (Hashimoto, 2004). Interestingly, studies have shown the tendency of the  $M_2C$  carbides to be metastable, decomposing usually into finer  $M_6C$  and  $MC$  carbides (Hashimoto, 2004; Tchuindjang, Sinnaeve, 2011; Zhou, 2012).

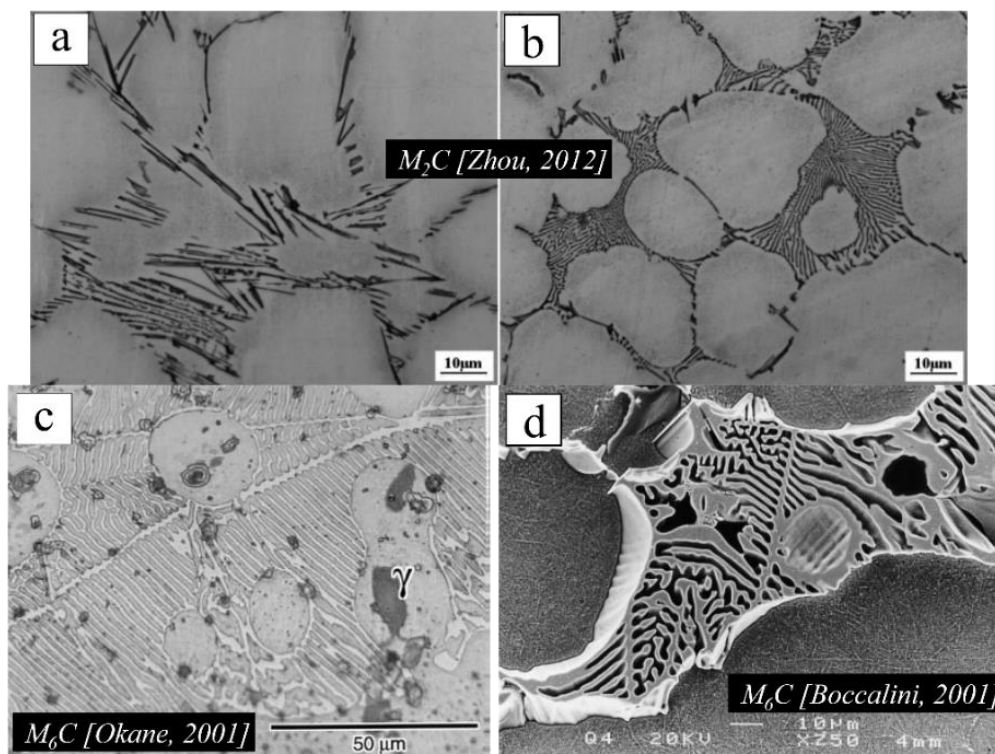


Fig. 2-5:  $M_2C$  carbides exhibit (a) irregular and (b) regular morphology (Zhou, 2012); (c and d)  $M_6C$  carbides exhibit a skeletal morphology in the intergranular spaces.

Another wide carbide category is composed of the  $M_7C_3$ ,  $M_3C$  and  $M_{23}C_6$  carbides, where “M” is typically associated with Cr and Fe.  $M_7C_3$  is the most associated with Cr and high cooling rates (Wieczerszak, 2016). This carbide could be observed as PCs or ECs depending on the Cr amount and it exhibits a characteristic pencil morphology (Buytoz, 2006; Ma, 2015). On the other hand,  $M_3C$  carbides (better known as cementite) are observed only as ECs in a compact or eutectic morphology (Lecomte-Beckers, 2009). Its formation is favoured by the presence of V and Si contents as minor alloying elements and low cooling rates (Bedolla-Jacuinde, 2013; Boccalini Jr, Serantoni, 2001; Sinatora, 1996). It exhibits high Fe amounts and lower Cr amounts compared to the  $M_7C_3$  carbides (Randle, 1993).  $M_{23}C_6$  carbide is commonly observed as SCs (Guo, 2017; Tchuindjang, 2014), but recent studies have shown its presence as ECs at high cooling rates (Imurai, 2014; Wieczerszak, 2016).  $Mn_{23}C_6$ ,  $Cr_{23}C_6$  and  $V_{23}C_6$  are the most stable cases among the  $M_{23}C_6$  binary carbides, whereas the formation of  $Co_{23}C_6$  and  $Ni_{23}C_6$  is unlikely (Medvedeva, 2015). Moreover, W, Mo and Si additions stabilize the  $M_{23}C_6$  carbide (Imurai, 2014, 2015; Wiengmoon, 2016).

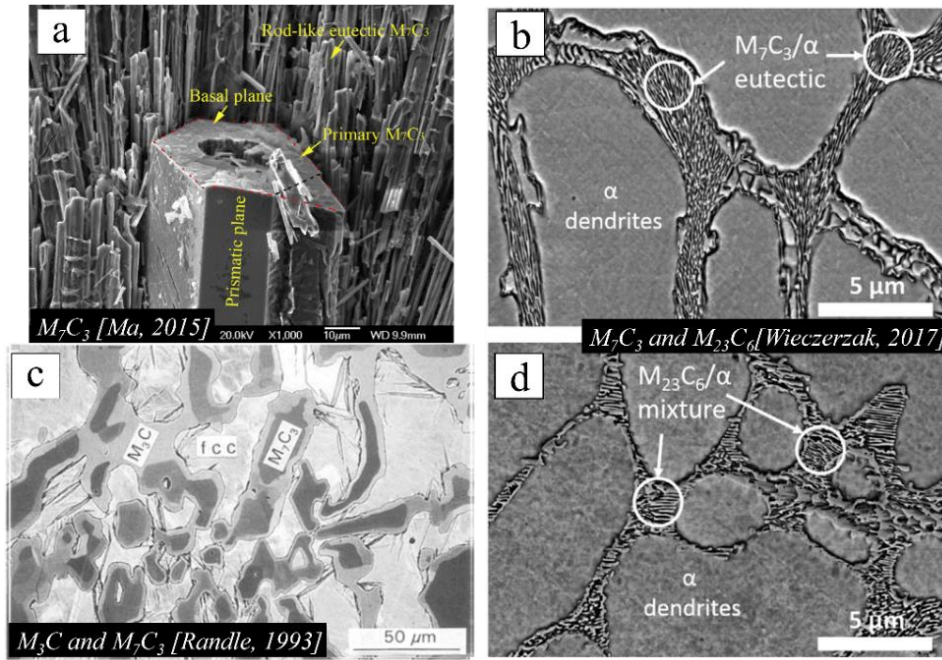


Fig. 2-6: (a) Pencil morphologies of a  $M_7C_3$  PC (Ma, 2015); (b and d) similar plate-like morphology of  $M_7C_3$  and  $M_3C$  ECs (Wieczorzak, 2016, 2017); (c) Electron backscatter micrograph of  $M_7C_3$  and  $M_{23}C_6$  ECs (Randle, 1993).

These three Cr-carbides may exhibit similar compositions, but they can be differentiated by their crystal lattice (i.e. hexagonal for the  $M_7C_3$  carbide (Yamamoto, 2014), orthorhombic for the  $M_3C$  carbide (Randle, 1993) and FCC for the  $M_{23}C_6$  carbide (Laigo, 2008)). On the other hand, the differentiation among all the FCC carbides shown in this section ( $M_3C$ ,  $M_6C$  and  $M_{23}C_6$  carbide), rarer carbides showed in the literature ( $M_4C$ ,  $M_{12}C$  and  $WC_{1-x}$ ) and austenite remains a hot topic in material characterization (Abderrahim, 2012; Cai, 2018; Kurlov, 2013). All these carbides adopt the same crystal symmetry with similar space groups (i.e., Fd-3m, Fd-3s, and Fm-3m) and exhibit only small differences in lattice parameters (T. F. Liu, 1990), leading to uncertainties in the microstructural analysis (Cai, 2018; Fang, 2010; Ho, 2018; L. Song, 2016; Tong, 2012).

### 2.2.2. AM microstructures

AM of metals, unlike AM of polymers, have distinct material kinetics, completely different from the classical manufacturing process due basically to the working principle of the processes (Herzog, 2016; Sames, 2016). Indeed, when metals are printed in the form of a track, it is quite small and at high temperatures, if compared to the surrounding solid material. This difference between the molten pool and the solid surroundings leads to high-temperature gradient (G) and high solidification rates (R) due to the fast exchange of heat (DebRoy, 2018; Herzog, 2016; John H. Martin, 2017). This exchange is subsequently translated into extremely high cooling rates ( $G \cdot R$ ) during the solidification of the metal (DebRoy, 2018; Köhnen, 2019).

Considering the G-R diagram in Fig. 2-7, which is the reference for the interpretation of the solidification modes in metals, the combinations of G and R lead to microstructures with different size ( $G \cdot R$ ) and various solidification modes (G/R) (Köhnen, 2019; Lee, 2014; P. Liu, 2019).

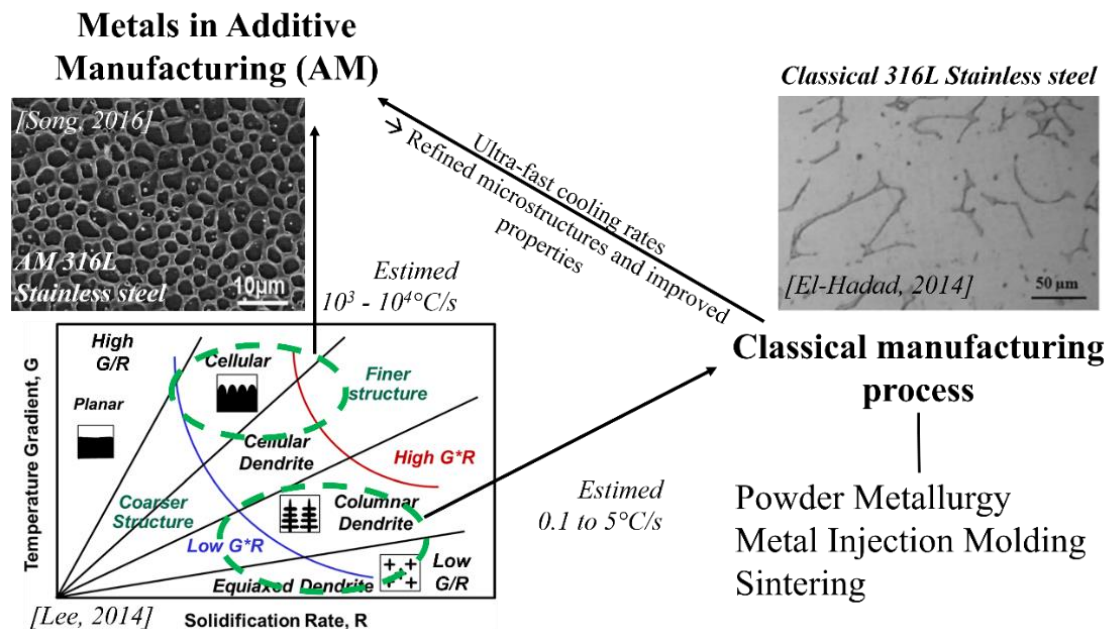


Fig. 2-7: Localization of AM and the classical manufacturing processes in the G-R diagram (adapted from (Lee, 2014)) with the corresponding cooling rates ( $G \cdot R$ ) and the different microstructures related to the ratio G/R.

In AM, the extremely high cooling rates ( $10^3$ - $10^4$   $^\circ\text{C/s}$ ) lead to refined microstructures (Köhnen, 2019; John H. Martin, 2017; Y. M. Wang, 2018). Furthermore, unlike the classical manufacturing process, where a dendritic microstructure is observed due to a low G/R, AM microstructures often exhibit a cellular microstructure due to especially the high G and high G/R (P. Liu, 2019). Indeed, as shown in Fig. 2-8, a cellular microstructure is observed when one or few elements can slightly segregate (Fig. 2-8f), forming the cell boundaries of complex hierarchical structures that range from the millimetres to the nanometres (John H. Martin, 2017; Tang, 2020; Y. M. Wang, 2018; Zhao, 2019).

Moreover, as shown in Fig. 2-7, low cooling rates ( $\sim 0.1$  to  $1$   $^\circ\text{C/s}$ ) largely allows the diffusion during the solidification and thus atoms segregate in their most stable thermodynamic positions (Luan, 2010). Therefore, microstructures of 316L and all the other alloys observed after most of the conventional manufacturing process are in an equilibrium state. On the other hand, with the increase of the cooling rates, the diffusion and the segregations of atoms decrease, leading to out-of-equilibrium microstructures, far away from their thermodynamic equilibrium (Aboulkhair, 2019; Herzog, 2016; Ho, 2018; Y. M. Wang, 2018). Indeed, in centrifugal casting (cooling rates =  $5$   $^\circ\text{C/s}$ ), out-of-equilibrium phases were observed although this process could be considered a conventional manufacturing process (Hashimoto, 2004; Tchuindjang, Sinnaeve, 2011; Zhou, 2012).

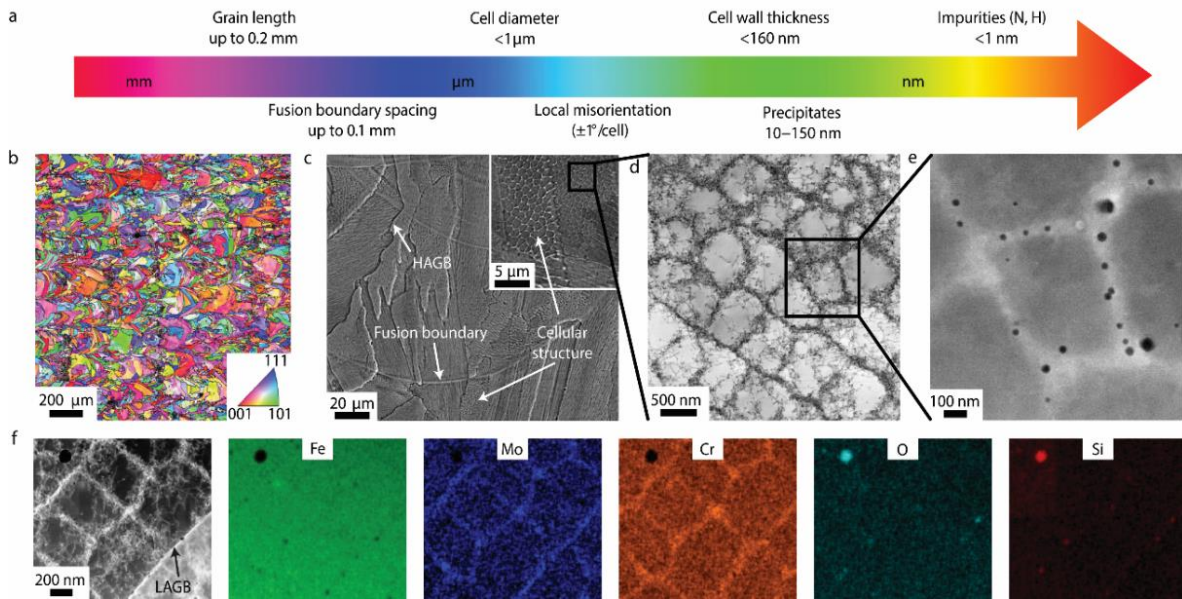


Fig. 2-8: Typical cellular microstructure produced by AM of 316L (adapted from (Y. M. Wang, 2018)). (a) Schematic of the various length scales of the hierarchical microstructure. Electron backscatter diffraction (EBSD) (b), scanning electron microscopy (SEM) (c), transmission electron microscopy (TEM) (d) and high-angle annular dark-field (HAADF) scanning TEM (STEM) show the different features of the cellular structure. (e) HAADF STEM (Z contrast) image shows Mo and Cr segregations at the cell boundaries.

Regarding HSS, compared to the microstructure after centrifugal casting (section 2.2.1 and Fig. 2-9d), the size and the morphology of the carbides after LC fabrication change as well (Hashemi, 2017). Indeed, the extremely high cooling rates lead to refined microstructure (Fig. 2-9a, b and c), where the cell boundaries are highlighted by mostly ECs and PCs. In Fig. 2-9, the compositions of the four alloys are also given and the phase identifications in (Hashemi, 2017) are in good agreement with the descriptions in section 2.2.1.

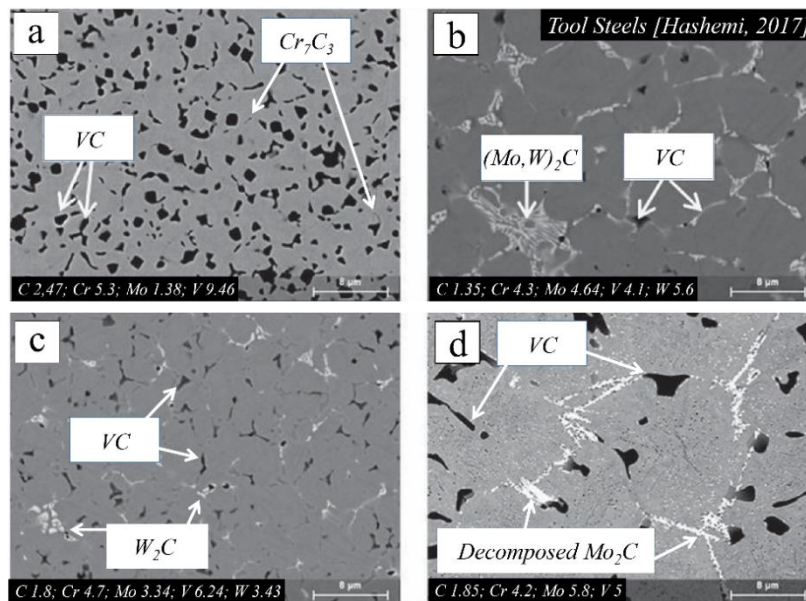


Fig. 2-9: Compositions, identified phases and SEM micrographs (BSE mode) of (a, b and c) three microstructures obtained by LC and (d) a microstructure obtained by centrifugal casting (adapted from (Hashemi, 2017)).

On the other hand, when displacive transformations occur and segregations do not highlight the cell boundaries, the cellular microstructure is not marked (Fig. 2-10). Nevertheless, Ti6Al4V exhibits peculiar microstructural variations, particularly linked to the thermal history during the AM process. As shown in (Paydas, 2015; Tran, 2017), the influence of the different thermal history was highlighted since three different microstructures were observed in the same specimen depending on the location. Indeed, with the progress of the deposition, the conditions vary depending on the process parameters, the size of the part and the temperature rise. Therefore, the solidification route and mode may vary since G and R are modified (Fig. 2-7).

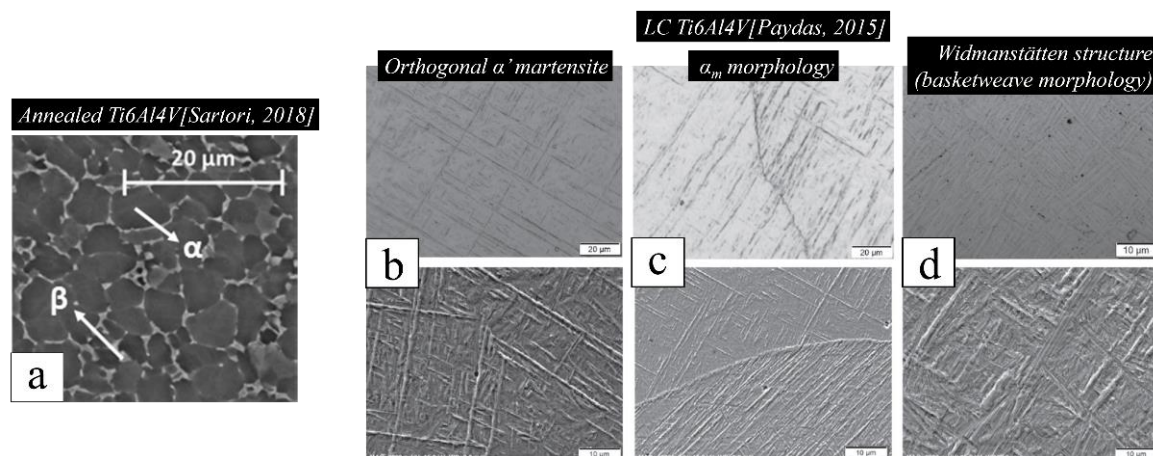


Fig. 2-10: (a) Ti6Al4V in annealed conditions (Sartori, 2018). Ti6Al4V microstructures after LC fabrication, where (a) martensite, (b)  $\alpha_m$  and (c) Widmanstätten microstructures could be respectively observed (adapted from (Paydas, 2015)).

These microstructures exhibit novel properties due mainly to their refinement and to the many different strengthening phenomena at play depending on the alloy (i.e. solid solution strengthening, in-situ precipitation, tailored orientations of solidification and other phase transformation) (N. Li, 2019; John H. Martin, 2017; Paydas, 2015; Tang, 2020; Y. M. Wang, 2018). Section 2.3 focus on the properties of AM alloys and in particular, on the 316L and its MMCs.

### 2.3. Properties of AM alloys

Characterization of the cellular microstructure shown in section 2.2.2 reveals a high density of dislocations at the cell boundaries (Fig. 2-8d). The size of the cells and the thickness of the cell boundaries are known to be connected to the solidification conditions of Fig. 2-7 (i.e. G, R and G\*R). Because of the distinct compositional difference between cells and cell boundaries, other phases are observed as cell boundaries (Fig. 2-9). Therefore, the nature of these boundaries affects the mechanical behaviour of these microstructures (Aversa, 2020; Zhao, 2019; Zhong, 2016). Highly fragile or coarsened phases may lead to poor mechanical performances, even with a finer microstructure compared to the conventional ones. Indeed, as shown in Fig. 2-11, the performances of AM steels are commonly reported as improved, but it strictly depends on the given alloy and the fabrication parameters (Y. M. Wang, 2018; Yakout, 2019).

Nevertheless, an increased strength is reported when a cellular microstructure is observed without these negative conditions, including Al-alloys, Ni-alloys and few AM steels as the 316L (Gorsse, 2017; Y. M. Wang, 2018). This improvement is attributed to the refinement of these hierarchical structures, following the Hall-Petch equation between yield strength ( $\sigma_y$ ) and the grain size (d) (Herzog, 2016; Y. M. Wang, 2018). Furthermore, the elongation is improved as well and it is related to different phenomena depending on the given material (Kuo, 2017; Z. Li, 2019; Y. M. Wang, 2018; Zhao, 2019).

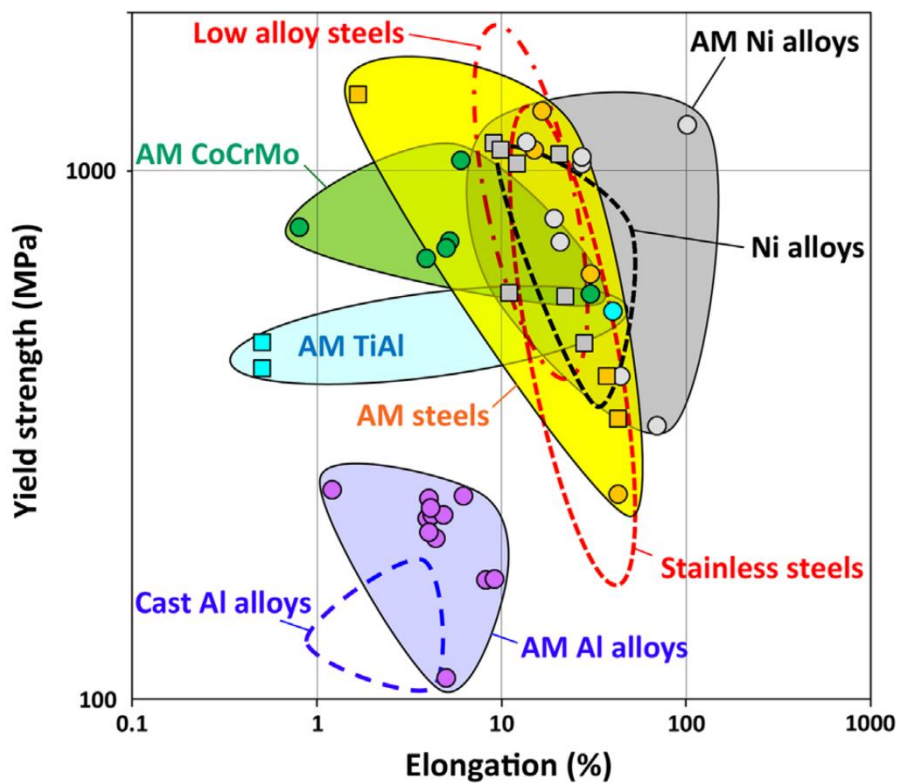


Fig. 2-11: CES chart for room temperature yield strength vs elongation of AM alloys and conventionally manufactured alloys (dashed lines) (Gorsse, 2017).

Furthermore, depending on the position in the fabricated part and the local position of the microstructure (i.e. heat affected zone (HAZ)), these properties could vary due to local thermal history (Paydas, 2015; Zhao, 2019). Macrohardness is a technique capable to evaluate microstructural variations. Indeed, it provides a simple and easy indication of the effect of microstructural features such as the phases in presence (Fig. 2-10), the composition of the alloy and the grain size (Xia, 2020; Zuback, 2018). It is common practice to consider macrohardness to evaluate the mechanical properties in AM parts since it allows the detection of microstructural variations caused by heat accumulation in the building structure (K. Li, 2015; Manvatkar, 2014; Paydas, 2015; Ur Rahman, 2018; Xia, 2020; Yadollahi, 2015). The decrease in the hardness value with the increase of the height of the part is a well-known feature of the AM fabrication and it is caused by heat accumulation in the building structure (K. Li, 2015; Manvatkar, 2014; Paydas, 2015; Ur Rahman, 2018; Xia, 2020; Yadollahi, 2015). Indeed, the heat accumulated with the progress of the fabrication leads to a coarsening of the microstructure and thus to a local evolution of these mechanical properties (Köhnen, 2019; Lee, 2014; Y. Liu, 2018; Yadroitsev, 2013), with the exception of the last deposited layer which has a different thermal history.

### 2.3.1. Wear performance of 316L and its MMC

The study of the wear behaviour of a single material considering many different wear tests is a challenging task. The difficulties arise from the complexity of the wear mechanisms reported in the literature and the variability of the wear tests i.e. counterbody, temperature, load, sliding speed and manufacturing state of this material. Indeed, the majority of the studies focus on the variation of the wear performances as function of the test parameters in a relative manner.

316L is a widely studied material due to its wide range of applications and numerous works evaluate its tribological performances (Bartolomeu, 2017; Dearnley, 2004; H. Li, 2018; J. Li, 2019; O'Donnell, 2010; L. Song, 2016; Sun, 2014), where the poor wear resistance of this material has always been highlighted. Abrasive wear is the main observed wear mechanism with a strong contribution of delamination (O'Donnell, 2010; L. Song, 2016). Nevertheless, in peculiar conditions, oxidative wear occurs with the formation of a protective oxide layer which leads to mild wear. The wear resistance of the AM 316L is reported to be improved compared to conventional technologies (i.e. casting and hot isostatic pressing) due again to the refined microstructure (Bartolomeu, 2017). Nevertheless, porosities or other defects in the AM parts could deteriorate the wear performances of the AM 316L (H. Li, 2018; Sun, 2014).

As mentioned in section 1.4, the relatively poor tribological properties of the 316L could be improved with the addition of hard reinforcements, creating an MMC. When the wear performances of these MMC were evaluated, an increase of the hardness corresponds to the improvement in wear resistance at room and high temperatures independently of the chosen test parameters (AlMangour, 2019; J. Li, 2019; L. Song, 2016). Wear damages typically observed on the 316L matrix (J. Li, 2019; O'Donnell,

2010; *L. Song, 2016*), such as delamination, pit, groove and material removal are also observed in the composite matrix. The solidification carbides of the microstructure lead to an increase in the occurrence of abrasive wear at the expense of a decrease of adhesive wear (*Fernández, 2015; L. Song, 2016; Weng, 2016*). Indeed, as observed in (*L. Song, 2016*), the toughness of the matrix rises due to the presence of a supersaturated solid solution and the solidification carbides, leading to a thin deformed layer that follows the sliding direction. Moreover, as demonstrated by (*J. Li, 2019; Tong, 2012*), solidification carbides are fragmented during this deformation and their fragments enrich a mechanically mixed layer (MML). The presence of these fragments significantly improves the work hardening ability of the matrix since they form an efficient barrier for dislocation glide.

## References section 2

- Abderrahim, F. Z., Faraoun, H. I., & Ouahrani, T. (2012). "Structure, bonding and stability of semi-carbides  $M_2C$  and sub-carbides  $M_4C$  ( $M=V, Cr, Nb, Mo, Ta, W$ ): A first principles investigation." *Physica B: Condensed Matter*, 407(18), 3833–3838. <https://doi.org/10.1016/j.physb.2012.05.070>
- Aboulkhair, N. T., Simonelli, M., Parry, L., Ashcroft, I., Tuck, C., & Hague, R. (2019). "3D printing of Aluminium alloys: Additive Manufacturing of Aluminium alloys using selective laser melting." *Progress in Materials Science*, 106(May), 100578. <https://doi.org/10.1016/j.pmatsci.2019.100578>
- Akinlabi, S. A., Kumpaty, S., Fatoba, O. S., & Akinlabi, E. T. (2019). "Improvement of wear resistance behaviour of laser metal deposited Ti6Al4V/Mo composites." *Materialwissenschaft Und Werkstofftechnik*, 50(6), 724–730. <https://doi.org/10.1002/mawe.201800226>
- AlMangour, B., Grzesiak, D., & Yang, J. M. (2017). "Selective laser melting of TiB<sub>2</sub>/316L stainless steel composites: The roles of powder preparation and hot isostatic pressing post-treatment." *Powder Technology*, 309, 37–48. <https://doi.org/10.1016/j.powtec.2016.12.073>
- AlMangour, B., Kim, Y. K., Grzesiak, D., & Lee, K. A. (2019). "Novel TiB<sub>2</sub>-reinforced 316L stainless steel nanocomposites with excellent room- and high-temperature yield strength developed by additive manufacturing." *Composites Part B: Engineering*, 156(June 2018), 51–63. <https://doi.org/10.1016/j.compositesb.2018.07.050>
- Arik, H., Ozcatalbas, Y., & Turker, M. (2006). "Dry sliding wear behavior of in situ Al-Al<sub>4</sub>C<sub>3</sub> metal matrix composite produced by mechanical alloying technique." *Materials and Design*, 27(9), 799–804. <https://doi.org/10.1016/j.matdes.2005.01.024>
- Aversa, A., Saboori, A., Librera, E., de Chirico, M., Biamino, S., Lombardi, M., & Fino, P. (2020). "The role of Directed Energy Deposition atmosphere mode on the microstructure and mechanical properties of 316L samples." *Additive Manufacturing*, 34(February), 101274. <https://doi.org/10.1016/j.addma.2020.101274>
- Bartolomeu, F., Buciumeanu, M., Pinto, E., Alves, N., Carvalho, O., Silva, F. S., & Miranda, G. (2017). "316L stainless steel mechanical and tribological behavior—A comparison between selective laser melting, hot pressing and conventional casting." *Additive Manufacturing*, 16, 81–89. <https://doi.org/10.1016/j.addma.2017.05.007>
- Bedolla-Jacuinde, A., Rainforth, M. W., & Mejía, I. (2013). "The role of silicon in the solidification of high-Cr cast irons." *Metallurgical and Materials Transactions A: Physical Metallurgy and Materials Science*, 44(2), 856–872. <https://doi.org/10.1007/s11661-012-1434-8>
- Behera, M. P., Dougherty, T., & Singamneni, S. (2020). "Selective laser melting of stainless steel and silicon nitride fibre metal matrix composites." *Proceedings of the Institution of Mechanical Engineers, Part B: Journal of Engineering Manufacture*, 234(12), 1513–1525. <https://doi.org/10.1177/0954405420928684>
- Boccalini Jr, M., Corrêa, A. V. O., & Goldenstein, H. (1999). "Rare earth metal induced modification of  $\gamma - M_2C$ ,  $\gamma - M_6C$ , and  $\gamma - MC$  eutectics in as cast M2 high speed steel." *Materials Science and Technology*, 15(6), 621–626. <https://doi.org/10.1179/026708399101506355>
- Boccalini Jr, M., & Goldenstein, H. (2001). "Solidification of high speed steels." *International Materials Reviews*, 46(2), 92–115. <https://doi.org/10.1179/095066001101528411>
- Boccalini Jr, M., Serantoni, C. R., Sinatora, A., & Matsubara, Y. (2001). "Effects of vanadium content and cooling rate on the solidification of multi-component white cast iron." *International Conference of the Science of Casting and Solidification*, 393–398. Retrieved from <https://www.villaresrolls.com/web/pt/tecnologia/Artigos Tcnicos/2001 - International Conference on The Science of Casting and Solidification - Effect V and CR on solidification of HSS.pdf>

- Buytoz, S. (2006). "Microstructural properties of M7C3 eutectic carbides in a Fe-Cr-C alloy." *Materials Letters*, 60(5), 605–608. <https://doi.org/10.1016/j.matlet.2005.09.046>
- Cai, X., Xu, Y., Liu, M., & Zhong, L. (2018). "Evaluation of microstructure and growth kinetics of tungsten carbide ceramics at the interface of iron and tungsten." *Journal of Alloys and Compounds*, 741, 666–676. <https://doi.org/10.1016/j.jallcom.2018.01.212>
- Candel, J. J., Amigó, V., Ramos, J. A., & Busquets, D. (2010). "Sliding wear resistance of TiCp reinforced titanium composite coating produced by laser cladding." *Surface and Coatings Technology*, 204(20), 3161–3166. <https://doi.org/10.1016/j.surfcoat.2010.02.070>
- Chen, L., Pei, J., Li, F., Zhang, Y., Wang, M., & Ma, X. (2016). "Decomposition Reaction of Metastable M<sub>2</sub>C Carbide in a Multi-Component Semi-High-Speed Steel." *Metallurgical and Materials Transactions A: Physical Metallurgy and Materials Science*, 47(12), 5662–5669. <https://doi.org/10.1007/s11661-016-3795-x>
- Coronado, J. J., & Sinatora, A. (2009). "Abrasive wear study of white cast iron with different solidification rates." *Wear*, 267(11), 2116–2121. <https://doi.org/10.1016/j.wear.2009.08.010>
- Dearnley, P. A., & Aldrich-Smith, G. (2004). "Corrosion-wear mechanisms of hard coated austenitic 316L stainless steels." *Wear*, 256(5), 491–499. [https://doi.org/10.1016/S0043-1648\(03\)00559-3](https://doi.org/10.1016/S0043-1648(03)00559-3)
- DebRoy, T., Wei, H. L., Zuback, J. S., Mukherjee, T., Elmer, J. W., Milewski, J. O., ... Zhang, W. (2018). "Additive manufacturing of metallic components – Process, structure and properties." *Progress in Materials Science*, 92, 112–224. <https://doi.org/10.1016/j.pmatsci.2017.10.001>
- Delaunois, F., Stanciu, V. I., & Sinnaeve, M. (2018). "Resistance to High-Temperature Oxidation and Wear of Various Ferrous Alloys Used in Rolling Mills." *Metallurgical and Materials Transactions A: Physical Metallurgy and Materials Science*, 49(3), 822–835. <https://doi.org/10.1007/s11661-017-4450-x>
- Deschuyteneer, D., Petit, F., Gonon, M., & Cambier, F. (2015). "Processing and characterization of laser clad NiCrBSi/WC composite coatings - Influence of microstructure on hardness and wear." *Surface and Coatings Technology*, 283, 162–171. <https://doi.org/10.1016/j.surfcoat.2015.10.055>
- Domitner, J., Aigner, M., Stern, T., Paar, A., Sommitsch, C., & Elizondo, L. (2019). "Thermo-Mechanical Wear Testing of Metal Matrix Composite Cladding for Potential Application in Hot Rolling Mills." *Steel Research International*, 1900478. <https://doi.org/10.1002/srin.201900478>
- Dutta Majumdar, J., Kumar, A., & Li, L. (2009). "Direct laser cladding of SiC dispersed AISI 316L stainless steel." *Tribology International*, 42(5), 750–753. <https://doi.org/10.1016/j.triboint.2008.10.016>
- Fang, C. M., van Huis, M. A., Sluiter, M. H. F., & Zandbergen, H. W. (2010). "Stability, structure and electronic properties of  $\gamma$ -Fe<sub>23</sub>C<sub>6</sub> from first-principles theory." *Acta Materialia*, 58(8), 2968–2977. <https://doi.org/10.1016/j.actamat.2010.01.025>
- Fernández, M. R., García, A., Cuetos, J. M., González, R., Noriega, A., & Cadenas, M. (2015). "Effect of actual WC content on the reciprocating wear of a laser cladding NiCrBSi alloy reinforced with WC." *Wear*, 324–325, 80–89. <https://doi.org/10.1016/j.wear.2014.12.021>
- Fischmeister, H. F., Riedl, R., & Karagöz, S. (1989). "Solidification of high-speed tool steels." *Metallurgical Transactions A*, 20(10), 2133–2148. <https://doi.org/10.1007/BF02650299>
- Gorsse, S., Hutchinson, C., Gouné, M., & Banerjee, R. (2017). "Additive manufacturing of metals: a brief review of the characteristic microstructures and properties of steels, Ti-6Al-4V and high-entropy alloys." *Science and Technology of Advanced Materials*, 18(1), 584–610. <https://doi.org/10.1080/14686996.2017.1361305>

- Gu, D., Hagedorn, Y. C., Meiners, W., Wissenbach, K., & Poprawe, R. (2011). "Nanocrystalline TiC reinforced Ti matrix bulk-form nanocomposites by Selective Laser Melting (SLM): Densification, growth mechanism and wear behavior." *Composites Science and Technology*, 71(13), 1612–1620. <https://doi.org/10.1016/j.compscitech.2011.07.010>
- Guo, J., Liu, L., Feng, Y., Liu, S., Ren, X., & Yang, Q. (2017). "Crystallographic characterizations of eutectic and secondary carbides in a Fe-12Cr-2.5Mo-1.5W-3V-1.25C alloy." *Metals and Materials International*, 23(2), 313–319. <https://doi.org/10.1007/s12540-017-6266-z>
- Hamar-Thibault, S., Adnane, L., & Kesri, R. (2001). "Miscibility of binary VC-MC carbides in quaternary Fe-V-M-C alloys." *Journal of Alloys and Compounds*, 317–318, 311–314. [https://doi.org/10.1016/S0925-8388\(00\)01362-1](https://doi.org/10.1016/S0925-8388(00)01362-1)
- Hashemi, N., Mertens, A., Montrieux, H. M., Tchuindjang, J. T., Dedry, O., Carrus, R., & Lecomte-Beckers, J. (2017). "Oxidative wear behaviour of laser clad High Speed Steel thick deposits: Influence of sliding speed, carbide type and morphology." *Surface and Coatings Technology*, 315, 519–529. <https://doi.org/10.1016/j.surfcoat.2017.02.071>
- Hashimoto, M., Kubo, O., & Matsubara, Y. (2004). "Analysis of carbides in multi-component white cast iron for hot rolling mill rolls." *ISIJ International*, 44(2), 372–380. <https://doi.org/10.2355/isijinternational.44.372>
- Herzog, D., Seyda, V., Wycisk, E., & Emmelmann, C. (2016). "Additive manufacturing of metals." *Acta Materialia*, 117, 371–392. <https://doi.org/10.1016/j.actamat.2016.07.019>
- Ho, I. T., Chen, Y. T., Yeh, A. C., Chen, C. P., & Jen, K. K. (2018). "Microstructure evolution induced by inoculants during the selective laser melting of IN718." *Additive Manufacturing*, 21(February), 465–471. <https://doi.org/10.1016/j.addma.2018.02.018>
- Imurai, S., Thanachayanont, C., Pearce, J. T. H., Tsuda, K., & Chairuangstri, T. (2014). "Effects of Mo on microstructure of as-cast 28 wt.% Cr-2.6 wt.% C-(0-10) wt.% Mo irons." *Materials Characterization*, 90, 99–112. <https://doi.org/10.1016/j.matchar.2014.01.014>
- Imurai, S., Thanachayanont, C., Pearce, J. T. H., Tsuda, K., & Chairuangstri, T. (2015). "Effects of W on microstructure of as-cast 28 wt.%Cr-2.6 wt.%C-(0-10)wt.%W irons." *Materials Characterization*, 99, 52–60. <https://doi.org/10.1016/j.matchar.2014.11.012>
- Jiang, L., Zhang, W.-Z. Z., Xu, Z.-F. F., Huang, H.-F. F., Ye, X.-X. X., Leng, B., ... Zhou, X.-T. T. (2016). "M<sub>2</sub>C and M<sub>6</sub>C carbide precipitation in Ni-Mo-Cr based superalloys containing silicon." *Materials and Design*, 112, 300–308. <https://doi.org/10.1016/j.matdes.2016.09.075>
- Kawalec, M., & Fraś, E. (2010). "Shaping of the microstructure in near- eutectic Fe-C-V alloys." *Archives of Foundry Engineering*, 10(4), 83–88.
- Kawalec, M., & Górny, M. (2012). "Alloyed White Cast Iron with Precipitates of Spheroidal Vanadium Carbides VC." *Archives of Foundry Engineering*, 12(4), 95–100. <https://doi.org/10.2478/v10266-012-0113-y>
- Kim, S. H., Shin, G. H., Kim, B. K., Kim, K. T., Yang, D. Y., Aranas, C., ... Yu, J. H. (2017). "Thermo-mechanical improvement of Inconel 718 using ex situ boron nitride-reinforced composites processed by laser powder bed fusion." *Scientific Reports*, 7(1), 1–13. <https://doi.org/10.1038/s41598-017-14713-1>
- Köhnen, P., Létang, M., Voshage, M., Schleifenbaum, J. H., & Haase, C. (2019). "Understanding the process-microstructure correlations for tailoring the mechanical properties of L-PBF produced austenitic advanced high strength steel." *Additive Manufacturing*, 30(September), 100914. <https://doi.org/10.1016/j.addma.2019.100914>

- Krakhmalev, P., & Yadroitsev, I. (2014). "Microstructure and properties of intermetallic composite coatings fabricated by selective laser melting of Ti-SiC powder mixtures." *Intermetallics*, 46, 147–155. <https://doi.org/10.1016/j.intermet.2013.11.012>
- Kuo, Y. L., Horikawa, S., & Kakehi, K. (2017). "Effects of build direction and heat treatment on creep properties of Ni-base superalloy built up by additive manufacturing." *Scripta Materialia*, 129, 74–78. <https://doi.org/10.1016/j.scriptamat.2016.10.035>
- Kurlov, A. S., & Gusev, A. I. (2013). *Tungsten Carbides: Structure, Properties and Application in Hardmetals*. Springer Series in Materials Science (Vol. 184). Springer Cham. <https://doi.org/10.1007/978-3-319-00524-9>
- Laigo, J., Christien, F., Le Gall, R., Tancret, F., & Furtado, J. (2008). "SEM, EDS, EPMA-WDS and EBSD characterization of carbides in HP type heat resistant alloys." *Materials Characterization*, 59(11), 1580–1586. <https://doi.org/10.1016/j.matchar.2008.02.001>
- Lecomte-Beckers, J. (2007). "Metallurgical assessment of two HSS rolls grades for Hot Strip Mill." *AISTech - Iron and Steel Technology Conference Proceedings*.
- Lecomte-Beckers, J., Sinnaeve, M., & Tchuindjang, J. T. (2012). "Current developments of alloyed steels for hot strip roughing mills - characterization of high chromium steel and semi high speed steel." *Iron & Steel Technology*, 2(9), 33–40. Retrieved from AIST.org
- Lecomte-Beckers, J., & Tchuindjang, J. T. (2009). "Structural Investigations of Solidification and Heat Treatments Influence on High Alloyed Cast Irons Grades with Nb-V-Ti additions." *Defect and Diffusion Forum Series*, 289–292, 77–86. <https://doi.org/10.4028/www.scientific.net/DDF.289-292.77>
- Lee, Y., Nordin, M., Babu, S. S., & Farson, D. F. (2014). "Effect of fluid convection on dendrite arm spacing in laser deposition." *Metallurgical and Materials Transactions B: Process Metallurgy and Materials Processing Science*, 45(4), 1520–1529. <https://doi.org/10.1007/s11663-014-0054-7>
- Li, B. C., Zhu, H. M., Qiu, C. J., & Zhang, D. K. (2020). "Development of high strength and ductile martensitic stainless steel coatings with Nb addition fabricated by laser cladding." *Journal of Alloys and Compounds*, 832. <https://doi.org/10.1016/j.jallcom.2020.154985>
- Li, C., Sun, S., Liu, C., Lu, Q., Ma, P., & Wang, Y. (2019). "Microstructure and mechanical properties of TiC/AlSi10Mg alloy fabricated by laser additive manufacturing under high-frequency microvibration." *Journal of Alloys and Compounds*, 794, 236–246. <https://doi.org/10.1016/j.jallcom.2019.04.287>
- Li, H., Ramezani, M., Li, M., Ma, C., & Wang, J. (2018). "Tribological performance of selective laser melted 316L stainless steel." *Tribology International*, 128(April), 121–129. <https://doi.org/10.1016/j.triboint.2018.07.021>
- Li, J., Zhao, Z., Bai, P., Qu, H., Liang, M., Liao, H., ... Huo, P. (2019). "Tribological behavior of TiC particles reinforced 316Lss composite fabricated using selective laser melting." *Materials*, 16(6). <https://doi.org/10.3390/ma12060950>
- Li, K., Li, D., Liu, D., Pei, G., & Sun, L. (2015). "Microstructure evolution and mechanical properties of multiple-layer laser cladding coating of 308L stainless steel." *Applied Surface Science*, 340, 143–150. <https://doi.org/10.1016/j.apsusc.2015.02.171>
- Li, N., Huang, S., Zhang, G., Qin, R., Liu, W., Xiong, H., ... Blackburn, J. (2019). "Progress in additive manufacturing on new materials: A review." *Journal of Materials Science and Technology*. The editorial office of *Journal of Materials Science & Technology*. <https://doi.org/10.1016/j.jmst.2018.09.002>

- Li, X. W., Wang, L., Dong, J. S., & Lou, L. H. (2014). "Effect of Solidification Condition and Carbon Content on the Morphology of MC Carbide in Directionally Solidified Nickel-base Superalloys." *Journal of Materials Science and Technology*, 30(12), 1296–1300. <https://doi.org/10.1016/j.jmst.2014.06.010>
- Li, Z., Zhao, S., Ritchie, R. O., & Meyers, M. A. (2019). "Mechanical properties of high-entropy alloys with emphasis on face-centered cubic alloys." *Progress in Materials Science*, 102(December 2018), 296–345. <https://doi.org/10.1016/j.pmatsci.2018.12.003>
- Lian, G., Zhao, C., Zhang, Y., Feng, M., & Jiang, J. (2020). "Investigation into micro-hardness and wear resistance of 316L/SiC composite coating in laser cladding." *Applied Sciences (Switzerland)*, 10(9). <https://doi.org/10.3390/app10093167>
- Liu, P., Wang, Z., Xiao, Y., Horstemeyer, M. F., Cui, X., & Chen, L. (2019). "Insight into the mechanisms of columnar to equiaxed grain transition during metallic additive manufacturing." *Additive Manufacturing*, 26(December 2018), 22–29. <https://doi.org/10.1016/j.addma.2018.12.019>
- Liu, T. F., Peng, S. W., Lin, Y. L., & Wu, C. C. (1990). "Orientation relationships among M<sub>23</sub>C<sub>6</sub>, M<sub>6</sub>C, and austenite in an Fe-Mn-Al-Mo-C alloy." *Metallurgical Transactions A*, 21(2), 567–574. <https://doi.org/10.1007/BF02671929>
- Liu, X. B., Meng, X. J., Liu, H. Q., Shi, G. L., Wu, S. H., Sun, C. F., ... Qi, L. H. (2014). "Development and characterization of laser clad high temperature self-lubricating wear resistant composite coatings on Ti-6Al-4V alloy." *Materials and Design*, 55, 404–409. <https://doi.org/10.1016/j.matdes.2013.09.038>
- Liu, Y., Zhang, J., & Pang, Z. (2018). "Numerical and experimental investigation into the subsequent thermal cycling during selective laser melting of multi-layer 316L stainless steel." *Optics and Laser Technology*, 98, 23–32. <https://doi.org/10.1016/j.optlastec.2017.07.034>
- Luan, Y., Song, N., Bai, Y., Kang, X., & Li, D. (2010). "Effect of solidification rate on the morphology and distribution of eutectic carbides in centrifugal casting high-speed steel rolls." *Journal of Materials Processing Technology*, 210(3), 536–541. <https://doi.org/10.1016/j.jmatprotec.2009.10.017>
- Ma, S., Xing, J., He, Y., Li, Y., Huang, Z., Liu, G., & Geng, Q. (2015). "Microstructure and crystallography of M<sub>7</sub>C<sub>3</sub> carbide in chromium cast iron." *Materials Chemistry and Physics*, 161, 65–73. <https://doi.org/10.1016/j.matchemphys.2015.05.008>
- Manvatkar, V., De, A., & Debroy, T. (2014). "Heat transfer and material flow during laser assisted multi-layer additive manufacturing." *Journal of Applied Physics*, 116(12). <https://doi.org/10.1063/1.4896751>
- Martin, J. Hunter, Yahata, B., Mayer, J., Mone, R., Stonkevitch, E., Miller, J., ... Pollock, T. (2020). "Grain refinement mechanisms in additively manufactured nano-functionalized aluminum." *Acta Materialia*, 200, 1022–1037. <https://doi.org/10.1016/j.actamat.2020.09.043>
- Martin, John H., Yahata, B. D., Hundley, J. M., Mayer, J. A., Schaedler, T. A., & Pollock, T. M. (2017). "3D printing of high-strength aluminium alloys." *Nature*, 549(7672), 365–369. <https://doi.org/10.1038/nature23894>
- Maurizi Enrici, T., Lecomte-Beckers (Official supervisor), J., Calliari (Official supervisor), I., & Tchuindjang (Co-supervisor), J. T. (2015). Study about thermal treatments on a multi-alloyed iron with free graphite. Master Thesis - Università degli studi di Padova; ULiège.
- Medvedeva, N. I., Van Aken, D. C., & Medvedeva, J. E. (2015). "Stability of binary and ternary M<sub>23</sub>C<sub>6</sub> carbides from first principles." *Computational Materials Science*, 96(PA), 159–164. <https://doi.org/10.1016/j.commatsci.2014.09.016>

- Muvvala, G., Patra Karmakar, D., & Nath, A. K. (2018). "In-process detection of microstructural changes in laser cladding of in-situ Inconel 718/TiC metal matrix composite coating." *Journal of Alloys and Compounds*, 740, 545–558. <https://doi.org/10.1016/j.jallcom.2017.12.364>
- O'Donnell, L. J., Michal, G. M., Ernst, F., Kahn, H., & Heuer, A. H. (2010). "Wear maps for low temperature carburised 316L austenitic stainless steel sliding against alumina." *Surface Engineering*, 26(4), 284–292. <https://doi.org/10.1179/026708410X12550773057901>
- Okane, T., & Umeda, T. (2001). "Interface temperature measurement of M2C and M6C eutectic carbides in the Fe-Mo-C system." *Science and Technology of Advanced Materials*, 60(1), 605–608. <https://doi.org/10.1016/j.matlet.2005.09.046>
- Pan, F., Hirohashi, M., Lu, Y., Ding, P., Tang, A., & Edmonds, D. V. (2004). "Carbides in high-speed steels containing silicon." *Metallurgical and Materials Transactions A: Physical Metallurgy and Materials Science*, 35 A(9), 2757–2766. <https://doi.org/10.1007/s11661-004-0222-5>
- Patankar, S. N., & Tan, M. J. (2000). "Role of reinforcement in sintering of SiC/316L stainless steel composite." *Powder Metallurgy*, 43(4), 350–352. <https://doi.org/10.1179/003258900666078>
- Paydas, H., Mertens, A., Carrus, R., Lecomte-Beckers, J., & Tchuindjang, J. T. (2015). "Laser cladding as repair technology for Ti-6Al-4V alloy: Influence of building strategy on microstructure and hardness." *Materials and Design*, 85, 497–510. <https://doi.org/10.1016/j.matdes.2015.07.035>
- Rajan, T. P. D., Pillai, R. M., & Pai, B. C. (2010). "Characterization of centrifugal cast functionally graded aluminum-silicon carbide metal matrix composites." *Materials Characterization*, 61(10), 923–928. <https://doi.org/10.1016/j.matchar.2010.06.002>
- Randle, V., & Laird, G. (1993). "A microtexture study of eutectic carbides in white cast irons using electron back-scatter diffraction." *Journal of Materials Science*, 28(15), 4245–4249. <https://doi.org/10.1007/BF00351261>
- Salman, O., Funk, A., Waske, A., Eckert, J., Scudino, S., & Scudino, S. (2018). "Additive Manufacturing of a 316L Steel Matrix Composite Reinforced with CeO<sub>2</sub> Particles: Process Optimization by Adjusting the Laser Scanning Speed." *Technologies*, 6(1), 25. <https://doi.org/10.3390/technologies6010025>
- Sames, W. J., List, F. A., Pannala, S., Dehoff, R. R., & Babu, S. S. (2016). "The metallurgy and processing science of metal additive manufacturing." *International Materials Reviews*, 61(5), 315–360. <https://doi.org/10.1080/09506608.2015.1116649>
- Samsonov, G. V. (2008). "Imperfection of carbon sublattice: Effect on the properties of refractory carbides of transition metals." *Powder Metallurgy and Metal Ceramics*, 47(1–2), 13–20. <https://doi.org/10.1007/s11106-008-0004-5>
- Sartori, S., Pezzato, L., Dabalà, M., Maurizi Enrici, T., Mertens, A., Ghiotti, A., & Bruschi, S. (2018). "Surface Integrity Analysis of Ti6Al4V After Semi-finishing Turning Under Different Low-Temperature Cooling Strategies." *Journal of Materials Engineering and Performance*, 27(9), 4810–4818. <https://doi.org/10.1007/s11665-018-3598-x>
- Sheikhzadeh, M., & Sanjabi, S. (2012). "Structural characterization of stainless steel/TiC nanocomposites produced by high-energy ball-milling method at different milling times." *Materials and Design*, 39, 366–372. <https://doi.org/10.1016/j.matdes.2012.02.011>
- Sinatora, A., Albertin, E., & Matsubara, Y. (1996). "An investigation of the transition from M<sub>7</sub>C<sub>3</sub> to M<sub>3</sub>C carbides in white cast irons." *International Journal Cast Metals Research*, 9(October), 9–15. <https://doi.org/10.13140/RG.2.1.2422.3446>
- Song, L., Zeng, G., Xiao, H., Xiao, X., & Li, S. (2016). "Repair of 304 stainless steel by laser cladding

- with 316L stainless steel powders followed by laser surface alloying with WC powders.” *Journal of Manufacturing Processes*, 24, 116–124. <https://doi.org/10.1016/j.jmapro.2016.08.004>
- Song, Y., He, G., Wang, Y., & Chen, Y. (2019). “Tribological behavior of boron nitride nanoplatelet reinforced Ni<sub>3</sub>Al intermetallic matrix composite fabricated by selective laser melting.” *Materials & Design*, 165, 107579. <https://doi.org/10.1016/j.matdes.2018.107579>
- Stefanescu, D. M., Moitra, A., Kacar, A. S., & Dhindaw, B. K. (1990). “The influence of buoyant forces and volume fraction of particles on the particle pushing/entrapment transition during directional solidification of Al/SiC and Al/graphite composites.” *Metallurgical Transactions A*, 21(1), 231–239. <https://doi.org/10.1007/BF02656440>
- Su, S., & Lu, Y. (2020). “Densified W-Cu composite fabricated via laser additive manufacturing.” *International Journal of Refractory Metals and Hard Materials*, 87(September 2019), 105122. <https://doi.org/10.1016/j.ijrmhm.2019.105122>
- Sun, Y., Moroz, A., & Alrbaey, K. (2014). “Sliding wear characteristics and corrosion behaviour of selective laser melted 316L stainless steel.” *Journal of Materials Engineering and Performance*, 23(2), 518–526. <https://doi.org/10.1007/s11665-013-0784-8>
- Tang, Y. T., Panwisawas, C., Ghousoub, J. N., Gong, Y., Clark, J., Németh, A., ... Reed, R. C. (2020). “Alloys-By-Design: Application to New Superalloys for Additive Manufacturing.” *Acta Materialia*, 202, 417–436. <https://doi.org/10.1016/j.actamat.2020.09.023>
- Tchuindjang, J. T., & Lecomte-Beckers, J. (2011). “Study of the Origin of the Unexpected Pearlite during the Cooling Stage of Two Cast High-Speed Steels.” *Solid State Phenomena*, 172–174, 803–808. <https://doi.org/10.4028/www.scientific.net/SSP.172-174.803>
- Tchuindjang, J. T., Sinnaeve, M., & Lecomte-Beckers, J. (2011). “Influence of High Temperature Heat Treatment on in situ Transformation of Mo-rich Eutectic Carbides in HSS and Semi-HSS Grades.” In 4th Conference ABRASION (pp. 61–75).
- Tchuindjang, J. T., Torres, I. N., Flores, P., Habraken, A. M., & Lecomte-beckers, J. (2015). “Phase Transformations and Crack Initiation in a High-Chromium Cast Steel Under Hot Compression Tests.” *Journal of Materials Engineering and Performance*, 24(5), 2025–2041. <https://doi.org/10.1007/s11665-015-1464-7>
- Tchuindjang, J. T., Torres, N., Habraken, A. M., Sinnaeve, M., Lecomte-beckers, J., Mms, D., & Liège, U. De. (2014). “Characterization of the Solidification Path, the Solid State Transformations and the Mechanical Behavior of a High Chromium Cast Steel.” In 5th Conference ABRASION.
- Tong, X., Li, F. H., Kuang, M., Ma, W. Y., Chen, X. C., & Liu, M. (2012). “Effects of WC particle size on the wear resistance of laser surface alloyed medium carbon steel.” *Applied Surface Science*, 258(7), 3214–3220. <https://doi.org/10.1016/j.apsusc.2011.11.066>
- Torres, H., Vuchkov, T., Rodríguez Ripoll, M., & Prakash, B. (2018). “Tribological behaviour of MoS<sub>2</sub>-based self-lubricating laser cladding for use in high temperature applications.” *Tribology International*, 126(September 2017), 153–165. <https://doi.org/10.1016/j.triboint.2018.05.015>
- Tran, H. S., Tchuindjang, J. T., Paydas, H., Mertens, A., Jardin, R. T., Duchêne, L., ... Habraken, A. M. (2017). “3D thermal finite element analysis of laser cladding processed Ti-6Al-4V part with microstructural correlations.” *Materials and Design*, 128(January), 130–142. <https://doi.org/10.1016/j.matdes.2017.04.092>
- Ur Rahman, N., Capuano, L., van der Meer, A., de Rooij, M. B., Matthews, D. T. A., Walmag, G., ... Römer, G. R. B. E. (2018). “Development and characterization of multilayer laser clad high speed steels.” *Additive Manufacturing*, 24(August), 76–85. <https://doi.org/10.1016/j.addma.2018.09.009>

- Vrancken, B., Thijs, L., Kruth, J. P., & Van Humbeeck, J. (2014). "Microstructure and mechanical properties of a novel  $\beta$  titanium metallic composite by selective laser melting." *Acta Materialia*, 68, 150–158. <https://doi.org/10.1016/j.actamat.2014.01.018>
- Wang, J., Li, L., & Tao, W. (2016). "Crack initiation and propagation behavior of WC particles reinforced Fe-based metal matrix composite produced by laser melting deposition." *Optics and Laser Technology*, 82, 170–182. <https://doi.org/10.1016/j.optlastec.2016.03.008>
- Wang, Y. M., Voisin, T., McKeown, J. T., Ye, J., Calta, N. P., Li, Z., ... Zhu, T. (2018). "Additively manufactured hierarchical stainless steels with high strength and ductility." *Nature Materials*, 17(1), 63–70. <https://doi.org/10.1038/NMAT5021>
- Weimer, A. W. (2012). *Carbide, nitride and boride materials synthesis and processing*. Berlin: Springer Science & Business Media.
- Weng, Z., Wang, A., Wu, X., Wang, Y., & Yang, Z. (2016). "Wear resistance of diode laser-clad Ni/WC composite coatings at different temperatures." *Surface and Coatings Technology*, 304, 283–292. <https://doi.org/10.1016/j.surfcoat.2016.06.081>
- Wieczorzak, K., Bala, P., Dziurka, R., Tokarski, T., Cios, G., Koziel, T., & Gondek, L. (2017). "The effect of temperature on the evolution of eutectic carbides and  $M_7C_3 \rightarrow M_{23}C_6$  carbides reaction in the rapidly solidified Fe-Cr-C alloy." *Journal of Alloys and Compounds*, 698, 673–684. <https://doi.org/10.1016/j.jallcom.2016.12.252>
- Wieczorzak, K., Bala, P., Stepień, M., Cios, G., & Koziel, T. (2016). "Formation of eutectic carbides in Fe-Cr-Mo-alloy during non-equilibrium crystallization." *Materials and Design*, 94, 61–68. <https://doi.org/10.1016/j.matdes.2016.01.028>
- Wiengmoon, A., Pearce, J. T. H., Nusen, S., & Chairuang Sri, T. (2016). "Effects of Si on microstructure and phase transformation at elevated temperatures in ferritic white cast irons." *Materials Characterization*, 120, 159–167. <https://doi.org/10.1016/j.matchar.2016.08.025>
- Wu, C. L., Zhang, S., Zhang, C. H., Zhang, J. B., Liu, Y., & Chen, J. (2019). "Effects of SiC content on phase evolution and corrosion behavior of SiC-reinforced 316L stainless steel matrix composites by laser melting deposition." *Optics and Laser Technology*, 115(February), 134–139. <https://doi.org/10.1016/j.optlastec.2019.02.029>
- Xia, Z., Xu, J., Shi, J., Shi, T., Sun, C., & Qiu, D. (2020). "Microstructure evolution and mechanical properties of reduced activation steel manufactured through laser directed energy deposition." *Additive Manufacturing*, 33(February), 101114. <https://doi.org/10.1016/j.addma.2020.101114>
- Xu, P., Lin, C., Zhou, C., & Yi, X. (2014). "Wear and corrosion resistance of laser cladding AISI 304 stainless steel/Al<sub>2</sub>O<sub>3</sub> composite coatings." *Surface and Coatings Technology*, 238, 9–14. <https://doi.org/10.1016/j.surfcoat.2013.10.028>
- Yadollahi, A., Shamsaei, N., Thompson, S. M., & Seely, D. W. (2015). "Effects of process time interval and heat treatment on the mechanical and microstructural properties of direct laser deposited 316L stainless steel." *Materials Science and Engineering A*, 644, 171–183. <https://doi.org/10.1016/j.msea.2015.07.056>
- Yadroitsev, I., Krakhmalev, P., Yadroitsava, I., Johansson, S., & Smurov, I. (2013). "Energy input effect on morphology and microstructure of selective laser melting single track from metallic powder." *Journal of Materials Processing Technology*, 213(4), 606–613. <https://doi.org/10.1016/j.jmatprotec.2012.11.014>
- Yakout, M., Elbestawi, M. A., & Veldhuis, S. C. (2019). "Density and mechanical properties in selective laser melting of Invar 36 and stainless steel 316L." *Journal of Materials Processing*

- Technology, 266(October 2018), 397–420. <https://doi.org/10.1016/j.jmatprotec.2018.11.006>
- Yamamoto, K., Inthidech, S., Sasaguri, N., & Matsubara, Y. (2014). “Influence of mo and w on high temperature hardness of  $M_7C_3$  carbide in high chromium white cast iron.” *Materials Transactions*, 55(4), 684–689. <https://doi.org/10.2320/matertrans.F-M2014801>
- Yikun, L., Nannan, S., Xiuhong, K., Dianzhong, L. I., Luan, Y. K., Song, N. N., ... Dianzhong, L. I. (2010). “A Study of the Carbides in High-Speed Steel Rolls.” *Materials Science Forum*, 638–642, 3356–3361. <https://doi.org/10.4028/www.scientific.net/MSF.638-642.3356>
- Yip, M. W., Barnes, S., & Sarhan, A. A. D. M. (2015). “Deposition of a silicon carbide reinforced metal matrix composite (P25) layer using  $CO_2$  laser.” *Journal of Manufacturing Science and Engineering, Transactions of the ASME*, 137(3), 1–8. <https://doi.org/10.1115/1.4029831>
- Zhang, Y. L., Li, J., Zhang, Y. Y., & Kang, D. N. (2020). “Evolution in microstructure and high-temperature oxidation behaviors of the laser-cladding coatings with the Si addition contents.” *Journal of Alloys and Compounds*, 827. <https://doi.org/10.1016/j.jallcom.2020.154131>
- Zhang, Z., Farahmand, P., & Kovacevic, R. (2016). “Laser cladding of 420 stainless steel with molybdenum on mild steel A36 by a high power direct diode laser.” *Materials and Design*, 109, 686–699. <https://doi.org/10.1016/j.matdes.2016.07.114>
- Zhao, L., Santos Macías, J. G., Ding, L., Idrissi, H., & Simar, A. (2019). “Damage mechanisms in selective laser melted AlSi10Mg under as built and different post-treatment conditions.” *Materials Science and Engineering A*, 764(July), 138210. <https://doi.org/10.1016/j.msea.2019.138210>
- Zhong, Y., Liu, L., Wikman, S., Cui, D., & Shen, Z. (2016). “Intragranular cellular segregation network structure strengthening 316L stainless steel prepared by selective laser melting.” *Journal of Nuclear Materials*, 470(December), 170–178. <https://doi.org/10.1016/j.jnucmat.2015.12.034>
- Zhou, X. F., Fang, F., Jiang, J. Q., Zhu, W. L., & Xu, H. X. (2012). “Study on decomposition behaviour of  $M_2C$  eutectic carbide in high speed steel.” *Materials Science and Technology*, 28(12), 1499–1504. <https://doi.org/10.1179/1743284712Y.0000000081>
- Zuback, J. S., & DebRoy, T. (2018). “The hardness of additively manufactured alloys.” *Materials*. <https://doi.org/10.3390/ma11112070>



### 3. Fabrication and characterization of alloys and MMC fabricated by LC

Section 1 introduced metal AM and the aim of this PhD research, which is to understand the metallurgy behind materials composed of 316L and hard carbides fabricated by AM. In the state of the art (section 2), the existing materials fabricated under very high cooling rates were reported. Particular attention was given to the fabrication methodologies, the formation of these microstructures and the correlation between mechanical properties and the observed phases. The general purpose of the work is cast into five specific sub-topics hereafter.

#### 3.1. Powder handling and preparation

The difficulty of MMC fabrication by AM is related to the differences between the characteristics of the two powders (i.e. morphology, density and size distribution). Compared to MMC fabrication by SLM, these differences become less critical in LC since the two streams of powders could be handled separately. Furthermore, as mentioned in section 1.3, the lower quantities of powders needed in LC allows the use of pre-mixed powder (Lang, 2020). Nevertheless, in both techniques, appropriate storage conditions to avoid contamination with moisture is a paramount demand in order to avoid porosities in the final part. As mentioned in section 1.4, materials composed of 316L and ceramic particles can be fabricated with different approaches, depending on the characteristics of the feedstock.

##### 3.1.1. Separate handling of the powders

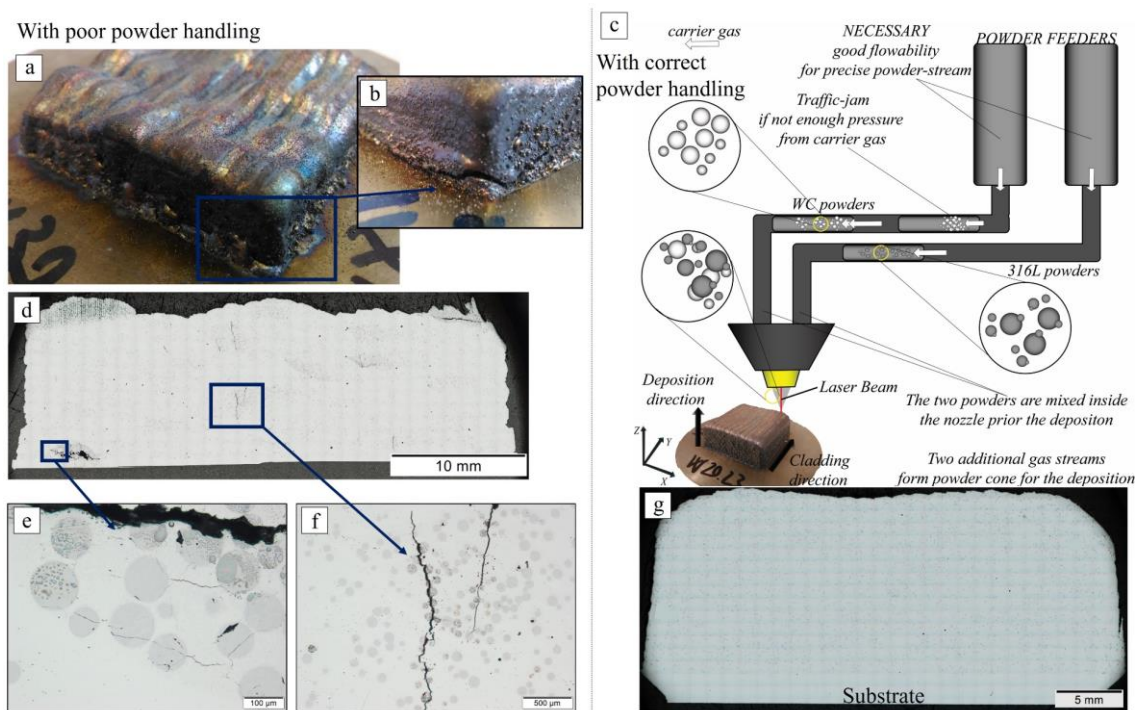


Fig. 3-1: Fabrication of the 316L + WC. External (a and b) and internal (d, e and f) defects caused by poor powder handling and improper process parameters. (c) Schematics of the LC fabrication with few critical issues. (g) Cross-section of the 316L+20%WC after correct powder handling.

The fabrication of the 316L + WC composite could be made efficiently by handling the two powders separately (see Article #2 and #3). Both powders exhibit spherical morphology and good flowability. Nevertheless, in addition to the most known laser power and scanning speed, many other process parameters must be adapted according to the characteristics of the considered powders (Deschuyteneer, 2015, 2017). The settling of the powders in the powder feeders (minimum 1 day of settling as common practice) and the output of outer gas flows respectively in the tubes and the nozzle must be taken into account (Fig. 3-1c). The complete set of process parameters is given in Table 3-1. The fabrication of the WC composites is further discussed in section 3.2.1.

### 3.1.2. Powder preparation

The fabrication of the 316L + SiC composites, handling the two powders separately, leads to the detachment of the deposit (Fig. 3-2a) and to high quantity of porosities (Fig. 3-2b). Both powders exhibit spherical morphology and good flowability, but SiC particles are partially porous (Fig. 3-2d) due to the spray drying and Acheson processes (Nandiyanto, 2019; Polozov, 2020; Weimer, 2012). During deposition, the gas in these closed porosities gathers and forms bubbles into the melt pool (see Article #5). Eventually, part of this gas could escape and leave cavities on the surface (Fig. 3-2b).

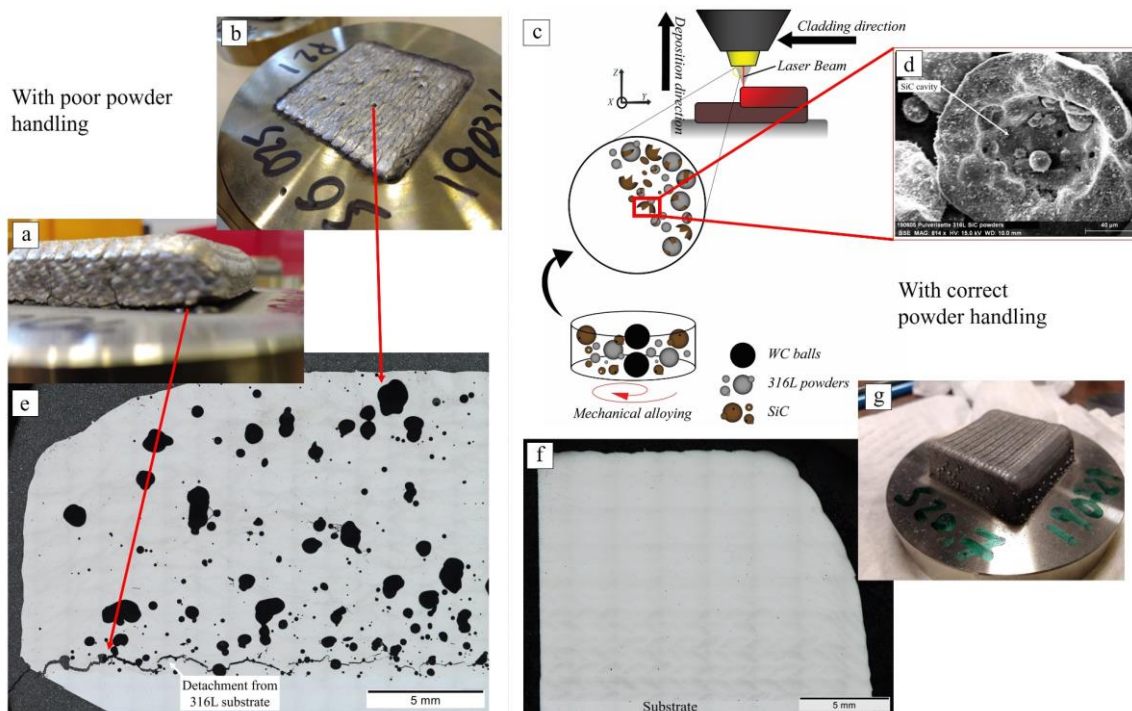


Fig. 3-2: Fabrication of the 316L + SiC. External (a and b) and internal (e) defects caused by poor powder handling and improper process parameters. (c) Schematics of the mechanical alloying procedure and LC fabrication. (d) SEM image of a fractured SiC, showing an internal cavity and porosities. Final 316L+20%SiC deposit (g) and its cross-section (f) after correct powder handling.

Large quantities of porosities and difficulties during fabrication were already reported in previous works, probably due to the presence of oxygen in the form of porosities or retained SiO<sub>2</sub> in the feedstock (Brytan, 2011; Yip, 2014). In order to achieve a sound deposit, a mechanical alloying procedure

(*Sheikhzadeh, 2012*) was implemented to fracture the SiC and close these porosities (Fig. 3-2c and d). Furthermore, DTA analyses were carried out on the milled powder mixtures to qualitatively assess the presence of oxygen (see Article #5 and (*Saggionetto, 2019*)).

With this procedure, the critical issue is the homogeneity of the powder mixture, which becomes more difficult to maintain with the increase of the volume percentage of SiC. Indeed, the composite with 30% SiC could not be fabricated due to the large quantity of SiC particles, which tend to segregate in the powder feeder due to their low density.

**Claim and contributions:**

A mechanical alloying procedure on the 316L+SiC mixture was elaborated (1h milling time with 1:5 wt. ratio of WC ball) in order to eliminate the pre-existing oxygen. Two composites having respectively 10% and 20% in volume of SiC were fabricated with high reproducibility (Fig. 3-2g and f) and without defects.

Besides, a similar procedure was applied to the mixture of 316L + TiC in order to attach the small TiC particles (2-10  $\mu\text{m}$ ) to the larger 316L particles (50-150  $\mu\text{m}$ ). Sound deposits with the addition of 15% in volume of TiC were fabricated in a protective atmosphere due to the high affinity of Ti with oxygen. This approach allows enlarging the possible range of particle size in LC (50-200  $\mu\text{m}$ ) since the hosting powder could carry finer reinforcements (*Ertugrul, 2020*). In addition, the attachment of carbides on the hosting powders by mechanical alloying increases their absorbance due to the higher absorptivity of the ceramics (*Tolochko, 2000*). Therefore, the process parameters must be adapted since higher absorbance drastically changes the thermal history and the solidification route.

### 3.2. Fabrication

#### 3.2.1. Process parameters

The final dimensions of the deposits were 35 x 35 mm side length and 13.5-14 mm height on average (Table 3-1). These dimensions were chosen to obtain suitable samples for wear tests (pin-on-disc tests) and to observe microstructural and property variations with the increase of the deposit height. These two topics will be faced respectively in sections 3.5 and 3.3. The details of the process parameters are given in Table 3-1. Lower power and scanning speed is applied during the curves of the deposition strategy (see Article #3 and (Fetni, 2021)). These streams of powders are the average value of all the relative deposits (N°). The parameters of the two powders for the 316L+WC composites are given separately (Fig. 3-1c) while for the other deposits (Fig. 3-2c and g), the average quantity of ceramic particles is given in parenthesis. The proportions for the deposits were calculated considering the density of the powder measured via a helium pycnometer. The values are measured before and after fabrication, weighting the stream of powder after 5 minutes to reach steady-state flow. Nevertheless, the measure after fabrication is the most representative since it corresponds to the actual steady-state during the process.

Table 3-1: Process parameters of the deposits fabricated by LC.

Name	Powder 1 (316L or mixture)		Powder 2 (WC)		N°	Power (W)	Traverse speed (mm/min)	Height (mm)
	Stream (gr/min)	Carrier Gas (sL/min)	Stream (gr/min)	Carrier Gas (sL/min)				
316L	3,03	3	/	/	12	400-570	270-290	13,75
316L+10%WC	3,02	3	0,73	3,5	12	400-570	270-290	13,49
316L+20%WC	3,05	3	1,59	3,5	13	400-570	270-290	13,97
316L+10%SiC	3,06 (0.12)	3	/	/	4	260-400	250-270	13,88
316L+20%SiC	3,03 (0.24)	3	/	/	7	260-400	250-270	13,50
316L+15%TiC	3,02 (0.24)	3	/	/	4	400-570	270-290	13,37

During the fabrication of WC composites, compared to steel powders, higher output of carrier gas (i.e. inert gas that carries powders from the powder feeder to the nozzle) must be applied to the WC powders due to their high density. This assures homogeneous streams and thus the desired volume percentage (vol.%) of WC into the composite. Heterogeneous streams lead to an inconstant quantity of deposited material (Fig. 3-1a and d) and high concentration of reinforcements (Fig. 3-1e) in a single track. As observed in (Wang, 2016), high quantities of WC reinforcements cannot stand the cyclical thermal stresses during deposition due to the coefficient of thermal expansion mismatch between WC particles and the surrounding metal matrix. Micro-cracks are observed to propagate through the grain boundaries and WC particles (Fig. 3-1f), thus leading to failure and often detachment from the substrate (Fig. 3-1b). The critical volume percentage of WC was set at 23.5 %, corresponding to the maximum allowable quantity of WC in a deposit with the chosen dimensions if the initial substrate is at room temperature.

3.2.2. Interactions between reinforcements and molten metal

Understanding the interactions between reinforcements and molten pool is a paramount demand for the design and fabrication of MMC. When the reinforcements are carbides, the chemical affinity with the matrix is usually high and a partial or total dissolution of the reinforcements leads to the modification of the matrix. Indeed, the dissolution of these reinforcements by interfacial reactions with the molten pool during process is a well-known challenge in the production of MMC. In particular, when WC is chosen as reinforcement, these physical and chemical interactions reinforce the matrix, leading to the formation of hard solidification carbides and of connection layers around the partially dissolved WC particles linking them to the matrix (Song, 2016; Tong, 2012). As shown in Fig. 3-3, the initial size distribution of the WC powders determines the quantity of solidification carbides and partially dissolved WC carbides. Small particles tend to dissolve completely, while larger ones dissolve only partially, leaving their cores in the final microstructure (Tong, 2012). Deeper attention will be given to the identification of the new solidification carbides in section 3.4.2.

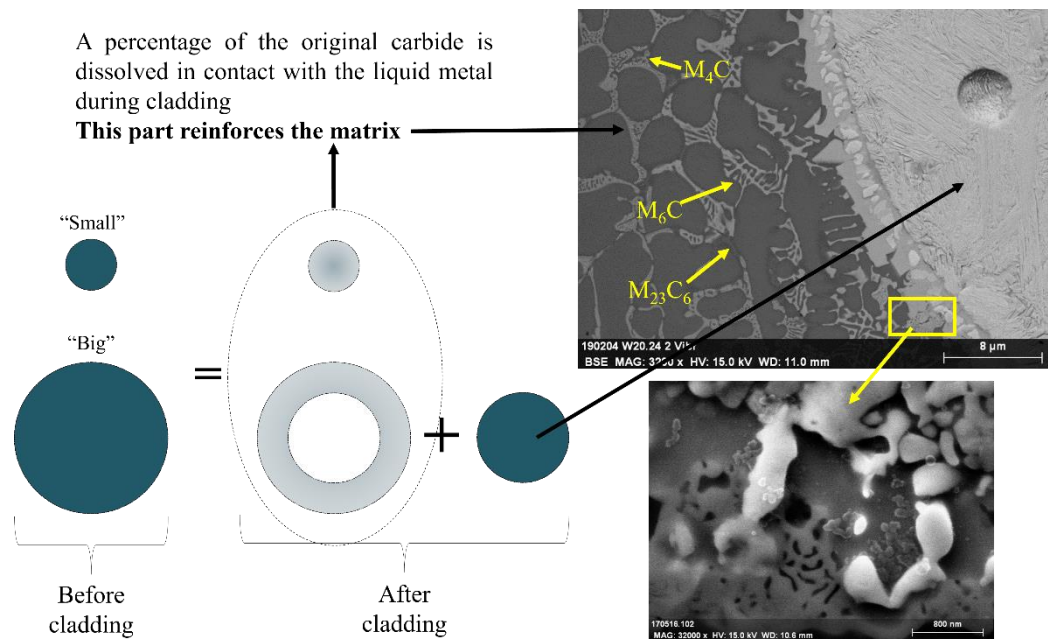
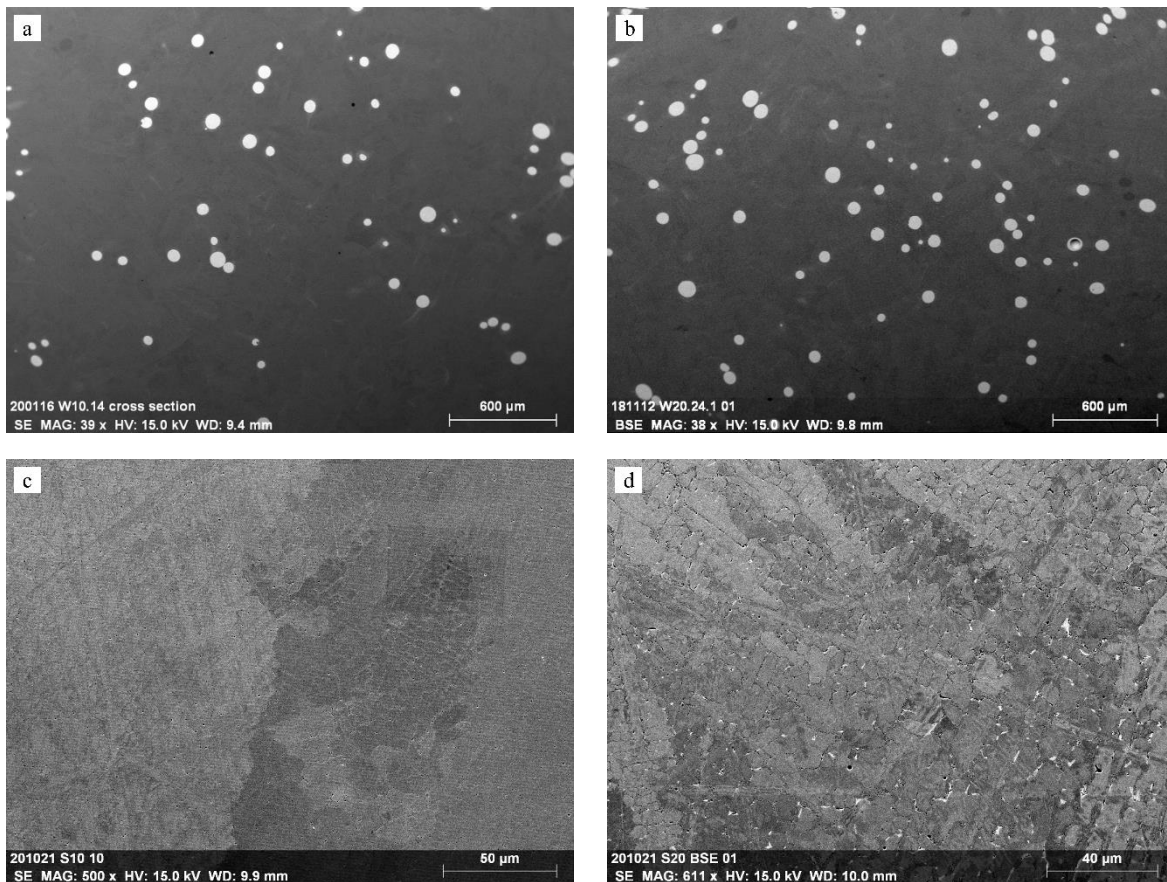


Fig. 3-3: Schematics representing the dissolution of the WC particles during the LC process depending on their initial size. The dissolved part of the original powders enrich the 316L composition and leads to the formation of solidification carbides during the cooling.

In both 316L+WC composites fabricated by LC (section 3.1), partially dissolved WC particles (Fig. 3-4a and b) are well distributed in an austenitic matrix reinforced by a network of reaction carbides (Fig. 3-3). On the other hand, in 316L+SiC materials, for both volume fraction of SiC (10 and 20%), (Fig. 3-4c and d), the complete dissolution of the SiC by interfacial reactions with the melt pool occurs in good agreement with previous works (Brytan, 2011; Lian, 2020; Yip, 2015). Therefore, these two combinations lead to the fabrication of two modified alloys, exhibiting a reinforced austenitic microstructure (see Article #5).



*Fig. 3-4: SEM micrographs (BSE mode) of the four deposits fabricated by LC. The MMC with respectively 10% (a) and 20% (b) of WC exhibit a different quantity of well-distributed WC carbides in the microstructure. The deposits with the addition of respectively 10% (c) and 20% (d) of SiC do not show any remaining reinforcement.*

In-depth microstructural characterization of WC and the 316L+WC composites reveals the traces of the interactions between the WC particles and the molten metal during deposition (see Article #2). Outward elemental flows from the WC particles enrich the composition of the original 316L matrix in W and C, while inward Fe and Ni elemental flows from the molten metal into the WC particles destabilize the phases that had been formed during gas atomization (*Levi, 1988*). These exchanges lead to the partial or total (for the smallest particles) dissolution of the WC particles (Fig. 3-3).

Indeed, image analysis measurements on the cross-sections (2D) of the MMC and on the original WC powders highlight the difference in the size distribution of the reinforcements and thus the quantity of material dissolved in the matrix (Fig. 3-5a). The larger quantity of WC in the 316L+20% WC leads to a lower dissolution of any given particle. Furthermore, EDS profile analyses on the 316L+20% WC (Fig. 3-5b) exhibit a steady value of the W amount in the microstructure away from the remaining WC cores (see Article #3). This value (9.5-9.7% wt. of W), measured from the 6<sup>th</sup> layer of a thick deposit (Fig. 3-1), corresponds to the saturation of the liquid in W and when this quantity is attained from the dissolution of the reinforcements, the remaining WC cores are stable in the molten metal and dissolution does not proceed any further (*Easton, 2016*).

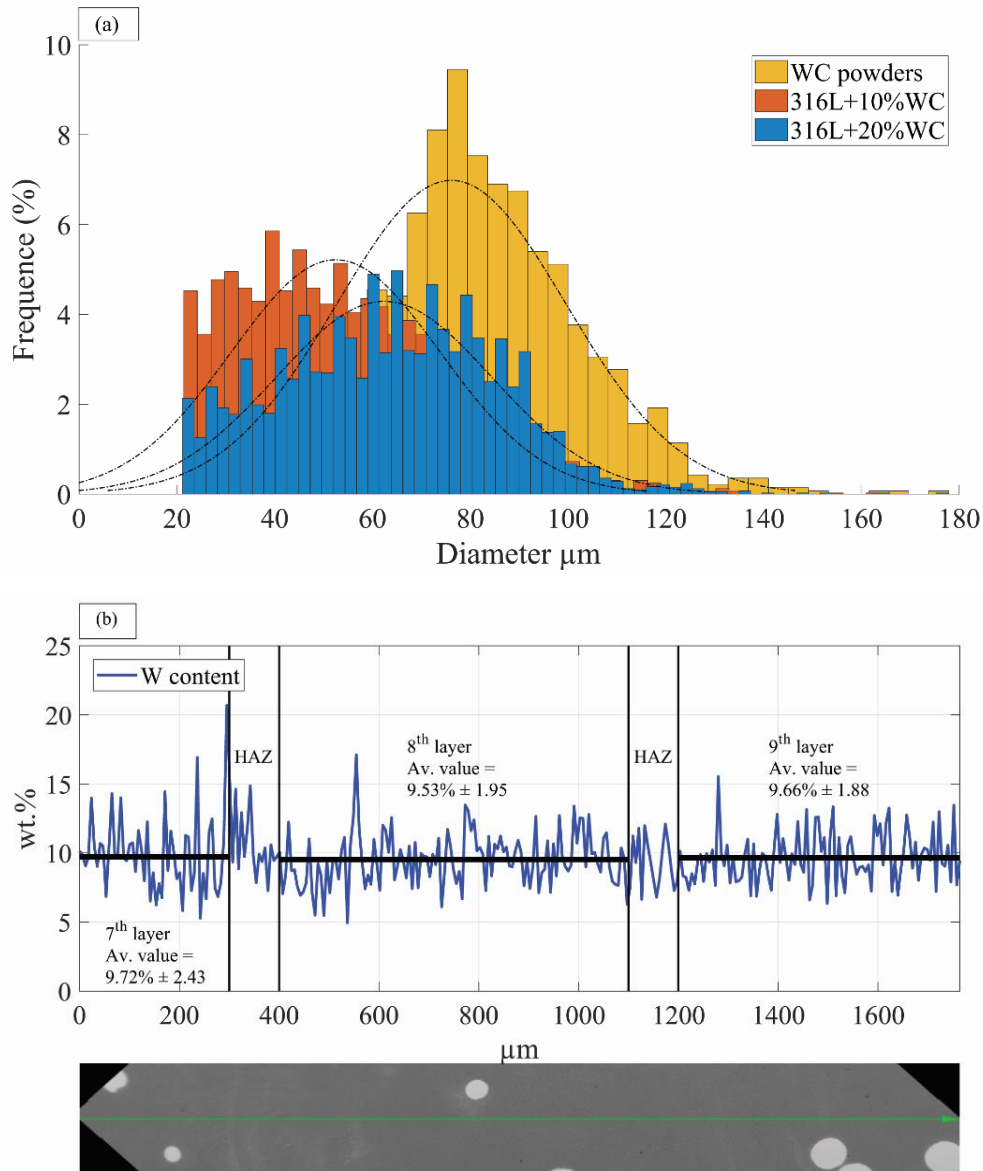


Fig. 3-5: (a) Histograms of the image analysis measurements on the cross-sections of the original WC powders and the two MMC. (b) SEM/EDS profile analysis along the substrate and first three deposited layers. The average value of the three different layers are reported and plotted as black lines.

Furthermore, reinforcement dissolution is linked to the liquid lifetime of the melt pool, which is also the time length of the interactions between reinforcements and the liquid. Indeed, EDS profile analyses on the 316L+10%WC reveal an increase of W amount with the increase of the deposit height but this value remains below 5.5 % wt. of W (Nordera, 2020). Therefore, high cooling rates and thus short liquid lifetime decrease the dissolution of the reinforcements for a given volume fraction. The influence of the process conditions on the reinforcements dissolution and the microstructure will be further addressed in section 3.3.

**Claim and contributions:**

The extent of dissolution for a given volume fraction of reinforcements is directly connected with the size distribution. In order to decrease the general dissolution, a tailored and higher size distribution may be adapted using only large particles. Moreover, high volume fraction may also help to stabilize the reinforcements in the molten metal. When liquid saturation is attained, the cores of the reinforcements are stable in the molten metal and dissolution does not proceed any further. Concerning the 316L+WC composites, the liquid saturation is set at 9.5-9.7% wt. of W.

Nevertheless, the complete dissolution of the SiC is achieved due to its high affinity with Fe-base alloys, even when using large particle sizes. The saturation of the liquid during deposition was not attained, independently of the volume fraction of reinforcement. EDS analyses measure a maximum of 3.5 % wt. of Si in the 316L+20%SiC alloy. The tendency of the reinforcements to dissolve in the molten metal and thus their chemical affinity with the matrix can be estimated by differential thermal analysis (DTA) tests of the original powders at high heating rates (i.e. high scans). Indeed, SiC particles are completely dissolved at any given scan while WC particles are only partially dissolved and precipitate at the bottom of the crucible during the test with a low scan rate of 0.3°C/s.

**Claim and contributions:**

The chemical affinity is the main characteristic that determines either the complete dissolution or a partial dissolution of the reinforcement in a given matrix. The high chemical affinity of Si with Fe and the high limit of liquid saturation of Si (higher than 3.5 % wt.) in Fe leads to the complete dissolution.

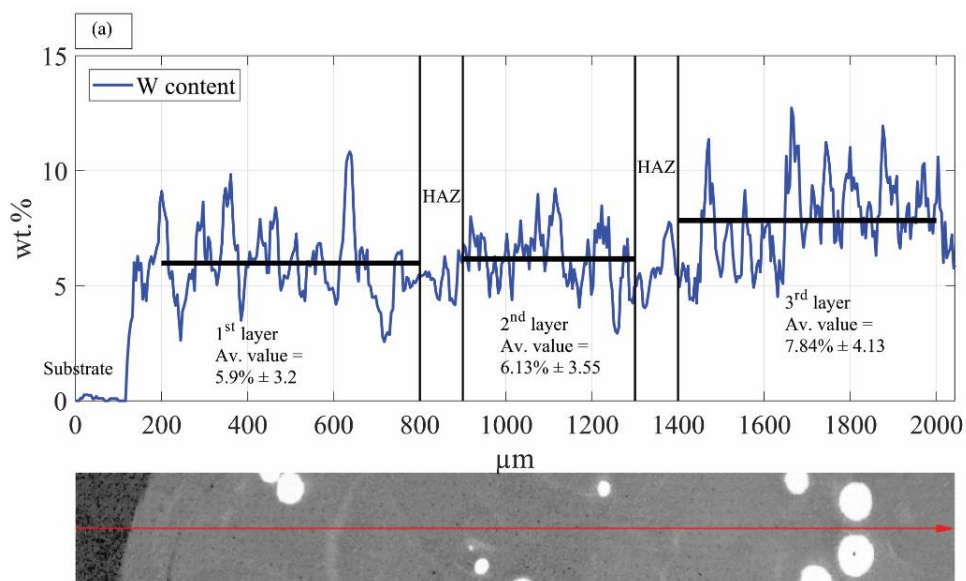
Indeed, in the 316L+15%TiC composite of (Ertugrul, 2020), as in the WC composites, EBSD analyses reveal the presence of both original and solidification TiC carbides. Furthermore, EDS profile analyses on the matrix away from the original TiC exhibit a constant value of 3.75-3.8% wt. of Ti. Therefore, even with a lower volume fraction and small particles of TiC, liquid saturation is attained and only partial dissolution occurs.

### 3.3. Macroscopic characterization

As already mentioned in sections 3.2.1, thick deposits were fabricated to evaluate possible microstructural variations with increasing height. Indeed, when keeping the process parameters constant with the progress of the fabrication, the heat from the already deposited layers accumulates, leading to local changes of the deposition conditions (Yang Liu, 2018; Manvatkar, 2014; Wirth, 2018; Yadollahi, 2015; Zhang, 2016). A well-known consequence of heat accumulation is the reduction of the cooling rates (Fig. 2-7) and thus the coarsening of the microstructure with increasing height (Manvatkar, 2014; Zuback, 2018). The influence of the heat accumulation on the fabrication of a composite and the resulting modification of the mechanical properties (section 3.3.3) are presented hereafter. The mechanical properties are considered in more depth in section 3.5. This topic was investigated especially on the WC composites since partial dissolution of the reinforcements occurs. The attention was focused more particularly on the 316L+20% WC composite due to the saturation of the liquid in W during the fabrication (Fig. 3-5). Nevertheless, these general considerations on the process conditions could be applied to any reinforcement or reactant.

#### 3.3.1. Detection of microstructural variations

As partially shown in section 3.2.2, the amount of W in the matrix (away from the WC cores) increases with the height in the 316L+10% WC composite. In the 316L+20% WC composite, liquid saturation in W is attained (9.5-9.7 % of W) from the 6<sup>th</sup> deposited layer (19 layers in total). Nevertheless, as in the 316L+10% WC composite, the first five layers of the 316L+20% WC composite exhibit an increase of the W amount in the matrix (with a high standard deviation) (Fig. 3-6a).



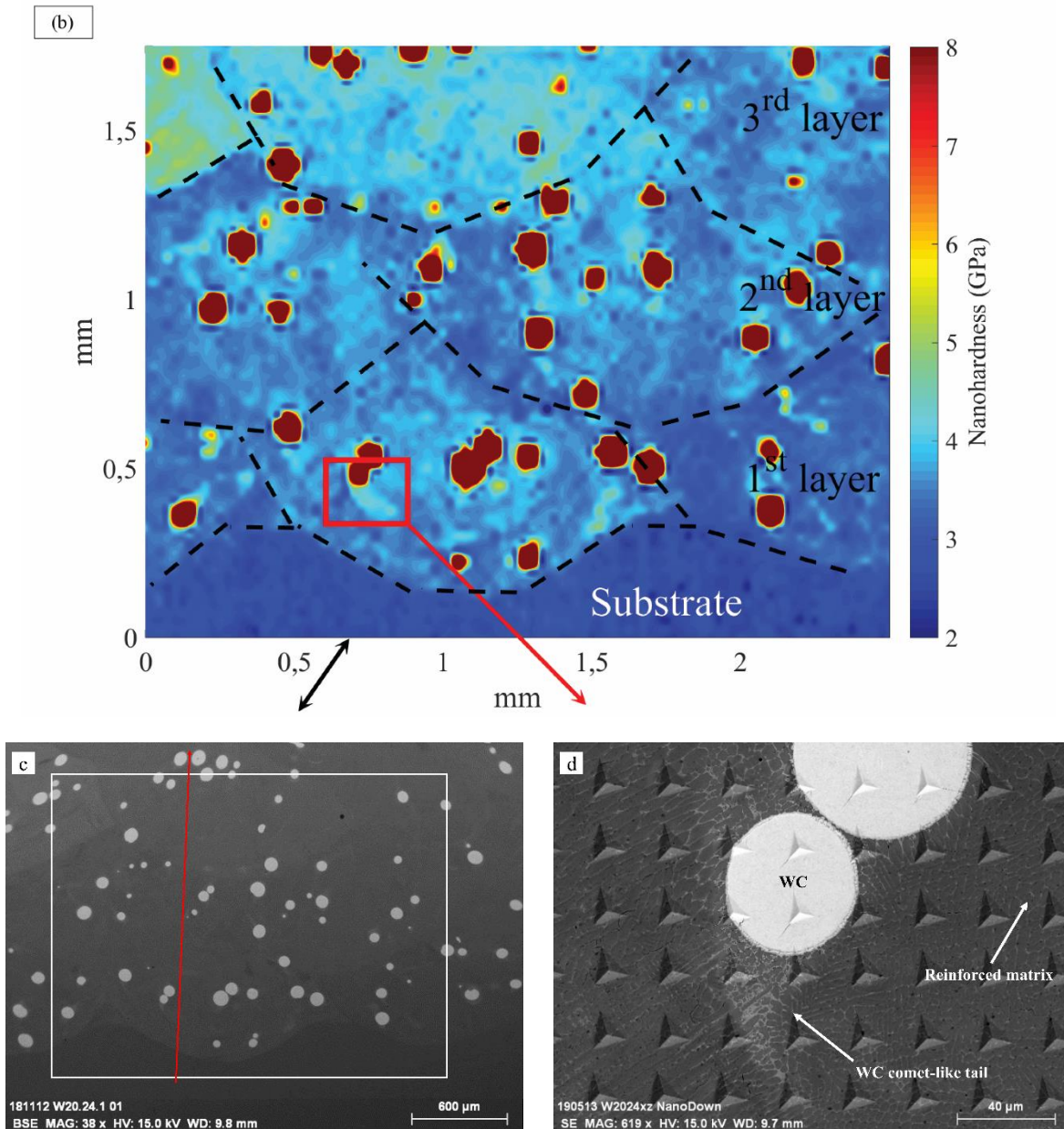


Fig. 3-6: (a) SEM/EDS profile analysis (red line in SEM micrograph (c)) across the substrate and first three deposited layers. (b) Nanoindentation map of the first 3 deposited layers highlighted by the white rectangle in the SEM micrograph (c). (d) BSE micrograph of the microstructure observed in the first deposited layers.

With the purpose to detect every possible microstructural variation both at the base of the deposits (Fig. 3-6a) and at higher heights, a novel characterization method was implemented inspired by (Randall, 2009), carrying out nanoindentation tests on large surfaces. In this method, in order to characterize multiphase materials, depending on the size of the phases in the microstructure and the area to analyse, a penetration displacement ( $h$ ) is chosen (Fig. 3-7). Then, nanoindentation grids are run automatically maintaining a minimum distance ( $d$ ) among the indents in order to avoid any overlapping of their affected volume (Fig. 3-7), which is linked to the chosen  $h$  (2000 nm in this case) (Jung, 2013; Mahabadi, 2012; Tillmann, 2017). Compared to the “force control”, the “displacement control” mode of the nanoindenter allows more precision of the analyses since it relates to microstructural features.

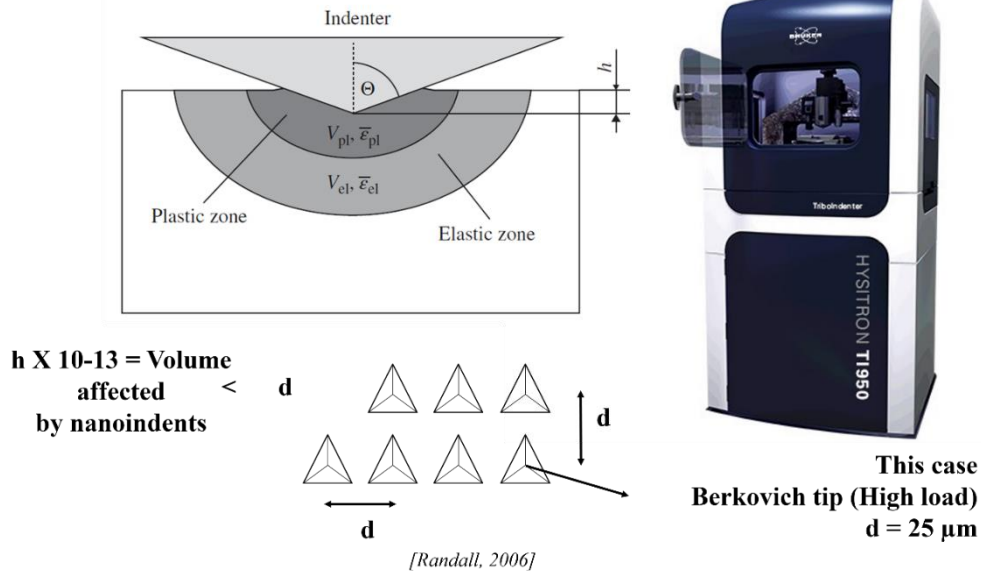


Fig. 3-7: Schematics of the volume affected by an indent and the relative distance to avoid the overlapping of the plastic zones in the nanoindentation grids.

The result of this grid is a nanoindentation map (Fig. 3-6b), where every track and layer can be distinguished. In particular, a high gradient of nanohardness between the softer 316L substrate (2-3 GPa) and the metal matrix of the first three layers (3-6 GPa) is measured. This is illustrated in Fig. 3-6d that shows the microstructure corresponding to the red square on the nanoindentation map of Fig. 3-6b. A comet-tail shaped area rich with solidification carbides (4-4,5 GPa) surrounds a WC core and its carbide crown (4,5-6 GPa). Such WC comet-like tails are observed only in the first two layers of the deposit. This high concentration of carbides is formed from a W-C-rich liquid after the partial or total dissolution of the reinforcements. As observed first in classical welding and in most AM technologies, surface tension gradients depending on the process parameters lead to the occurrence of the Marangoni effect, i.e. fluid flows patterns directed inward according to the moving direction of the laser (AlMangour, 2018; Dass, 2019; Lienert, 2011; Yadollahi, 2015). Similarly to radioactive tracker particles during a nuclear medicine test, some WC particles in the first deposited layers are observed to exhibit these comet-like tail marking their movement, as they are transported by the flows (AlMangour, 2018; Lee, 2014; Quested, 2004; Wirth, 2018). The combination of SEM observations and nanoindentation grids is thus efficient to reveal local microstructural variations in large surfaces of heterogeneous microstructures.

### 3.3.2. Microstructural variation due to heat accumulation

As shown in Fig. 3-6b, in the third layer, the comet-like tails are not observed and the microstructure is more homogeneous due to the stronger mixing of the melt pool. Indeed, as a consequence of the temperature rise due to the heat accumulation, liquid lifetime and Marangoni effect increase with the increase in height (Yang Liu, 2018; Manvatkar, 2014; Wirth, 2018; Yadollahi, 2015; Zhang, 2016). Under those conditions, the transport of the WC particles is enhanced resulting in an increase of the

liquid in contact with a given particle and a stronger mixing of the melt pool (Wirth, 2018; Zhang, 2016). This increasing interaction leads to a larger quantity of elements dissolved in the liquid until liquid saturation (Easton, 2016), as measured at 9.5-10% of W (% wt.) (Fig. 3-5b).

In addition, the stronger mixing results in a more homogeneous distribution of W and C in the molten metal and leads to a general reinforcement of the track after solidification, as opposed to the formation of the comet-like tails in the first two layers (see Article #3). With the increase of the distance from the 316L substrate, the value of the nanohardness maps stabilizes between 3-6 GPa in a similar trend to that observed for the W amount in the matrix (Fig. 3-5b) (see Article #3).

**Claim and contributions:**

The movements of the WC carbides in the melt pool are shown through the WC comet-like tails. These carbide structures formed as a result of the interaction between the molten metal and the WC powders, while the WC particles are transported by Marangoni flow. With the increase of the deposition height, these carbide structures are not observed anymore and the microstructure is more homogeneous.

On the other hand, in the 316L+10%WC composite, the temperature rise leads to a continuous increase of the melt pool stirring and of the dissolution of the WC since the saturation cannot be attained (Nordera, 2020). Indeed, as mentioned in section 3.2.2, the W amount in the matrix increases with the increase of the distance from the substrate. Therefore, the increase of heat accumulation, liquid lifetime and Marangoni effect increase the dissolution of the reinforcements and in order to preserve the reinforcements, short liquid lifetime and low heat accumulation are needed.

Nevertheless, heat accumulation is beneficial since it homogenizes the microstructures due to the stirring during deposition. Besides, heat accumulation also decreases the thermal stresses since the cooling rates decrease (Yang Liu, 2018; Manvatkar, 2014; Wirth, 2018; Yadollahi, 2015; Zhang, 2016). These effects may be exploited to deposit MMC with a higher volume fraction of reinforcements, or FGM with materials that require the preheating of the substrate in order to be printed (i.e. tool steels) (Corongiu, 2020; Gingell, 2019).

**Claim and contributions:**

Heat accumulation allows to increase the volume fraction of reinforcements since it decreases the thermal stresses and increases the homogeneity, but with more dissolution. Moreover, heat accumulation allows depositing gradient material, using the first material to preheat the substrate where such preheating is needed to deposit successfully the second material.

In the design of a MMC, the choice of the fabrication conditions depends on the targeted application since faster cooling rates and a cold substrate leads to lower dissolution, but also to a more heterogeneous material since the matrix is less modified from the dissolution of the reinforcements. On the other hand, when the cooling rates are lower, the matrix is more homogeneous, but the dissolution is higher.

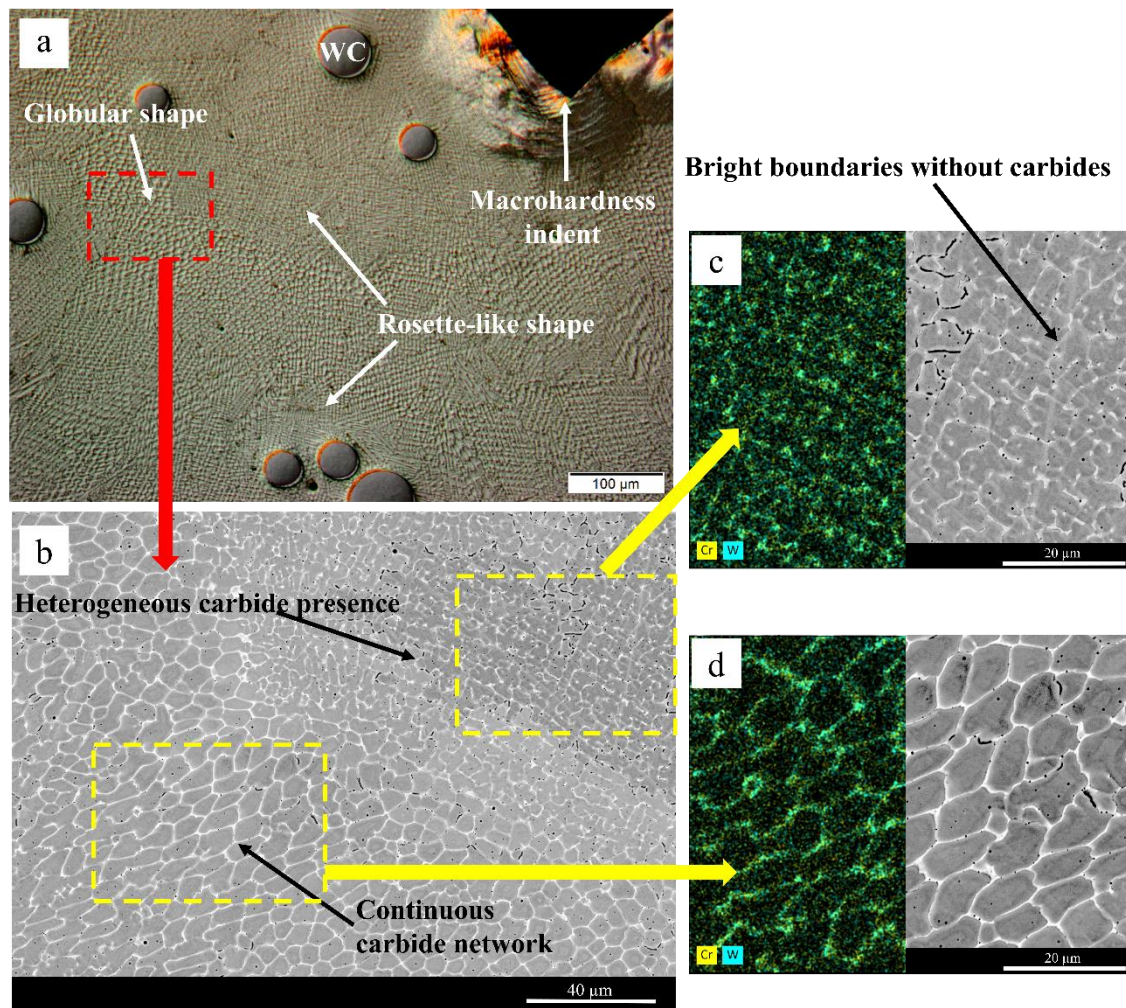


Fig. 3-8: (a) Optical micrograph (200x) of the composite microstructure with a macro-hardness indent performed at 6 mm from the substrate. (b) SEM micrograph (BSE mode) corresponding to the microstructure in the red square in (a). SEM micrographs corresponding at the rosette-like shape (c) and the globular shape (d) with the Cr and W element distribution.

In the 316L+20%WC composite, the stabilisation of the WC carbides in the melt pool leads to the formation of a rosette-like shape (Fig. 3-8c), in addition to the more usual globular structure (Fig. 3-8d). The presence of those WC particles moving in a liquid saturated with W promotes heterogeneous nucleation during solidification since WC reinforcements act as nucleation sites or grain refiner (Easton, 2016; Ho, 2018; Lienert, 2011; Queded, 2004). Indeed, the size of the dendritic-cellular morphology around the partially dissolved carbides is smaller (Fig. 3-8). Besides, as reported in (Amin-Ahmadi, 2010), fragmentation of the dendrites nucleated on the WC particles may occur due to turbulence of the

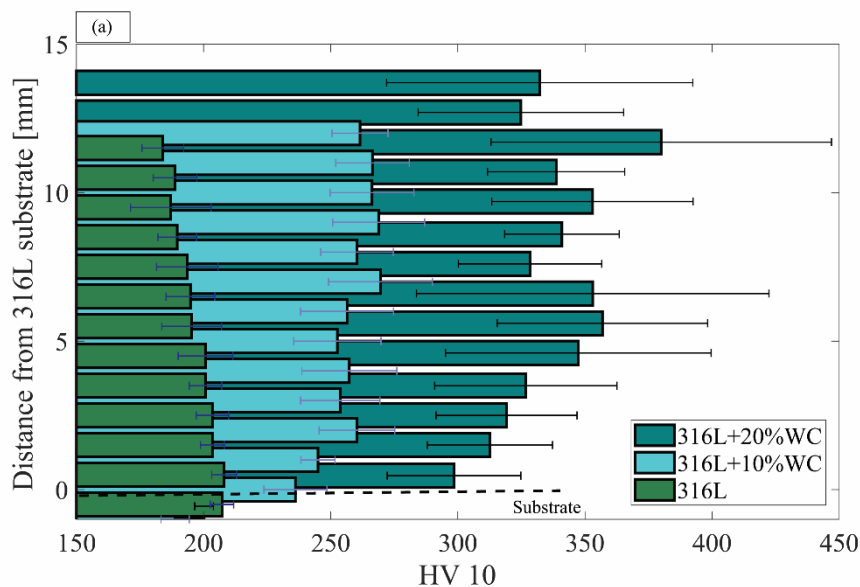
molten metal or to plastic deformation of the dendrite arms. The fragments may then act as additional heterogeneous nuclei for solidification inside the melt pool (see Article #3). The consequence of the refined morphology will be discussed in section 3.5.

**Claim and contributions:**

A cellular and a rosette-like morphologies are distinguished in the microstructure of the thick deposit. Detailed microstructural characterization reveals that undissolved WC particles act as sites for heterogeneous nucleation, leading to the formation of the finer rosette-like morphology.

*3.3.3. Evolution of the macrohardness*

Large grids of macrohardness measurements were carried out in order to evaluate the effect of the microstructural variations observed in section 3.3.2 on the mechanical properties. The results of the five macro-hardness grids on the four proposed materials and 316L reference are shown in Fig. 3-9. The hardness line below 0 is related to the 316L substrate. The average hardness of the 316L deposit is 197 HV, slightly lower than that of the two substrates at 204 HV. The hardness of the 316L and the SiC alloy deposit constantly decreases with increasing distance from the 316L substrate (Fig. 3-9b) due to a coarsening of the microstructure (*Feenstra, 2020; Herzog, 2016; K. Li, 2015; Song, 2016; Ur Rahman, 2018; Zuback, 2018*). Indeed, EBSD analyses on large zones on the 316L deposit show an increase of the grain size with increasing distance from the substrate (*Ertugrul, 2020*).



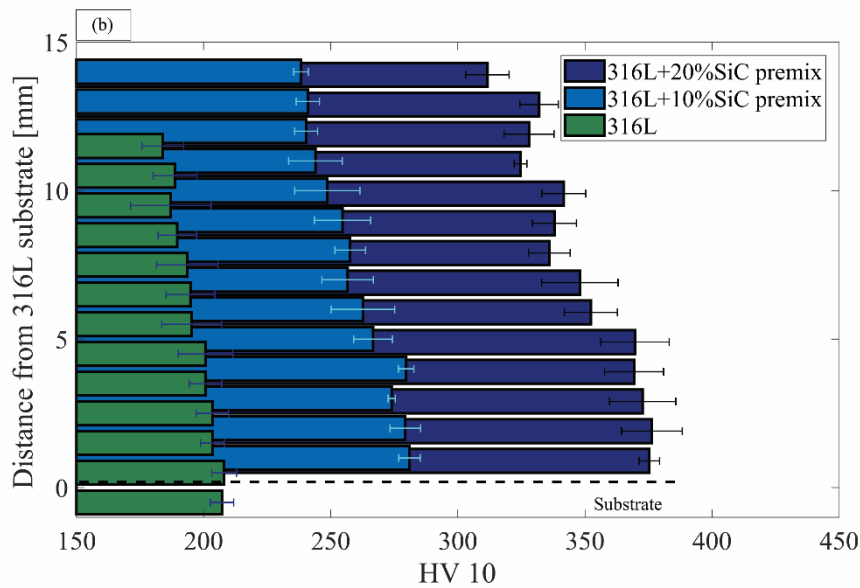


Fig. 3-9: (a) Macro-hardness evolution of the WC deposits and the 316L deposit fabricated with the same parameters, with the relative standard deviation for each measurement row. (b) Macro-hardness evolution of the SiC deposits and the 316L deposit fabricated with the same parameters.

The reinforced microstructures of the WC composite deposits (Fig. 3-9a) exhibit an average hardness value of respectively 258 HV and 337 HV with a large standard deviation due to the presence of partially dissolved WC giving rise to local value as high as 450-500 HV. The standard deviation is higher in some rows of the grid due to a locally higher number of partially dissolved carbides (*Deschuyteneer, 2017; Tong, 2012*), e.g. at 12 mm from the substrate in the 316L+20%WC deposit.

The hardness of the 316L+10%WC composite continuously increases (Fig. 3-9a) due to the phenomenon of the heat accumulation described in section 3.3.2 and thus the increase of the dissolution, which leads to an increase of the solidification carbides amount (*Nordera, 2020*).

In the 316L+20%WC composite, the hardness values increase up to the 6<sup>th</sup>-7<sup>th</sup> measurement row ( $\pm 6$  mm from the substrate) then decrease slightly but constantly (Fig. 3-9a), up to the top of the deposit. As in the 316L+10%WC, the phenomenon of heat accumulation leads to this trend. Indeed, the first increase of the hardness value is linked to an increase of the dissolution and an enhancement of the stirring of the melt pool (Fig. 3-6), which leads to the general reinforcement of the microstructure with solidification carbides. In addition, when the saturation of the liquid in W is attained, the remaining WC cores act as nuclei for heterogeneous nucleation (*Easton, 2016*). Indeed, EBSD analyses on large zones of this composite show a decrease of the grain size up to 6 mm from the substrate. At higher heights, the coarsening of the microstructure is observed as in the 316L (see Article #3).

On the other hand, the average hardness of the 316L+10%SiC and 316L+20%SiC alloys is respectively 261 HV and 353 HV, i.e. higher than for the WC composites. The presence of the Cr-carbides in the 316L+10%SiC deposit (Fig. 3-13e) and the quasi-continuous carbide network in the 316L+20%SiC deposit (Fig. 3-13g) lead to these hardness increase (see Article #5).

### 3.4. Characterization of complex microstructures

The solidification of metals has always been widely investigated due to the large interest in the industry. The interpretation of the solidification route is often considered with thermodynamic tools (i.e. CALPHAD, Thermocalc etc), assuming equilibrium conditions and considering databases mainly established for binary or ternary systems (Boettinger, 2007; Mancini, 2017; Paar, 2016; Petrovič, 2011; Roca, 2018). Transposition to multicomponent complex alloys produced at high cooling rates involves making approximations to pseudo-binary phase diagrams, which will often lead to discrepancies between the prediction and the actual microstructure (Boccalini Jr, 2001; Drozdová, 2018; Tchuindjang & Lecomte-Beckers, 2011; Wiczerzak, 2016).

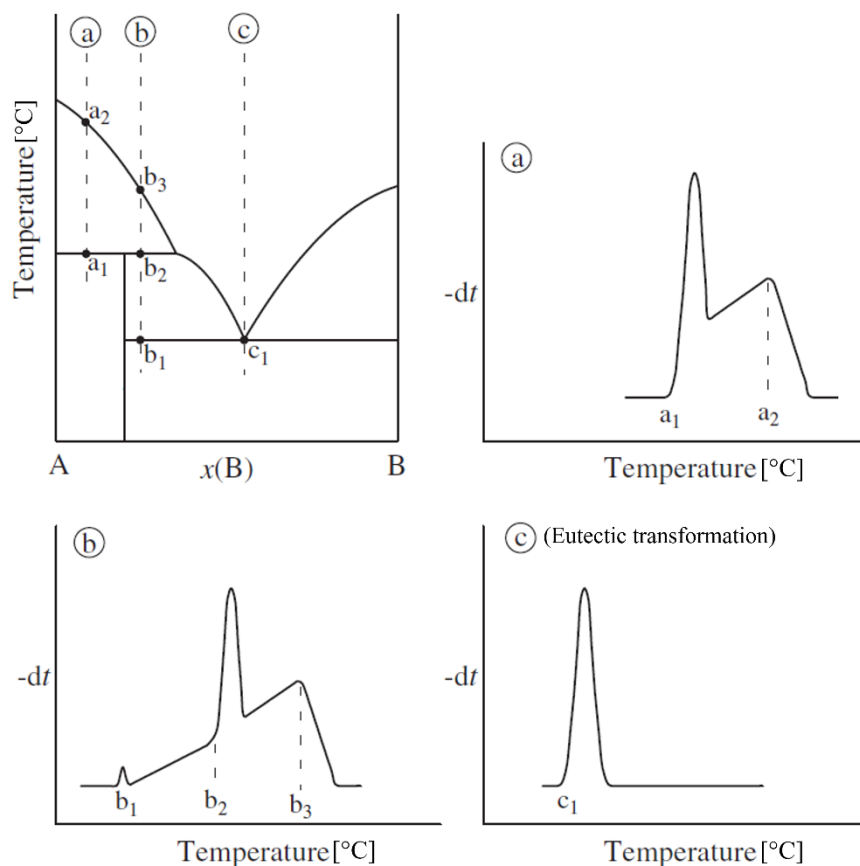


Fig. 3-10: A-B phase diagram with three examples of DTA heating curves depending on the initial composition  $x(B)$  (adapted from (Boettinger, 2007)).

As far as experimental tests are concerned, DTA is an efficient technique to investigate endothermic or exothermic reactions that are related to phase transformations (Fig. 3-10), while simultaneously identifying the critical transition point. DTA is thus useful to build phase diagrams (Fig. 3-10), in equilibrium conditions or close to equilibrium. However, because the cooling rate strongly influences both undercooling and solute partitioning, DTA cooling (cooling rates between 0.1 and 0.8°C/s) hardly corresponds to the actual solidification sequence which occurs during industrial processes (Boettinger, 2007).

Nevertheless, as shown in Fig. 3-10, the peaks of the DTA heating curves could be associated with the composition of the phases present in the considered sample (*Boettinger, 2007; Tchuindjang & Lecomte-Beckers, 2011*). Sharp peaks correspond to narrow compositions ( $a_1$ ,  $b_2$  and  $c_1$  in Fig. 3-10) while continuous changes of the composition correspond to a wide peak ( $a_2$  and  $b_3$  in Fig. 3-10). If elements diffusion does not modify the composition of the phases in the specimen during the progress of the test, the features and the position of each peak is kept at every scan rate (rate referred to thermal analyses). With the increase of the scan rate, the distance among the peak decreases and thus the overlapping increases.

In this PhD research, a methodology was developed to determine the solidification sequence of complex alloys fabricated under high cooling rates, considering the possibilities of the DTA heating curves. This method is called reverse analysis since it allows to elucidate the solidification of a microstructure observed at room temperature through the consideration of the melting curve. Each peak is associated with a phase of the microstructure depending on the microstructural characteristics (i.e. composition, crystallography and lattice status). These features were evaluated with the cross consideration of EBSD and EDS analyses as in (*Godec, 2010; Laigo, 2008*).

As mentioned in section 1.4, this methodology was first developed on an alloy manufactured by centrifugal casting, a conventional manufacturing process, where the cooling rate (Fig. 3-11) lead to out-of-equilibrium and metastable phases (*Hashimoto, 2004; Tchuindjang, Sinnaeve, 2011*). The chosen complex alloy is a graphitic HSS (HSSGr), where large amounts of carbide forming elements and of silicon lead to the simultaneous formation of graphite and of several carbides (see Article #1).

The same methodology was then applied to AM microstructures formed under even higher cooling rates (Fig. 3-11), where, as mentioned in section 2.2.2, elements segregations and diffusion are limited, leading to refined microstructure and to completely different solidification routes (see Article #2).

**Claim and contributions:**

A novel methodology, so-called “reverse analysis”, has been developed and applied efficiently on out-of-equilibrium microstructures, elucidating the solidification sequence. The backwards evaluation of the DTA heating curve is combined for the phase identification with the cross-consideration of the phase composition (SEM/EDS analyses) and lattice order (EBSD analyses).

The two cases will be presented hereafter, showing the microstructure manufactured either with the process of interest or after DTA analysis to highlight the effect of different cooling rates.

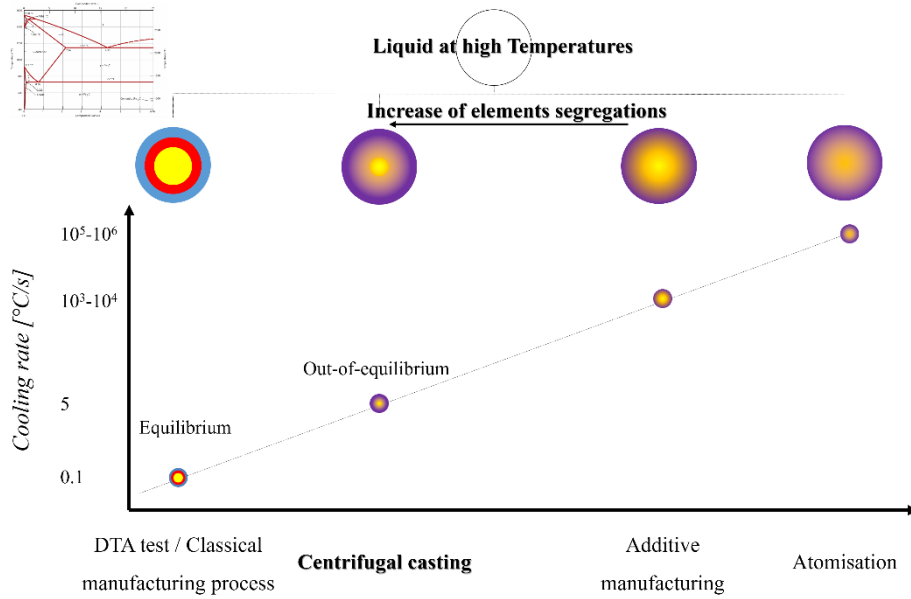
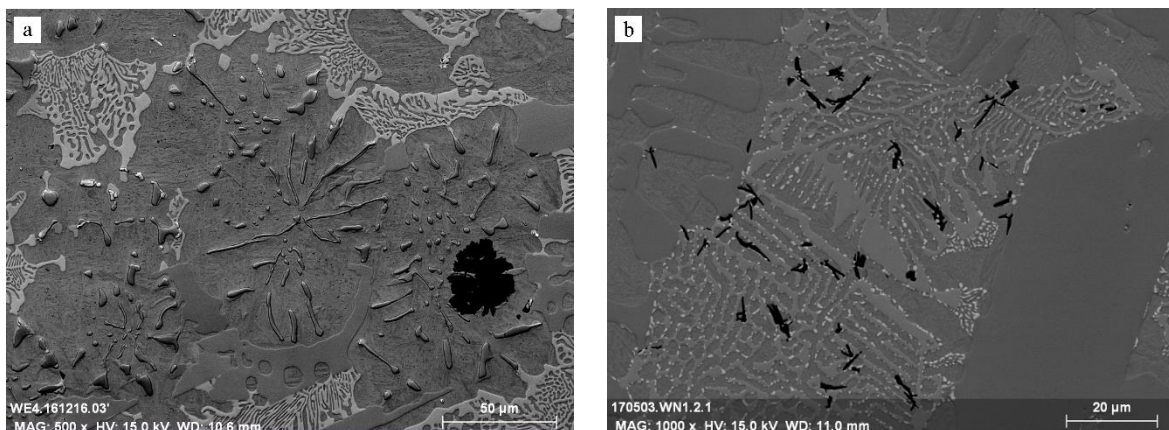


Fig. 3-11: Representation of the variation of the segregations and cooling rates occurring in the different manufacturing process.

### 3.4.1. Metastable carbides in centrifugal casting

As mentioned in section 2.2.1 and shown in (Boccalini Jr, 2001; Tchuindjang, Sinnaeve, 2011), relatively high cooling rates (Fig. 3-11) on systems containing large amounts of many carbide-forming elements lead to the formation of complex microstructures. This complexity derives from the presence of many phases, which exhibit “mixed” compositions in comparison to the conventional ones (Boccalini Jr, 2001). Indeed, as is classical in metallurgy and crystallography, phases and in particular, carbides are described as pure phases composed of carbon with one or two main carbide-forming elements. Furthermore, these carbides are formed under equilibrium conditions, allowing the atoms to diffuse in their most thermodynamically stable positions. Therefore, the crystallographic databases refer to these equilibrium lattice structures, far away from the manufacturing conditions of the centrifugal casting (Rivera, 2008; Wiczerzak, 2016).



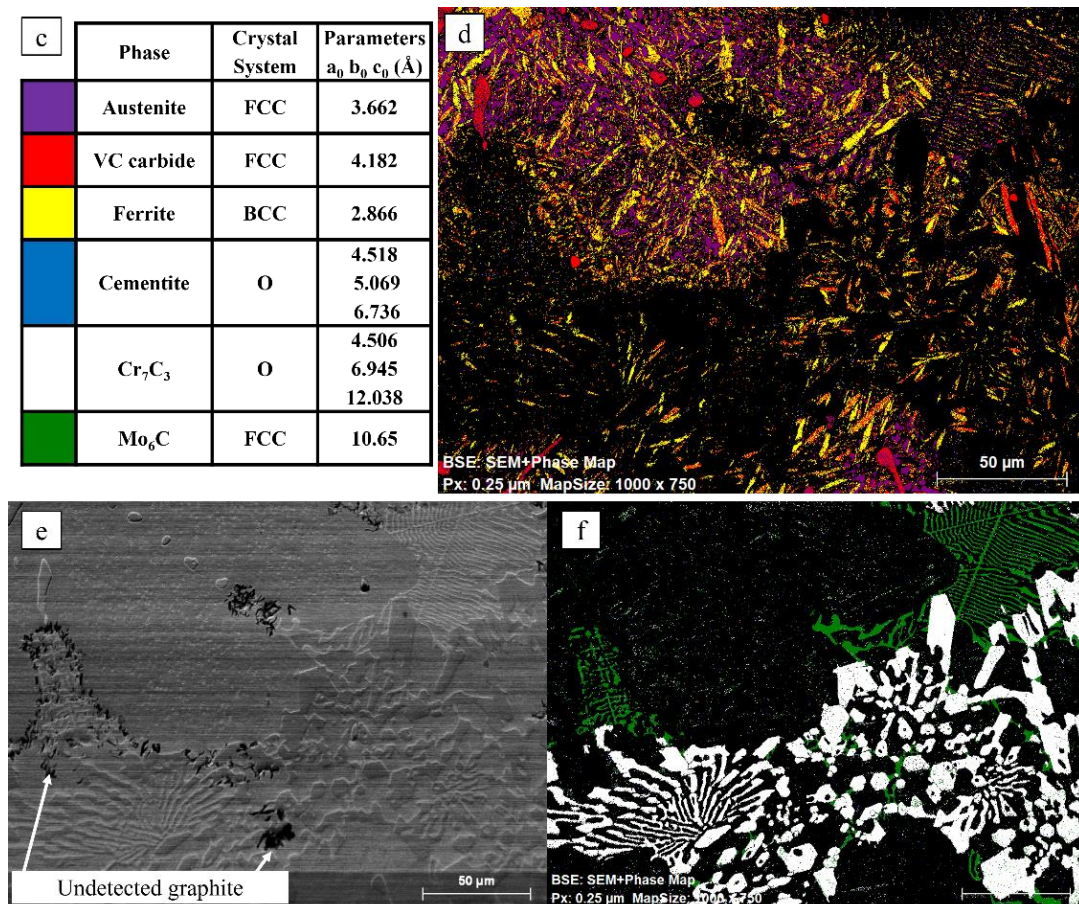
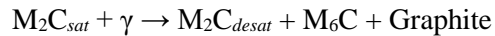


Fig. 3-12: Microstructure of the HSSGr (a) fabricated via centrifugal casting, (b) after thermal treatment up to 1025°C (Maurizi Enrici, 2017) and (e) after being cooled at 0.1°C/s from the liquid via DTA test. (d and f) Results of the EBSD analysis on Fig. 3-12e and (c) the phases considered in the analysis.

Indeed, as shown in Fig. 3-12a and e, the microstructures cooled at respectively 5°C/s (Fig. 3-12a) and 0.1°C/s (Fig. 3-12e) exhibit a large difference of size. Furthermore, Fig. 3-12f highlights the morphologies of the ECs ( $M_7C_3$  and  $M_6C$  carbide) which are the carbides conventionally described in the literature (Bedolla-Jacuinde, 2013; Okane, 2001) and their crystal order is identified as such via EBSD analyses (Ding, 1993; Ma, 2015). In contrast, the ECs in the out-of-equilibrium microstructure ( $M_2C$  and  $M_3C$  carbide in Fig. 3-12a) exhibits previously reported morphologies (Boccalini Jr, 2001; Lecomte-Beckers, 2009), but with unique compositions. Furthermore, these out-of-equilibrium ECs cannot be identified via EBSD analyses (see Article #1). These carbides only can be identified by considering “exotic” phases with the same crystal structure due to a distortion of the lattice. This modification of the lattice parameter is due to high cooling rates achieved during solidification, where more elements are retained within the carbide lattice compared to the equilibrium conditions.

Furthermore, as previously shown by (Hashimoto, 2004; Tchuindjang, Sinnaeve, 2011), a metastable supersaturated  $M_2C$  carbide was observed. The distortion of this  $M_2C$  carbide is strong enough to prevent matching with any existing structure. It was only identified as a base-centred monoclinic crystal

after a destabilisation treatment (1025°C/60'/calm air), due to the decomposition reaction which occurred during the treatment:



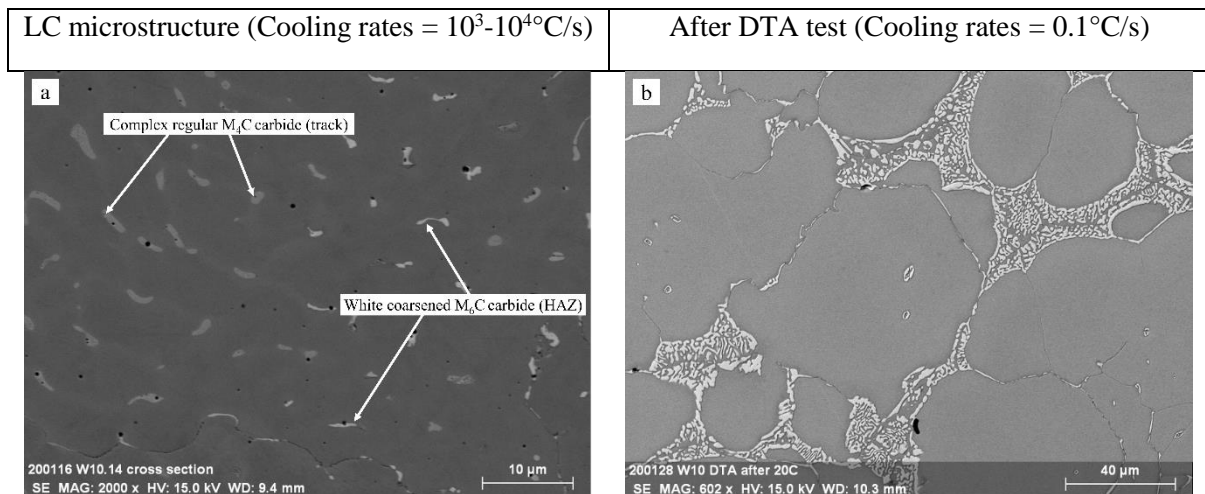
In particular, the anomalously high quantity of Si and the high Mo amount could disturb the arrangement of the crystal structure from the classical  $M_2C$  carbide lattices to an unknown one (see Article #1). When the distortion is strong enough to prevent the identification with any existing lattice, the phase is supersaturated and thus metastable. In the considered case, a specific thermal treatment allows to destabilize the carbide and then identify its crystal order. Interestingly, the decomposition of this carbide leads to the formation of fine SCs and small graphite flakes (so-called “secondary graphite”) due to the presence of Si, unlike previous studies where only carbides were observed (*Hashimoto, 2004; Tchuindjang, Sinnaeve, 2011*).

**Claim and contributions:**

High cooling rates lead to the formation of distorted lattice due to the presence of more elements within the conventional lattice compared to equilibrium conditions. Based on the composition, these phases could be identified considering phases with similar lattice order.

*3.4.2. Out-of-equilibrium microstructures in AM*

As shown in Fig. 3-11, in AM, due to the increasing cooling rates, the phenomena described in section 3.4.1 are amplified, especially in presence of many alloying elements in Fe-based alloy. Fig. 3-13 shows the major differences between the same alloys in out-of-equilibrium conditions after LC and in close-to-equilibrium conditions after DTA test.



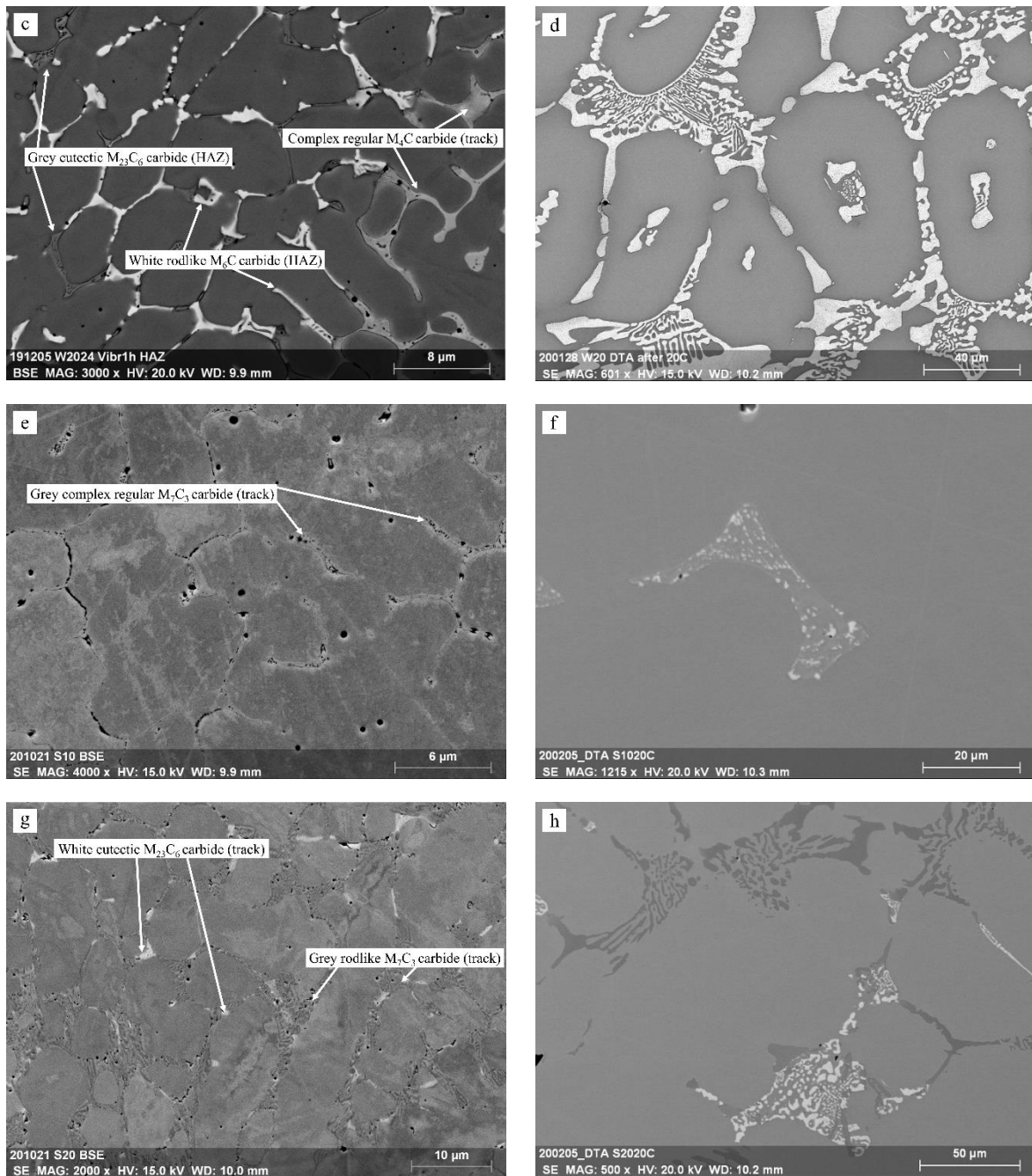
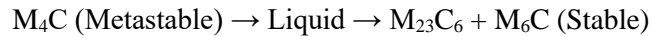


Fig. 3-13: SEM micrographs (BSE mode) of the 316L+10%WC (a and b), 316L+20%WC (c and d), 316L+10%SiC (e and f) and 316L+20%SiC (g and h). (a, c, e and g) Zoom of the microstructure in Fig. 3-4. The WC composites are shown at the HAZ and away from the partially dissolved WC carbides. (b, d, f and h). Microstructure of the composite after complete remelting and cooled to room temperature.

As shown in Fig. 2-7, the conditions during LC lead to microstructural refinement and to a change of solidification mode to cellular microstructures (Bartolomeu, 2017; Hashemi, 2017). Moreover, the influence of undercooling and solute partitioning leads to the occurrence of the peritectic reaction under low cooling rates in the WC composites (Inoue, 2017; Rahimi, 2018) and to change of elemental distribution in the Si alloys, thus changing morphology and nature of carbides. In particular, for the 316L+20%WC composite, this difference is enhanced due to the formation of a metastable  $M_4C$  carbide

during deposition, which dissociates in a  $M_{23}C_6$  and a  $M_6C$  carbide in the heat affected zone (HAZ). The dissociation reaction can be written as follows:



This dissociation is due to the local reheating after the deposition of the subsequent track, giving way to temperatures between the solidus and liquidus temperature.

The methodology described in section 3.4 also allows to detect differences among phases (Fig. 3-13c and Fig. 3-3) in the complex microstructure of the 316L+20%WC (see Article #2). In particular, the main challenge in this composite is the differentiation of the solidification carbides (Cai, 2018; Yangzhen Liu, 2014). The  $M_4C$  carbide and the austenitic matrix adopt a face-centered cubic (FCC) symmetry with similar space groups and exhibit only small differences in lattice parameters, leading to uncertainties in microstructural analysis (Cai, 2018; Ho, 2018; Tong, 2012). Finally, it is the cross-consideration of the local chemical composition (obtained by EDS analysis), of the lattice parameters (determined by EBSD analysis) and of the phase stability that allows to identify the different phases belonging to the Fe-C-W system or the W-C system present in the microstructure of the 316L+20%WC composite (Gustafson, 1987; Kurlov, 2013), despite the similarities of their (FCC) crystal structures.

**Claim and contributions:**

In the HAZ, metastable phases with mixed compositions formed at high cooling rates dissociate in more stable phases due to local reheating up to the solidus temperature.

On the other hand, in the 316L+10%WC composites, solidification carbides exhibit partially distorted lattice due to high cooling rates, but the dissociation phenomenon is not observed in the HAZ. During the local reheating due to the deposition of a further layer,  $M_4C$  carbides coarsen and its crystal structure adapts towards an equilibrium status (Nordera, 2020; Saggionetto, 2019). Indeed, only  $M_6C$  carbide is observed in the HAZ, which is brighter since it enriches in W during this phenomenon (Fig. 3-13a).

The dissociation of  $M_4C$  carbides occurs only in the 316L+20%WC due to the composition resulting from the dissolution of the reinforcements in the melt pool. The presence of a high amount of C together with high amounts of the two carbide-forming elements i.e. Cr and W leads to a metastable mixed carbide, which dissociates in a Cr-rich and a W-rich carbide if diffusion is allowed. In contrast, in 316L+10%WC composites, the W and C amounts are still low, while in the SiC composites, Si is not a carbide-forming element. Indeed, in the two Si alloys, most of the carbides are  $Cr_7C_3$  carbides that are stabilized at extremely high cooling rates due to the high Cr amount. Finally, in the 316L+20%SiC alloy, Mo-rich  $M_{23}C_6$  carbides may also form from the remaining liquid due to the high C amount (see Article #5).

### 3.5. Characterization of the properties

#### 3.5.1. Strengthening of the matrix

As shown by nanoindentation measurements on the matrix (Fig. 3-14), both Si alloys exhibit a remarkable increase of the nanohardness of the austenitic cells with the increase of the Si content (see Article #5), compared to the 316L+20%WC composite (Fig. 3-6c and Fig. 3-8).

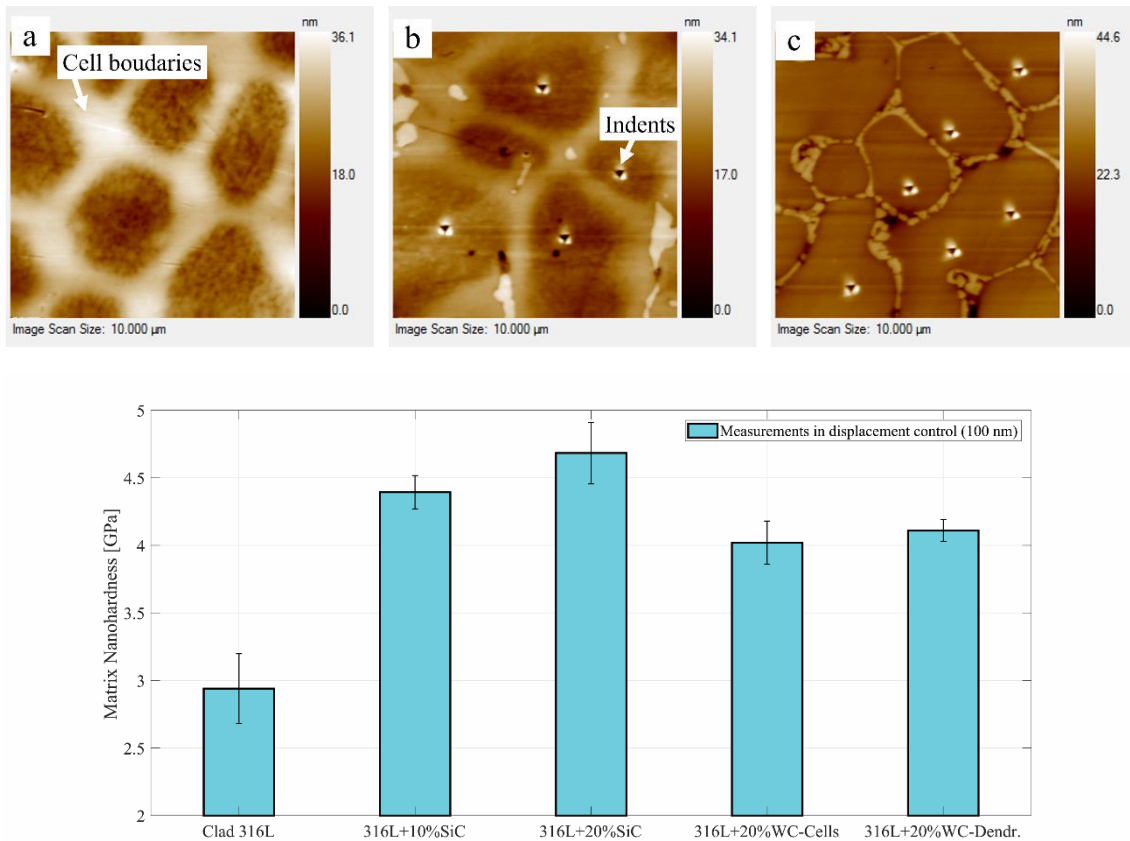


Fig. 3-14: Nanoscans of (a) 316L, (b) 316L+10% SiC and (c) 316L+20% SiC microstructure, etched with aqua regia. (d) Results of the nanohardness measurements on the austenitic cells of clad 316L, the SiC alloys and both morphologies of the 316L+20%WC composite.

Indeed, the nanohardness increase in the 316L+10%SiC alloy is due to a remarkable increase of the lattice distortion and of the consequent solid solution strengthening effect of Si (Raabe, 2015). Si atom leads to higher lattice strains of the FCC crystal lattice than other solute atoms like Cr, Ni and Mn (Morinaga, 2019). Furthermore, as discussed in section 3.4, the fast cooling rates of LC reduce the segregation, often leading to out-of-equilibrium and supersaturated microstructures. In these microstructures, the amount of a given atom in the system is not limited by its solubility at equilibrium conditions. Supersaturation enhances the solid solution strengthening effect in comparison to the predictions under equilibrium conditions (Garibaldi, 2016; Yang, 2017). The nanohardness increase of the austenite of the 316L+10%SiC alloy is then directly correlated to the macrohardness increase (Fig. 3-9b) since the amount of carbides is very small (Fig. 3-13e and Fig. 3-14b).

With the increase of the Si content and the decrease of the Cr content (see Article #5), the distortion of the lattice further increases in the 316L+20% SiC and leads to nanohardness values up to 5 GPa (Fig. 3-14d). Therefore, the macrohardness improvement can be attributed to both the higher carbide presence at the cell boundaries (Fig. 3-14b and c) and the higher amount of Si in the austenite (see Article #5) (Zuback, 2018).

V, Ti, W and Mo atoms lead to a high expansion of the FCC crystal order and thus can lead to a theoretical improvement of the mechanical properties via solid solution strengthening (Morinaga, 2019), but their strengthening effect is lower than for Si (Fig. 3-14d). Furthermore, the tendency of these strong carbide-forming elements to form carbides and their solubility in the FCC lattice (Ertugrul, 2020) limit their addition to AM compositions in order to avoid possible fragile phases and thus decrease the printability of the alloys (Tang, 2020). Therefore, Si addition is revealed to be promising to improve the mechanical properties of AM stainless steels (Fig. 3-14).

### 3.5.2. *Wear behaviour and performances*

The modification of the 316L wear properties was considered via pin-on-disc tests. The focus of the test campaign was on the WC composites since the reinforcements are completely dissolved in the SiC alloys. The aim was to determine the influence of the reinforcements on wear behaviour and performances. For this purpose, the novel approach of the interrupted tests was applied (see Article #4), where wear tests are performed under the same conditions and strategically stopped at times corresponding to specific variations of friction coefficient (CoF) and penetration depth (PDe). Alumina (Mario, 2019; Nordera, 2020) and WC-Co ball (Serrano Martín, 2020) were chosen as counterbody. In order to associate the variations of both CoF and PDe to the different successive wear mechanisms, post-mortem observations of the specimens and counterbody were performed for each of these interrupted tests. Furthermore, long pin-on-disc tests (22000 laps – 1105 m of total sliding distance) were performed on the clad 316L reference and the 316L+20%SiC alloy for comparison purposes. The addition of SiC particles by LC can also significantly improve the wear resistance of the 316L against both WC-Co and alumina counterbodies (Fig. 3-15a) due to the strengthened matrix (Fig. 3-14d).

For the 316L+WC composites, the influence of the partially dissolved WC on the wear behaviour is investigated. Under dry sliding conditions, the addition of WC particles by LC significantly improves the wear resistance of the 316L against both counterbodies (Fig. 3-15a) due to the partially dissolved original reinforcement particles and to the reinforced matrix. As a consequence, there is a significant decrease in the wear rate within the composites compared to the 316L (Fig. 3-15a). It is assumed that WC carbides protect the matrix (Fig. 3-15b and d) and at the same time contribute to the formation of an oxide layer (Fig. 3-15c) which protects both the clad material and the counterbody. Indeed, both counterbodies are worn, due to the presence of partially dissolved reinforcements (Fig. 3-15b and d), as illustrated in Fig. 3-15a for the case of the alumina ball. It is assumed that adhesive wear is the main

wear mechanism in both counterbodies. In comparison, the wear cap observed on the WC-Co balls after wear test is negligible. Furthermore, after an initial plastic flow of the matrix, fragments of the solidification carbides enrich a mechanically mixed layer (MML) and increase its strength (Fig. 3-15e), helping to improve the wear resistance in comparison with the MML in the 316L references.

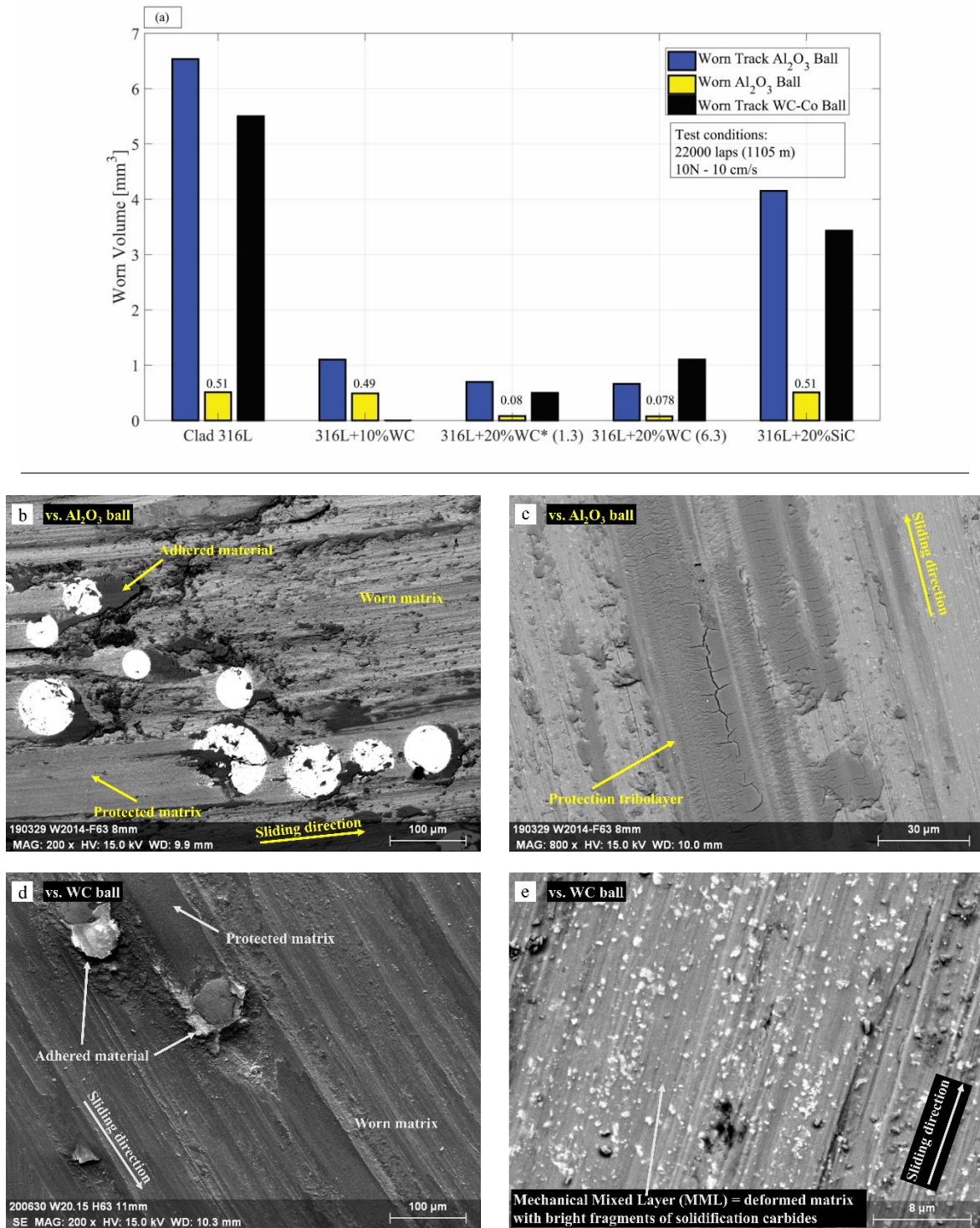


Fig. 3-15: (a) Measured worn volumes of wear track against two counterbody and alumina cap after the same test conditions (22000 laps – 10N – 10 cm/s) on a surface at 6.3 mm from the substrate. \*The same measurements of the same test on the 316L+20% at 1.3 mm from the substrate.

The study of these materials highlights the complexity of the wear behaviour of composite microstructures, the difficulty to generalize and to assess the wear performances. Indeed, depending on the counterbody and the tested microstructure, the performances and the wear behaviour vary.

As a matter of fact, alumina has been often used as countermaterial against stainless steel due to its high hardness and theoretically inert nature (Bartolomeu, 2017; Dearnley, 2004; C. X. Li, 2006; O'Donnell, 2010; Vardavoulis, 1994). In addition, using alumina as counterbody allows to easily determine the nature of the debris during post-mortem observations since Al is not usually present in the composition of the tested materials. At the same time, it has been well established that during sliding conditions, alumina reacts with the oxides present on the surface of steels, depending on the temperatures at the ball-specimen interface (also called flash temperature) and the local pressures during wear test (O'Donnell, 2010; Ravikiran, 1995). The combination of this chemical reaction and the mechanical constraints during test lead to the wear of the counterbody. Similarly, under the same test conditions, the reactions between the alumina ball and the chromia ( $\text{Cr}_2\text{O}_3$ ) present on the surface of stainless steels can occur. Indeed, previous studies have reported the formation of a stable  $(\text{Al-Cr})_2\text{O}_3$  solid solution under similar conditions (i.e. temperatures and pressures), exhibiting superior wear resistance compared to the parent alumina (Chráska, 1997; Gangopadhyay, 1990). Therefore, debris formed from these reactions contributes to the wear of the ball. On the one hand, the wear of the counterbody generates debris and enrich the protective tribolayer. On the other hand, it perturbs the evaluation of the wear performances since the contact area increases and leads to the occurrence of oxidative wear (i.e. mild wear) (Costa, 2017). The tendency of alumina to form debris and indirectly contribute to the formation of a protective tribolayer may hide the effect of microstructural differences. Indeed, as mentioned in section 3.3.2, heat accumulation influences the formation of the final microstructure and its properties. As shown in Fig. 3-15a, wear tests carried out at 1.3 mm from the substrate against alumina exhibit almost no differences compared to the same tests carried out at 6.3 mm from the substrate.

**Claim and contributions:**

The interrupted tests approach is found efficient for the interpretation of complex wear behaviour considering the evolution of the wear features and the wear volumes during the pin-on-disc test. Variations of the CoF and PDe correspond to changes in the test conditions, which are related to the wear of both the specimen and the ball and to the nature of the formed debris.

In contrast, the use of WC-Co as counterbody allows to obtain a better estimation of the wear resistance since the wear of the ball is negligible. Interestingly, pin-on-disc tests carried out against WC-Co on the 316L+20%WC composite exhibits remarkable differences in the worn volume (Fig. 3-15a) depending on the depth within the deposit (1.3 and 6.3 mm). In particular, tests on the 316L+20%WC

composite at 1.3 mm depth within the deposit and all the tests carried out on the clad 316L against WC-Co ball exhibit a lower worn volume (Fig. 3-15a) compared to the wear tests against alumina ball. As a matter of fact, this is due to the formation of a protective tribolayer (*Serrano Martín, 2020*). As mentioned in section 3.3.2, the matrix of the 316L+20%WC composite is less modified by the interactions with the reinforcements in the first deposited layers and thus the matrix is more similar to the parent 316L. With the increase of the deposit height, the microstructure of the 316L+20%WC composite is more homogeneous and the amount of solidification carbides increases compared to the microstructure at the first layers. As reported in (*Guo, 2012; Weng, 2016*), such reinforced microstructures lead to an increase in the toughness compared to the original alloys and abrasive wear takes more relevance at the expense of the adhesive wear. Indeed, at this height the features of the debris do not lead to a stable tribolayer (*Song, 2016; Weng, 2016*), thus leading to a higher worn volume (Fig. 3-15a). Therefore, without the influence of the interactions with the ball and thus the formation of a large quantity of debris from the counterbody, microstructural differences are highlighted with the application of the WC-Co as counterbody. Nevertheless, when materials containing WC reinforcements are considered, the use of WC-Co ball as counterbody leads to more difficulties in the interpretation of the wear mechanisms during the post-mortem investigations.

**Claim and contributions:**

Oxidative wear is often observed during pin-on-disc tests against  $\text{Al}_2\text{O}_3$  ball with the formation of a protective oxide layer due to the wear of the ball and to the nature of the formed debris. This tendency hides the effect of microstructural variations in the specimen, but this comes with an easy comprehension of the wear mechanisms.

On the other hand, pin-on-disc tests against WC-Co ball are more efficient in revealing the effective performances of the tested materials and highlighting the effect of microstructural differences, but the interpretation of the wear mechanisms is more complex.



### References section 3

- AlMangour, B., Grzesiak, D., Cheng, J., & Ertas, Y. (2018). "Thermal behavior of the molten pool, microstructural evolution, and tribological performance during selective laser melting of TiC/316L stainless steel nanocomposites: Experimental and simulation methods." *Journal of Materials Processing Technology*, 257(November 2017), 288–301. <https://doi.org/10.1016/j.jmatprotec.2018.01.028>
- Amin-Ahmadi, B., & Aashuri, H. (2010). "Semisolid structure for M2 high speed steel prepared by cooling slope." *Journal of Materials Processing Technology*, 210(12), 1632–1635. <https://doi.org/10.1016/j.jmatprotec.2010.05.011>
- Bartolomeu, F., Buciumeanu, M., Pinto, E., Alves, N., Carvalho, O., Silva, F. S., & Miranda, G. (2017). "316L stainless steel mechanical and tribological behavior—A comparison between selective laser melting, hot pressing and conventional casting." *Additive Manufacturing*, 16, 81–89. <https://doi.org/10.1016/j.addma.2017.05.007>
- Bedolla-Jacuinde, A., Rainforth, M. W., & Mejía, I. (2013). "The role of silicon in the solidification of high-Cr cast irons." *Metallurgical and Materials Transactions A: Physical Metallurgy and Materials Science*, 44(2), 856–872. <https://doi.org/10.1007/s11661-012-1434-8>
- Boccalini Jr, M., & Goldenstein, H. (2001). "Solidification of high speed steels." *International Materials Reviews*, 46(2), 92–115. <https://doi.org/10.1179/095066001101528411>
- Boettinger, W. J., Kattner, U. R., Moon, K.-W., & Perepezko, J. H. (2007). "Dta and Heat-Flux Dsc Measurements of Alloy Melting and Freezing." In J.-C. Zhao (Ed.), *Methods for Phase Diagram Determination* (NIST, pp. 151–221). Washington: Elsevier Science Ltd. <https://doi.org/10.1016/b978-008044629-5/50005-7>
- Brytan, Z., Dobrzański, L. a, & Pakieła, W. (2011). "Laser surface alloying of sintered stainless steels with SiC powder." *Journal of Achievements in Materials and Manufacturing Engineering*, 47(1), 42–56.
- Cai, X., Xu, Y., Liu, M., & Zhong, L. (2018). "Evaluation of microstructure and growth kinetics of tungsten carbide ceramics at the interface of iron and tungsten." *Journal of Alloys and Compounds*, 741, 666–676. <https://doi.org/10.1016/j.jallcom.2018.01.212>
- Chráska, P., Dubsky, J., Neufuss, K., & Pisacka, J. (1997). "Alumina-base plasma-sprayed materials part I: Phase stability of alumina and alumina-chromia." *Journal of Thermal Spray Technology*, 6(3), 320–326. <https://doi.org/10.1007/s11666-997-0066-9>
- Corongiu, C., Mertens (Official supervisor), A., & Maurizi Enrici (Co-supervisor), T. (2020). *Development and characterization of a gradient structured material elaborated by direct deposition additive manufacturing*. Master Thesis - ULiège.
- Costa, H. L., Oliveira Junior, M. M., & de Mello, J. D. B. (2017). "Effect of debris size on the reciprocating sliding wear of aluminium." *Wear*, 376–377, 1399–1410. <https://doi.org/10.1016/j.wear.2016.10.025>
- Dass, A., & Moridi, A. (2019). "State of the art in directed energy deposition: From additive manufacturing to materials design." *Coatings*. <https://doi.org/10.3390/COATINGS9070418>
- Dearnley, P. A., & Aldrich-Smith, G. (2004). "Corrosion-wear mechanisms of hard coated austenitic 316L stainless steels." *Wear*, 256(5), 491–499. [https://doi.org/10.1016/S0043-1648\(03\)00559-3](https://doi.org/10.1016/S0043-1648(03)00559-3)
- Deschuyteneer, D., Petit, F., Gonon, M., & Cambier, F. (2015). "Processing and characterization of laser clad NiCrBSi/WC composite coatings - Influence of microstructure on hardness and wear." *Surface and Coatings Technology*, 283, 162–171. <https://doi.org/10.1016/j.surfcoat.2015.10.055>

- Deschuyteneer, D., Petit, F., Gonon, M., & Cambier, F. (2017). "Influence of large particle size – up to 1.2 mm – and morphology on wear resistance in NiCrBSi/WC laser cladded composite coatings." *Surface and Coatings Technology*, 311, 365–373. <https://doi.org/10.1016/j.surfcoat.2016.12.110>
- Ding, P., Shi, G., & Zhou, S. (1993). "As-cast carbides in high-speed steels." *Metallurgical Transactions A*, 24(6), 1265–1272. <https://doi.org/10.1007/BF02668195>
- Drozdová, L., Smetana, B., Zlá, S., Novák, V., Kawuloková, M., Rosypalová, S., ... Dostál, P. (2018). "Study of phase transformation temperatures of alloys based on Fe–C–Cr in high-temperature area." *Journal of Thermal Analysis and Calorimetry*, 133(1), 41–48. <https://doi.org/10.1007/s10973-018-7012-6>
- Easton, M. A., Qian, M., Prasad, A., & StJohn, D. H. (2016). "Recent advances in grain refinement of light metals and alloys." *Current Opinion in Solid State and Materials Science*, 20(1), 13–24. <https://doi.org/10.1016/j.cossms.2015.10.001>
- Ertugrul, O., Maurizi Enrici, T., Paydas, H., Saggionetto, E., Boschini, F., & Mertens, A. (2020). "Laser cladding of TiC reinforced 316L stainless steel composites: Feedstock powder preparation and microstructural evaluation." *Powder Technology*, 375, 384–396. <https://doi.org/10.1016/j.powtec.2020.07.100>
- Feenstra, D. R., Cruz, V., Gao, X., Molotnikov, A., & Birbilis, N. (2020). "Effect of build height on the properties of large format stainless steel 316L fabricated via directed energy deposition." *Additive Manufacturing*, 34(April), 101205. <https://doi.org/10.1016/j.addma.2020.101205>
- Fetni, S., Maurizi Enrici, T., Niccolini, T., Tran, H., Dedry, O., Duchêne, L., ... Habraken, A. M. (2021). "Thermal model for the directed energy deposition of composite coatings in 316 L stainless steel enriched with tungsten carbides." *Materials & Design*, 109661. <https://doi.org/10.1016/j.matdes.2021.109661>
- Gangopadhyay, A. K., Janon, F. B., Fine, M. E., & Cheng, H. S. (1990). "Enhanced wear resistance of  $\alpha$ -alumina by surface modification with chromia and titania." *Tribology Transactions*, 33(1), 96–104. <https://doi.org/10.1080/10402009008981935>
- Garibaldi, M., Ashcroft, I., Simonelli, M., & Hague, R. (2016). "Metallurgy of high-silicon steel parts produced using Selective Laser Melting." *Acta Materialia*, 110, 207–216. <https://doi.org/10.1016/j.actamat.2016.03.037>
- Gingell, R. (2019). "Alloys by Design: The future of materials for Additive Manufacturing." *Metal Additive Manufacturing*, 5(4), 119–127.
- Godec, M., Batič, B. Š., Mandrino, D., Nagode, A., Leskovšek, V., Škapin, S. D., & Jenko, M. (2010). "Characterization of the carbides and the martensite phase in powder-metallurgy high-speed steel." *Materials Characterization*, 61(4), 452–458. <https://doi.org/10.1016/j.matchar.2010.02.003>
- Guo, C., Chen, J., Zhou, J., Zhao, J., Wang, L., Yu, Y., & Zhou, H. (2012). "Effects of WC-Ni content on microstructure and wear resistance of laser cladding Ni-based alloys coating." *Surface and Coatings Technology*, 206(8–9), 2064–2071. <https://doi.org/10.1016/j.surfcoat.2011.06.005>
- Gustafson, P. (1987). "A Thermodynamic Evaluation of the C-Fe-W System." *Metallurgical and Materials Transactions A*, 18(February), 175–188.
- Hashemi, N., Mertens, A., Montrieux, H. M., Tchuindjang, J. T., Dedry, O., Carrus, R., & Lecomte-Beckers, J. (2017). "Oxidative wear behaviour of laser clad High Speed Steel thick deposits: Influence of sliding speed, carbide type and morphology." *Surface and Coatings Technology*, 315, 519–529. <https://doi.org/10.1016/j.surfcoat.2017.02.071>
- Hashimoto, M., Kubo, O., & Matsubara, Y. (2004). "Analysis of carbides in multi-component white

- cast iron for hot rolling mill rolls.” *ISIJ International*, 44(2), 372–380. <https://doi.org/10.2355/isijinternational.44.372>
- Herzog, D., Seyda, V., Wycisk, E., & Emmelmann, C. (2016). “Additive manufacturing of metals.” *Acta Materialia*, 117, 371–392. <https://doi.org/10.1016/j.actamat.2016.07.019>
- Ho, I. T., Chen, Y. T., Yeh, A. C., Chen, C. P., & Jen, K. K. (2018). “Microstructure evolution induced by inoculants during the selective laser melting of IN718.” *Additive Manufacturing*, 21(February), 465–471. <https://doi.org/10.1016/j.addma.2018.02.018>
- Inoue, H., & Koseki, T. (2017). “Solidification mechanism of austenitic stainless steels solidified with primary ferrite.” *Acta Materialia*, 124, 430–436. <https://doi.org/10.1016/j.actamat.2016.11.030>
- Jung, B. B., Lee, H. K., & Park, H. C. (2013). “Effect of grain size on the indentation hardness for polycrystalline materials by the modified strain gradient theory.” *International Journal of Solids and Structures*, 50(18), 2719–2724. <https://doi.org/10.1016/j.ijsolstr.2013.05.002>
- Kurlov, A. S., & Gusev, A. I. (2013). *Tungsten Carbides: Structure, Properties and Application in Hardmetals*. Springer Series in Materials Science (Vol. 184). Springer Cham. <https://doi.org/10.1007/978-3-319-00524-9>
- Laigo, J., Christien, F., Le Gall, R., Tancret, F., & Furtado, J. (2008). “SEM, EDS, EPMA-WDS and EBSD characterization of carbides in HP type heat resistant alloys.” *Materials Characterization*, 59(11), 1580–1586. <https://doi.org/10.1016/j.matchar.2008.02.001>
- Lang, M. (2020). “From aerospace engineering to AM: Melanie Lang on FormAlloy and the future of Directed Energy Deposition (DED).” *Metal Additive Manufacturing*, 6(3), 145–152.
- Lecomte-Beckers, J., & Tchuindjang, J. T. (2009). “Structural Investigations of Solidification and Heat Treatments Influence on High Alloyed Cast Irons Grades with Nb-V-Ti additions.” *Defect and Diffusion Forum Series*, 289–292, 77–86. <https://doi.org/10.4028/www.scientific.net/DDF.289-292.77>
- Lee, Y., Nordin, M., Babu, S. S., & Farson, D. F. (2014). “Effect of fluid convection on dendrite arm spacing in laser deposition.” *Metallurgical and Materials Transactions B: Process Metallurgy and Materials Processing Science*, 45(4), 1520–1529. <https://doi.org/10.1007/s11663-014-0054-7>
- Levi, C. G. (1988). “Thermal considerations on the recalescence of alloy powders.” *Metallurgical Transactions A*, 19(3), 687–697. <https://doi.org/10.1007/BF02649283>
- Li, C. X., Xia, J., & Dong, H. (2006). “Sliding wear of TiAl intermetallics against steel and ceramics of Al<sub>2</sub>O<sub>3</sub>, Si<sub>3</sub>N<sub>4</sub> and WC/Co.” *Wear*, 261(5–6), 693–701. <https://doi.org/10.1016/j.wear.2006.01.044>
- Li, K., Li, D., Liu, D., Pei, G., & Sun, L. (2015). “Microstructure evolution and mechanical properties of multiple-layer laser cladding coating of 308L stainless steel.” *Applied Surface Science*, 340, 143–150. <https://doi.org/10.1016/j.apsusc.2015.02.171>
- Lian, G., Zhao, C., Zhang, Y., Feng, M., & Jiang, J. (2020). “Investigation into micro-hardness and wear resistance of 316L/SiC composite coating in laser cladding.” *Applied Sciences (Switzerland)*, 10(9). <https://doi.org/10.3390/app10093167>
- Lienert, T., Siewert, T. A., Babu, S. S., & Acoff, V. L. (2011). “Welding Fundamentals and Processes, vol. 6A.” In S.W.P. Specifications, ASM International (Vol. 06A, pp. 89–114). OH: Materials Park.
- Liu, Yang, Zhang, J., & Pang, Z. (2018). “Numerical and experimental investigation into the subsequent thermal cycling during selective laser melting of multi-layer 316L stainless steel.” *Optics and Laser Technology*, 98, 23–32. <https://doi.org/10.1016/j.optlastec.2017.07.034>

- Liu, Yangzhen, Jiang, Y., Zhou, R., & Feng, J. (2014). "First-principles calculations of the mechanical and electronic properties of Fe-W-C ternary compounds." *Computational Materials Science*, 82, 26–32. <https://doi.org/10.1016/j.commatsci.2013.09.040>
- Ma, S., Xing, J., He, Y., Li, Y., Huang, Z., Liu, G., & Geng, Q. (2015). "Microstructure and crystallography of  $M_7C_3$  carbide in chromium cast iron." *Materials Chemistry and Physics*, 161, 65–73. <https://doi.org/10.1016/j.matchemphys.2015.05.008>
- Mahabadi, O. K., Randall, N. X., Zong, Z., & Grasselli, G. (2012). "A novel approach for micro-scale characterization and modeling of geomaterials incorporating actual material heterogeneity." *Geophysical Research Letters*, 39(1). <https://doi.org/10.1029/2011GL050411>
- Mancini, E., Mertens (Official supervisor), A., Calliari (Official supervisor), I., & Maurizi Enrici (Co-supervisor), T. (2017). Microstructural heterogeneities in laser clad stainless steel + tungsten carbides composite coatings. Master Thesis - ULiège.
- Manvatkar, V., De, A., & Debroy, T. (2014). "Heat transfer and material flow during laser assisted multi-layer additive manufacturing." *Journal of Applied Physics*, 116(12). <https://doi.org/10.1063/1.4896751>
- Mario, D., Mertens (Official supervisor), A., Calliari (Official supervisor), I., Maurizi Enrici (Co-supervisor), T., & Dedry (Co-supervisor), O. (2019). Room temperature wear behavior of laser clad 316L + WC composite coating. Master Thesis - ULiège.
- Maurizi Enrici, T., Dedry, O., Sinnaeve, M., Lecomte-beckers, J., & Tchuindjang, J. T. (2017). "New Insights on the in-situ Destabilization of the  $M_2C$  Eutectic Carbides under Thermal Treatment in a Multicomponent Cast Iron Grade." In 6th Conference ABRASION.
- Morinaga, M. (2019). Local Lattice Strains Around Alloying Elements in Metals. A Quantum Approach to Alloy Design. <https://doi.org/10.1016/b978-0-12-814706-1.00011-x>
- Nandiyanto, A. B. D., Ogi, T., Wang, W. N., Gradon, L., & Okuyama, K. (2019). "Template-assisted spray-drying method for the fabrication of porous particles with tunable structures." *Advanced Powder Technology*, 30(12), 2908–2924. <https://doi.org/10.1016/j.appt.2019.08.037>
- Nordera, M., Mertens (Official supervisor), A., Calliari (Official supervisor), I., Maurizi Enrici (Co-supervisor), T., & Dedry (Co-supervisor), O. (2020). Correlation between wear properties and microstructure of the 316L + 10 % WC composite. Master Thesis - ULiège.
- O'Donnell, L. J., Michal, G. M., Ernst, F., Kahn, H., & Heuer, A. H. (2010). "Wear maps for low temperature carburised 316L austenitic stainless steel sliding against alumina." *Surface Engineering*, 26(4), 284–292. <https://doi.org/10.1179/026708410X12550773057901>
- Okane, T., & Umeda, T. (2001). "Interface temperature measurement of  $M_2C$  and  $M_6C$  eutectic carbides in the Fe-Mo-C system." *Science and Technology of Advanced Materials*, 60(1), 605–608. <https://doi.org/10.1016/j.matlet.2005.09.046>
- Paar, A., Elizondo, L., Brandner, M., Trickl, T., Sonderegger, B., Beal, C., & Sommitsch, C. (2016). "Application of Thermo-Calc TCFE7 to High-Alloyed Mottled Cast Iron." *Materials Science Forum*, 879, 1431–1436. <https://doi.org/10.4028/www.scientific.net/MSF.879.1431>
- Petrovič, D. S., Klančnik, G., Pirnat, M., & Medved, J. (2011). "Differential scanning calorimetry study of the solidification sequence of austenitic stainless steel." *Journal of Thermal Analysis and Calorimetry*, 105(1), 251–257. <https://doi.org/10.1007/s10973-011-1375-2>
- Polozov, I., Razumov, N., Masaylo, D., Silin, A., Lebedeva, Y., & Popovich, A. (2020). "Fabrication of silicon carbide fiber-reinforced silicon carbide matrix composites using binder jetting additive manufacturing from irregularly-shaped and spherical powders." *Materials*, 13(7).

<https://doi.org/10.3390/MA13071766>

- Quested, T. E., & Greer, A. L. (2004). "The effect of the size distribution of inoculant particles on as-cast grain size in aluminium alloys." *Acta Materialia*, 52(13), 3859–3868. <https://doi.org/10.1016/j.actamat.2004.04.035>
- Raabe, D., Tasan, C. C., Springer, H., & Bausch, M. (2015). "From high-entropy alloys to high-entropy steels." *Steel Research International*, 86(10), 1127–1138. <https://doi.org/10.1002/srin.201500133>
- Rahimi, R., Biermann, H., Volkova, O., & Mola, J. (2018). "On the origin of subgrain boundaries during conventional solidification of austenitic stainless steels." *IOP Conference Series: Materials Science and Engineering*, 373(1). <https://doi.org/10.1088/1757-899X/373/1/012005>
- Randall, N. X., Vandamme, M., & Ulm, F. J. (2009). "Nanoindentation analysis as a two-dimensional tool for mapping the mechanical properties of complex surfaces." *Journal of Materials Research*, 24(3), 679–690. <https://doi.org/10.1557/jmr.2009.0149>
- Ravikiran, A., Nagarajan, V. S., Biswas, S. K., & Bai, B. N. P. (1995). "Effect of Speed and Pressure on Dry Sliding Interactions of Alumina against Steel." *Journal of the American Ceramic Society*, 78(2), 356–364. <https://doi.org/10.1111/j.1151-2916.1995.tb08808.x>
- Rivera, G., Calvillo, P. R., Boeri, R., Houbaert, Y., & Sikora, J. (2008). "Examination of the solidification macrostructure of spheroidal and flake graphite cast irons using DAAS and EBSD." *Materials Characterization*, 59(9), 1342–1348. <https://doi.org/10.1016/j.matchar.2007.11.009>
- Roca, A. S., Fals, H. D. C., & Zoqui, E. J. (2018). "In situ differential thermal analysis device for evaluating high-speed phase transitions." *Journal of Thermal Analysis and Calorimetry*, 134(3), 1589–1597. <https://doi.org/10.1007/s10973-018-7629-5>
- Saggionetto, E., Mertens (Official supervisor), A., Calliari (Official supervisor), I., & Maurizi Enrici (Co-supervisor), T. (2019). Microstructural characterization of the laser clad 316L+SiC composite coating. Master Thesis - ULiège.
- Serrano Martín, I., Mertens (Official supervisor), A., Maurizi Enrici (Co-supervisor), T., & Dedry (Co-supervisor), O. (2020). Study of wear behavior of SS316L+WC composites: Role of the counter material. Master Thesis - ULiège.
- Sheikhzadeh, M., & Sanjabi, S. (2012). "Structural characterization of stainless steel/TiC nanocomposites produced by high-energy ball-milling method at different milling times." *Materials and Design*, 39, 366–372. <https://doi.org/10.1016/j.matdes.2012.02.011>
- Song, L., Zeng, G., Xiao, H., Xiao, X., & Li, S. (2016). "Repair of 304 stainless steel by laser cladding with 316L stainless steel powders followed by laser surface alloying with WC powders." *Journal of Manufacturing Processes*, 24, 116–124. <https://doi.org/10.1016/j.jmapro.2016.08.004>
- Tang, Y. T., Panwisawas, C., Ghousoub, J. N., Gong, Y., Clark, J., Németh, A., ... Reed, R. C. (2020). "Alloys-By-Design: Application to New Superalloys for Additive Manufacturing." *Acta Materialia*, 202, 417–436. <https://doi.org/10.1016/j.actamat.2020.09.023>
- Tchuindjang, J. T., & Lecomte-Beckers, J. (2011). "Study of the Origin of the Unexpected Pearlite during the Cooling Stage of Two Cast High-Speed Steels." *Solid State Phenomena*, 172–174, 803–808. <https://doi.org/10.4028/www.scientific.net/SSP.172-174.803>
- Tchuindjang, J. T., Sinnaeve, M., & Lecomte-Beckers, J. (2011). "Influence of High Temperature Heat Treatment on in situ Transformation of Mo-rich Eutectic Carbides in HSS and Semi-HSS Grades." In 4th Conference ABRASION (pp. 61–75).
- Tillmann, W., Hagen, L., & Kokalj, D. (2017). "Embedment of eutectic tungsten carbides in arc sprayed

- steel coatings.” *Surface and Coatings Technology*, 331(October), 153–162. <https://doi.org/10.1016/j.surfcoat.2017.10.044>
- Tolochko, N. K., Laoui, T., Khlopkov, Y. V., Mozzharov, S. E., Titov, V. I., & Ignatiev, M. B. (2000). “Absorptance of powder materials suitable for laser sintering.” *Rapid Prototyping Journal*, 6(3), 155–160. <https://doi.org/10.1109/CCNC.2017.7983268>
- Tong, X., Li, F. H., Kuang, M., Ma, W. Y., Chen, X. C., & Liu, M. (2012). “Effects of WC particle size on the wear resistance of laser surface alloyed medium carbon steel.” *Applied Surface Science*, 258(7), 3214–3220. <https://doi.org/10.1016/j.apsusc.2011.11.066>
- Ur Rahman, N., Capuano, L., van der Meer, A., de Rooij, M. B., Matthews, D. T. A., Walmag, G., ... Römer, G. R. B. E. (2018). “Development and characterization of multilayer laser clad high speed steels.” *Additive Manufacturing*, 24(August), 76–85. <https://doi.org/10.1016/j.addma.2018.09.009>
- Vardavoulias, M. (1994). “The role of hard second phases in the mild oxidational wear mechanism of high-speed steel-based materials.” *Wear*, 173(1–2), 105–114. [https://doi.org/10.1016/0043-1648\(94\)90262-3](https://doi.org/10.1016/0043-1648(94)90262-3)
- Wang, J., Li, L., & Tao, W. (2016). “Crack initiation and propagation behavior of WC particles reinforced Fe-based metal matrix composite produced by laser melting deposition.” *Optics and Laser Technology*, 82, 170–182. <https://doi.org/10.1016/j.optlastec.2016.03.008>
- Weimer, A. W. (2012). *Carbide, nitride and boride materials synthesis and processing*. Berlin: Springer Science & Business Media.
- Weng, Z., Wang, A., Wu, X., Wang, Y., & Yang, Z. (2016). “Wear resistance of diode laser-clad Ni/WC composite coatings at different temperatures.” *Surface and Coatings Technology*, 304, 283–292. <https://doi.org/10.1016/j.surfcoat.2016.06.081>
- Wieczorzak, K., Bala, P., Stepień, M., Cios, G., & Koziel, T. (2016). “Formation of eutectic carbides in Fe-Cr-Mo-alloy during non-equilibrium crystallization.” *Materials and Design*, 94, 61–68. <https://doi.org/10.1016/j.matdes.2016.01.028>
- Wirth, F., Arpagaus, S., & Wegener, K. (2018). “Analysis of melt pool dynamics in laser cladding and direct metal deposition by automated high-speed camera image evaluation.” *Additive Manufacturing*, 21(May), 369–382. <https://doi.org/10.1016/j.addma.2018.03.025>
- Yadollahi, A., Shamsaei, N., Thompson, S. M., & Seely, D. W. (2015). “Effects of process time interval and heat treatment on the mechanical and microstructural properties of direct laser deposited 316L stainless steel.” *Materials Science and Engineering A*, 644, 171–183. <https://doi.org/10.1016/j.msea.2015.07.056>
- Yang, C. C., Hang Chau, J. L., Weng, C. J., Chen, C. S., & Chou, Y. H. (2017). “Preparation of high-entropy AlCoCrCuFeNiSi alloy powders by gas atomization process.” *Materials Chemistry and Physics*, 202, 151–158. <https://doi.org/10.1016/j.matchemphys.2017.09.014>
- Yip, M. W., Barnes, S., & Sarhan, A. (2014). “Effects of laser cladding of silicon carbides particles and iron based powder.” *Applied Mechanics and Materials*, 548–549, 289–293. <https://doi.org/10.4028/www.scientific.net/AMM.548-549.289>
- Yip, M. W., Barnes, S., & Sarhan, A. A. D. M. (2015). “Deposition of a silicon carbide reinforced metal matrix composite (P25) layer using CO<sub>2</sub> laser.” *Journal of Manufacturing Science and Engineering, Transactions of the ASME*, 137(3), 1–8. <https://doi.org/10.1115/1.4029831>
- Zhang, Z., Farahmand, P., & Kovacevic, R. (2016). “Laser cladding of 420 stainless steel with molybdenum on mild steel A36 by a high power direct diode laser.” *Materials and Design*, 109, 686–699. <https://doi.org/10.1016/j.matdes.2016.07.114>

Zuback, J. S., & DebRoy, T. (2018). "The hardness of additively manufactured alloys." *Materials*.  
<https://doi.org/10.3390/ma11112070>



#### 4. Conclusions

- **Powder handling and preparation**

- ✓ LC demonstrates its interest in the fabrication of FGM. In particular, the exploitation of its versatility leads to tailored microstructures. On the one hand, fabrication with separate powders leads to larger reinforcements and greater freedom to change the volume fraction of reinforcements during deposition, but the raw materials are limited. On the other hand, the use of composite powders enlarges the choice of available raw materials, but it increases the FGM fabrication complexity since more powder feeders are needed. Besides, the size of the reinforcements must be smaller than the hosting powder which results in a high probability of complete dissolution of the reinforcement during fabrication. Furthermore, process parameters must be adapted to any volume percentage since mechanical alloying increases the absorbance of the hosting powders.
- ✓ Mechanical alloying is a powerful tool in order to obtain composite powders and to handle powders that are not specifically manufactured for AM. This approach broadens the available compositions and the reinforcement (or reactant) choices for new composites and modified alloys.

- **Fabrication and macroscopic characterization**

- ✓ Process parameters must be adapted to the characteristics of the raw materials (density, flowability and tendency to segregate). The chemical affinity between the reinforcements and the original alloy is crucial for the tailoring of the composite. High chemical affinity and small sizes of the reinforcements lead to high dissolution. Low cooling rates and high temperatures enhance the dissolution of the reinforcements. Indeed, SiC reactants are completely dissolved during the process due to their high affinity with the molten metal although they have a comparable size to WC reinforcements, which are only partially dissolved.
- ✓ Partial or total dissolution of reinforcements in the molten metal during fabrication changes the initial composition of the melt, thus leading to the modification of the solidification route.
- ✓ An expected cellular and an unexpected dendritic or rosette-like morphologies are distinguished in the microstructure of the thick deposit. Detailed microstructural characterization reveals that undissolved WC particles act as nuclei leading to the formation of a finer rosette-like morphology.
- ✓ Heat accumulation decreases both cooling rates and thermal stresses. Therefore, heat accumulation can be used for in-situ preheating of the first layers when processing alloys that are known to undergo martensitic transformations upon cooling.

- **Microstructures**

- ✓ High cooling rates lead to the solidification of out-of-equilibrium microstructures, where some phases are metastable. During solidification under these conditions, elements cannot

move to their thermodynamically stable positions in the lattice, thus giving way to lattice distortions. The metastability is often associated with supersaturation due to the entrapment of additional atoms within the lattice structure compared to the equilibrium conditions.

- ✓ After AM process, at the local scale, metastable phases are observed within the melt pool since these phases directly solidify from the liquid, in opposition to the HAZ that is subjected to further thermal cycles. At the macroscale, when a heat treatment is carried out, metastable phases tend to destabilize and evolve to a condition closer to equilibrium. In the case of a supersaturated matrix, destabilisation leads to precipitation inside the matrix. On the other hand, for metastable carbides, decomposition or dissociation phenomenon will occur depending on the size of the parent carbide and the thermal history of the process. In particular, in carbides, the metastable condition is enhanced when its composition exhibits high amounts of two or more strong carbide-forming elements.
- ✓ “Reverse analysis” of DTA curves combined with the crystallography and chemical composition of any given phase in the microstructure allows to identify out-of-equilibrium microstructures.
- **Properties**
  - ✓ V, Ti, W and Mo atoms lead to a high expansion of the FCC crystal order and thus allow to improve the mechanical properties via solid solution strengthening. Nevertheless, their tendency to form carbides and their solubility in the FCC lattice limit their addition to AM compositions. On the other hand, as revealed by nanoindentation measurements, Si addition in the FCC lattice is shown very promising to improve the mechanical properties of AM austenitic stainless steels.
  - ✓ WC composites exhibit improved wear resistance compared to both the reference 316L and the Si-rich alloys, and this is due to the combined presence of hard solidification carbides and the partially dissolved WC original reinforcement particles.
  - ✓ The interrupted tests approach highlights the dynamic in the wear behaviour of simple and complex materials.
  - ✓ The wear mechanisms during wear tests are complex and depend on both the characteristics of the phases in the microstructure and the nature of the counterbody. In particular, the nature of the debris formed as a result of the interactions between the specimen and the counterbody determine the stabilisation of a protective tribolayer.
  - ✓ Oxidative wear mechanism is often observed during pin-on-disc tests against  $\text{Al}_2\text{O}_3$  ball with the formation of a protective oxide layer due to the wear of the ball and to the nature of the formed debris. This tendency hides the effect of microstructural differences variations in the specimen, but this comes with an easy comprehension of the wear mechanisms. On the other hand, pin-on-disc tests against WC-Co ball are more efficient in revealing the effective

performances of the tested materials and highlight the effect of microstructural differences, but the interpretation of the wear mechanisms is more complex.



## 5. Perspectives

### • WC composites

- This thesis confirms the different tendency of the reinforcements powders to dissolve during LC processing depending on their size. The original normal size distribution of the reinforcements can be modified in order to be shifted either toward larger or smaller diameters while keeping the good flowability of the powders. This approach allows to further tailor the resulting microstructure.
- Heat accumulation leads to a decrease in the thermal stresses during deposition since it increases the apparent substrate temperature and decreases the cooling rates. This phenomenon could be exploited to achieve 316L+WC composites with 30 and 40 vol.% of WC, overcoming the vol.% limit of 23.5%.
- Pin-on-disc tests against WC-Co ball exhibits the effective performances of the tested material and highlights the microstructural differences. Therefore, it is interesting to investigate the microstructural differences observed in the WC-Co composites due to heat accumulation via a pin-on-disc campaign against WC-Co ball at different distances from the substrate, at both room and high temperatures.
- Development of corrosion tests to determine corrosion resistance of composites and alloys, and to highlight both the effect of matrix composition and the interfaces between carbides and matrix, which are known to promote local corrosion. The effect of volume fraction should be check under corrosion tests.

### • Si-rich alloys

- The initial SiC powder can be modified in order to decrease its tendency to segregate. In particular, a sieving step on the SiC powders allows to determine which particles contain initially more oxygen and which particle population enhances the segregation among the powder mixture. This approach could lead to achieve the composite composed in 316L and 30 vol.% of SiC, which is close to the saturation of the melt in Si, and thus incomplete dissolution of the reinforcements can be expected and studied.
- With the increase of the Si addition in the composition, a thin protective oxide layer composed of silica is often observed. Indeed, silica formation is thermodynamically favoured compared to chromia formation. XPS analyses might be interesting in order to evaluate the presence of silica on the surface and the evolution of the oxide layer with different volume fraction.
- Such oxide layer is reported to increase the corrosion resistance in different alloys due to the higher thermodynamic stability of silica and to its higher resistance in harsh environments compared to chromia, opening interesting prospects in terms of corrosion properties for the new Si alloys.

- **General**

- The pin-on-disc tests on the composites highlighted the demand to better understand the interactions between specimen and counterbody. Further investigations would be welcome in that respect.
- In order to test coatings fabricated by LC in conditions closer to actual applications, pins could be obtained from the tick deposits and used as counterbody against reference wear specimens (i.e. cast 316L or cast 430L). Both the wear of the pin and the wear specimen could be measured and lead to a more realistic estimation of the wear resistance of the LC coatings.
- Any given reinforcement should yield different benefits depending on its nature, size, tendency to dissolve and new phases formed in the resulting microstructure. The fabrication of hybrids with more than one reinforcement could lead to novel microstructure with combined strengthening mechanisms.

## Appendix

Table A-1: List of the five main contributions of this PhD research.

Article	Complete title [status]
1	Maurizi Enrici, T., Mertens, A., Sinnaeve, M., & Tchuindjang, J. T. (2019). "Elucidation of the solidification sequence of a complex graphitic HSS alloy under a combined approach of DTA and EBSD analyses." <i>Journal of Thermal Analysis and Calorimetry</i> , 1–15. <a href="https://doi.org/10.1007/s10973-019-09093-9">https://doi.org/10.1007/s10973-019-09093-9</a>
2	Maurizi Enrici, T., Dedry, O., Boschini, F., Tchuindjang, J. T., & Mertens, A. (2020). "Microstructural and Thermal Characterization of 316L+WC Composite Coatings obtained by Laser Cladding." <i>Advanced Engineering Materials</i> , 13, 1–12. <a href="https://doi.org/10.1002/adem.202000291">https://doi.org/10.1002/adem.202000291</a>
3	Maurizi Enrici, T., Dedry, O., Mario, D., Paydas, H., Tchoufang, J., & Mertens, A. (n.d.). "Heat accumulation in multiple layers 316L + WC composite fabricated by DED: influence on local microstructure and hardness" Submitted to Additive Manufacturing.
4	Maurizi Enrici, T., Mario, D., Dedry, O., Castagne, S., Tchuindjang, J. T., & Mertens, A. (n.d.). "Wear behaviour of laser clad 316L + WC composite against alumina." Submitted to Additive Manufacturing.
5	Maurizi Enrici, T., Saggionetto, E., Dedry, O., Ertugrul, O., Boschini, F., Tchuindjang, J. T., & Mertens, A. (n.d.). "On the microstructures and strengthening mechanisms of new high-silicon austenitic stainless steels obtained by Laser Cladding" [In preparation]





# Elucidation of the solidification sequence of a complex graphitic HSS alloy under a combined approach of DTA and EBSD analyses

Tommaso Maurizi Enrici<sup>1</sup> · Anne Mertens<sup>1</sup> · Mario Sinnaeve<sup>2</sup> · Jérôme Tchoufang Tchuindjang<sup>1</sup>

Received: 6 June 2019 / Accepted: 23 November 2019 / Published online: 4 December 2019  
© Akadémiai Kiadó, Budapest, Hungary 2019

## Abstract

In this work, a complex graphitic high-speed steel (Gr-HSS) obtained from a spin-casting process that allows high cooling rates during solidification is considered. Differential thermal analysis is carried out at a moderate and constant heating scan speed until complete remelting. This allows linking each of the peaks observed in the DTA curve to a related phase transformation that had occurred during the initial solidification in the spin-casting process. The phases that were formed during the spin-casting process, especially solidification carbides, are characterized through light microscopy (distribution) and scanning electron microscopy (morphology) either associated with EDS (chemical composition) or associated with EBSD (crystal lattice identification). A discussion is opened about the influence of solidification rates on both supersaturation and lattice distortions in the solidification carbides. The combination of reverse DTA and SEM/EDS–EBSD applied here to the complex Gr-HSS alloy constitutes a relevant approach to understand the phase transformations during complex casting processes where relatively high solidification rates are achieved.

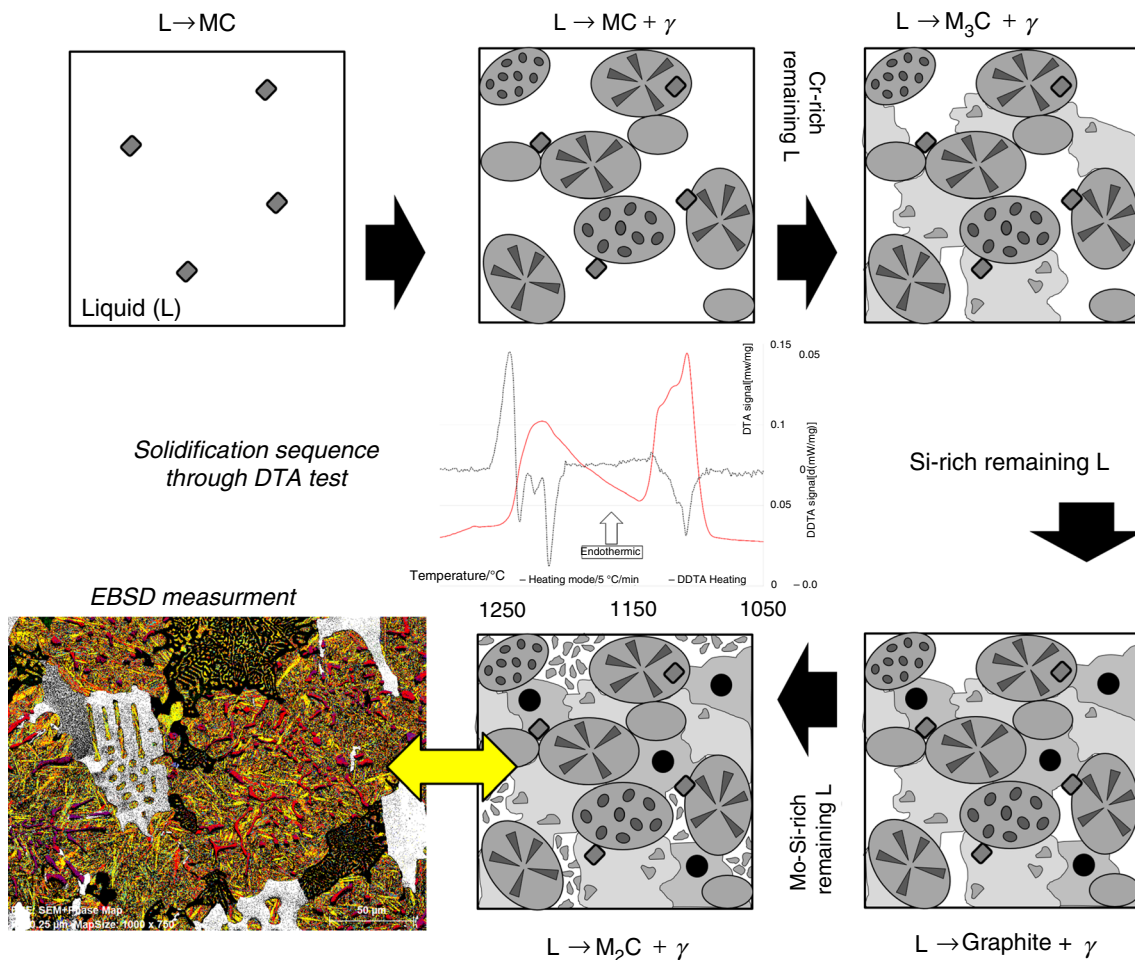
---

✉ Jérôme Tchoufang Tchuindjang  
j.tchuindjang@uliege.be

<sup>1</sup> Metallic Materials Science (MMS), University of Liège,  
Quartier Polytech 1; Allée de la Découverte 13 (B52),  
4000 Liège, Belgium

<sup>2</sup> Marichal Ketin, Verte Voie 39, 4000 Sclessin, Belgium

## Graphic abstract



**Keywords** Solidification sequence · High-speed steel · Free graphite · Differential thermal analysis (DTA) · Electron backscattered diffraction (EBSD) · Carbides characterization

## Introduction

High-speed steels (HSSs) and high-alloyed cast irons (HACIs) are widely used in a great variety of applications including cutting operations, hot strip mills, high-speed machining and moulding. Due to their great versatility and to their relatively wide range of chemical compositions, they have received great attention so far, focusing on the understanding of their solidification mechanisms [1, 2].

Considering HSS grades, the carbon content ranges between 0.3 and 2.0 mass%, with the presence of strong carbide-forming elements such as V, W, Nb or Mo that lead to the formation of hard solidification carbides in a martensitic or bainitic matrix. The designation “multi-component white cast iron” (MWCI) used in Japan may correspond more to HSS grades than cast irons (CIs), because such grades

contain several strong carbide-forming elements, but neither cementite nor free graphite [3–5]. The nature, morphology and composition of the carbides will depend on the alloy chemical composition and on the cooling rate during solidification [6–8]. Both the carbides content and distribution may influence the mechanical properties of HSS, such as their strength, hot hardness, wear resistance or fracture toughness [5, 9–11]. The carbides can be of various types, i.e. primary, eutectic and secondary carbides, depending on the moment of their formation during the casting process. Primary carbides (PCs) precipitate from the liquid, as the first solid before the nucleation of grains or cells that correspond to the matrix. Therefore, PCs set the liquidus temperature. Under spin-casting process, PCs could be distributed randomly within the material, depending on their density compared to the remaining liquid metal [12]. Eutectic carbides (ECs) are formed at

the end of solidification, and they set the solidus temperature. ECs are located at cell or grain boundaries. Finally, secondary carbides (SCs) precipitate in the solid state and are most often located inside cells or grains [12–15].

Compared to the HSS grades, the carbon and silicon contents of cast irons (CIs) are significantly higher, above 2 mass/% C and above 1 mass/% Si, leading to the presence of ledeburite made of austenite and cementite, which as the main EC sets the definition of such an alloy [10, 16]. In addition, free graphite can be found in the microstructure of grey CIs, whereas white CIs do not contain graphite. Contrary to HSS, the number of strong carbide-forming elements in CIs will be reduced to one or two species. In high chromium cast steel and high chromium cast irons, Cr is the main alloying element, leading to a high amount of  $M_7C_3$  carbide at the expense of cementite [17–19]. In high-alloyed cast irons (HACIs), the presence of several transition elements promotes MC carbides formation [1]. The austempered cast irons (ACIs) exhibiting free graphite and solidification carbides in a retained austenite matrix can also be considered as mixed structure [20], like Ni-hard-type cast irons [21]. For all these mixed structures containing both free graphite and solidification carbides other than cementite, efforts have focused on the characterization of the microstructure [4, 7, 22] and mechanical behaviour [10, 13, 20], for processing conditions close to equilibrium [1, 23]. “Graphitic HSS” (Gr-HSS) grades have also been investigated in Japan and in Europe for abrasion-resistant parts [11, 24, 25]. These complex Gr-HSS alloys actually belong to both the Fe–C stable system and the Fe– $Fe_3C$  metastable system, but only little attention has been given to the study of their microstructure.

These examples show that improved properties can be achieved using HSS, HACI and Gr-HSS. However, the identification of the solidification sequence of these complex alloys under the cooling rates pertaining to their industrial casting conditions is still a matter of concern. Indeed, concerning the study of solidification sequence in complex HSS alloys, most of the work can be divided according to two approaches, i.e. experimental or based on thermodynamic simulations.

As experimental tests are concerned, thermal analysis (TA) under directional solidification has been widely used. Directed solidification allows to vary the thermal gradients and modify the morphology of the solidification interface, which in turn directly influences dendritism [21, 24, 26, 27]. Macroscopic parameters such as primary/secondary dendrite arms spacing (PDAS/SDAS), solidification mode and grain size can then be determined [6, 28–35]. In addition, the temperature profiles can be obtained along the length of the casting. Thus, TA provides a global thermal history, determining the beginning and end of solidification. Eutectic plateaus which depend on the cooling scan can also be observed, but this does not include the identification of the phases involved [24, 29–31].

Differential thermal analysis (DTA) is another technique to investigate the endothermic or exothermic reactions that are related to phase transformations, while simultaneously identifying the critical transition points [31, 32, 34, 36–38]. The highest achievable cooling rates (i.e.  $50\text{ }^\circ\text{C min}^{-1}$ ) remain several orders of magnitude lower than those achieved under industrial casting processes. DTA is thus useful to build phase diagrams, in equilibrium conditions or close to equilibrium [29, 36, 38, 39]. However, because the cooling rate strongly influences both undercooling and solute partitioning during solidification, the crystallization behaviour achieved under DTA hardly corresponds to the actual solidification sequence which occurs during industrial casting processes [23, 40].

Similarly, thermodynamic simulations allow the quick determination of the solidification sequence based on equilibrium conditions [12, 33, 39, 41, 42]. The databases used to calculate the Gibbs free energies are mainly established for binary and ternary systems [33, 34, 38]. Transposition to multi-component complex alloys such as HSS involves making approximations to pseudo-binary phase diagrams and will often lead to discrepancies between the prediction and the actual microstructure [3, 5, 6, 12, 14, 18, 29, 31, 39, 40].

Developing a methodology to determine the solidification sequence and to identify the phases formed within complex alloys under sophisticated casting processes remains a hot topic for scientists. A new approach will thus be attempted in this work, by combining different characterization techniques. In particular, the cross-consideration of EDS analysis (composition) and EBSD analysis (information about lattice) appears as very promising to overcome the limitations specific to each of these techniques considered separately [18, 43]. Electron backscattered diffraction (EBSD) is seldom employed for the characterization of complex or multi-alloyed microstructures, as the databases only consider classical simple phases [18, 44]. In this work, an attempt is made to link the actual chemical composition determined by EDS with the crystal lattice information obtained by EBSD in order to identify the carbides such as V-rich or Nb-rich MC [1, 45], Mo- and W-rich  $M_2C$  or  $M_6C$  [19, 22], Fe-rich and Cr-rich  $M_7C_3$  or  $M_3C$  [11, 40] that are formed during solidification. Moreover, the solidification sequence is established through the development of a reverse analysis of DTA remelting tests.

## Materials and methods

### Material and sampling

The studied material is made of a Gr-HSS alloy corresponding to the shell part of a bimetallic work roll produced by a vertical spin-casting process. Its average chemical

composition is given in Table 1. The external diameter of the roll is around 800 mm with a total length around 2500 mm. The core material that is poured after the shell is made of nodular CI. The cooling rates achieved during the casting process range between 100 and 300 °C min<sup>-1</sup>, the highest cooling rates being achieved close to the surface [9]. A prismatic bar of square section (25 mm side) has been cut within the shell and on the top of the roll and then submitted to a double tempering at 530 °C for 24 h followed by furnace cooling. The post-heat treatment allows achieving a fully martensitic matrix [17, 46]. Both cylinders and cube specimens are then cut out of the heat-treated block by electro-discharge machining, these samples being, respectively, dedicated to DTAs and microstructure characterization.

## Experimental methods

### Reverse approach on differential thermal analyses (DTAs)

Cylindrical samples with their axes parallel to that of the work roll are used for DTA. They are located at a depth of 18 mm from the external surface, with the following sizes: Ø 5 mm and 5 mm height, for approx. 0.97 g mass. DTA tests are carried out on a NETZCH 449C Jupiter apparatus in heating mode at a constant scan of 5 °C min<sup>-1</sup> up to 1300 °C, so as to achieve a complete remelting of the Gr-HSS alloy. DTA tests are performed twice, the final DTA curve being the average of two tests.

The first derivative of the DTA curve (DDTA) is computed using NETZSCH Proteus<sup>®</sup> Thermal Analysis software. This helps identify individual peaks when overlapping occurs [33, 35, 38]. Until now, this first derivative approach has been commonly used in dilatometry to highlight solid state transformations within the matrix during heating [47, 48]. In the melting range, few works using this approach can be found related to non-ferrous alloys, which are based either on TA [29, 30, 35, 39], or on DSC and DTA studies [33, 38, 49, 50]. The onset and the end of any phase transformation are given by the beginning of the DDTA peak and the maximum of the DTA peak, i.e. to DDTA = 0 (maximum of the first slope on DDTA curve), respectively [33, 36, 38]. The second slope from the maximum down to the DTA baseline corresponds to the relaxation stage [36]. Depending whether the DTA peak looks sharp or broad, it is assumed that the composition of the related phase involved in the reaction will be fixed or will vary.

### Classical microstructure characterization

A cube sample with an edge length of 10 mm, and located between 5 and 15 mm from the external surface of the roll, is used for microstructure characterization. This sample undergoes a preliminary metallographic preparation consisting of a hot mounting with an electrically conductive epoxy resin followed by grinding and polishing down to 1 µm, prior to final super polishing down to 0.06 µm with colloidal silica, which is an active oxide polishing suspension (OPS). The as-polished samples are used for SEM analyses. Light microscope (LM) analyses are done on both as-polished and etched conditions. Etching consists of 30-s immersion in 3% Nital reagent, thus allowing to better reveal the matrix martensite type.

LM analyses are performed using an Olympus BX-60 M microscope equipped with a motorized stage, a UC-30 digital camera and Stream Analysis<sup>®</sup> software for data processing. Optical microscopy is used to get a large overview of the phase distribution within the microstructure.

The areas of interest identified under LM are subsequently analysed with SEM, using a Philips XL30 FEG-ESEM microscope equipped with a 10-mm<sup>2</sup> Bruker SDD-type EDS detector, and a retractable Quantax e-Flash (Bruker) EBSD camera. The data processing software coupled to the detectors is ESPRIT<sup>®</sup> 1.7. Both BSE mode and EDS profiles help to study carbides morphology and to determine the spatial distribution of elements within the microstructure. ZAF algorithm is performed on EDS spectra to obtain the relative amounts of elements, either in mass or in atomic percentages.

### Iterative approach through EBSD analyses

EBSD analyses have been carried out using an accelerating voltage of 20 kV, at 15 mm of working distance with a 30-µm aperture. A pixel size of 0.25 µm was set for EBSD images. A minimum number of seven bands were subsequently set within ESPRIT software in order to identify both the crystal structure and the lattice parameters. AMCSD, ICSD-Demo, BAXS and PDF4+ (reference 01-018-1479) from the International Centre for Diffraction Data (ICDD) XRD databases are considered as reference for the allowable phases in EBSD analyses. These XRD databases are established for binary or ternary systems. They list phases that are different from the complex carbides found in the present work, which can contain up to six elements.

**Table 1** Average chemical composition of the investigated Gr-HSS grade

Element	C	Si	V	Cr	Mn	Ni	Mo	Nb	Fe
Mass/%	2.0–3.0	2.0–4.0	1.0–3.0	2.0–5.0	1.0–3.0	2.0–6.0	3.0–5.0	0–2.0	Bal.

The EBSD technique relies on the comparison between phases indexed based on the Kikuchi patterns and available databases, and it is not possible to identify a crystal phase if the analysis of the Kikuchi patterns does not lead to the correct crystal structure with the correct parameters [18, 43, 51]. The image quality (IQ) map describes the quality of a diffraction pattern, and the contrast observed can arise from strain, grain boundaries, phase, surface topology, and/or other features of the microstructure [46, 52]. In other words, the pattern quality allows determining whether a phase is well indexed or not. Starting from this consideration, the approach proposed in this paper is to consider together the crystal structure and the composition obtained by EDS analyses in order to identify phases with unique compositions. “Exotic” phases can be considered, that have the same crystal structure but a more similar composition to the observed phase [53]. If the lattice of such an “exotic” phase is indexed and lead to an increase in the identification percentage of the analysis, it is more similar to the observed phase than to the “classical” phase of the database. Then, a comparison is made with the theoretical phase to discuss phenomena such as supersaturation or reduced solubility of the elements previously identified during the EDS analysis. For phases that are poorly indexed or that do not have equivalent crystallographic lattices in the XRD database, further possible metallurgical phenomena are highlighted.

## Results

### Gr-HSS heat-treated microstructure

The typical microstructure of the Gr-HSS alloy is illustrated in Fig. 1, showing white ECs in the intergranular spaces and light grey MC carbides uniformly distributed. Graphite

nodules remain dark in the as-polished conditions or after etching.

### Differential thermal analysis (DTA)

The DTA heating curve and its first derivative (DDTA) within the remelting zone are illustrated in Fig. 2. Two large and complex peaks are observed in this range (Fig. 2a), the first one (H1 + H2 + H3) looking sharp and the second one (H4 + H5 + H6) looking wider. Straightforward inspection of both DTA complex peaks leads to indeterminations regarding the onset of phase transformations, the uncertainty being illustrated by a question mark as mentioned in Table 2. The deconvolution of the two complex peaks based on the derivative curve makes it possible to remove the uncertainty, except for peak H6, thus allowing to distinguish six small superimposed peaks (Fig. 2b), as summarized in Table 2.

The first DTA peak is complex (H1 + H2 + H3), high, and relatively sharp (in the range 1092–1131 °C). The second DTA peak also looks complex (H4 + H5 + H6), but it is lower and broader than the first one (1147–1238 °C). The three DDTA peaks related to H1 + H2 + H3 are very sharp and exhibit sudden changes of slope. The first DDTA peak (H1) is almost complete and looks isolated, while the two following DDTA peaks (H2 and H3) are overlapping, with only the last section of H3 clearly distinguishable. The first DDTA peak (H4) related to H4 + H5 + H6 exhibits a discontinuity in its first side prior to a plateau (Fig. 2b). The following two DDTA peaks H5 and H6 show a large overlap with H4.

### Distribution, morphology and chemical composition of solidification carbides

BSE mode allows identifying solidification carbides within the microstructure, based on their apparent chemical

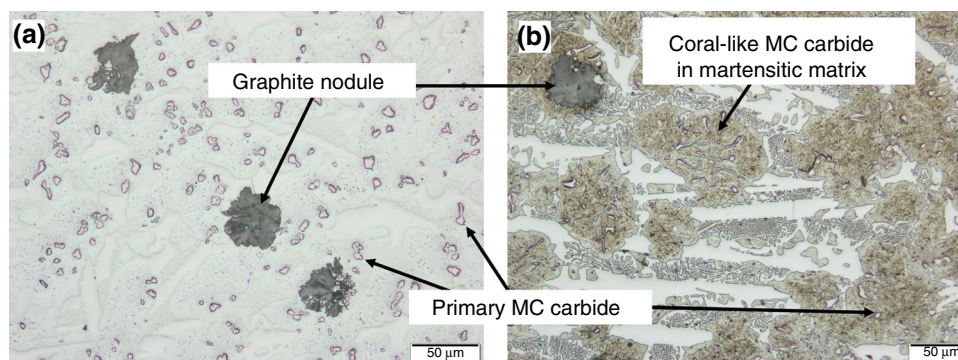


**Fig. 1** Optical micrographs of the Gr-HSS microstructure after double tempering. **a** Angular primary MC carbides (pink) uniformly distributed and free graphite nodules (dark grey) in the as-polished conditions (after OPS); **b** enhancement of the martensitic matrix

containing coral-like MC carbides, with the presence of eutectic carbides (white) more or less connected to free graphite nodules at grain boundaries (Nital etched)

**Fig. 2 a** Overview of the DTA heating curve runs at  $5\text{ }^{\circ}\text{C min}^{-1}$  up to complete remelting of as-cast Gr-HSS alloy showing two complex peaks, and the relative first derivative curve (DDTA); **b** zoom corresponding to the DTA remelting zone where DDTA curve helps identifying the different reactions peaks (H1–H3, and H2–H6)

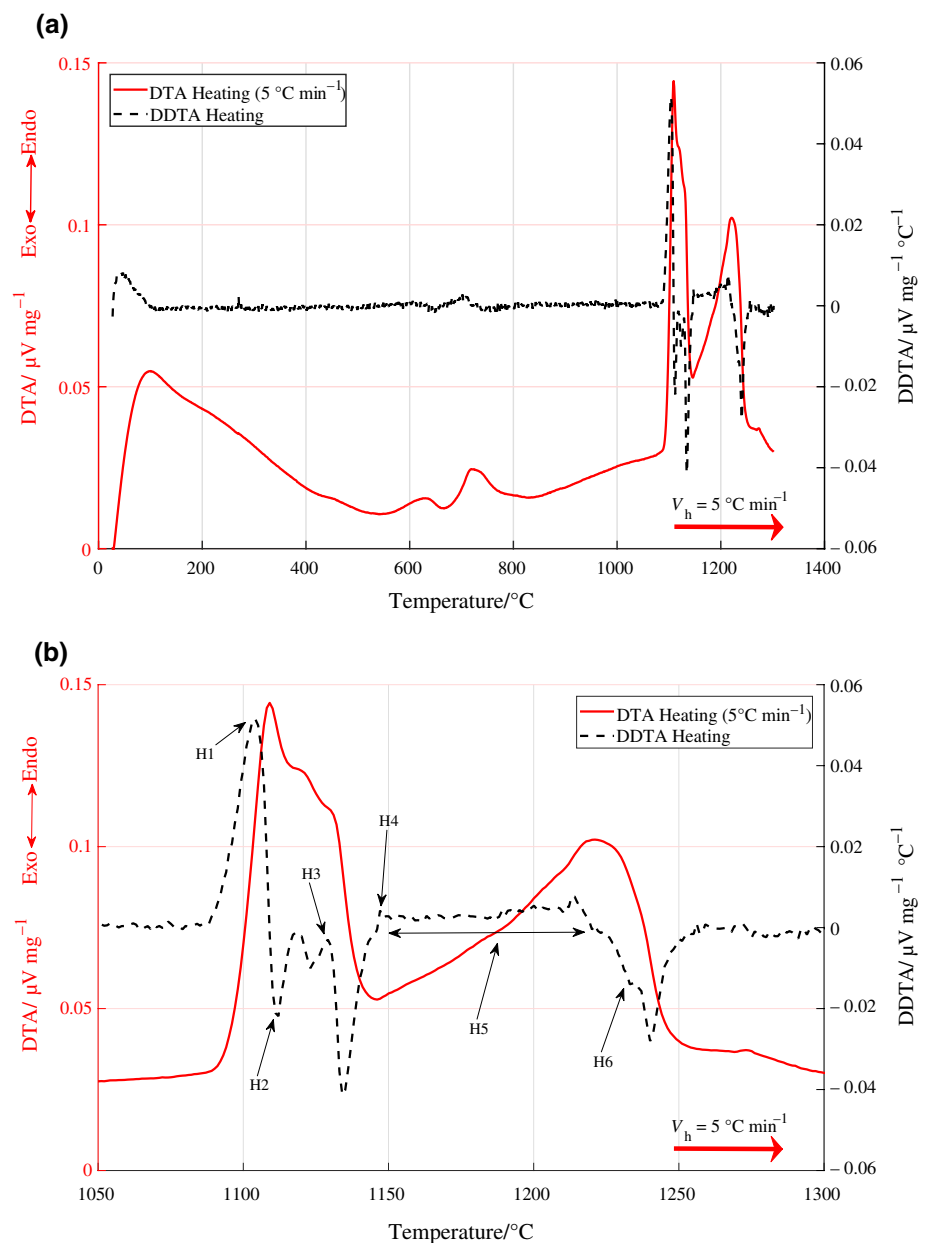


**Table 2** List of the peaks observed during remelting, as obtained from the DTA curve and from the first derivative (DDTA)

No	Range for DTA peak	Range for D(DDTA) peak	Shape of the peak
H1 + H2 + H3	1092–1131		
H1	1092–1109	1088–1104	Sharp
H2	?–1121	1115–1119	Sharp
H3	?–1131	1124–1129	Sharp
H4 + H5 + H6	1147–1238		
H4	1147–1149	1145–1148	Large
H5	?–1221	1145–1214	Large
H6	?–1238	?–1236	Large

contrast. Therefore, MC,  $M_2C$  and  $M_3C$  (or cementite) will, respectively, appear dark grey [1, 54], white, or in shades of light grey [12, 14, 40]. In what follows, solidification carbides will be described depending on their distribution, starting from the intercellular ones and ending by the intracellular ones.

### MC carbides

The different types of MC carbides that are present in the Gr-HSS microstructure are illustrated in Fig. 3. The primary carbides (PCs) exhibit a globular or spherical morphology. They are evenly distributed within the material as they are the first solid to precipitate when solidification

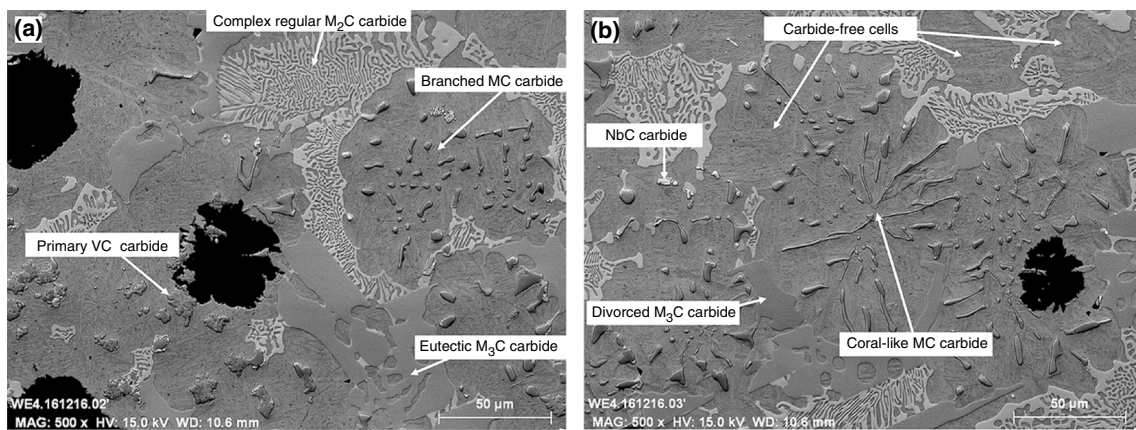


**Fig. 3** **a** Close-up view of a region exhibiting primary MC (dark grey and globular), coral-like intragranular MC, and  $M_3C$  carbides (light grey) and large complex regular  $M_2C$  carbides (white or bright)

located at grain boundaries (BSE mode). **b** Close-up view of a region exhibiting several MC carbides, together with eutectic and divorced  $M_3C$  carbides, located at grain boundaries (BSE mode)

**Fig. 4** SEM/EDS profile on different MC carbides present in the Gr-HSS microstructure (from Fig. 3a). **a** Evolution of the main carbide-forming elements in mass/% (top view); **b** close-up view of the evolution of both C and Si in mass/%

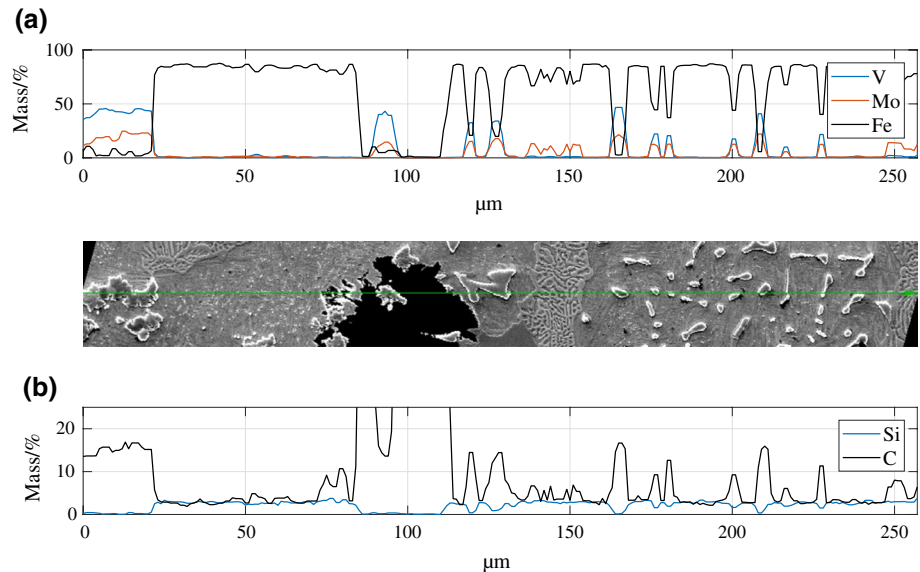


**Table 3** Chemical compositions (mass/%) of the different MC carbides related to the EDS profile

MC carbide (mass/%)	Position/ $\mu\text{m}$	C	Si	V	Cr	Mn	Fe	Ni	Mo	Nb
PC	0–20	$15.2 \pm 1.1$	$0.2 \pm 0.1$	$42.5 \pm 3.0$	$2.1 \pm 0.5$	$0.1 \pm 0.1$	$4.7 \pm 3.0$	$0.4 \pm 0.4$	$19.3 \pm 4.1$	$14.1 \pm 4.2$
PPC + $\gamma$ (close to cell boundary)	160–190	$6.1 \pm 4.7$	$2.3 \pm 0.9$	$9.9 \pm 15.4$	$1.5 \pm 0.4$	$0.7 \pm 0.4$	$66.8 \pm 28.5$	$4.1 \pm 1.9$	$5.5 \pm 7.2$	$2.4 \pm 3.5$
PPC + $\gamma$ (centre of the cell)	190–220	$5.3 \pm 4.0$	$2.4 \pm 0.7$	$6.2 \pm 11.2$	$1.6 \pm 0.9$	$1.0 \pm 0.4$	$73.4 \pm 22.4$	$4.5 \pm 1.5$	$3.9 \pm 6.11$	$1.4 \pm 2.7$

starts (Figs. 1a, 3a). MC coral-like pseudo-primary carbides (PPCs) are located inside the grains, with their core located at the centre of the grain (Fig. 3b). The core also corresponds to the carbide nucleus [24, 54]. Depending on the orientation, PPCs may sometimes exhibit a branched dendritic shape with the nucleus as a central rib (Fig. 3a) [5, 10].

The average chemical composition of MC carbides is obtained from EDS profiles (Fig. 4) and summarized in Table 3. The amount of transition elements is much higher in the primary MC compared to the pseudo-primary carbides. There is a large variation in the amount of V, Nb and Mo for the primary MC and the PPCs (Table 3). Most of the MC

carbides are V-rich, and a few small carbides are Nb-rich (Fig. 3b), both corresponding to the PCs. PPCs, on the other hand, exhibit a high standard deviation of the concentration of the carbide-forming elements, indicating a wide range of possible compositions. There is a clear tendency of the elements to be fixed either in the carbides (C, V and Mo) or in the matrix (Fe and Si), as shown in Fig. 4a, b.

The SEM/EDS profile between 160 and 220  $\mu\text{m}$  (Fig. 4 and Table 3) provides information on the evolution of the chemical composition of the growing cell during solidification. The amount of Fe decreases from the centre or core of the cell (located in the range 190–220  $\mu\text{m}$ ) to the grain boundary (in the range 160–190  $\mu\text{m}$ ). V, Mo and Nb, on the other hand, exhibit an opposite trend.

### $\text{M}_3\text{C}$ carbide

The light grey  $\text{M}_3\text{C}$  carbides share the intergranular spaces with the white  $\text{M}_2\text{C}$  carbides (Fig. 3). They exhibit a smooth boundary that clearly underlines their limits with the matrix or the  $\text{M}_2\text{C}$  carbides. The SEM micrographs of Fig. 3 show two different morphologies of the  $\text{M}_3\text{C}$  carbide, i.e. the divorced and the eutectic morphologies [10, 16, 40]. These two morphologies correspond to the same carbide, observed according to different sections. In the eutectic morphology, the circular spaces inside the carbides are associated with the eutectic matrix. Each  $\text{M}_3\text{C}$  carbide appears homogeneous in composition as indicated by the SEM images in BSE mode (Fig. 3), but two nearby  $\text{M}_3\text{C}$  carbides can present slight colour differences (Fig. 3b) [40]. Table 4 reports the mean values of the compositions for the eutectic and divorced morphologies of  $\text{M}_3\text{C}$  carbides. This carbide contains two main metallic elements (Fe and Cr) and traces of Mo and V, corresponding to the stoichiometric formula  $(\text{Fe}, \text{Cr})_3\text{C}$ . The higher standard deviation in the eutectic morphology is due to the larger contribution from the matrix in the interaction volume [43]. The divorced morphology of  $\text{M}_3\text{C}$  carbide is considered to exhibit a narrow range of composition in view of its low standard deviation (Table 4). Indeed, the divorced morphology is more compact and less influenced by contribution from the matrix.

### $\text{M}_2\text{C}$ carbide

The complex regular  $\text{M}_2\text{C}$  carbide is present in the intergranular spaces and is characterized by a smooth boundary that clearly outlines its interface with the matrix [6, 8, 14]. The periphery of the  $\text{M}_2\text{C}$  carbide tends to present larger lamellae than the centre, as shown in Fig. 3a. Their morphology changes gradually from an ordered centre to a rod-like edge. The composition of the  $\text{M}_2\text{C}$  carbide is obtained from the EDS profile in Fig. 5, and the average composition is summarized in Table 5 for the ordered centre and the rod-like

edge, respectively. The  $\text{M}_2\text{C}$  carbide is in the centre of the profile (in the range from 60 to 170  $\mu\text{m}$ ). The carbide exhibits a high content of Fe and Si [21, 51], the latter being similar to the one of matrix (Fig. 4b). It is composed of carbide lamellae arranged inside an eutectic matrix. As noted previously, due to the effect of the size of the interaction volume, the contribution of the matrix to the measured composition of a given lamella increases when the size of the lamella decreases, resulting in higher standard deviations [40]. The molybdenum content increases from the centre to periphery.

### Lattice identification by EBSD measurement

Figure 6 shows the results of an EBSD analysis, together with the main crystal lattice parameters used in the indexation [16, 46, 51]. This map was divided into two different images showing (i) the matrix and the VC carbides [14] (Fig. 6b) and (ii) all the other carbides (Fig. 6d). The pattern quality map of Fig. 6c shows that all the phases are well indexed, except for the pattern of martensite that is of slightly poorer quality (note the small darker spots in Fig. 6c) [46]. The matrix is identified as a BCC crystal system corresponding to ferrite, while it is actually known to be martensite as a result of the double tempering thermal treatment (see [Material and sampling](#) section). Some MC and fine secondary  $\text{M}_{23}\text{C}_6$  carbides are homogeneously distributed in the matrix. The MC carbides are identified as VC, exhibiting a FCC crystal system with varying lattice parameters [46]. The  $\text{M}_3\text{C}$  carbides are indexed considering the lattice of cohenite, which gives a better rate of indexation compared to cementite [16, 53]. Cohenite is a natural iron carbide mineral with chemical structure  $(\text{Fe}, \text{Ni}, \text{Co})_3\text{C}$ . Cementite and cohenite both have an orthorhombic (O) crystal system, with slightly different lattice parameters (Fig. 6a) as will be discussed in [“Influence of casting route on the composition and the crystallography of carbides”](#) section. The graphite was not indexed due to the low backscattering efficiency of carbon [44]. The  $\text{M}_2\text{C}$  carbide was not identified even if it was indexed [15, 22, 51, 55].

## Discussion

### Elucidation of the solidification sequence by a reverse DTA approach

Undercooling is the driving force for nucleation during solidification, in particular for a homogeneous nucleation. For heterogeneous nucleation that is promoted by a substrate or by the presence of inclusions, the undercooling should be less marked at the beginning of the solidification (liquidus temperature), but it can be more pronounced for the solidus temperature [23, 30, 33, 35], especially when high cooling

**Table 4** Compositions (mean values and standard deviation) of the two morphologies of the  $M_3C$  carbide (in mass/% and in atomic/%) in Fig. 5

Mass/%	Profile position/ $\mu\text{m}$	C	Si	V	Cr	Mn	Fe	Ni	Mo	Nb
Divorced	6–16	$7.5 \pm 0.6$	$0.1 \pm 0.2$	$1.8 \pm 0.4$	$5.8 \pm 0.9$	$1.7 \pm 0.4$	$78.3 \pm 2.4$	$1.3 \pm 0.7$	$3.2 \pm 1.0$	$0.0 \pm 0.0$
Eutectic	30–40	$5.8 \pm 2.4$	$1.4 \pm 1.2$	$1.1 \pm 0.6$	$3.2 \pm 2.1$	$1.4 \pm 0.2$	$81.7 \pm 3.0$	$3.6 \pm 2.3$	$1.7 \pm 1.1$	$0.0 \pm 0.0$
Atomic/%	Profile position/ $\mu\text{m}$	C	Si	V	Cr	Mn	Fe	Ni	Mo	Nb
Divorced	6–16	$27.3 \pm 2.0$	$0.2 \pm 0.4$	$1.6 \pm 0.3$	$4.9 \pm 0.7$	$1.4 \pm 0.3$	$61.9 \pm 2.8$	$1.0 \pm 0.5$	$1.5 \pm 0.4$	$0.0 \pm 0.0$
Eutectic	30–40	$21.6 \pm 8.0$	$2.3 \pm 2.1$	$1.0 \pm 0.5$	$2.8 \pm 1.7$	$1.2 \pm 0.2$	$67.3 \pm 6.7$	$2.9 \pm 2.1$	$0.8 \pm 0.5$	$0.0 \pm 0.0$

**Fig. 5** SEM/EDS profile analysis along the large  $M_2C$  carbide and  $M_3C$  carbide in Fig. 3a. Mo and Si are shown in the upper graph (atomic/%) ; C and Fe are plotted in the lower graph (atomic/%). Table 5 reports the main results

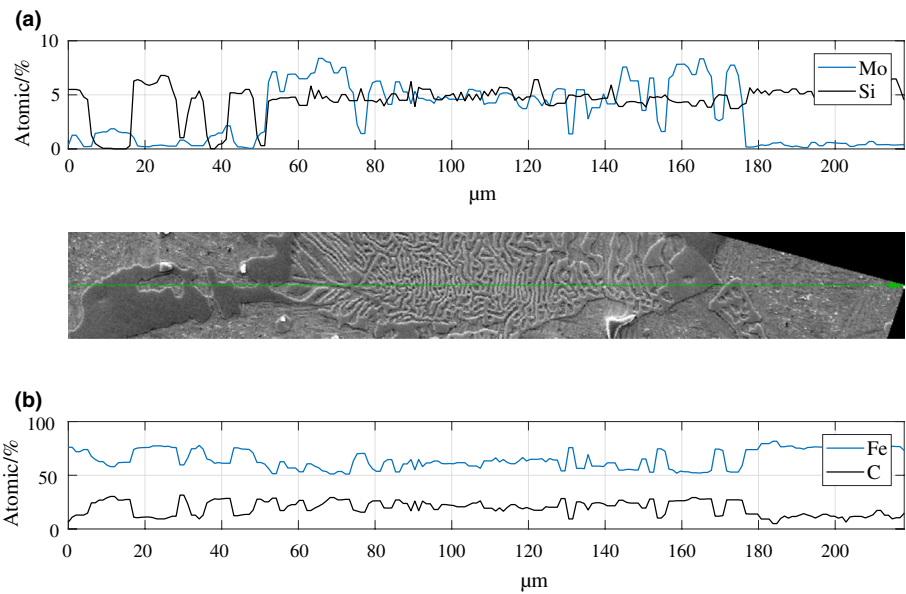


**Table 5** Compositions (mean values and standard deviation of 10  $\mu\text{m}$  of analysis) along the large  $M_2C$  carbide (in mass/% and in atomic/%) in Fig. 5

Mass/%	Profile position/ $\mu\text{m}$	C	Si	V	Cr	Mn	Fe	Ni	Mo	Nb
$M_2C$ left side	70–80	$5.9 \pm 1.5$	$2.8 \pm 0.2$	$1.3 \pm 0.5$	$3.2 \pm 1.0$	$1.3 \pm 0.5$	$71.7 \pm 6.5$	$3.2 \pm 1.2$	$10.6 \pm 5.0$	$0.2 \pm 0.2$
$M_2C$ centre	90–100	$5.7 \pm 0.9$	$3.0 \pm 0.3$	$1.1 \pm 0.4$	$2.7 \pm 0.6$	$1.3 \pm 0.3$	$73.1 \pm 2.0$	$3.4 \pm 0.7$	$9.7 \pm 0.8$	$0.1 \pm 0.1$
$M_2C$ right side	140–150	$6.0 \pm 0.8$	$2.7 \pm 0.3$	$1.4 \pm 0.5$	$3.4 \pm 0.8$	$1.2 \pm 0.3$	$70.3 \pm 4.6$	$3.5 \pm 0.7$	$11.2 \pm 3.3$	$0.1 \pm 0.1$
	Mean value	5.9	2.8	1.3	3.1	1.3	71.7	3.4	10.5	0.1
Atomic/%	Profile position/ $\mu\text{m}$	C	Si	V	Cr	Mn	Fe	Ni	Mo	Nb
$M_2C$ left side	70–80	$22.8 \pm 5.2$	$4.6 \pm 0.4$	$1.1 \pm 0.4$	$2.8 \pm 0.8$	$1.1 \pm 0.4$	$59.4 \pm 7.9$	$2.6 \pm 1.2$	$5.1 \pm 2.3$	$0.1 \pm 0.1$
$M_2C$ centre	90–100	$22.0 \pm 3.1$	$5.0 \pm 0.5$	$1.0 \pm 0.4$	$2.4 \pm 0.5$	$1.1 \pm 0.2$	$61.0 \pm 2.6$	$2.7 \pm 0.6$	$4.7 \pm 0.3$	$0.0 \pm 0.1$
$M_2C$ right side	140–150	$23.1 \pm 2.6$	$4.4 \pm 0.6$	$1.3 \pm 0.4$	$3.0 \pm 0.6$	$1.0 \pm 0.2$	$58.7 \pm 4.4$	$2.8 \pm 0.6$	$5.4 \pm 1.5$	$0.0 \pm 0.0$
	Mean value	22.6	4.7	1.1	2.7	1.1	59.7	2.7	5.0	0.1

rates are considered. In order to elucidate the solidification sequence of a Gr-HSS grade, the distribution, chemical composition and morphological features of the phases present in the microstructure are correlated with the corresponding peaks observed using both DTA and DDTA curves (Fig. 2).

As shown in Fig. 2, six peaks were identified using the first derivative. The peaks observed at higher temperatures (H4, H5 and H6) are related to the matrix and the MC carbides. The H1, H2 and H3 peaks are related to the other ECs and to graphite.

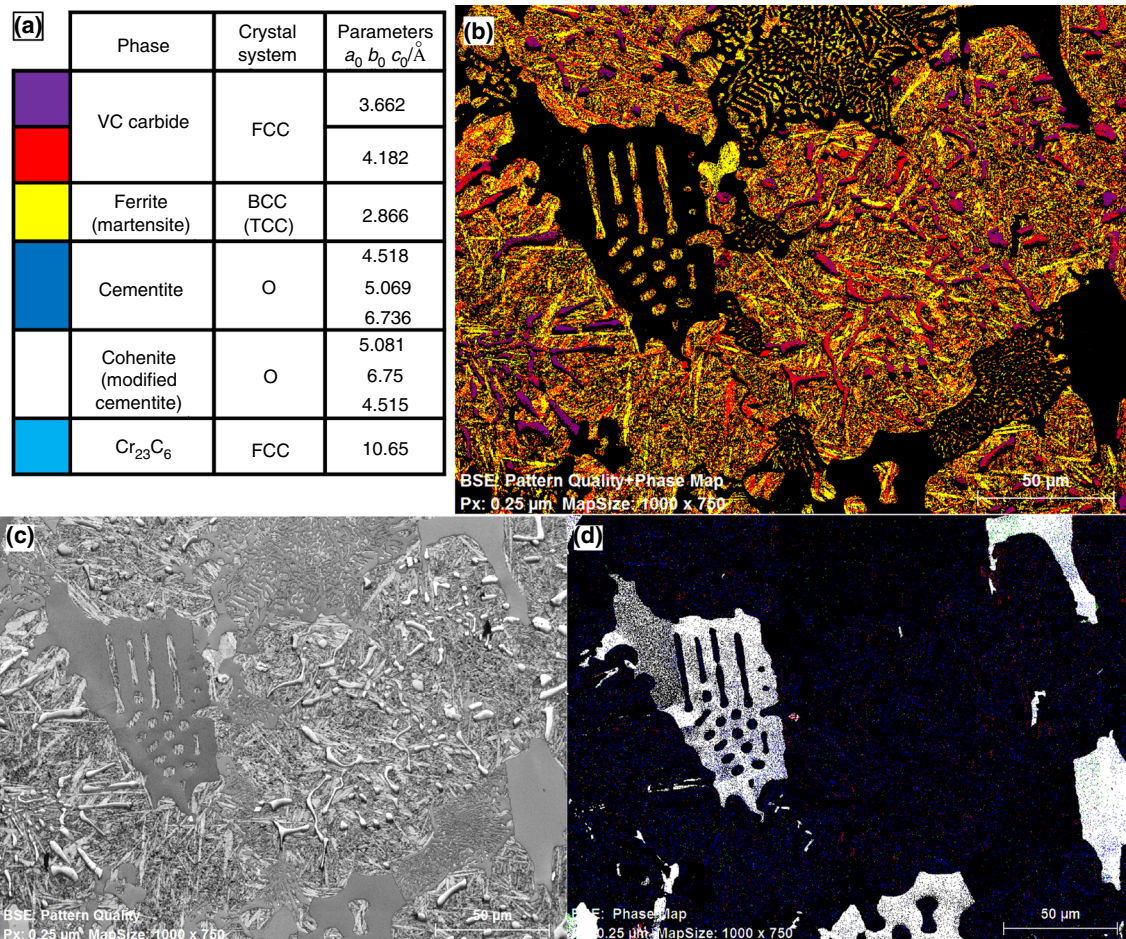


**Fig. 6** **a** Phase considered for the EBSD analysis with the relative lattice characteristics; **b** EBSD phase map showing the matrix (martensite) and VC carbides; **c** image quality (IQ) map; and **d** EBSD phase map showing eutectic MC and fine  $\text{M}_{23}\text{C}_6$  secondary carbides

The solidification starts at the liquidus temperature (peak H6) that corresponds to the formation of primary MC carbides, uniformly distributed in the microstructure (Fig. 1). Their homogeneous distribution may also be linked to the spin-casting process, as primary MC is free to move within the melt [1, 9]. The enlarged shape of the DTA peaks associated with the MC carbides can be related to their chemical composition that varies over a wide range, especially for transition elements such as V, Mo and Nb (Table 3 and Fig. 4). It is well established that the principal carbide-forming element of primary MC may change during their formation, since some carbides may act as nuclei for other carbides with different compositions [7, 45].

The second constituent (peak H5) formed during the solidification of a Gr-HSS alloy is made of MC coral-like PPC associated with intracellular austenite ( $\gamma$ ), by a process of cooperative growth (Fig. 3). This process leads to a gradient of composition for transition elements from the core to the boundary of the cell [9]. Due to their size and to

the time necessary for their formation, this chemical gradient presents a higher scattering for PPCs than for PCs as observed from EDS analyses (Table 3) [9, 24, 54]. Small  $\gamma$  cells free of carbides can also be found, corresponding to secondary or tertiary dendrite arms that formed after the primary cells containing the PPCs (Fig. 3). The broad shape of the peaks associated with the PPC +  $\gamma$  cells (Fig. 2 and Table 2) thus corresponds to a large chemical gradient (Table 3). This takes into account not only the formation of the main cells or dendrites made of PPCs +  $\gamma$ , but also the subsequent formation of secondary dendrite arms  $\gamma$ , some of which are PPC-free.

The third phase to form corresponds to a few small NbC carbides (peak H4) that precipitate directly within the remaining liquid in the intercellular regions. Residual Nb that has not been retained into previously formed PPCs tends to segregate in the remaining liquid. PPCs thus exhibit a composition gradient with the centre part poorer in Nb than the tips (Table 3). This phenomenon corresponds to

micro-segregations commonly observed during spin casting [2, 7, 45]. The globular morphology of NbC carbides is related to the low carbon content of the residual liquid. Indeed, higher amount of carbon has been shown to promote the Chinese script morphology for NbC carbides [54]. Besides, the solidification rate can also influence the shape of these NbC carbides [1].

$M_3C$  carbide is the fourth phase to precipitate during the solidification. It corresponds to the first eutectic mixture that is represented by  $M_3C + \gamma$ . This constituent is located in the intergranular areas. The sharpness of peak H3 (in the temperature range between 1124 and 1131 °C) corresponding to this carbide is correlated with its narrow and homogeneous composition (Table 4) [10, 21, 24].

Free nodular graphite appears in the fifth position in the solidification sequence of Gr-HSS. At this stage, the residual intercellular liquid is enriched with both C and Si, while other elements such as Nb, V and Cr have already been retained in the previously formed carbides [1, 2, 21, 24, 44]. The sharpness of the related H2 peak (1115–1121 °C) is in good agreement with the very narrow composition of graphite nodules that are only made of carbon (Fig. 4) [27, 28, 44]. This result is consistent with other studies establishing that graphite solidification occurs as a result of a specific composition of the residual liquid. Graphite formation occurs when Mo content is low. Conversely, for higher amount of Mo in the residual liquid, the graphitizing effect of Si will be inhibited, thus leading to the formation of  $M_2C$  carbide at lower temperatures [2, 24, 27, 37].

A sixth phase is formed at the end of the solidification sequence (solidus point) of Gr-HSS. It corresponds to  $M_2C$  EC located in the intercellular regions. Indeed,  $M_2C$  carbide appears to envelop the extremities of the pre-existing  $M_3C$  carbide (Fig. 3). The H1 peak corresponding to the formation of  $M_2C$  is sharp, but it is wider than the H3 peak related to  $M_3C$ . The slightly wider temperature range for the DTA H1 peak (1088–1109 °C) compared to the DTA H3 peak is consistent with the chemical composition of the  $M_2C$  carbide, which exhibits some slight heterogeneity between the core and the edge (Fig. 5 and Table 5). In addition to Fe and Mo that are expected in the composition of the  $M_2C$  carbide, there is an abnormally high Si content together with relatively low amounts of V, Nb and Cr (Table 5). High cooling rates can promote the formation of  $M_2C$  carbide with unusually high amount of Si [9, 51, 56]. Therefore, it can be assumed that either the solidification sequence or the cooling rates achieved during the spin-casting process make it possible to precipitate a Si-rich  $M_2C$  EC as the last solid.

The different reactions that occur during the solidification of Gr-HSS and which are considered in their chronological order of appearance, are summarized in Table 6. The schematics of the solidification sequence are illustrated in Fig. 7.

## Influence of casting route on the composition and the crystallography of carbides

The relevance of the EBSD results depends both on pattern quality and on the content of the XRD databases. For instance, the tempered martensite matrix has been easily indexed as a BCC lattice that represents ferrite [16]. Even if martensite has a tetragonal structure, its crystal lattice will fit the crystal lattice of ferrite as long as distortions due to carbon supersaturation and to the presence of dislocations remain weak [46]. This is the reason why tempering is carried out on fresh martensite, so as to allow stress relief together with the completion of the transformation of the retained austenite. The characterization of the carbides of the Gr-HSS is more complex. Three types of solidification carbides have been found, i.e. MC,  $M_3C$  and  $M_2C$ . This list corresponds to the chronological order of formation during solidification.

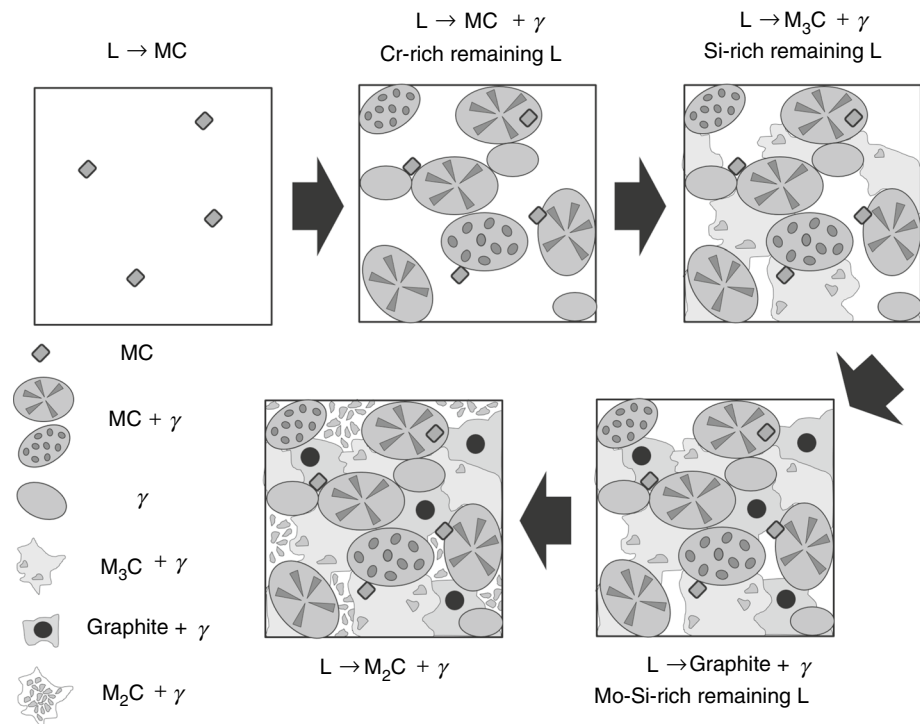
The characterization of MC carbide using EBSD analyses is straightforward, regardless of its composition and morphology. MC carbides match with a FCC lattice that is sometimes mistaken for austenite [46]. The chemical composition gradient that exists in this carbide does not seem to affect the EBSD pattern quality. Therefore, it can be assumed that FCC lattice is not disturbed by the arrangement of the different atoms that enter in the composition of MC.

For the  $M_3C$  carbide, the EBSD pattern quality ranges between average and good (Fig. 6c). Small discrepancies in contrast are assumed to arise from the differences in elastic strains which are more or less uniformly distributed both among carbides and inside the crystal lattice of a given carbide [52]. Where the elastic strain is homogeneous, corresponding to a bright pattern quality, the so-called cohenite fits better the lattice of the  $M_3C$  carbide than the expected cementite. When the elastic strain is heterogeneous (no longer satisfying the Bragg condition), the analysis is less accurate [16, 46]. Both cementite and cohenite have similar crystallographic lattices, but with different lattice parameters (Fig. 6a). Overall, the cohenite fits the lattice of the  $M_3C$  carbide, with some traces of cementite and some undefined areas. Furthermore, taking into account the high cooling rate achieved during solidification, more elements can be retained within the carbide lattice compared to equilibrium conditions, as indeed confirmed by the observed chemical composition (Fig. 4 and Table 3). This leads to the formation of cementite with modified lattice parameters. Similar results have been obtained by many researchers for various types of carbides [4, 6, 17, 54].

For the  $M_2C$  carbide, the brighter contrast on IQ map (Fig. 6c) suggests a better detection than for the  $M_3C$  carbide. However, none of the three lattices available in the database for this type of carbide, namely hexagonal, orthorhombic or monoclinic [15, 22, 55, 56], is suitable for

**Table 6** List of the peaks related to the DTA curves of Fig. 2, with the corresponding phase transformations

Reaction number	DTA peak	Nature and location of the phase transformation	Type of the reaction
1	H6	Direct precipitation of globular V-rich carbides within the melt as the first solid to form (liquidus)	$L_0 \rightarrow MC^0 (+L_1)$
2	H5	Nucleation and growth of dendrites/cells made of V-rich coral-like $MC + \gamma$ Some secondary dendrites may correspond to carbide-free $\gamma$	$L_1 \rightarrow MC^1 + \gamma_1 (+L_2)$ $L_2 \rightarrow \gamma_2 (+L_3)$
3	H4	Direct precipitation of Nb-rich globular $MC$ carbides, close to cells boundaries	$L_3 \rightarrow MC^2 (+L_4)$
4	H3	Eutectic reaction leading to the formation of $M_3C$ at cell boundaries (first eutectic carbide)	$L_4 \rightarrow M_3C/\gamma_3 (+L_5)$
5	H2	Direct precipitation of nodular graphite in intercellular regions	$L_5 \rightarrow Graphite (+L_6)$
6	H1	Last eutectic reaction leading to the formation of $M_2C$ at cell boundaries (second eutectic carbide = solidus)	$L_6 \rightarrow M_2C/\gamma_4$

**Fig. 7** Schematics of the Gr-HSS solidification sequence during the fast cooling ( $100\text{--}300\text{ }^\circ\text{C min}^{-1}$ )

its identification. Therefore, it is assumed that the distortion of the  $M_2C$  carbide lattice is strong enough to prevent matching with any existing structure. The bright grey shade of the carbides in the pattern quality image (Fig. 6c) reveals that this distortion of the lattice is uniform, satisfying the Bragg condition and leading to a good detection [52]. As reported in Table 5, the anomalous Si content (4–5 in atomic%) and the unexpected low C and high Fe amounts could disturb the arrangement of the crystal structure from the classical  $M_2C$  carbide lattices to an unknown one. The chemical composition of the very last remaining liquid, together with the high cooling rates achieved during spin casting, may lead to the substitution of smaller C atoms by larger Si atoms and in turn cause a homogeneous elastic strain within the lattice

[56]. The stoichiometry formula of this carbide is considered as a  $(Fe, Mo)_2(C, Si)$ .

From the above considerations,  $M_2C$  carbide was assumed to be metastable with a supersaturated crystal lattice. A destabilization treatment ( $1025\text{ }^\circ\text{C}/60'/\text{calm air}$ ) has been carried out in order to validate the assumption of the supersaturation of Si and Mo in the  $M_2C$ . The main results of microstructural characterization after this destabilization treatment are illustrated in Fig. 8. The initial carbide undergoes a decomposition phenomenon, as already reported in numerous studies [3, 4, 8, 17]. The destabilized carbide presents a different chemical composition due to the decrease in C, Mo and Si contents, resulting in a darker contrast in BSE image, compared to the brighter initial carbide (Fig. 8a).

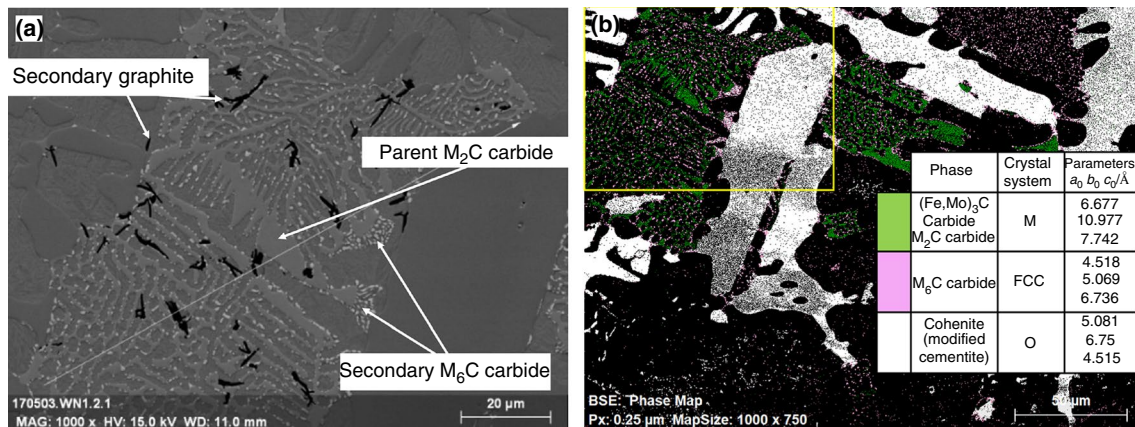


**Fig. 8** **a** Close-up view of the framed region of the EBSD map, exhibiting fine secondary M<sub>6</sub>C carbides (white) and secondary graphite (black) at the interfaces between the parent M<sub>2</sub>C carbide (light

grey) and the matrix (BSE mode). **b** EBSD phase map enhancing the phases involved in the decomposition phenomenon (except graphite) and the M<sub>3</sub>C carbide, with the related legend

However, the decomposition observed in the Gr-HSS alloy is different from the previous results in the literature. Indeed, the reaction products present free lamellar secondary graphite, in addition to the expected Mo-rich M<sub>6</sub>C carbides. This has not been mentioned elsewhere. The new decomposition reaction can therefore be written as follows:



M<sub>6</sub>C carbides are clearly identified as such after EBSD analysis. Moreover, the EBSD pattern of the decomposed M<sub>2</sub>C carbide now fits the base-centred monoclinic (BCM) lattice (Fig. 8b). The increased cooling rates achieved during solidification are thus assumed to promote a freezing of alloying elements in the pro-eutectic liquid. When eutectic carbides are formed under such conditions, they can exhibit crystal lattices that are different from those expected under equilibrium conditions. Depending on the size, the type and the location of a given atom in the supersaturated carbide lattice, more or less distortion can arise, thus influencing the pattern quality for subsequent EBSD investigation.

## Conclusions

- The connection between the characteristics of a microstructure formed at high cooling rates and the relative DTA heating curve at lower scan was verified. Taking into account the chemical characteristics of the phases and their position in the microstructure, it is possible to associate phases and DTA peaks. Moreover, the use of the first derivative of the DTA curve helps to interpret

complex peaks associated with either several different phases or a large range of compositions for a given phase.

- The solidification sequence of a graphitic high-speed steel (Gr-HSS) at high cooling rate can be assumed as follows: MC carbide, MC carbide + matrix, M<sub>3</sub>C carbide, graphite (in nodules) and M<sub>2</sub>C carbide.
- The characterization of the microstructure revealed the presence of anomalous M<sub>2</sub>C carbide with a high Si content (4–5% in atomic percentage). The morphology of these M<sub>2</sub>C carbides may vary, depending on changes in its composition.
- The consequences of the high cooling rates achieved during spin casting were evaluated by microscopy and EBSD analyses. ECs exhibit modified lattice parameters and anomalous compositions. Cementite (M<sub>3</sub>C carbide) was identified as cohenite (with a similar lattice but different lattice parameters) due to the modification of the lattice parameters by solute atoms as V and Mo. In the case of the M<sub>2</sub>C carbide, the analysis could not identify the lattice of the phase with any existing phase in the databases. The distortion of the lattice of the M<sub>2</sub>C carbide is explained by its supersaturation due to the high cooling rate and undercooling. This leads to the modification of the lattice parameters by Si and Fe atoms.

**Acknowledgements** The authors acknowledge the CAREM of the ULiège for providing SEM/EDS/EBSD facilities. They also wish to kindly thank the retired professor Jacqueline Lecomte-Beckers for all the chances and the inspiration that she offered to the MMS unit.

**Funding** This work has been supported by the Service Public de Wallonie (ENDEFINU project—Grant Number 6929).

## References

- Lecomte-Beckers J, Tchuindjang JT. Structural investigations of solidification and heat treatments influence on high alloyed cast irons grades with Nb–V–Ti additions. *Defect Diffus Forum Ser.* 2009;289–292:77–86.
- Cole GS. Inhomogeneities and their control via solidification. *Metall Trans.* 1971;2:357–70.
- Hashimoto M, Kubo O, Matsubara Y. Analysis of carbides in multi-component white cast iron for hot rolling mill rolls. *ISIJ Int.* 2004;44:372–80.
- Chen L, Pei J, Li F, Zhang Y, Wang M, Ma X. Decomposition reaction of metastable  $M_2C$  carbide in a multi-component semi-high-speed steel. *Metall Mater Trans A Phys Metall Mater Sci.* 2016;47:5662–9.
- Lecomte-Beckers J, Sinnaeve M, Tchuindjang JT. Current developments of alloyed steels for hot strip roughing mills—characterization of high chromium steel and semi high speed steel. *Iron Steel Technol.* 2012;9:33–40.
- Boccalini M, Goldenstein H. Solidification of high speed steels. *Int Mater Rev.* 2001;46:92–115.
- Fischmeister HF, Riedl R, Karagöz S. Solidification of high-speed tool steels. *Metall Trans A.* 1989;20:2133–48.
- Ding P, Shi G, Zhou S. As-cast carbides in high-speed steels. *Metall Trans A.* 1993;24:1265–72.
- Luan Y, Song N, Bai Y, Kang X, Li D. Effect of solidification rate on the morphology and distribution of eutectic carbides in centrifugal casting high-speed steel rolls. *J Mater Process Technol.* 2010;210:536–41.
- Coronado JJ, Sinatora A. Abrasive wear study of white cast iron with different solidification rates. *Wear.* 2009;267:2116–21.
- Delaunoy F, Stanciu VI, Sinnaeve M. Resistance to high-temperature oxidation and wear of various ferrous alloys used in rolling mills. *Metall Mater Trans A.* 2018;49:822–35. <https://doi.org/10.1007/s11661-017-4450-x>.
- Tchoufang Tchuindjang J, Lecomte-Beckers J. Study of the origin of the unexpected pearlite during the cooling stage of two cast high-speed steels. *Solid State Phenom.* 2011;172–174:803–8.
- Tchuindjang JT, Torres IN, Flores P, Habraken AM, Lecomte-beckers J. Phase transformations and crack initiation in a high-chromium cast steel under hot compression tests. *J Mater Eng Perform.* 2015;24:2025–41.
- Luan YK, Song NN, Kang XH, Lee DZ. A study of the carbides in high-speed steel rolls. *Mater Sci Forum.* 2010;638–642:3356–61.
- Guo J, Liu L, Feng Y, Liu S, Ren X, Yang Q. Crystallographic characterizations of eutectic and secondary carbides in a Fe–12Cr–2.5Mo–1.5W–3V–1.25C alloy. *Met Mater Int.* 2017;23:313–9.
- Trepczyńska-Lent M. XRD and EBSD measurements of directional solidification Fe–C eutectic alloy. *Arch Foundry Eng.* 2016;16:169–74.
- Hwang KC, Lee S, Lee HC. Effects of alloying elements on microstructure and fracture properties of cast high speed steel rolls: part I: microstructural analysis. *Mater Sci Eng A.* 1998;254:282–95.
- Wieczorzak K, Bala P, Stepien M, Cios G, Koziel T. Formation of eutectic carbides in Fe–Cr–Mo–alloy during non-equilibrium crystallization. *Mater Des.* 2016;94:61–8. <https://doi.org/10.1016/j.matdes.2016.01.028>.
- Imurai S, Thanachayanont C, Pearce JTH, Tsuda K, Chairuangstri T. Effects of Mo on microstructure of as-cast 28 wt% Cr–2.6 wt% C–(0–10) wt% Mo irons. *Mater Charact.* 2014;90:99–112. <https://doi.org/10.1016/j.matchar.2014.01.014>.
- Ghaderi AR, Nili Ahmadabadi M, Ghasemi HM. Effect of graphite morphologies on the tribological behavior of austempered cast iron. *Wear.* 2003;255:410–6.
- Villanueva Bravo S, Yamamoto K, Miyahara H, Ogi K, Bravo SV, Yamamoto K, et al. Control of carbides and graphite in Ni-hard type cast iron for hot strip mills. *Mater Sci Forum.* 2007;561–565:1023–6.
- Zhou XF, Fang F, Li F, Jiang JQ. Morphology and microstructure of  $M_2C$  carbide formed at different cooling rates in AISI M2 high speed steel. *J Mater Sci.* 2011;46:1196–202.
- Bleckmann M, Gleinig J, Hufenbach J, Wendrock H, Giebeler L, Zeisig J, et al. Effect of cooling rate on the microstructure and properties of FeCrVC. *J Alloys Compd.* 2015;634:200–7. <https://doi.org/10.1016/j.jallcom.2015.02.004>.
- Villanueva Bravo S, Yamamoto K, Miyahara H, Ogi K. Control of carbides and graphite in cast irons type alloy's microstructures for hot strip mills. *J Metall.* 2012;2012:1–6.
- Yamamoto K, Kubota T, Murai N, Ogi N. Solidification process and crystallization of graphite in high carbon high speed steel type alloy. *J Japan Foundry Eng Soc.* 1998;70:786–92.
- Barkalow RH, Kraft RW, Goldstein JL. Solidification of M2 high speed steel. *Metall Trans.* 1972;3:919–26.
- Pietrowski S, Gumienny G. Microsegregation in nodular cast iron with carbides. *Arch Foundry Eng.* 2012;12:127–34.
- Rashidi MM, Idris MH. The effects of solidification on the microstructure and mechanical properties of modified ductile Ni-resist iron with a high manganese content. *Mater Sci Eng A.* 2014;597:395–407. <https://doi.org/10.1016/j.msea.2013.12.070>.
- Klančnik U, Habjan J, Klančnik G, Medved J. Thermal analysis of indefinite chill cast iron modified with ferrovanadium and ferrotungsten. *J Therm Anal Calorim.* 2017;127:1–8.
- Guo E, Wang L, Feng Y, Wang L, Chen Y. Effect of cooling rate on the microstructure and solidification parameters of Mg–3Al–3Nd alloy. *J Therm Anal Calorim.* 2019;135:2001–8. <https://doi.org/10.1007/s10973-018-7446-x>.
- Drozdová L, Smetana B, Zlá S, Novák V, Kawuloková M, Rosypalová S, et al. Study of phase transformation temperatures of alloys based on Fe–C–Cr in high-temperature area. *J Therm Anal Calorim.* 2018;133:41–8. <https://doi.org/10.1007/s10973-018-7012-6>.
- Gajavalli K, Mikaelian G, Barrachin M, Decreton A, Fischer E, Rogez J, et al. Interrupted heating DTA for liquidus temperature determination of Ag–Cd–In alloys. *J Therm Anal Calorim.* 2019;135:2209–19. <https://doi.org/10.1007/s10973-018-7442-1>.
- Roca AS, Fals HDC, Zoqui EJ. In situ differential thermal analysis device for evaluating high-speed phase transitions. *J Therm Anal Calorim.* 2018;134:1589–97. <https://doi.org/10.1007/s10973-018-7629-5>.
- Steiner Petrovič D, Klančnik G, Pirnat M, Medved J. Differential scanning calorimetry study of the solidification sequence of austenitic stainless steel. *J Therm Anal Calorim.* 2011;105:251–7.
- Mostafapoor S, Malekan M, Emamy M. Effects of Zr addition on solidification characteristics of Al–Zn–Mg–Cu alloy using thermal analysis. *J Therm Anal Calorim.* 2018;134:1457–69. <https://doi.org/10.1007/s10973-018-7426-1>.
- Boettinger WJ, Kattner UR, Moon K-W, Perepezko JH. Dta and heat-flux DSC measurements of alloy melting and freezing. In: *Methods for phase diagram determination.* Elsevier Science Ltd; 2007. p. 151–221.
- Boccalini M Jr, Corrêa AVO, Goldenstein H. Rare earth metal induced modification of  $\gamma$ - $M_2C$ ,  $\gamma$ - $M_6C$ , and  $\gamma$ -MC eutectics in cast M2 high speed steel. *Mater Sci Technol.* 1999;15:621–6.
- Jabłońska M, Maciąg T, Nowak M, Rzychoń T, Czerny M, Kowalczyk K. Thermal and structural analysis of high-tin bronze of chemical composition corresponding to the composition of the singing bowl. *J Therm Anal Calorim.* 2019;137:735–41. <https://doi.org/10.1007/s10973-019-08015-z>.

39. Król M, Staszuk M, Mikuszewski T, Kuc D. Refinement effect of RE in light weight Mg–Li–Al alloys. *J Therm Anal Calorim.* 2018;134:333–41. <https://doi.org/10.1007/s10973-018-7290-z>.
40. Sinatora A, Albertin E, Matsubara Y. An investigation of the transition from  $M_7C_3$  to  $M_3C$  carbides in white cast irons. *Int J Cast Met Res.* 1996;9:9–15.
41. Lentz J, Röttger A, Theisen W. Solidification and phase formation of alloys in the hypoeutectic region of the Fe–C–B system. *Acta Mater.* 2015;99:119–29. <https://doi.org/10.1016/j.actamat.2015.07.037>.
42. Paar A, Elizondo L, Brandner M, Trickl T, Sonderegger B, Beal C, et al. Application of thermo-calc TCFE7 to high-alloyed mottled cast iron. *Mater Sci Forum.* 2016;879:1431–6.
43. Laigo J, Christien F, Le Gall R, Tancret F, Furtado J. SEM, EDS, EPMA-WDS and EBSD characterization of carbides in HP type heat resistant alloys. *Mater Charact.* 2008;59:1580–6.
44. Rivera G, Calvillo PR, Boeri R, Houbaert Y, Sikora J. Examination of the solidification macrostructure of spheroidal and flake graphite cast irons using DAAS and EBSD. *Mater Charact.* 2008;59:1342–8.
45. Filipovic M, Kamberovic Z, Korac M, Gavrilovski M. Microstructure and mechanical properties of Fe–Cr–C–Nb white cast irons. *Mater Des.* 2013;47:41–8. <https://doi.org/10.1016/j.matdes.2012.12.034>.
46. Godec M, Batič BŠ, Mandrino D, Nagode A, Leskovšek V, Škapin SD, et al. Characterization of the carbides and the martensite phase in powder-metallurgy high-speed steel. *Mater Charact.* 2010;61:452–8.
47. García De Andrés C, Caballero FG, Capdevila C, Álvarez LF. Application of dilatometric analysis to the study of solid-solid phase transformations in steels. *Mater Charact.* 2002;48:101–11.
48. Hayoune A, Hamana D. Structural evolution during non-isothermal ageing of a dilute Al–Cu alloy by dilatometric analysis. *J Alloys Compd.* 2009;474:118–23.
49. Ceipidor UB, Brizzi E, Bucci R, Magrí AD. Using thermoanalytical data. Part 7. DSC/DTA/DTG peak shapes depending on operational settings, equipment features, sample kinetic and thermodynamic parameters. *Thermochim Acta.* 1994;247:347–56.
50. Moukhina E, Kaisersberger E. Temperature dependence of the time constants for deconvolution of heat flow curves. *Thermochim Acta.* 2009;492:101–9.
51. Jiang L, Zhang W-ZZ, Xu Z-FF, Huang H-FF, Ye X-XX, Leng B, et al.  $M_2C$  and  $M_6C$  carbide precipitation in Ni–Mo–Cr based superalloys containing silicon. *Mater Des.* 2016;112:300–8.
52. Wright SI, Nowell MM. EBSD image quality mapping. *Microsc Microanal.* 2006;12:72–84.
53. Keller LP. A transmission electron microscope study of iron-nickel carbides in the matrix of the Semarkona unequibrated ordinary chondrite. *Meteorit Planet Sci.* 1998;33:913–9.
54. Li XW, Wang L, Dong JS, Lou LH. Effect of solidification condition and carbon content on the morphology of MC carbide in directionally solidified nickel-base superalloys. *J Mater Sci Technol.* 2014;30:1296–300.
55. Velikanova TA, Karpets MV, Artyukh SU, Balanetskii SO, Petyukh VM, Agraval PG, et al. Projection of the solidus surface of the Fe–Mo–C system in the composition range 0–40 at.% C. *Powder Metall Met Ceram.* 2011;50:1–10.
56. Jiang L, Ye XX, Wang ZQ, Yu C, Dong JS, Xie RB, et al. The critical role of Si doping in enhancing the stability of  $M_6C$  carbides. *J Alloys Compd.* 2017;728:917–26. <https://doi.org/10.1016/j.jallcom.2017.09.042>.

**Publisher's Note** Springer Nature remains neutral with regard to jurisdictional claims in published maps and institutional affiliations.



# Microstructural and Thermal Characterization of 316L + WC Composite Coatings Obtained by Laser Cladding

Tommaso Maurizi Enrici, Olivier Dedry, Frédéric Boschini, Jérôme Tchoufang Tchuindjang, and Anne Mertens\*

Herein, a metal matrix composite (MMC) composed of 316L stainless steel and 20% in volume of tungsten carbides (WC), fabricated by laser cladding (LC) is considered. LC is an additive manufacturing technique, characterized by ultrafast cooling rates and limited diffusion, thus giving rise to out-of-equilibrium microstructures. The microstructure of the MMC is found to consist of partially dissolved WC well distributed in an austenitic matrix reinforced by a network of reaction carbides. Those mixed reaction carbides are formed from a liquid enriched in W and C due to the dissolution of the original WC in contact with the molten metal during deposition. Distribution, chemical composition, crystallographic features, and stability of the different phases are characterized in details by combining electron microscopy, electron backscattered diffraction, and dilatometry. This combination of techniques allows to distinguish among  $M_6C$ ,  $M_{23}C_6$ ,  $M_4C$ , and  $WC_{1-x}$  carbide, belonging to the Fe–W–C system and all exhibiting a face-centered cubic lattice. Moreover, results of reverse thermal analyses are considered together with microstructural data to elucidate the genesis of this complex microstructure, differentiating the phases formed in the melt pool, in the vicinity of partially dissolved WC and in the heat-affected zone between two successive tracks.

thus leaving behind a coating or object. LC involves ultrafast cooling rates during the solidification stage and subsequent solid-state transformations with limited diffusional phenomena, thus giving rise to out-of-equilibrium phases.<sup>[1–3]</sup>

Stainless steel (SS) 316L is a workhorse material due to its excellent corrosion resistance and good mechanical properties, but it exhibits a relatively weak wear resistance. To improve on this weakness, metal matrix composite (MMC) coatings could be applied by LC.<sup>[1,2,4]</sup> Tungsten carbide (WC) is a common reinforcement in Ni-based alloys for applications above 600 °C and in Fe-based alloys for applications up to 400 °C.<sup>[1,3,5,6]</sup> WC is considered a good ceramic reinforcement due to its high melting point and good wettability with both alloys.<sup>[6]</sup> Moreover, WC can retain its room temperature hardness up to 1400 °C. Its dissolution by interfacial reactions with the molten metal during casting is a well-known challenge in the production of metal matrix composites. These physical

## 1. Introduction


Additive manufacturing (AM), and in particular laser cladding (LC), is a suitable technique for the manufacturing of metal coatings, allowing for a large variability in raw materials. In LC, a stream of powder, or a mixture of different powders, is fed into a focused laser beam while being scanned across a substrate,

and chemical interactions reinforce the matrix, leading to the formation of hard solidification carbides (SCs) and connection layers around the partially dissolved WC particles linking them to the matrix.<sup>[7,8]</sup> The initial size distribution of the WC powders determines the quantity of SCs and of partially dissolved WC carbides. Small particles tend to dissolve completely, whereas larger ones dissolve only partially, leaving their cores in the final microstructure.<sup>[8]</sup> In addition, the spherical or globular morphology of the reinforcements increases their stability in contact with the molten metal and decreases the cracking behavior during deposition.<sup>[2,5]</sup> Conversely, an elevated chemical affinity of the reinforcements with the matrix strongly decreases their presence at the end of the deposition.<sup>[3,6]</sup> The properties of the coating are directly linked to the nature, the stability, and the mechanical properties of the new out-of-equilibrium phases produced by the interactions between the original particles and the matrix.<sup>[5,8,9]</sup>

Previous studies on WC-reinforced composites have focused on feasibility issues,<sup>[4,10]</sup> on the influence of the feedstock<sup>[5,8]</sup> and the mechanical properties.<sup>[1–3]</sup> However, there are very few studies focusing on the nature of the carbides formed in the microstructure of those composites, when the solidification is

T. Maurizi Enrici, O. Dedry, J. T. Tchuindjang, Prof. A. Mertens  
 Metallic Materials Science (MMS)  
 A&M Department  
 University of Liège  
 Quartier Polytech 1, Allée de la Découverte 13A (B52), 4000 Liège, Belgium  
 E-mail: anne.mertens@uliege.be

Dr. F. Boschini  
 GREnMat Laboratory  
 University of Liège  
 Allée du 6 août, 13 (B6a), 4000 Liège, Belgium

 The ORCID identification number(s) for the author(s) of this article can be found under <https://doi.org/10.1002/adem.202000291>.

DOI: 10.1002/adem.202000291

achieved at extremely high cooling rates. The main difficulties are found in the identification and the differentiation of those new mixed carbides. Indeed, according to the phase diagrams for the binary W–C and the ternary Fe–W–C systems,<sup>[11,12]</sup> a number of metastable phases exist, exhibiting a certain polymorphism, i.e., (Fe,W)<sub>4</sub>C, (Fe,W)<sub>6</sub>C, (Fe,W)<sub>12</sub>C, and (Fe,W)<sub>23</sub>C<sub>6</sub>.<sup>[9,13,14]</sup> Indeed, those various carbides and the austenite adopt a face-centered cubic (FCC) symmetry with similar space groups (i.e., Fd-3m, Fd-3s, and Fm-3m) and exhibit only small differences in lattice parameters, leading to uncertainties in microstructural analysis.<sup>[7–10,15,16]</sup> Moreover, the high cooling rates prevailing during LC may increase the difficulty in differentiating the phases, as metastable phases may be formed at room temperature due to the limited diffusional phenomena, whereas the classical lattice parameters of stable phases may be modified due to chemical super saturation.<sup>[11,12,14,15,17–19]</sup>

In this work, the mixed carbides present in a MMC composed of SS316L and 20% in volume of WC are identified. Furthermore, the microstructural genesis is elucidated distinguishing the phases formed by direct solidification from the liquid and the ones formed by local reheating in the heat-affected zone (HAZ). Indeed, in laser-based manufacturing processes, the deposition of a new track or layer is known to alter locally the microstructure of the substrate or previous layer(s) in a zone that is reheated in a temperature range below the melting temperature.<sup>[20,21]</sup> Two methods

will be combined, namely scanning electron microscopy combined with electron backscattered diffraction (SEM + EBSD) to identify the complex carbides, and differential thermal analysis (DTA) to restore the solidification sequence by means of a reverse analysis carried out on reheating. This approach that had been developed to elucidate the microstructural genesis of a complex graphitic high-speed steel (HSS) processed by centrifugal casting has proven efficient to identify the phases present in such complex out-of-equilibrium microstructures obtained at higher cooling rates and to gain insights in their formation.<sup>[17]</sup> The microstructure within the melt pool (MP) will be differentiated from the microstructure present in the HAZ, as the latter is known to strongly influence mechanical properties.<sup>[20–23]</sup>

## 2. Results

### 2.1. Microstructure of the Clad 316L + WC Composite

The microstructure of the metal matrix composite is shown in **Figure 1a**. Partially dissolved WC particles are well distributed in an austenitic matrix reinforced by a network of reaction carbides. The formation of those new SCs (W, Cr)<sub>x</sub>C<sub>y</sub> results from partial or total dissolution of the original WC particles (Figure S1b, Supporting Information) within the metal matrix.<sup>[3,8,10]</sup> The HAZ is highlighted by the presence of

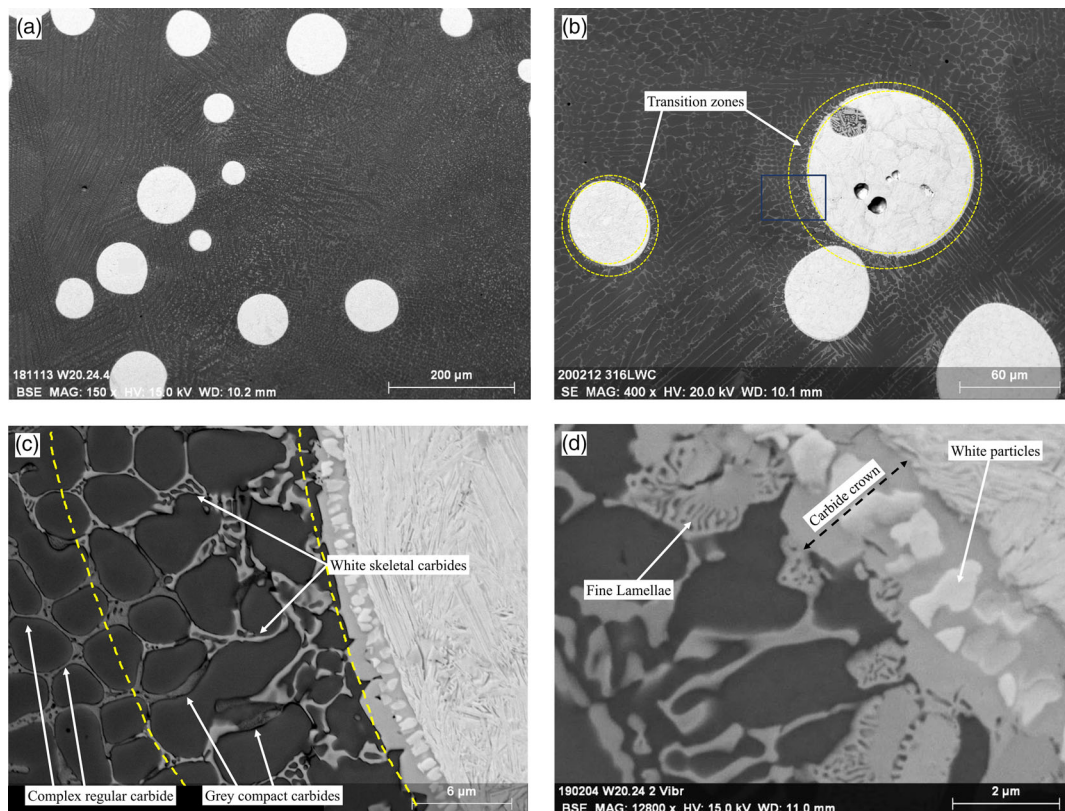


**Figure 1.** a) SEM micrograph of the 316L + 20%WC composite. Partially dissolved WC carbides (bright circles) are homogeneously dispersed in a reinforced matrix. b) Overview of the microstructure of the 316L + 20%WC composite with a focus on partially dissolved WC carbide (light gray) and the surrounding TZs. c) Close-up view of (b) showing the solidification carbides formed in the TZ of the partially dissolved WC particle. d) Higher-magnification close-up view of (c) showing the structure of the carbide crown and the fine lamellar morphology of the carbide crystals.

brighter-modified solidification carbides. The microstructures of the MP and the WC powders are considered in Section 2.1.1, whereas the nature of SCs in the HAZ and MP is further analyzed based on high-magnification EBSD observations in Section 2.1.2.

### 2.1.1. Microstructure of the MP

In Figure 1b, a cellular-dendritic-reinforced microstructure surrounds a partially dissolved WC located inside the MP of the composite. Observing closely the cross section of the partially dissolved WC, a “carbide crown” comprising large carbide crystals together with some internal white particles is observed around the undissolved WC core (Figure 1d). The thickness of the carbide crown is around 3 μm and decreases with increasing size of the WC. Energy dispersion X-ray spectrometry (EDS) analyses (Table 1) show that the white particles in the carbide crown have a high W content. The internal crown is richer with W and C than the external part, whereas the external part is richer with Fe and Cr than the internal part. The carbide crown may also exhibit very fine lamellae (Figure 1d).

As shown in Figure 1c, white skeletal carbides and gray compact carbides are observed in a transition zone (TZ) between the carbide crown and the MP. The white carbides exhibit a relatively high W content, while the gray carbides exhibit a high Cr content. In the skeletal morphology, large eutectic spaces can be observed.<sup>[24]</sup> This morphology leads to a higher contribution from the matrix in the interaction volume in comparison with the compact morphology of the gray carbide.<sup>[25]</sup> Indeed, the composition of the skeletal carbide (Table 1) exhibits high standard deviation for many elements and a remarkable Fe and Ni content. In the TZ, the matrix exhibits a particularly high content of W, higher than the W content of the gray carbide.

As shown in Figure 1b,c, far away from the partially dissolved WC and outside the TZ, the quasicontinuous carbide network of the MP is composed of complex regular carbides in the intercellular spaces. This morphology is characterized by a smooth boundary that clearly outlines the interface with the matrix.<sup>[17,26]</sup> The average compositions of the complex regular carbide and the

matrix of the MP are shown in Table 1. The complex regular carbide exhibits a higher Mo content in comparison with the SCs in the TZ as well as high contents of Cr and W. In the MP, the matrix exhibits lower contents of C and W in comparison with the matrix of the TZ.

Figure 2b,e shows, respectively, the results of EBSD analyses focusing on the raw WC powder (Figure S1b, Supporting Information) and on the partially dissolved WC carbide observed after cladding (Figure 1b). The main lattice parameters used for indexing both EBSD maps are shown in Figure 2d. The WC powders and the partially dissolved WC core are composed of well-indexed crystals together with darker zones, as shown in the pattern quality maps (Figure 2a,c).<sup>[27]</sup> The dark zones may correspond to supersaturated phases formed during gas atomization.<sup>[17,18,27]</sup>

The WC particles are composed of crystals of Qusongite (hexagonal WC), orthorhombic W<sub>2</sub>C, and trigonal W<sub>2</sub>C. Moreover, as shown in Figure 2b, part of the small WC particles are identified as a body-centered cubic (BCC) crystal system corresponding to pure W, whose formation can be ascribed to recalescence taking place during gas atomization.<sup>[18]</sup>

After cladding, partially dissolved WC cores are also composed of crystals of Qusongite (hexagonal WC) and traces of orthorhombic W<sub>2</sub>C (Figure 2e). The carbide crown and all the solidification carbides formed around the partially dissolved WC particles are indexed as FCC. Those phases are identified considering the lattice of (Fe,W)<sub>6</sub>C carbide, which gives a better rate of indexation compared with other FCC phases.<sup>[9,13]</sup> White particles of the carbide crown are identified as pure W (BCC). In view of their slightly poorer quality of indexation (Figure 2c), complex regular SCs are further considered in Section 2.1.2, together with the SCs of the HAZ using a higher magnification. Finally, the matrix is identified as austenite (FCC crystal system) with varying lattice parameters.<sup>[16]</sup>

### 2.1.2. Heat-Affected Zone

The HAZ of the clad 316 L + WC composite exhibits a cellular-dendritic-reinforced microstructure (Figure 3a) with a coarse

**Table 1.** Chemical composition (at%) of the different phases observed in the vicinity of the partially dissolved WC particles and in the MP, away from the WC particles (Neg. = Negligible amount).

Phase [at%]	C	Cr	Mn	Fe	Ni	Mo	W
Partially dissolved WC carbide							
WC core	49.9 ± 4.3	Neg.	Neg.	1.5 ± 1.1	Neg.	Neg.	47.9 ± 4.2
Internal crown	33.0 ± 2.6	7.7 ± 1.3	Neg.	24.5 ± 2.6	2.2 ± 0.8	Neg.	32.1 ± 2.8
White clusters	31.1 ± 2.2	5.0 ± 1.3	Neg.	11.8 ± 0.7	0.7 ± 0.6	Neg.	51.1 ± 1.1
External crown	28.5 ± 4.7	11.0 ± 1.3	0.5 ± 0.5	30.7 ± 3.9	2.6 ± 1.1	0.8 ± 0.6	25.9 ± 2.9
TZ							
Gray compact carbide	23.0 ± 2.1	28.5 ± 2.7	1.2 ± 0.6	40.1 ± 3.2	2.9 ± 0.5	1.0 ± 0.2	3.1 ± 1.0
White skeletal carbide	19.8 ± 4.0	14.1 ± 1.1	0.8 ± 0.5	48.7 ± 4.4	5.9 ± 1.2	0.9 ± 0.4	9.8 ± 1.8
Matrix of TZ	14.2 ± 3.3	13.1 ± 1.3	1.1 ± 0.4	59.0 ± 2.2	7.8 ± 1.1	0.5 ± 0.3	4.2 ± 0.9
MP							
Complex regular carbide	21.5 ± 3.4	23.0 ± 1.8	0.8 ± 0.4	38.3 ± 2.5	5.1 ± 0.9	2.8 ± 0.3	8.3 ± 0.6
Matrix of MP	12.7 ± 2.7	13.3 ± 0.9	1.2 ± 0.5	58.3 ± 2.0	10.8 ± 1.0	0.7 ± 0.2	2.8 ± 0.5

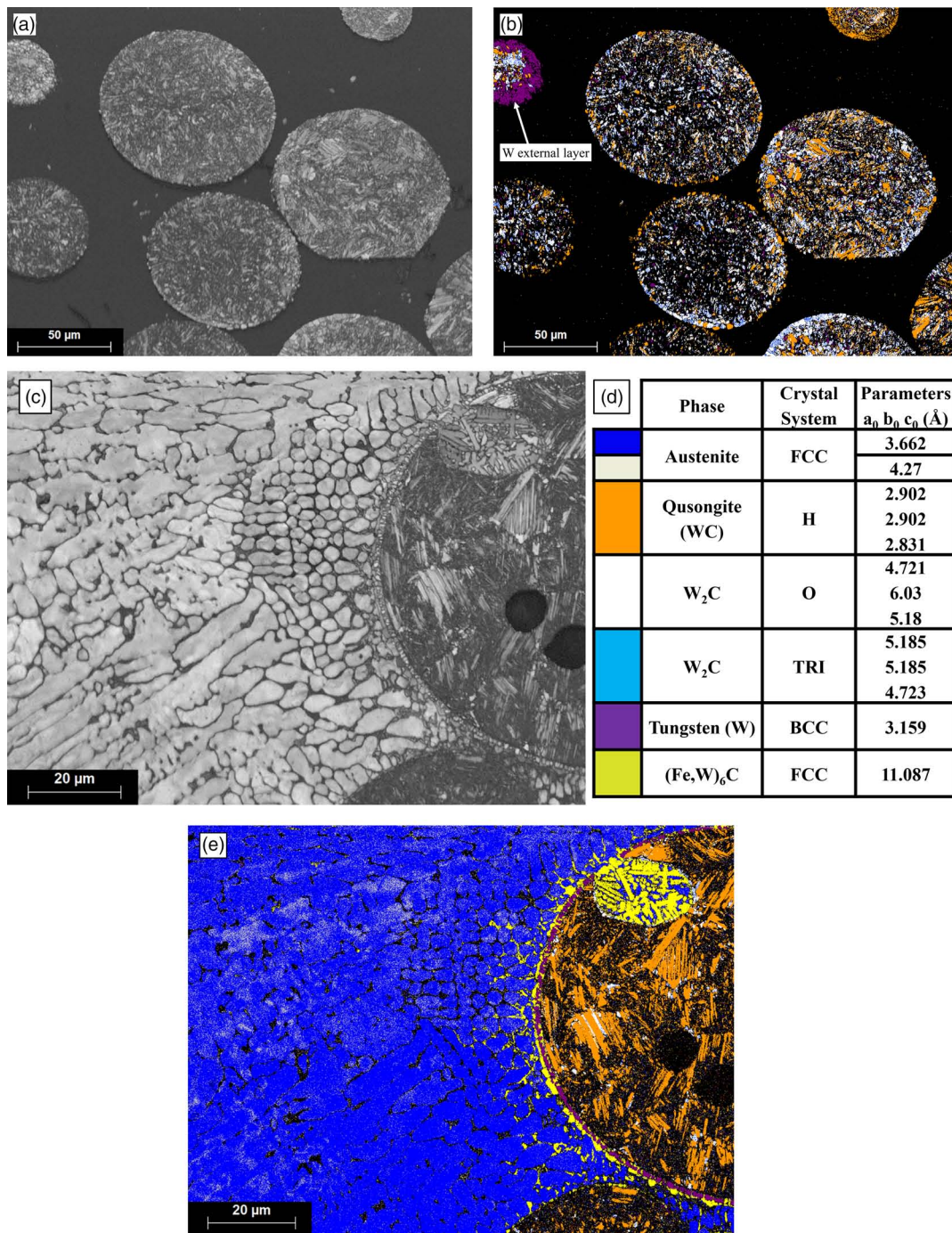


**Figure 2.** EBSD analyses on raw WC powders and on SS316L + 20%WC composite. a) Pattern quality map and b) EBSD phase map of the EBSD analysis on the raw WC powders. c) Pattern quality map and e) EBSD phase map of the zone shown in Figure 1b. d) Phases considered for both EBSD analyses with their relative lattice characteristics.

carbide network,<sup>[20,22,23]</sup> composed of gray eutectic carbides and white rod-like carbides.<sup>[24]</sup> Gray eutectic carbides in the HAZ appear of larger size in comparison to the gray carbides observed around the WC reinforcements inside the MP (Figure 1c), whereas the white rod-like carbides appear of smaller size (Figure 3b). In both morphologies, circular spaces inside

the carbides are associated to eutectic matrix. As shown in Figure 1a and 3a, partially dissolved WC carbides and their TZ do not present any differences in morphology and composition when comparing the core of the MP and the HAZ.

Moreover, the composition of the austenitic matrix does not change significantly between the MP and the HAZ. Comparing

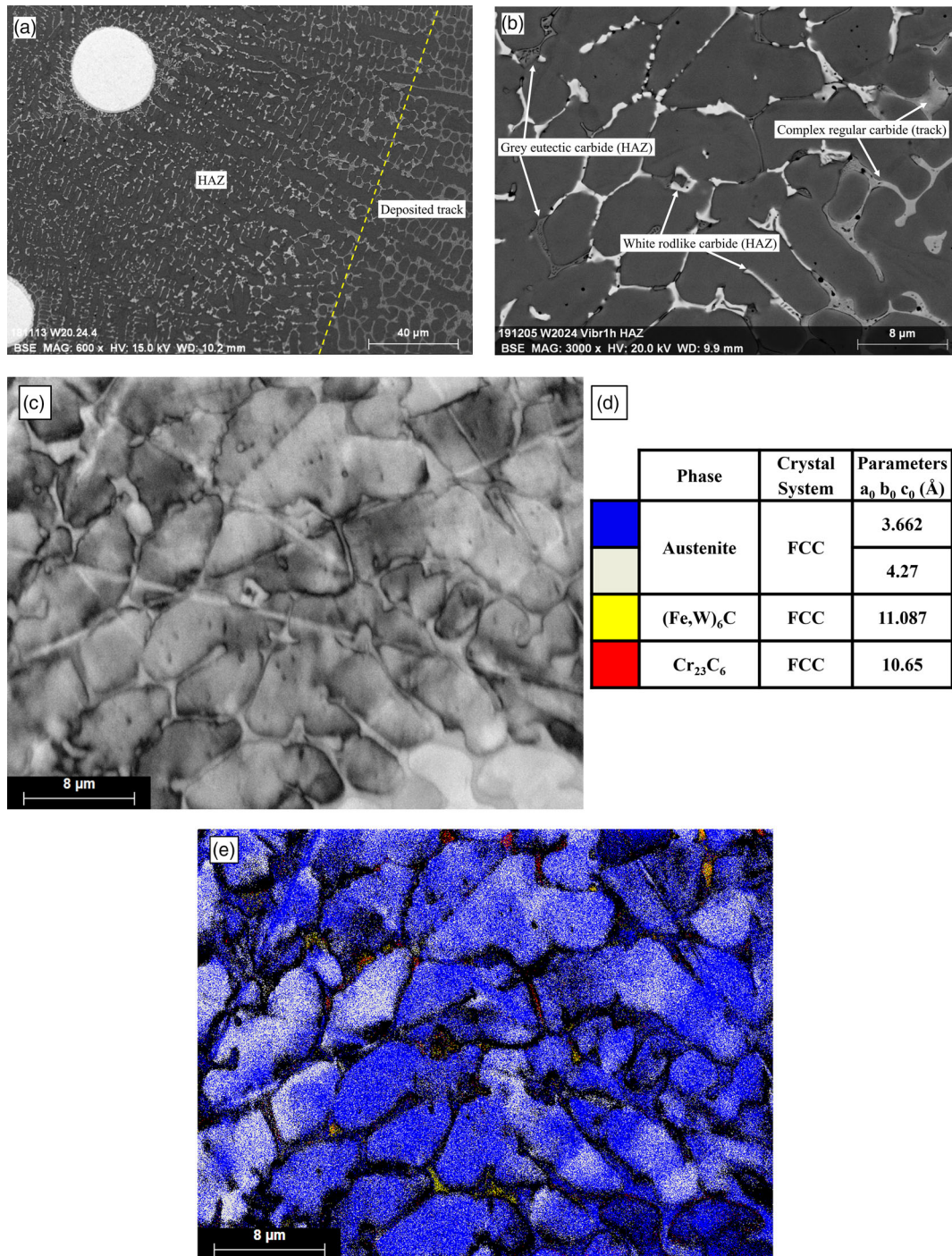


**Figure 3.** a) Close-up view of Figure 1a showing two WC particles in the HAZ of the 316L + 20%WC composite. b) SEM micrograph of the HAZ (on the left) and the MP in the core of a track (on the right). c) Pattern quality map and e) EBSD phase map of the EBSD analysis of the HAZ shown in Figure 3b. d) Phases considered for the EBSD analyses with their relative lattice characteristics.

the compositions of the carbides dispersed in the matrix in both the MP and the HAZ (Table 1 and 2), the gray carbides of the HAZ also exhibit a relatively high Cr content, whereas the white carbides also exhibit a high W content. Nevertheless, in particular for the gray carbides, the contribution of the matrix of the HAZ in the interaction volume increases due to the increased presence

of eutectic spaces, leading to slightly higher Fe and Ni contents in comparison with the gray carbide in the TZ.<sup>[17,25]</sup> In addition, it is worth noting that the carbides dispersed in the matrix of the HAZ present very little differences in comparison with the carbides present in the TZ around WC particles, except for a higher Mo content.

**Table 2.** Chemical composition (at%) of the carbides observed in the HAZ, away from the partially dissolved WC.

Carbide [at%]	C	Cr	Mn	Fe	Ni	Mo	W
Gray eutectic carbide	17.0 ± 4.6	23.0 ± 4.7	1.2 ± 0.5	47.1 ± 4.4	6.6 ± 1.5	1.6 ± 0.6	3.4 ± 0.4
White rod-like carbide	20.6 ± 3.4	17.0 ± 1.6	0.8 ± 0.2	42.1 ± 2.8	6.5 ± 1.0	2.6 ± 0.6	10.2 ± 1.6

EBSD analysis at higher magnification of the HAZ and MP is shown in Figure 3e, together with the main crystal lattice parameters used in the indexation in Figure 3d. Figure 3c shows that all SCs are well indexed at higher magnification.<sup>[27]</sup> Matrix and solidification carbides away from partially dissolved WC carbides are identified as FCC crystal system.<sup>[13,14,16]</sup> The matrix is identified as austenite, exhibiting a FCC crystal system with varying lattice parameters. Locally, some carbides of the matrix of the HAZ are also indexed considering the lattice of austenite. The same identification is proposed for the complex regular carbides of the matrix of the MP (Section 2.1.1),<sup>[13,16]</sup> who also exhibit a relatively high Mo content similarly to the carbides in the matrix of the HAZ (Table 1 and 2). Finally, gray eutectic carbides are identified as Cr<sub>23</sub>C<sub>6</sub>, whereas rod-like carbides are identified as (Fe,W)<sub>6</sub>C.

The phases analyzed in Section 2.1 are shown in Table 3 considering their position in the microstructure of the 316 L + 20%WC composite.

## 2.2. DTA Analysis and Dilatometer Test

The DTA heating curves covering both the solid state and remelting temperature ranges are shown in Figure 4. The two curves obtained at 2 and 5 °C min<sup>-1</sup> are plotted together with the dilatometry curves in Figure 4a to consider the transformations in solid state. First derivatives of the DTA curves (DDTA) are also shown in Figure 4b to help the deconvolution of the peaks observed at high temperatures for both heating rates.

Several single peaks (H1 to H4) and one complex peak (H5 + H6 + H7 + H8 + H9) are observed for both heating rates in the same temperature range. Classically, the lower heating scan allows a larger spread of the signal.<sup>[28]</sup> The deconvolution of the complex peak at high temperature, based on the first derivative, allows to distinguish four superimposed peaks for 2 °C min<sup>-1</sup>, as shown in Table 4. Moreover, an additional fifth

**Table 3.** List of the carbides observed in MP and in the HAZ depending on the distance to the partially dissolved WC particles.

	Melt pool	HAZ
Away from WC	Complex regular carbide	Gray eutectic White rod-like
Nearby WC	Partially dissolved WC core Carbide crown TZ (gray compact + white skeletal) Complex regular carbide	Partially dissolved WC core Carbide crown TZ (gray compact + white skeletal) Gray eutectic White rod-like

peak is observed for 5 °C min<sup>-1</sup> (Figure 4b) as will be discussed in Section 3.2.

The first two peaks (H1 and H2) in the dilatometry curve correspond to a contraction of the sample. They can be related to the precipitation and dissolution of secondary carbides in the intracellular spaces, as also shown by peaks H1 and H2 in the DTA curve.<sup>[29]</sup> The exothermic peak H3 is related to the relaxation of the system prior to the solidus temperature (peak H4).<sup>[30]</sup> The complex DTA peak (H5 + H6 + H7 + H8 + H9) in the range 1333–1400 °C is high and relatively sharp in both heating rates. At a heating rate of 2 °C min<sup>-1</sup> overlapping of the complex peak decreases, creating a separation between H5 + H6 and the peaks at higher temperatures.

Looking more closely at the complex (H5 + H6 + H7 + H8 + H9) peaks, the first two peaks (H5 and H6) in the DDTA curve are overlapping and occur at the same temperatures for both heating rates (Figure 4b). In this range, the first derivative exhibits an increase after the peak H4 followed by a plateau. After peak H6, the DDTA curves exhibit very sharp and sudden changes of slope. At a heating rate of 2 °C min<sup>-1</sup>, the peak H9 is not observed and the distance between peaks H7 and H8 decreases. Furthermore, a peak H10 is clearly visible at the higher heating rate that corresponds to the liquidus temperature.

## 3. Discussion

### 3.1. Differentiation of the Mixed (Fe, W) Carbides

Interactions between the molten metal and WC powders during LC lead to a partial or total dissolution of the initial WC particles. This dissolution enriches the composition of the original SS316L, giving way to the formation of new solidification mixed carbides in the microstructure.<sup>[6,8]</sup> Those new phases link the partially dissolved WC to the matrix and reinforce the microstructure.

In what follows, microstructural features will be discussed first for the HAZ, then for the microstructure in the vicinity of the WC particles and finally far away from those latter areas, in a progression from simple toward more complex phase identification.

#### 3.1.1. Heat-Affected Zone

With regards to the mixed carbides observed in the HAZ (Figure 3), the characterization using EBSD analysis is straightforward and in agreement with EDS analyses (Table 2). The gray eutectic carbides are identified as (Fe, Cr)<sub>23</sub>C<sub>6</sub>,<sup>[10,16,19]</sup> and the white rod-like carbides are identified as (Fe, W)<sub>6</sub>C.<sup>[7,8,24]</sup> The carbides observed in the HAZ can be considered closer to an equilibrium condition as a result of the reheating experienced

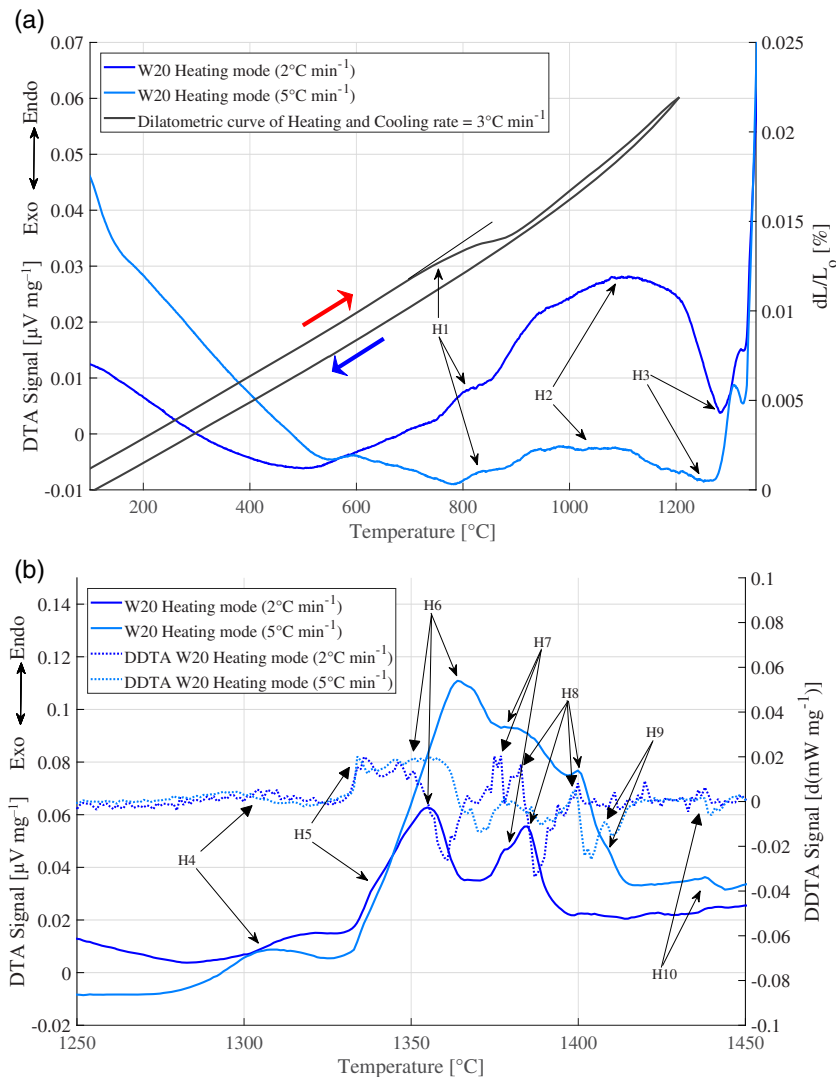


**Figure 4.** DTA heating curves run at 2 and 5 °C min<sup>-1</sup> up to complete remelting and dilatometer test run at 3 °C min<sup>-1</sup> up to 1200 °C for the 316L + 20%WC composite. a) Graph corresponding to the range tested by the dilatometer test where both thermal measurements can clarify the nature of the DTA reaction peaks in the solid state. b) Zoom corresponding to the DTA remelting temperature range where DDTA curve helps identifying the different reaction peaks.

in the HAZ during the deposition of the next layer of the clad, and consistently with the fact that their crystal lattices are easily identified (Figure 3e).

### 3.1.2. WC Particles and TZ

According to the EBSD analysis shown in Figure 2e, starting from the WC particles, the carbide crown observed around the partially dissolved WC is mistaken for M<sub>6</sub>C carbide. However, considering its high C and W contents (Table 1), it should rather be associated to the γ-WC<sub>1-x</sub> carbide.<sup>[12,15]</sup> This carbide is the only phase in the W-C system that exhibits a FCC structure (Fm-3m), and it is considered as a high-temperature modification (stable at 2300–2750 °C) of W<sub>2</sub>C. This W-rich phase has already been observed under conditions

where rapid cooling prevents the phase transformation toward equilibrium.<sup>[12,15]</sup> The modification of this carbide composition by Fe, Cr, and Ni (Table 1) as a result of interactions with the molten metallic matrix may enlarge its thermodynamic stability to room temperature and leads to the formation of large carbide crystals around the partially dissolved WC core.<sup>[12,15,17,31]</sup> Indeed, the morphology of the crystals shown in Figure 1b suggests that this phase nucleates and grows on the partially dissolved WC core by heterogeneous nucleation.<sup>[15,32]</sup>

Moving to the solidification carbides formed in the TZ, the skeletal carbides with a relatively high W content are confirmed as (Fe,W)<sub>6</sub>C,<sup>[24]</sup> as indicated by the EBSD analysis (Figure 2e). As in the case of the carbide crown, the high Fe and Cr contents (Table 1) of the gray compact carbides suggest that they may be identified as (Fe, Cr)<sub>23</sub>C<sub>6</sub>.<sup>[19,25]</sup> The presence of W in the composition of the M<sub>23</sub>C<sub>6</sub> carbide (Table 1) may increase its

**Table 4.** List of the peaks as obtained from the dilatometry curves and from the two DTA curves and their first derivatives (DDTA).

N°	DTA (2 °C min <sup>-1</sup> )		DTA (5 °C min <sup>-1</sup> )		Dilatometry (3 °C min <sup>-1</sup> )
	Range for DTA peak	Range for DDTA peak	Range for DTA peak	Range for DDTA peak	
H1	707–748	701–736	713–799	705–764	728–872
	800–854	792–833	834–881	809–850	Contraction
H2	954–1100	936–1074	γ <sup>a)</sup> –980	947–973	884–990
					Expansion
H3	1177–1279	1194–1249	1114–1261	1083–1213	
H4	1282–1314	1270–1307	1272–1306	1263–1297	Solidus
H5 + H6 + H7 + H8 + H9	1333–1383		1333–1411		
H5	1333–1338	1325–1336	1333–1337	1325–1334	
H6	γ <sup>a)</sup> –1354	1339–1346	γ <sup>a)</sup> –1364	1340–1354	
H7	1371–1378	1361–1376	γ <sup>a)</sup> –1381	1372–1380	
H8	γ <sup>a)</sup> –1383	γ <sup>a)</sup> –1383	1396–1399	1388–1398	
H9	/	/	γ <sup>a)</sup> –1411	1404–1408	
H10	γ <sup>a)</sup> –1402	1402–1403	1417–1439	1422–1437	Liquidus

<sup>a)</sup>Undetermined.

stability,<sup>[19]</sup> but it may also lead to the identification of a crystal lattice similar to the one of M<sub>6</sub>C (Figure 2d) in the EBSD analyses due to the polymorphism within the Fe–W–C system.<sup>[17,31]</sup>

### 3.1.3. Matrix of the MP (Far from the Partially Dissolved WC)

As shown in Figure 2e and 3e, the matrix is identified as austenite with two different lattice parameters, corresponding to a slight distortion of the classical lattice parameter for austenite. This local enlargement of the lattice parameter is due to the extremely high cooling rates achieved during solidification, that leads to increased retention of large atoms such as W and Mo (Table 1 and 2) in supersaturation in the austenite crystal lattice.<sup>[7,17]</sup> The metastable condition of the austenitic matrix is confirmed by dilatometry and DTA observations. Indeed, the thermal cycle imposed during the dilatometer test below the solidus temperature leads to the desaturation of the supersaturated matrix and thus to its contraction (Figure 4a). The desaturation is associated to the precipitation of secondary carbides, as observed in the DTA curves (peaks H1 and H2 in Figure 4 and Table 4)<sup>[29]</sup> and in the SEM micrograph of Figure 5 that shows small secondary carbides in some of the intracellular spaces, especially around the partially dissolved WC. In addition to the precipitation of secondary carbides in the intracellular spaces, it is worth noting that the thermal treatment imposed during the dilatometry test leads to the modification of the partially dissolved WC and of the complex regular carbide (Figure 5) as these are metastable as well. All these metastable carbides were formed under extremely high cooling rates. Reheating allows their structure and lattices to evolve toward a condition closer to equilibrium.<sup>[6,15,18]</sup> The long thermal cycle at high temperature during the dilatometry test leads to an expansion of the γ-WC<sub>1-x</sub> carbide crown while in contact with a Fe-based matrix.<sup>[9,15]</sup> Indeed, the carbide crown is observed to grow inward in the partially dissolved WC core,

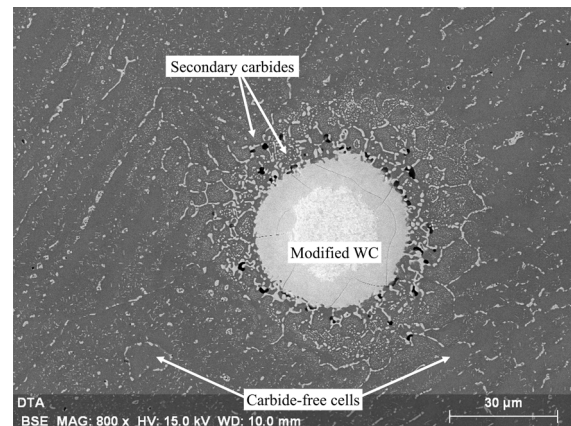


**Figure 5.** SEM micrograph of the microstructure of the 316L + 20%WC composite after a dilatometry test up to 1200 °C.

increasing its thickness from ≈3 μm up to ≈15 μm (compare Figure 1 and 5).

The complex regular carbides dispersed in the matrix far from the original WC particles possess a crystal lattice that is well indexed at high magnification as confirmed by the high pattern quality (bright zones in Figure 3c). However, this lattice is distorted and mistakenly identified as austenite (Figure 3d,e).<sup>[13,14,16]</sup> Small variations in the contrast of its pattern are assumed to arise from differences in elastic strains.<sup>[17,27]</sup> The chemical composition of the very last remaining liquid of the track (Table 1), together with the high cooling rates achieved during deposition, may lead to this contraction of the crystal lattice due once again to the retention of more elements in solution within the carbide lattice compared with its equilibrium condition.<sup>[17]</sup>

Similar lattice distortions have been observed on metastable carbides prior to their destabilization during thermal treatments

at specific temperatures accompanied by the precipitation of new phases.<sup>[17,33,34]</sup> This is, e.g., the case in the HAZ as its formation results from the local increase in temperature induced by the deposition of a new track on the previously deposited tracks.<sup>[20,21,23]</sup> In the HAZ, the reheating temperature is high enough to reach locally the solidus temperature, but it remains below the melting temperature of the austenite.<sup>[35]</sup> Indeed, the compositions of the matrix in the MP and HAZ do not exhibit remarkable differences (Table 1). Based on these observations regarding the matrix of the MP and HAZ and on the previous considerations on the decomposition of metastable carbides, it is assumed that the complex regular carbides dissociate when reheated, thus leading to the formation of (Fe, Cr)<sub>23</sub>C<sub>6</sub> and (Fe, W)<sub>6</sub>C in the intercellular spaces of the HAZ (Table 2).<sup>[23]</sup> Considering the FCC crystal structure of the complex regular carbide, the polymorphism in the Fe–C–W and previous works on decomposition or dissociation phenomena,<sup>[17,33,34]</sup> the complex regular carbide can thus be associated only to (Fe,W)<sub>4</sub>C. Indeed, the stoichiometry of the parent metastable carbide in a dissociation reaction must exhibit a higher C content than the products of the reaction and in this case, it must also exhibit a FCC structure (Figure 3d).<sup>[17]</sup> Furthermore, previous studies show that the M<sub>4</sub>C carbide is the less stable among the mixed (Fe,W) carbides, matching the features of the considered complex regular carbide.<sup>[9,11,14]</sup> The dissociation reaction caused by a reheating up to the solidus temperature during cladding<sup>[17,23,33]</sup> can then be written as follows



### 3.2. Elucidation of the Microstructure Genesis

The microstructure of the 316L + 20%WC composite presents local heterogeneities, e.g., in the vicinity of the partially dissolved WC reinforcements and in the HAZ. To elucidate the microstructure genesis of this complex composite material, the morphological features, the distribution, the crystallographic nature, and the chemical composition of the different phases are correlated with the peaks observed in the DTA and DDTA curves (Figure 4). Moreover, dilatometry results are considered to complete the analysis.

As shown in Figure 4a, three peaks H1, H2, and H3 were identified by considering together the DTA and the dilatometry curves. As discussed in Section 2.2 and 3.1.3, those peaks are related to the desaturation of the matrix and the relaxation of the system prior to the solidus temperature.<sup>[29,30]</sup>

As shown in Table 3, the solidification route of the 316L + 20%WC composite depends on the liquid composition during solidification and more particularly on the interactions between the molten metallic matrix and the WC particles immediately before the beginning of the solidification of the matrix. The solidification sequence can be assumed from the reverse consideration of the thermal analyses (Figure 4) and the microscopy observations following the procedure proposed in the study by Maurizi Enrici et al.<sup>[17]</sup>

At high temperatures, large composition gradients between the molten metal and the WC particles lead to a modification of the local compositions during the deposition.<sup>[6]</sup> Diffusion is

limited due to the high cooling rates and the short liquid lifetime,<sup>[36]</sup> but composition gradients are large enough to induce outward and inward flows of elements from and to the WC particles. Outward flows of W and C from the WC particles enrich the composition of the molten metal by dissolution, until the extreme situation of complete dissolution of the WC particles.<sup>[8]</sup> The amount of the W and C enrichment depends on the distance to the original WC carbide (Table 1), as shown by the presence of the different reaction carbides in the TZ and in the MP far from the WC particles (Figure 1b). Furthermore, pure W particles are observed in the carbide crown (Figure 1d) and in the virgin WC particles (Figure 2b). As C atoms can diffuse faster in the metallic matrix, they leave W atoms behind both in gas atomization and in LC conditions (Figure 2b,e). With the progress of these elemental flows, W particles may be dissolved by the molten metal or converted into the carbide crown during solidification. Simultaneously, inward flows of Fe, Cr, and Ni into the original WC particles lead to the modification of the phases that had been formed during gas atomization (Figure 2b,d).<sup>[12]</sup> As shown in Figure 5, the WC particle in contact with a Fe-based matrix continues to evolve during the thermal cycle imposed by the dilatometry test, thus leading to the thickening of the carbide crown.

On cooling from these high temperatures, the solidification starts at the liquidus temperature (peak H10, Figure 4b and Table 4). This corresponds to the solidification of large crystals of  $\gamma$ -WC<sub>1-x</sub> carbide, forming a carbide crown around the partially dissolved WC particles (Figure 1b).<sup>[1]</sup> The remaining WC cores act as heterogeneous nucleation sites.<sup>[15,32]</sup> The enlarged shape of the H10 peak on the DTA curve (Figure 4) can be associated with the partially dissolved WC cores that transformed completely to  $\gamma$ -WC<sub>1-x</sub> (Figure 5) at the end of the DTA thermal cycle. Indeed, the chemical composition of the  $\gamma$ -WC<sub>1-x</sub> varies from the cores to the edges of the particles. This applies especially for elements such as W, Fe, and Ni, as observed between the internal and external parts of the carbide crown (Table 1).

The second phase to form on solidification corresponds to the austenite with two different compositions (peaks H8 + H9, Figure 4). The two different chemical compositions (Table 1) correspond to the two separated peaks. Moreover, the shift of peak H8 and the disappearance of peak H9 at the lower heating rate (Figure 4b) can be related to the homogenization of the matrix by diffusion phenomena that are favored at the slower heating rate. The first stage of nucleation of the austenite may occur locally on the partially dissolved WC particles by heterogeneous nucleation (Figure 1c) from liquid that is enriched locally in W and C by the partial dissolution of the WC (Table 1).<sup>[15,32]</sup> Then, the second stage of nucleation may occur at the edges of the MP, on the previously deposited solid layer (Figure 3a).<sup>[37]</sup>

In the TZ, the solidification of the austenite is followed locally by the formation of the M<sub>6</sub>C skeletal carbides that precipitate around the partially dissolved WC. The morphology of the skeletal carbides reflects on the high local W content in the TZ (Table 1). This step is represented by M<sub>6</sub>C +  $\gamma$  in Table 5.<sup>[24]</sup> The broad shape and the position of peak H7 (in the temperature range 1361–1376 °C for a heating rate of 2 °C min<sup>-1</sup>, Figure 4b) are in good agreement with the composition (Table 1) and the size of these carbides, corresponding to their relatively large chemical gradient. Following the formation

**Table 5.** List of the peaks related to the DTA curves of Figure 4b, with the corresponding phase transformations that occur inside the track and locally in the vicinity of the WC particles during the deposition of the 316L + 20%WC composite.

Away from WC	Nearby WC	Nature and location of the phase transformation	Type of reaction
1	1	Direct precipitation of crystals of $\gamma$ -WC as a carbide crown	$L_0^1 \rightarrow \gamma\text{-WC} / \gamma (+L_1)$
	2	Nucleation and growth of austenite with different compositions	$L_1 \rightarrow \gamma (+L_2)$ $L_0^2 \rightarrow \gamma (+L_3)$
	3	Local eutectic precipitation leading to the formation of $M_6C$	$L_2 \rightarrow M_6C/\gamma (+L_4)$
2	5	Eutectic precipitation leading to the formation of $M_4C$	$L_3 \rightarrow M_4C/\gamma$
	4	Local eutectic precipitation leading to the formation of $M_{23}C_6$	$L_4 \rightarrow M_{23}C_6/\gamma$
3 + 4	6 + 7	Reaction of dissociation of $M_4C$ leading to the formation of $M_6C$ and $M_{23}C_6$	$M_4C \rightarrow L_5 \rightarrow M_6C + M_{23}C_6$

of the skeletal  $M_6C$ , the residual intercellular liquid in the TZ is enriched with both C and Cr, whereas other elements such as W, Fe, and Ni have been already retained in the matrix and the skeletal carbide. As result, small Cr-rich  $M_{23}C_6$  appears in the remaining liquid as the next step in the solidification process of the TZ (Figure 1c).

When moving away from the partially dissolved WC carbides, in contrast, the complex regular  $M_4C$  carbide is formed from the remaining liquid in the intercellular spaces after the solidification of the austenite (Figure 3). In this case,  $M_4C$  is the last phase formed by direct solidification, and their formation thus corresponds to the solidus temperature.<sup>[14]</sup> As shown in Table 4, the sharpness of the related peak H6 (in the temperature range 1339–1346 °C for a heating rate of 2 °C min<sup>-1</sup>, Figure 4b) can be related to smaller variations of the chemical composition of  $M_4C$  than for the other carbides (Table 1 and 2).

Finally, the formation of white rod-like  $M_6C$  carbides in the HAZ may be associated with peak H5 in view of its similar composition, containing Mo and W, as the  $M_4C$  carbide (Figure 4b, Table 1 and 2). Peak H4, in contrast, corresponds to the precipitation of the gray  $M_{23}C_6$  carbides. Their small size and wide range of composition (Table 1 and 2) correspond to the last broad peak in the DTA curves (in the temperature range 1270–1307 °C for a heating rate of 2 °C min<sup>-1</sup>).

These different reactions leading to the final complex microstructure of the SS316L + 20%WC composites are shown in Table 5 in their chronological order of appearance.

#### 4. Conclusions

The cross-consideration of the local chemical composition (obtained by EDS), lattice parameters (determined by EBSD) and of the phase stability (characterized by dilatometry tests) allowed to identify and differentiate the different phases belonging to the Fe–C–W system or to the W–C system that are present in the microstructure of the SS316L + 20%WC laser clad composite, in spite of the similarities of their (FCC) crystal structures.

Exhaustive characterization of the microstructure revealed the traces of the interactions between the WC particles and the molten metal during deposition. Outward elemental flows from the WC particles enrich the composition of the original 316L matrix in W and C, whereas inward Fe and Ni elemental flows from the molten metal into the WC particles destabilize the

phases that had been formed during gas atomization. These exchanges lead to the partial or total (for the smallest particles) dissolution of the WC particles. The extent of dissolution for a given volume percentage of reinforcements is directly connected with the size distribution. To decrease the general dissolution, a tailored and higher size distribution may be adopted using only large particles. The balance between the presence of large reinforcements or an extensive dissolution is determined by the mechanical properties and corrosion resistance needed for the specific application.

The genesis of the complex microstructure of SS316L + 20%WC composite has been elucidated, thanks to the combination of detailed microstructural characterization and of thermal analyses carried out in reverse mode. This approach that had been proposed previously to elucidate the solidification sequence of complex HSS alloy under centrifugal casting has now been proven efficient for gaining insights in the microstructure genesis of laser clad composite under much faster solidification and cooling rates, typical of AM techniques. Furthermore, thermal analyses are confirmed as very sensitive techniques, able to detect phase transformations and to provide insights on the nature of those phases even in relatively small amounts, as in the vicinity of the WC reinforcements in the SS316L + 20%WC composites.

The solidification sequence of the 316 L + 20%WC composite in the vicinity of partially dissolved WC particles can be assumed as follow: 1) modified  $\gamma$ -WC<sub>1-x</sub> carbide forming on the undissolved WC cores by heterogeneous nucleation, 2) austenite, 3)  $M_6C$  carbide, 4)  $M_{23}C_6$  carbide, and 5)  $M_4C$  carbide. Away from the WC particles, the solidification sequence is composed only of 1') the formation of austenite and 2') the formation of  $M_4C$  carbide. In the HAZ, a dissociation of the  $M_4C$  carbide is assumed to take place, resulting in the formation of  $M_6C$  carbide and  $M_{23}C_6$  carbide in the intercellular spaces due to reheating up to the solidus temperature.

#### 5. Experimental Section

**Samples Fabrication:** A metal matrix composite coating composed of SS316L and reinforcements of tungsten carbide (WC) particles was deposited on a SS316L substrate using a 5-axis Irepa LC system with a Nd-YAG laser source. The two powders used for the production of the parts were SS316L and WC gas atomized powders with a granulometry between 50 and 200  $\mu$ m, having a spherical shape (Figure S1, Supporting

Information). The powders were stored in two separate containers to avoid segregations due to the difference of density and then carried to the nozzle by inert gas, where they were mixed before being fed into the focused laser beam. The laser power was varied between 400 and 570 W for a corresponding traverse speed of 270–290 mm min<sup>-1</sup>, and the layer thickness was set to 600 μm. The stream of powder was focused into the laser beam by an inert gas flow and directed toward the substrate at an angle of 38°–45°. About 19 layers thick SS 316L–WC coatings were produced with 20% in volume fraction of WC. The final dimensions of those deposits were 35 × 35 mm<sup>2</sup> side length and 14 mm height (Figure S2, Supporting Information).

**Microstructural Characterization:** A cube sample with an edge length of 7 mm, and located between 2 and 9 mm of distance from the substrate was used for microstructure characterization. This sample was hot mounted with an electrically conductive epoxy resin, then grinded and polished down to 1 μm, chemically etched with aqua regia and finally polished with a vibrometer using colloidal silica. The as-polished samples were used for SEM analyses. This procedure was applied to create an optimal roughness for the observations and to eliminate scratches from the initial grinding.

EBSA analyses were carried out using an accelerating voltage of 20 kV, at a working distance of 15 mm with a 30 μm aperture. The pixel size was set at 1/180 (normal definition) and 1/240 (high definition) of the scale bar for EBSA images. The image quality (IQ) or pattern quality was considered to evaluate the result of the phase indexation.<sup>[17,27]</sup> A minimum number of seven bands were subsequently set within ESPRIT software to identify both the crystal structure and the lattice parameters. AMCSD, ICSD-Demo, BAXS, and PDF4+ (reference 01-018-1479) from the International Centre for Diffraction Data (ICDD) XRD databases were considered as reference for the allowable phases in EBSA analyses. Crystal structure and composition obtained by EDS analyses were considered together with EBSA to identify phases with unique compositions.<sup>[17]</sup>

**Thermal Analyses:** About Ø 5 mm cylindrical samples with their axes parallel to the scanning direction were used for DTA and dilatometer tests. They were located at 7 mm from the 316L substrate to avoid the dilution zone. DTA samples (5 mm height, for ≈0.85 g mass) and dilatometer samples (25 mm height) were obtained from those cylinders by electro-discharge machining.

DTA tests were conducted on a NETZSCH 449C Jupiter apparatus in heating mode at constant scans of 2 or 5 °C min<sup>-1</sup> up to 1450 °C, so as to achieve a complete remelting of the clad composite. The first derivative of the DTA curve (DDTA) was computed using NETZSCH Proteus Thermal Analysis software. This helped to identify individual peaks when overlapping occurred.<sup>[17,38]</sup>

Furthermore, dilatometer tests were conducted on a NETZSCH DIL 402C apparatus. Dilatometer tests consisted of a reheating stage up to 1200 °C followed by cooling down to room temperature to detect metastable phases that had been formed at high cooling rates during LC. Constant low heating and cooling rates of 3 °C min<sup>-1</sup> allowed phase transformations by diffusional phenomena in the solid state from the out-of-equilibrium condition to a stable state.<sup>[29]</sup> Dilatometry curves and DTA heating curves were thus plotted together to evaluate the stability of the phases after LC.

## Supporting Information

Supporting Information is available from the Wiley Online Library or from the author.

## Acknowledgements

This work was benefited from the financial support of the European Fund for Regional Development and the Walloon Region under convention FEDER “Iawatha.” The authors acknowledge the CAREM of the ULiège for providing SEM/EDS/EBSA facilities. They also thank Sylvie Salieri for the sample preparation, Samuel Rondia for the substrates preparation,

Laura Zorretto for helpful discussion, Vincent Delaval for powder characterization, and the SIRRIS Research Centre for providing access to the laser cladding equipment.

## Conflict of Interest

The authors declare no conflict of interest.

## Keywords

additive manufacturing, electron backscattered diffraction, Fe–W–C system, laser cladding, microstructures

Received: March 12, 2020

Revised: May 20, 2020

Published online:

- [1] J. Domitner, M. Aigner, T. Stern, A. Paar, C. Sommitsch, L. Elizondo, *Steel Res. Int.* **2019**, *91*, 1900478.
- [2] A. Mertens, T. L'Hoest, J. Magnien, R. Carrus, J. Lecomte-Beckers, *Mater. Sci. Forum* **2017**, *879*, 1288.
- [3] D. Deschuyteneer, F. Petit, M. Gonon, F. Cambier, *Surf. Coat. Technol.* **2015**, *283*, 162.
- [4] A. Plati, J. C. Tan, I. O. Golosnoy, R. Persoons, K. van Acker, T. W. Clyne, *Adv. Eng. Mater.* **2006**, *8*, 619.
- [5] D. Deschuyteneer, F. Petit, M. Gonon, F. Cambier, *Surf. Coat. Technol.* **2017**, *311*, 365.
- [6] A. I. Mertens, J. Lecomte-Beckers, in *New Trends 3D Print* (Ed: I. V. Shishkovsky), InTech, Rijeka, Croatia **2016**, p. 187.
- [7] L. Song, G. Zeng, H. Xiao, X. Xiao, S. Li, *J. Manuf. Process.* **2016**, *24*, 116.
- [8] X. Tong, F. H. Li, M. Kuang, W. Y. Ma, X. C. Chen, M. Liu, *Appl. Surf. Sci.* **2012**, *258*, 3214.
- [9] X. Cai, Y. Xu, M. Liu, L. Zhong, *J. Alloys Compd.* **2018**, *741*, 666.
- [10] J. Wang, L. Li, W. Tao, *Opt. Laser Technol.* **2016**, *82*, 170.
- [11] P. Gustafson, *Metall. Mater. Trans. A* **1987**, *18*, 175.
- [12] A. S. Kurlov, A. I. Gusev, in *Tungsten Carbides: Structure, Properties and Application in Hardmetals*, Series Materials Science, Springer International Publishing, Heidelberg, New York, Dordrecht, London **2013**, p. 5.
- [13] Y. Liu, Y. Jiang, R. Zhou, J. Feng, *Comput. Mater. Sci.* **2014**, *82*, 26.
- [14] F. Z. Abderrahim, H. I. Faraoun, T. Ouahrani, *Phys. B: Condens. Matter* **2012**, *407*, 3833.
- [15] I. T. Ho, Y. T. Chen, A. C. Yeh, C. P. Chen, K. K. Jen, *Addit. Manuf.* **2018**, *21*, 465.
- [16] C. M. Fang, M. A. van Huis, M. H. F. Sluiter, H. W. Zandbergen, *Acta Mater.* **2010**, *58*, 2968.
- [17] T. Maurizi Enrici, A. Mertens, M. Sinnaeve, J. T. Tchuindjang, *J. Therm. Anal. Calorim.* **2019**, <https://doi.org/10.1007/s10973-019-09093-9>.
- [18] C. G. Levi, *Metall. Trans. A* **1988**, *19*, 687.
- [19] N. I. Medvedeva, D. C. Van Aken, J. E. Medvedeva, *Comput. Mater. Sci.* **2015**, *96*, 159.
- [20] C. R. Xavier, H. G. Delgado, J. A. De Castro, A. F. Ferreira, *Mater. Res.* **2016**, *19*, 520.
- [21] J. Delahaye, J. T. Tchuindjang, J. Lecomte-Beckers, O. Rigo, A. M. Habraken, A. Mertens, *Acta Mater.* **2019**, *175*, 160.
- [22] L. Zhao, J. G. Santos Macías, L. Ding, H. Idrissi, A. Simar, *Mater. Sci. Eng. A* **2019**, *764*, 138210.
- [23] J. Leunda, C. Soriano, C. Sanz, V. G. Navas, *Phys. Procedia* **2011**, *12*, 345.
- [24] P. Ding, G. Shi, S. Zhou, *Metall. Trans. A* **1993**, *24*, 1265.

- [25] J. Laigo, F. Christien, R. Le Gall, F. Tancret, J. Furtado, *Mater. Charact.* **2008**, 59, 1580.
- [26] M. Boccalini, H. Goldenstein, *Int. Mater. Rev.* **2001**, 46, 92.
- [27] S. I. Wright, M. M. Nowell, *Microsc. Microanal.* **2006**, 12, 72.
- [28] W. J. Boettinger, U. R. Kattner, K.-W. Moon, J. H. Perepezko, in *Methods for Phase Diagram Determination* (Ed.: J.-C. Zhao), Elsevier Science Ltd, Washington **2007**, p. 151.
- [29] J. T. Tchuindjang, I. N. Torres, P. Flores, A. M. Habraken, J. Lecomte-Beckers, I. N. Torres, P. Flores, D. Concepcio, A. M. Habraken, *J. Mater. Eng. Perform.* **2015**, 24, 2025.
- [30] N. Kumar, P. N. Rao, R. Jayaganthan, H. G. Brokmeier, *Mater. Chem. Phys.* **2015**, 165, 177.
- [31] Y. Li, Y. Gao, B. Xiao, T. Min, Z. Fan, S. Ma, L. Xu, *J. Alloys Compd.* **2010**, 502, 28.
- [32] M. A. Easton, M. Qian, A. Prasad, D. H. StJohn, *Curr. Opin. Solid State Mater. Sci.* **2016**, 20, 13.
- [33] M. Hashimoto, O. Kubo, Y. Matsubara, *ISIJ Int.* **2004**, 44, 372.
- [34] E. Tavares Galvani, S. Simoes, C. H. Novaes Banov, H. L. Rosa, E. Cannizza, E. Burgos Cruz, *Mech. Prop. Perform. Eng. Ceram. Compos. XI* **2017**, 37, 195.
- [35] H. L. Wei, J. W. Elmer, T. DebRoy, *Acta Mater.* **2016**, 115, 123.
- [36] Y. Liu, J. Zhang, Z. Pang, *Opt. Laser Technol.* **2018**, 98, 23.
- [37] P. Liu, Z. Wang, Y. Xiao, M. F. Horstemeyer, X. Cui, L. Chen, *Addit. Manuf.* **2019**, 26, 22.
- [38] M. Jabłońska, T. Maciąg, M. Nowak, T. Rzychoń, M. Czerny, K. Kowalczyk, *J. Therm. Anal. Calorim.* **2019**, 137, 735.

---

---

## ***Heat accumulation in multiple-layer 316L+WC composite deposit fabricated by directed energy deposition: Influence on local microstructure and hardness***

*Tommaso Maurizi Enrici, Olivier Dedry, Daniele Mario, Hakan Paydas, Jérôme Tchoufang Tchuindjang, Anne Mertens*

### **Abstract**

This work focuses on the local variation of the microstructure and hardness as a function of the height in a thick metal matrix composite (MMC) deposit made of 316L stainless steel and 20% in volume of WC carbide, fabricated by directed energy deposition. Macrohardness and nanoindentation grids were carried out to detect local variations of mechanical properties with the progress of deposition, and these results were correlated with a detailed microstructural characterization. The 316L+20%WC composite exhibits a significantly higher average macrohardness in comparison to the parent 316L due to the presence of partially dissolved WC and to the formation of a modified matrix exhibiting a hierarchical cellular structure with new solidification carbides. Furthermore, the role of the interactions taking place during solidification between the WC particles and the molten metal was determined. Heat accumulation during fabrication is found beneficial as it promotes the homogenization of the melt pool through Marangoni convection and the stabilisation of undissolved WC that act as heterogeneous nucleation sites during solidification. These two effects enhance the reinforcement of the matrix through new solidification carbides and a refined grain size.

**Keywords:** Directed energy deposition; Heat accumulation; Metal matrix composite; Refinement effect; Microstructure

### **1. Introduction**

Additive manufacturing (AM) has experienced significant growth over the past 25 years in several areas, ranging from the conception of new machines to the number and complexity of produced parts. Consequently, this has been translated into a growing number of publications and patents [1–5]. As far as metallic materials are concerned, the complex phenomena occurring during AM are attracting much attention in the scientific community with experimental investigations on one side [6–12] and numerical modelling on the other [13–18]. The main purposes are to reach a deeper understanding and to predict the complex microstructures formed under the extremely high cooling rates prevailing in AM processes.

316L stainless steel (SS) is widely used in construction, automotive and medicine due to its excellent corrosion resistance and mechanical properties [6,9,19]. Microstructural characterization of SS 316L parts fabricated by AM reveals hierarchical macro-, micro- and nano-structures [9,15,19] as a result of specific segregations at various scales induced by the extremely high cooling rates characteristic of AM. Moreover, these high cooling rates often lead to different solidification routes compared with the classical manufacturing processes and to peculiar mechanical properties due to the combination of various strengthening mechanisms. As in the research works of [9,19,20], the sample produced in the

current study present brighter Cr and Mo-rich cell boundaries (Fig. 1), which form a network where both cells and cell boundaries are austenite.

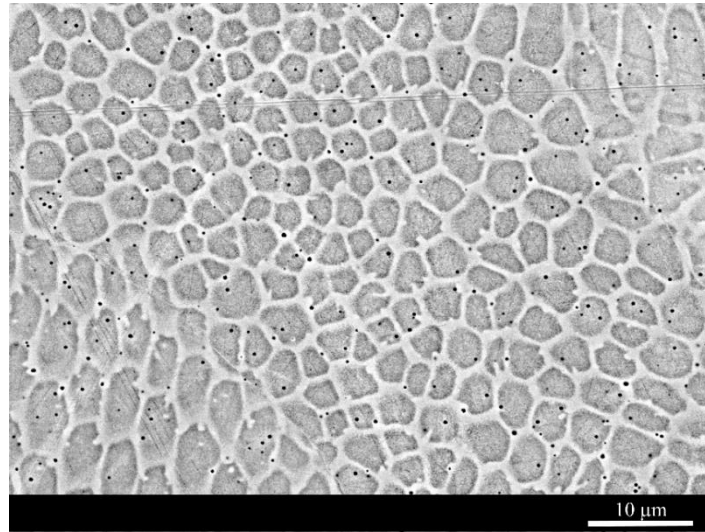


*Fig. 1 : SEM micrograph (BSE mode) of SS 316L fabricated by directed energy deposition, leading to a cellular microstructure (aqua regia etched).*

The main drawback of SS 316L is its relatively weak resistance to wear. Improvement in wear resistance can be achieved by the introduction of a harder reinforcement during fabrication by Directed Energy Deposition (DED) [3,21,22], creating a Metal Matrix Composite (MMC) deposit on the surface of the SS 316L part [22–26]. DED allows to handle two different powders that are fed into a focused laser beam while being scanned across a substrate, thus leaving behind a coating or an object. Among the possible reinforcements, tungsten carbide (WC) is a promising candidate due to its hardness, chemical affinity with Fe-based alloys and theoretical melting temperature higher than 2200°C. WC carbide application as reinforcement in thin coatings has already been considered by numerous studies, where the focus has been given to the nature of the out-of-equilibrium microstructures [23,28–30] and the improvement of the mechanical properties [21,22,27,31]. Indeed, because of carbide dissolution by interfacial reactions with the molten metal, the composition of the original SS 316L is enriched in W and C [25,31]. This enrichment modifies the solidification route and leads to the precipitation of hard solidification carbides in the intercellular spaces and to the formation of connection layers around the partially dissolved carbides linking them to the matrix [25,30–32]. In particular, in a previous study of SS 316L+WC composites by the present authors [24], the solidification route has been elucidated and the solidification carbides have been identified as  $M_6C$ ,  $M_{23}C_6$  and  $M_4C$ . Moreover, the impact of the local reheating due to the deposition of the following track and the formation of a heat affected zone (HAZ) as a result of microstructure coarsening and of the dissociation of the  $M_4C$  carbides has also been studied [24]. However, little attention has been given so far to the local variation of the microstructure and mechanical properties as a function of height in a thick deposit as a result of local variations of the thermal history during the solidification of the composite material.

Indeed, in DED, as the build height and the process time increase, the heat accumulates in the deposit, which results in the rise of the average temperature of the track [15–17,33]. At the beginning of the deposition, the first layer can efficiently transfer heat into the cold substrate generating a large thermal gradient and a high cooling rate. With the deposition of the subsequent layers, the maximum temperature increases resulting in a decrease of the thermal gradient and cooling rate [15,34]. Therefore, the overall temperature of the building deposit is rising as well. However, the temperature increase slows down with the progress of the deposition since heat loss, convection and radiation effects on the side of the deposit increase as well [16]. These changes in the thermal gradient and cooling rate affect the solidification route, leading to a coarsening of the microstructure and to local variations of the mechanical properties [11,35].

Macrohardness is one of the most commonly evaluated mechanical property. Measurements are quick and provide a simple indication of the effect of microstructural features such as the phases in presence, the composition of the alloy and the grain size [17,33] on mechanical properties. In opposition to the yield strength or wear resistance that quite often shows a significant scatter in literature as a result of internal defects or due to different measurement conditions [19,20,33,35], macrohardness is commonly considered to evaluate the mechanical properties in DED coatings and thick deposits, since it allows the detection of microstructural variations caused by heat accumulation in as-built conditions [8,16,17,36–38]. Indeed, the local evolution of hardness with deposit height can be understood in relation to both grain and cell sizes [15,34,39,40], with the exception of the last deposited layer which has a different thermal history. In this regard, it is widely reported that the macrohardness of a large variety of AM alloys constantly decreases with increasing distance from the substrate due to a coarsening of the microstructure [11,33,35]. Interestingly, in this work, the 316L+WC composite material exhibits a different evolution, with an initial increase of the macrohardness up to 6 mm from the 316L substrate and then a decrease upon further increase of the deposit height.

The current work thus focuses on this abnormal variation of the local hardness in a thick MMC deposit based on SS 316L and 20% (in volume) of WC carbide. Macrohardness and nanoindentation grids are carried out to detect the local variation of properties when the deposition process goes on. Furthermore, a detailed microstructural characterization of the core of the tracks is performed, including the measurement of the grain size by electron backscattered diffraction (EBSD) analyses and of the cell size by a linear intercept method. In particular, in order to capture an adequate representation of the size of the microstructure, a linear intercept method involving the average volume-weighted size value ( $d_v$ ) is applied [41,42]. Finally, in order to establish a general scenario for the observed evolution, the interactions between the WC reinforcements and the molten metal during solidification and their variation with the progress of the deposition are considered.

## 2. Materials and Methods

### 2.1. Fabrication

This work considers a thick MMC deposit composed of SS 316L and reinforcements of WC particles. It has been deposited on a SS 316L substrate using a 5-axis Irepa DED system with a Nd-YAG laser source. The two powders used for the production of the parts were SS 316L and WC powders with a granulometry between 50 and 200  $\mu\text{m}$ , having a spherical shape [25]. The laser power ( $P$ ) was varied between 400-570W for a corresponding traverse speed ( $V$ ) of 270-290 mm/min, and the layer thickness was set equal to 600  $\mu\text{m}$ . The moving direction was maintained in between two successive layers, following in loop 4 different paths as shown in Fig. 2a. A shift of a half-track width was applied every two layers to allow a good overlapping of the layers. The stream of powder was focused into the laser beam by an inert gas flow and directed towards the substrate at an angle of 38–45°. 19 layers-thick stainless steel 316L – WC deposits were produced with 20% in volume fraction of WC. The final dimensions of those deposits were 35 x 35 mm side length and 14 mm height (Fig. 2a). Furthermore, thick stainless steel 316L deposits were fabricated as reference with the same parameters on a SS 316L substrate (Fig. 1).

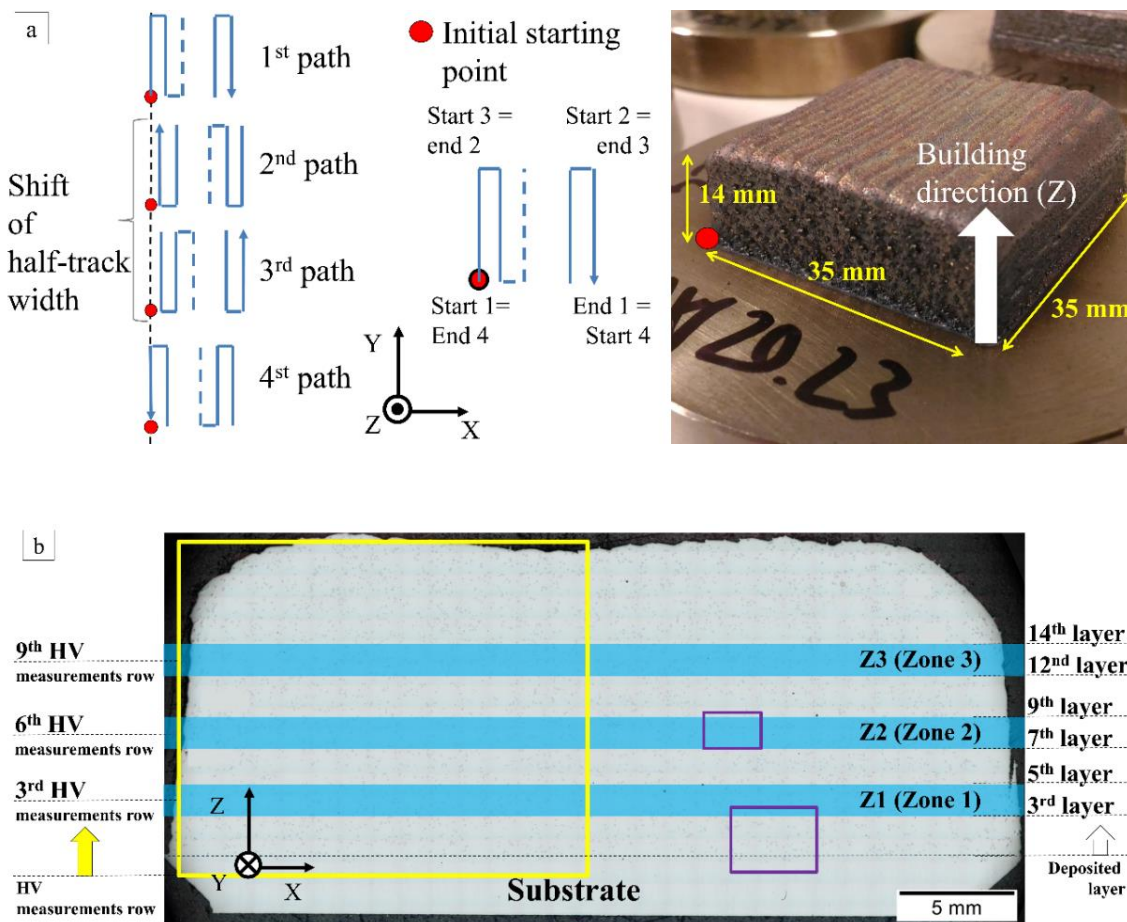


Fig. 2 : (a) Deposition strategy and dimensions of the sample; (b) Zones selected for analyses on the cross-section.

## 2.2. Sample preparation and metallographic characterization

The samples were machined by spark erosion, embedded in phenolic resin and then polished to a mirror finish, as shown in Fig. 2b. In addition, a chemical etching (aqua regia i.e. 55% HCl, 20% HNO<sub>3</sub> and 25% of methanol) was applied to reveal the cell boundaries.

Optical microstructural observations were carried out by means of an Olympus BX-60M microscope equipped with a motorized stage and a UC-30 digital camera. Stream Analysis® software for data processing was used to calculate the distribution of WC particles on the xz-plane (Fig. 2b). The areas of interest previously identified under optical microscope (OM) were analysed with SEM, using a Philips XL30 FEG-ESEM microscope equipped with a 10 mm<sup>2</sup> Bruker SDD type EDS detector, and a retractable Quantax e-Flash (Bruker) EBSD camera. Chemical analyses were carried out by means of a Zeiss Sigma 300 field emission gun SEM equipped with two Bruker EDX detectors (XFlash® 6|30 SDD energy dispersive spectrometer). The operating conditions used for data acquisition were 20 kV acceleration voltage, 20nA and 8.5 mm working distance.

The WC particles distribution was considered only in the central zone of the sample to avoid any imprecise overlapping of the layers at the sample edges. The particles were considered in the range of 20-150 µm to verify the actual size of the WC by optical and SEM images. The amount of the WC carbides was then plotted every 50 µm, starting below the substrate level (dotted line in Fig. 2b) to account for the few carbides present in the substrate melting zone of the first layer, up to 14 mm from the substrate. Further analyses were carried out to correlate quantitative microstructural features with macro- and nano-hardness variations (see sections 2.3 and 2.4).

The size of the subgrains or hierarchical cellular structures is commonly measured by automatic image analysis (e.g. linear intercept method) [15,34] or by direct observations on SEM or Optical Microscope (OM) [39,40]. These measurements are time consuming, as they often require to trace manually the cell boundaries, and as they consider a small statistical population. Moreover, they do not allow to detect the actual size distribution, especially in AM heterogeneous microstructures [19,36]. Instead, in this work, the linear intercept method in four evenly spaced directions was used, considering the average volume-weighted cell size ( $d_v$ ) [41,42]. This method, commonly applied to grain size estimation, uses a rule of mixtures approach for determining a characteristic size of a heterogeneous microstructure. The average volume-weighted size value is able to account for the size dispersion of a large population in just one value. This approach gives a better representation of the main size population than the classical average value. The average volume-weighted cell size was calculated using OM images at a magnification of 400x, in a zone corresponding to the first 11 rows of hardness measurements (Fig. 2b), so as to evaluate the size evolution with height. At every height, minimum 10 images were considered until reaching stability of the average value ( $A_{v_n}$ ) [7]. The stability was achieved when the mean value and the standard deviation exhibited a variation lower than 5% at the addition of a new image.

Furthermore, special attention was given to the zones shown in light blue in Fig. 2b. EBSD analyses were carried out at a magnification of 100x to estimate the average grain size using ESPRIT<sup>®</sup> processing software (Bruker). EBSD analysis allows to detect efficiently the grain size distribution by considering the misorientation angle (commonly fixed at 15°) in order to distinguish between two adjacent grains [19,24,39]. Z1 (Zone 1 – 2.5 mm from the substrate) was set up based on the nanoindentation tests and in order to avoid the substrate dilution zone. The grain size was measured every 3 mm (i.e. at 5.6 and 8.6 mm from the substrate) considering three deposited layers for each zone. The measurements have been carried out using an accelerating voltage of 20 kV, at 15 mm of working distance with a 30 µm aperture. A pixel size of 3.12 µm was set for EBSD images.

### **2.3. Macro-Hardness test**

10 kg Vickers hardness tests were carried out on both the reference 316L and the composite deposits using a universal hardness device equipped with an electronic cell force (in as polished state). Specifically, a grid of 18 x 14 measurement points was carried out in the yellow rectangle of Fig. 2b, in order to assess variations in hardness depending on the deposit height. A distance of 1 mm was set between test points (horizontally and vertically) to avoid interactions between adjacent indents [37,42]. The results were considered calculating the average value and the standard deviation for each row.

### **2.4. Nanoindentation grids**

The nano-hardness analyses are conducted by means of nano-indentation grids on the violet rectangles in Fig. 2b. The bottom zone considers the first three deposited layers, while the middle zone considers the seventh through to the ninth deposited layer. The nano-indentations were carried out using a HYSITRON TI 950 TriboIndenter<sup>TM</sup> at controlled displacement equal to 2000 nm using a Berkovich indenter tip on a high load transducer. The load was continuously monitored. All curves were selected deleting a few erratic measurements involving pop-in, detection delays and cracking. The displacement was chosen based on the phases average size in order to consider all phases and local variations of properties. Owing to the chosen displacement, a minimum distance of 25 µm was maintained between the indents in order to avoid any overlapping of their affected volumes [43–45]. The most representative two grids are reported in this study. For a clearer graphic representation of the local modifications, intermediate points between the actual nano-hardness indents were generated in MATLAB using a “triangle-based cubic interpolation” as in the case of the macro-hardness grid [37,45].

### 3. Results

#### 3.1. Microscopy characterization

##### 3.1.1. Distribution of WC carbides in the composite

The result of the image analysis on the central part of Fig. 2b is shown in Fig. 3. The positions of the WC reinforcements were located on the  $xz$ -plane, perpendicular to the moving direction of the laser during deposition. This distribution is plotted in Fig. 3a and superimposed on the original image in Fig. 3d. The distributions along the  $z$  and  $x$  axis are plotted respectively in Fig. 3b and c. The distribution of the WC reinforcements appears homogeneous on both axes with an average reinforcement of 65 particles every 50  $\mu\text{m}$  on the  $x$  axis and 130 particles on the  $z$  axis. The irregular top surface of the deposit leads to slightly higher values at the sides of the sample on the  $x$  axis and to a smaller value at the top of the considered zone on the  $z$  axis. Slight local variations observed on the  $z$  axis are due to random fluctuation of the reinforcement size during the deposition. Indeed, small particles among the original WC powder size distribution tend to melt completely in the melt pool, while large WC particles tend to be only partially dissolved, thus leaving an undissolved core [27].

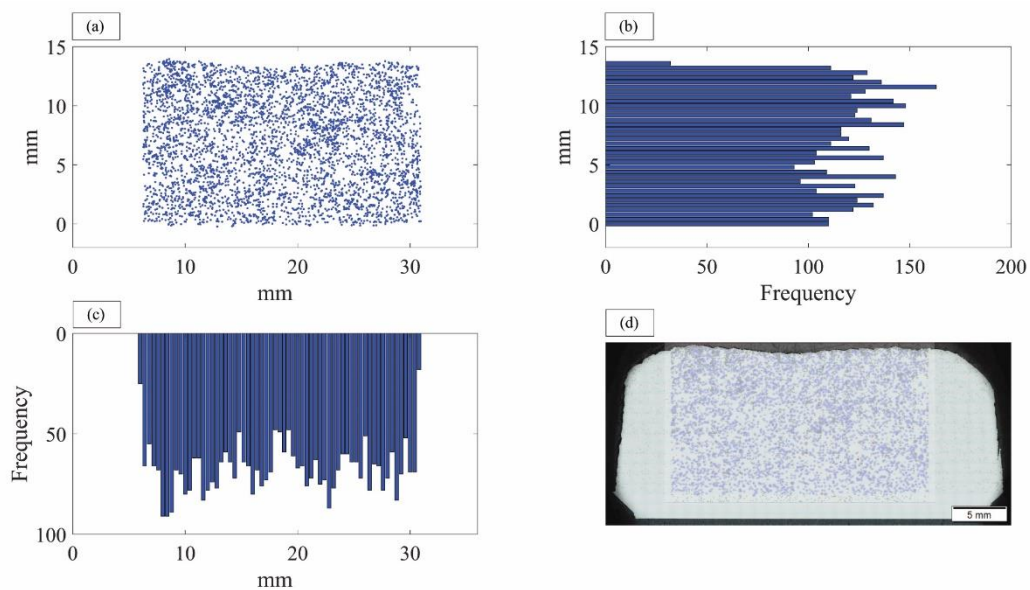


Fig. 3 : Position of undissolved WC on the  $xz$ -plane (a and d); distribution of undissolved WC along the height ( $z$ -axis) (b) and the width ( $x$ -axis) (c) of the deposits.

##### 3.1.2. Microstructure of the 316L+20%WC composite

The microstructure of the MMC is shown in Fig. 4. WC reinforcements are well distributed in an austenitic matrix reinforced by a network of new solidification carbides. As mentioned previously, the formation of these new  $(\text{W}, \text{Cr})_x\text{C}_y$  carbides results from the partial dissolution of the original WC powders in the molten metal matrix [22,23,25]. As shown in [25] by the present authors, these carbides are identified as  $\text{M}_6\text{C}$ ,  $\text{M}_{23}\text{C}_6$ ,  $\text{M}_4\text{C}$  and  $\text{WC}_{1-x}$  carbides based on the cross consideration of SEM, EDS

and EBSD analyses. The new solidification carbides are observed together with a crown composed of a mixture of carbide and of pure tungsten precipitates around the cores of the original WC. This reaction crown forms a connection layer between the reinforcements and the matrix [25,30,31]. Enrichment of the initial 316L alloy with W is observed, which depends on the volume fraction and size of the reinforcements [27,46].

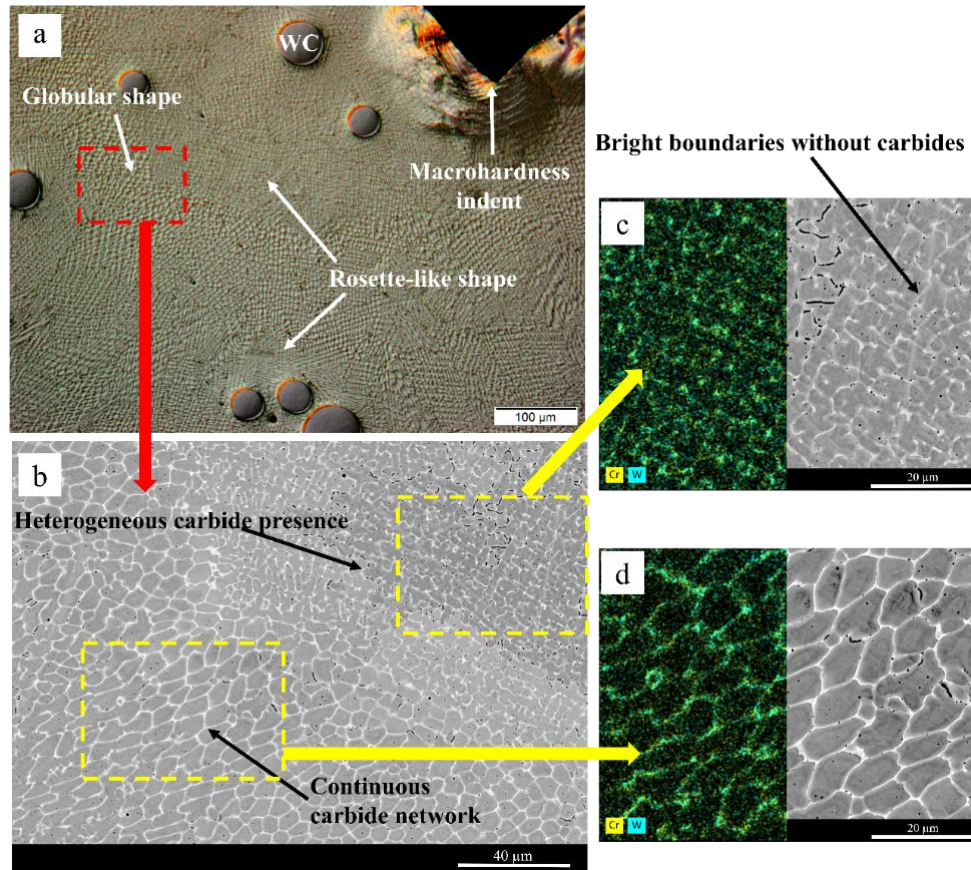


Fig. 4 : (a) Optical micrograph (200x) of the composite microstructure with a macro-hardness indent performed at 6 mm from the substrate. (b) SEM micrograph (BSE mode) corresponding to the microstructure in the red square in Fig. 4a. SEM micrographs corresponding at the rosette-like shape (c) and the globular shape (d) with the Cr and W elemental distribution.

The dissolution of the original WC particles in the metallic matrix decreases when the WC content increases. Dissolution is enhanced upon decreasing the WC size, at a given volume percentage [27,29,46,47]. The W enrichment of the SS316L matrix starts from the first track and then increases with increasing height and number of layers, as shown in Fig. 5a. Indeed, the composition of the first layer (excluding WC carbides) exhibits 5.9 wt.% of W due to the dissolution of the smaller WC carbides. The average W content then increases during the deposition. In zone Z1 (Fig. 2b), the average W content is around 6.7 wt.% with some local peaks at 12-13 wt.%. Instead, in zone Z2 and Z3, the average value is stable at 9.5-10 wt.% as shown in Fig. 5b.

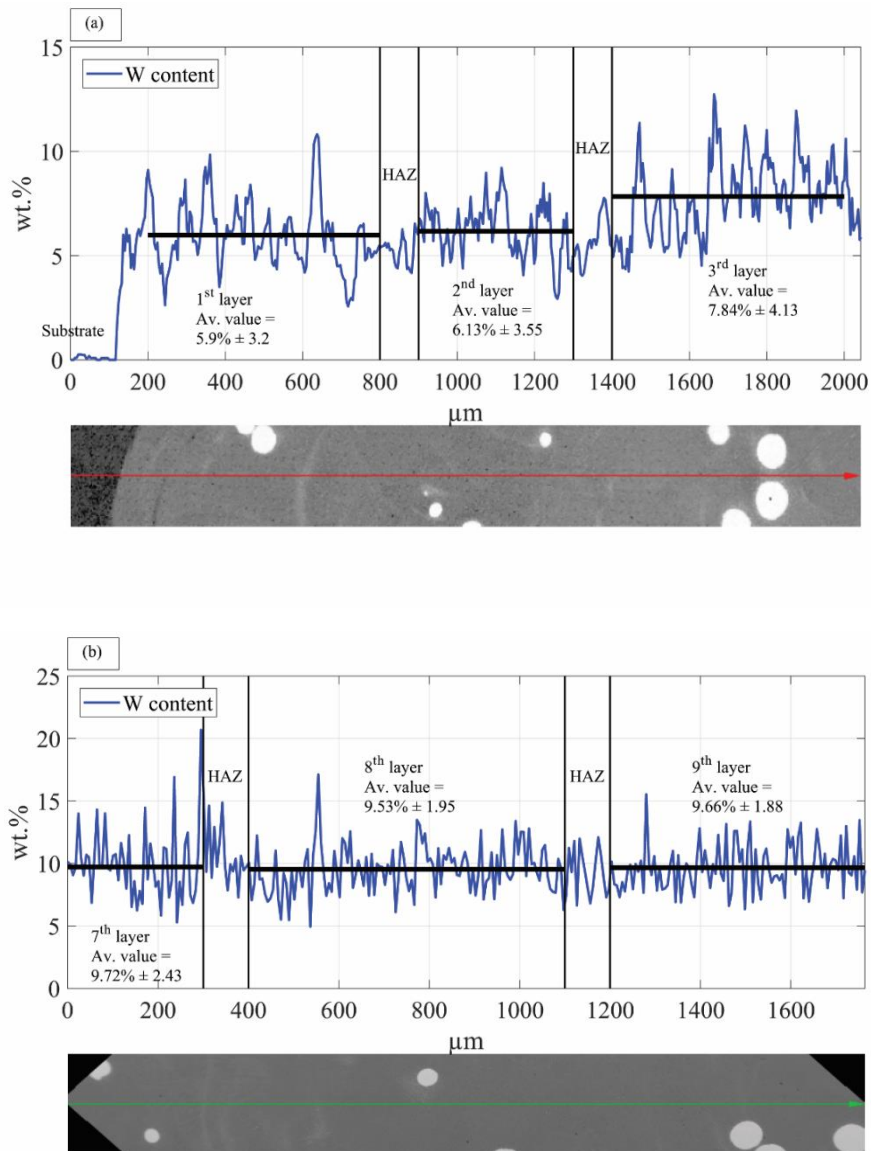


Fig. 5 : (a) SEM/EDS profile analysis across the substrate and first three deposited layers. (b) SEM/EDS profile analysis across the seventh to ninth layers. Chemical analyses were carried out every 4 μm. The average value of the three different layers are reported and plotted as black lines.

As shown in Fig. 4a and b, the reinforced matrix presents a dendritic-cellular morphology. The cells exhibit a globular shape and a carbide network clearly underlines the cell boundaries, as shown in Fig. 4d. On the other hand, degenerated cells with various shapes reminder of dendritical solidification (rosette-like, stretched or irregular) are observed around the WC reinforcements (Fig. 4c) [48]. Chemical segregations in the cellular or rosette-like dendritic zones differ significantly. W and Cr are homogeneously distributed in carbides at the globular cell boundaries (Fig. 4d). By comparing Fig. 4c and d, it appears that the rosette-like shape microstructure exhibits a smaller cell size with some carbide-less boundaries similar to the bright boundaries observed in the reference SS 316L microstructure (Fig. 1), as also reported in [6,9,19]. Indeed, in rosette-like cells, W and Cr are heterogeneously distributed and the BSE micrograph of Fig. 4c shows bright boundaries with a high amount of heavy elements like

Cr and W. Columnar cellular and dendritic solidification are observed throughout the deposit. The proportion of the rosette-like cells increases with increasing height.

### 3.1.3. Grain and Cell size evolution

The evolution of the grain and cell size as a function of height inside the 316L+20%WC deposit is reported in Fig. 6. The overall average volume-weighted cell size of the deposit is  $3.1 \mu\text{m}$  and the average grain size is  $79.1 \mu\text{m}$ . The cell size tends to increase slightly with increasing height. Moreover, the standard deviation varies depending on the position due to the change of the proportion between the two morphologies (globular and rosette) observed in the deposit (Fig. 4b), with rosette-like cells exhibiting a lower cell size at a given height.

As mentioned above (see section 1), the grain size in AM parts generally increases with the increase of the build height since heat accumulates during deposition [16,17,33]. In contrast, in the 316L+20%WC deposit, the measured grain size exhibits an uncommon trend when compared to similar alloys processed by DED [33,35,38] (Fig. 2b). Indeed, the grain size decreases from Z1 to Z2, and then increases from Z2 to Z3. Because over 500 grains were included for each grain size distribution analysis, the results should be considered reliable to represent the state of the microstructure [30].

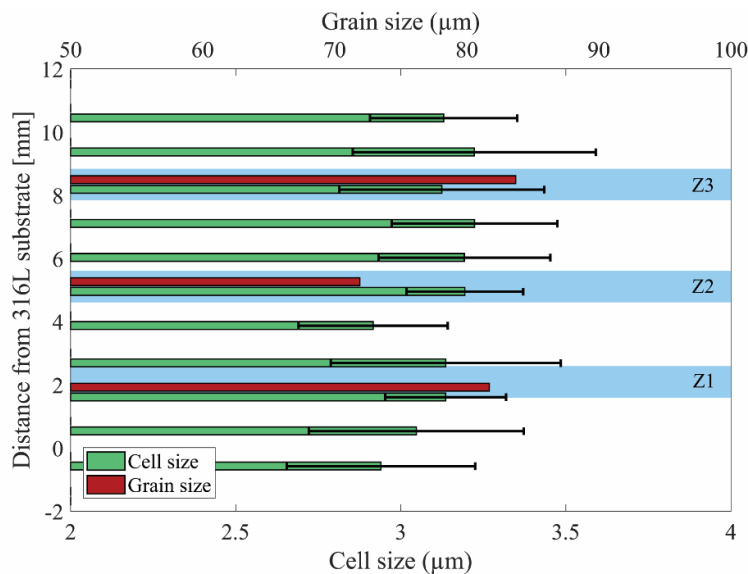


Fig. 6 : Cell size measured at the heights corresponding to the macro-hardness rows and grain size measured in the 3 zones highlighted in blue (as in Fig. 2).

## 3.2. Macro-hardness

The results of the two macro-hardness grids on the 316L+20%WC composite and 316L reference are shown in Fig. 7. The hardness line below 0 is related to the 316L substrate. The influence of the WC particles on the hardness was determined. The average hardness of the 316L deposit is 197 HV, slightly lower than that of the substrate at 204 HV. The hardness of the 316L deposit constantly decreases with increasing distance from the substrate due to the coarsening of the microstructure [2,6,8,29,33,38].

The reinforced microstructure of the composite exhibits an average hardness value of 337 HV with a large standard deviation due to the presence of partially dissolved WC, with local value as high as 450-500 HV. The standard deviation is higher in some rows of the grid due to a locally higher number of partially dissolved carbides [27,46], e.g. at 12 mm from the substrate. The hardness values increase up to the 6<sup>th</sup>-7<sup>th</sup> measurement row ( $\pm 6$  mm from the substrate). The hardness values then decrease slightly but constantly, up to the top of the deposit.

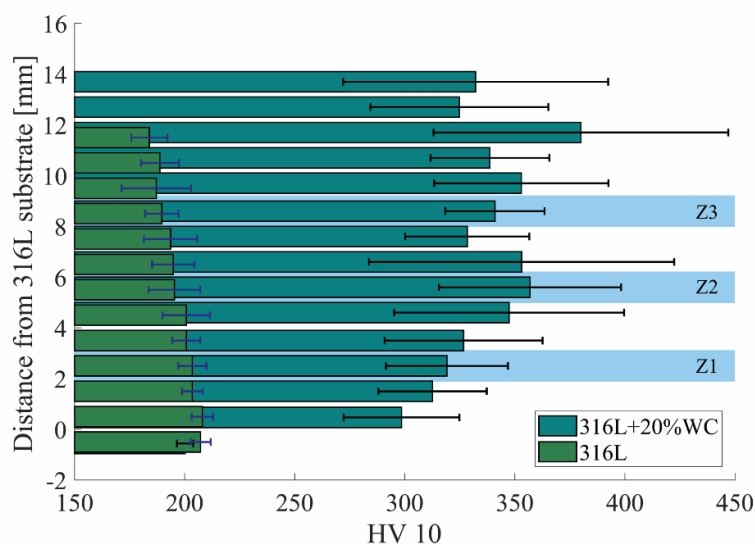


Fig. 7: Macro-hardness evolution of the 316L+20%WC deposit and of the reference 316L deposit fabricated with the same parameters, with the relative standard deviation for each measurement row.

### 3.3. Nanoindentation tests

The nanoindentation maps are shown in Fig. 8 and in Fig. 9. The cores of the large WC carbides are out of scale with a nanohardness of 30-32 GPa [45]. The first three layers exhibit a continuous increase in the average nanohardness, as shown in Fig. 8a where dashed lines underline tracks belonging to different layers. On the other hand, in Fig. 9a the nanohardness of Z2 is rather homogeneous.

In Fig. 8b the first deposited layers exhibit a brighter colour than the substrate due to the change of composition as a result of the partial dissolution of WC. This change corresponds to a high gradient of nanohardness between the softer 316L substrate (2-3 GPa) and the metal matrix of the first three layers (3-6 GPa). Fig. 8c shows the microstructure corresponding to the red square on the nanoindentation map of Fig. 8a. A comet-tail shaped area rich with solidification carbides (4-4,5 GPa) surrounds a WC core and its carbide crown (4,5-6 GPa) [25]. Such WC comet-like tails are observed only in the first two layers of the deposit. They are formed by the partial or total dissolution of the reinforcements and follow their movements in the melt pool due to the Marangoni effect [3,10,24,27,47]. In Z1, the nanohardness value increases with the increase of the height up to the third layer, together with the

content of solidification carbide. Nevertheless, at the scale of a given track, nanohardness is relatively homogeneous.

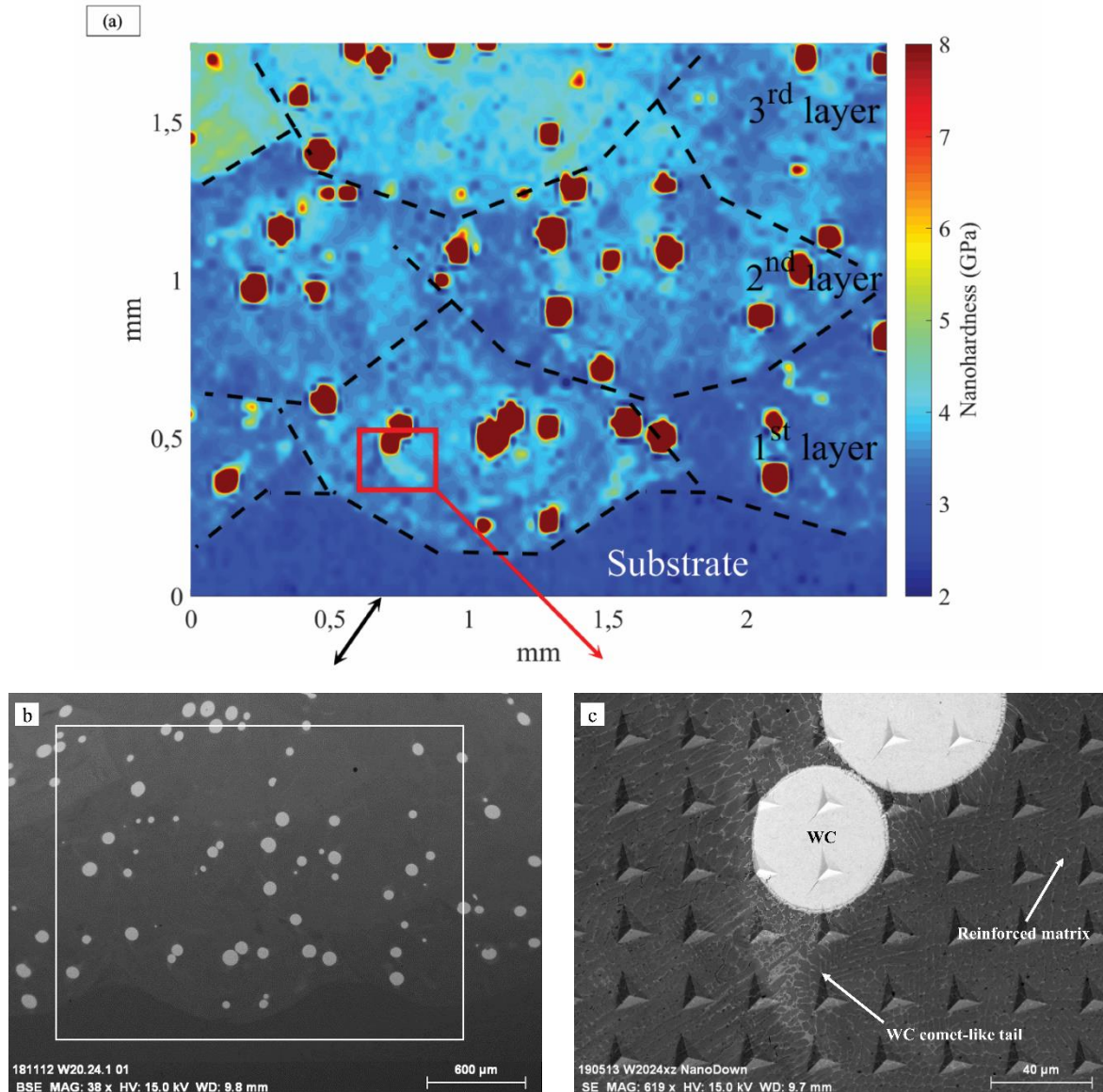


Fig. 8 : (a) Nanoindentation map of the first 3 deposited layers highlighted by the white rectangle in the SEM micrograph (b). (c) BSE micrograph of the microstructure observed in the first deposited layers.

In the zone shown in Fig. 9b, the nanohardness map is relatively uniform with a value of 3-6 GPa as observed in the third layer in Fig. 8a. A typical microstructure after nanoindentations is reported in Fig. 9c, where rosette-like cells are observed with a quasi-continuous network of solidification carbides. The rosette-like and the cellular morphologies do not exhibit large differences in nanohardness value. The network of solidification carbides deforms during the indentation test without cracks [48]. Comet-like tails are not observed in this zone. The microstructure in the single track is homogeneous with a locally higher concentration of carbides close to the partially dissolved WC particles.

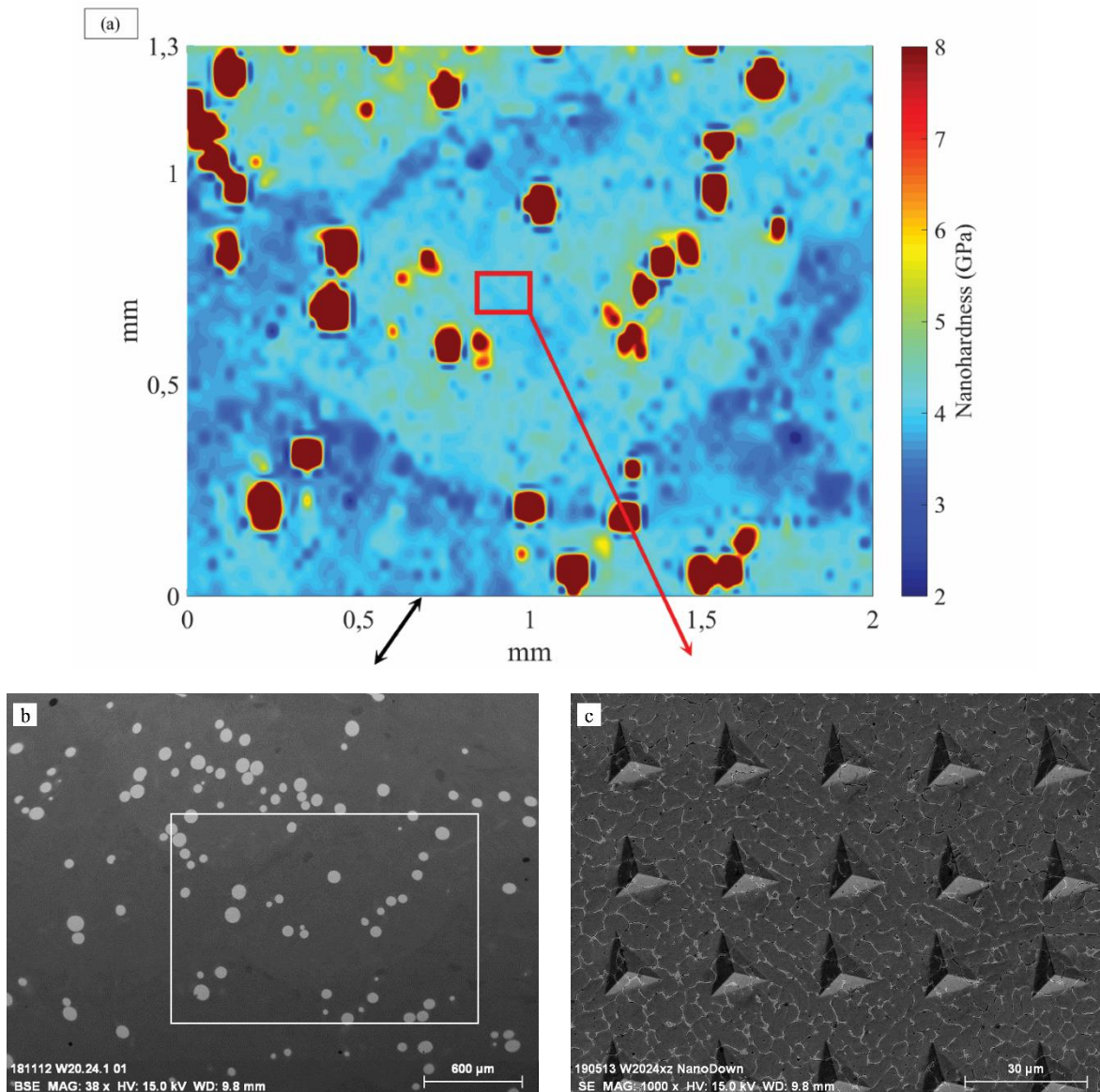


Fig. 9 : (a) Nanoindentation map of a track of the 8<sup>th</sup> deposited layer highlighted by the white rectangle in the SEM micrograph (b). (c) BSE micrograph of the red rectangle in Fig. 9a.

## 4. Discussion

### 4.1. Reinforcement interactions with the matrix

The presence of WC particles during the deposition of 316L+20% WC composite leads to the formation of a new reinforced microstructure (Fig. 4), exhibiting obvious differences in comparison to the hierarchical microstructure of the parent SS 316L (Fig. 1) processed by AM [9,19,20]. The partial or total dissolution of the large WC carbides during fabrication, followed by the precipitation of new solidification carbides, leads to this new microstructure [25,27,29,31]. Leaving aside the formation of a HAZ that has already been discussed in details in [25], the microstructures observed in section 3 exhibit variations depending on the location in a given melt pool (Fig. 4) but also, at a larger scale, as a function of height in the thick deposit (Fig. 7). These latter variations that are due to a combination of phenomena occurring during fabrication as Marangoni convection, heat accumulation, and the presence of partially dissolved WC in the melt pool [4,24,25,40] are discussed hereafter.

#### 4.1.1. W enrichment of the 316L melt pool

As observed first in classical welding and in most AM technologies, surface tension gradients depending on the process parameters lead to the occurrence of the Marangoni effect, i.e. fluid flows patterns directed inward according to the moving direction of the laser [3,24,36,49]. Similarly to radioactive tracker particles during a nuclear medicine test, some WC particles are observed to exhibit a comet-like tail marking their movement (Fig. 8 and Fig. 10a), as they are transported by the flows [10,24,40,50]. In addition, particle shape may influence the movement through the buoyancy effect [18,24,47]. The carbide structures forming the comet-like tail are observed only in the first two layers of thick deposits (Fig. 8c).

As consequence of the temperature rise due to the heat accumulation, liquid lifetime and Marangoni effect increase with the increase in height [10,15,16,36,51]. As shown in Fig. 10b, under those conditions, the transport of the WC particles is enhanced resulting in an increase of the liquid in contact with a given particle and in a stronger mixing of the melt pool [10,51]. This increasing interaction leads to a larger quantity of elements dissolved in the liquid until the saturation of the liquid is reached [32], as measured at 9.5-10% of W (%wt.) (Fig. 5b). Indeed, the W content in the matrix increases upon increasing height (Fig. 5a) and it is also related to local variation of the quantity of WC particles in a given track (Fig. 8b) [27,29]. As shown in Fig. 8b, in the third layer, the comet-like tails are not observed and the microstructure is more homogeneous due to the stronger mixing of the melt pool. In addition, the nanohardness is higher and more homogeneous than in the first two deposited layers (Fig. 8a). Indeed, the stronger mixing results in a more homogeneous distribution of W and C in the molten metal and leads to a general reinforcement of the track after solidification (Fig. 4b and Fig. 10b), as opposed to the formation of the comet-like tails in the first two layers (Fig. 10a).

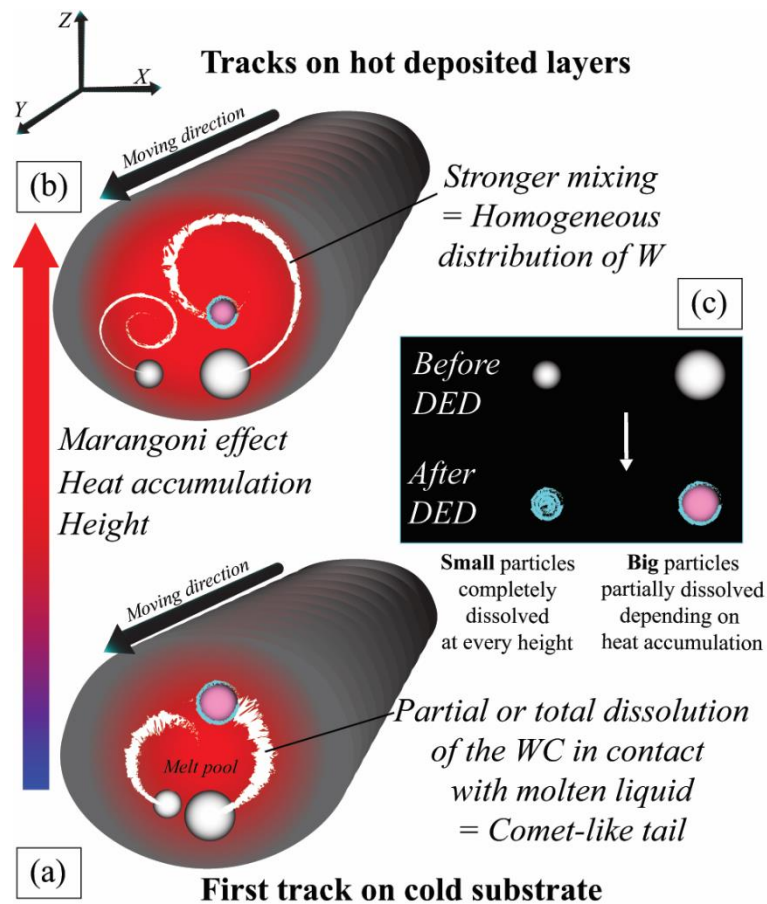


Fig. 10: Schematics of (a and b) heat accumulation effect on the mixing of the melt pool through Marangoni flows during deposition and (c) the dissolution of the WC particles depending on their initial size.

Nevertheless, as shown in the OM observations (Fig. 3), the increase of the interaction between WC carbides and melt pool does not lead to a clear decrease in the number of carbides. Considering the W content observed in the first deposited track (5.9 wt.%) and the saturation observed in zone Z2 (9.5-10% wt.%) in Fig. 5, it is supposed that the smallest carbides of the initial WC powder are completely dissolved in the molten metal already in the first layer. On the other hand, the large ones are partially dissolved leaving their core in the final microstructure (Fig. 10c). With the progress of the deposition, the dissolution of any given large WC carbides increases slightly until the liquid is saturated with W (Fig. 5). The detection of this phenomenon by OM is not possible since the detected size of a spherical particle is affected by the position of the observation plane. In general terms, the image analysis provides a valid value only when the cross-section corresponds to the diameter of the particle.

#### 4.1.2. Solidification route

The optical and SEM micrographs of Fig. 4 reveal two different types of reinforced microstructures i.e. a rosette-like shape structure, on the one hand, and a globular structure on the other hand. Morphological and chemical observations of these two types of microstructure shed light on the effect of the presence of the partially dissolved WC particles in the track during solidification. Indeed, the rosette-like or

dendritic morphology is observed around the WC particles while a cellular morphology is observed in the rest of the track, further away from the WC particles (Fig. 4a). The rosette-like morphology appears with a smaller size (Fig. 4c) and stronger chemical segregations, in particular of W and Cr, in comparison to the nearby cellular morphology (Fig. 4d).

Solidification features under different heat source configurations can be rationalized by considering melt pool parameters such as the temperature gradient ( $G$ ), the solidification rate ( $R$ ) and the cooling rate ( $G \times R$ ) in the  $G$ -versus- $R$  diagram [1,24,34,49,52] (Fig. 11).

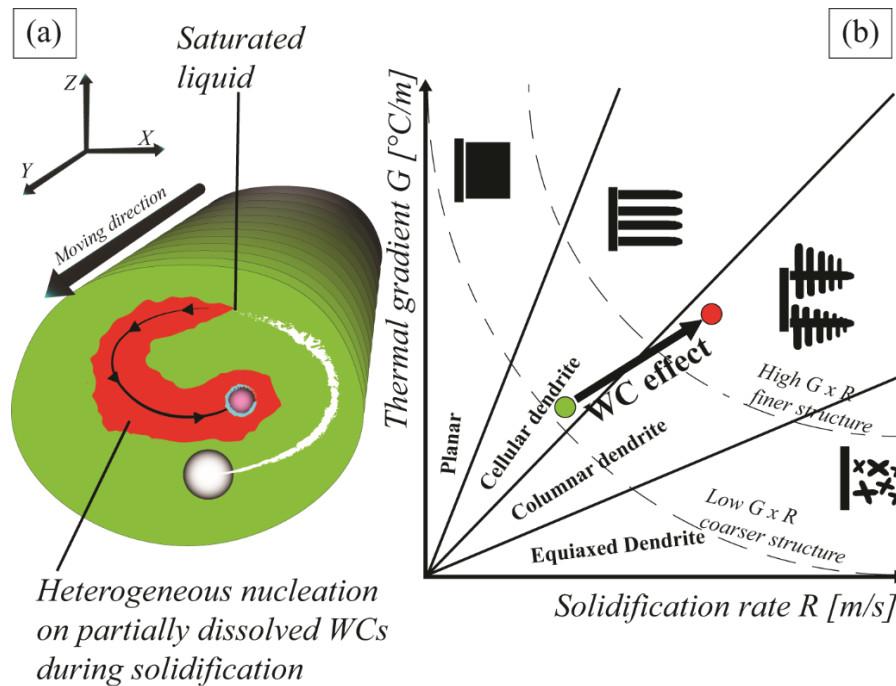


Fig. 11: Schematics view illustrating the effect of the WC movements on the morphology of the microstructure during (a) the solidification of the melt pool and (b) on the  $G$ -versus- $R$  diagram (adapted from [1,40,49]). The rosette-like morphology is located around the WC particles and on their paths after reaching liquid saturation with W (in red), while the cellular morphology is present in the rest of the track (in green).

The green zone of the melt pool in Fig. 11a and the green circle in the diagram of Fig. 11b correspond to the cellular solidification observed throughout the deposit. Instead, the red zone in Fig. 11a and the red circle in the diagram of Fig. 11b correspond to the cellular-dendritic solidification observed mainly around the WC particles. The presence of those WC particles moving in a liquid saturated with W promotes heterogeneous nucleation during solidification as WC reinforcements act as nucleation sites or grain refiner [30,32,49,50]. Indeed, stability of the nucleant particles in the saturated liquid and crystallographic matching between nucleation sites and matrix promotes grain refinement [22,30,50]. In addition, as reported in [48], fragmentation of the dendrites nucleated on the WC particles may occur due to turbulences of the molten metal or to plastic deformation of the dendrite arms. The fragments may then act as additional heterogeneous nuclei for solidification inside the melt pool. The resulting

refinement effect is marked on the G-versus-R diagram (Fig. 11b) based on the microstructural observations. Both G and R increase in view of the change of morphology and finer cell size (Fig. 4b).

The increase in the thermal gradient (G) is related to the heat accumulation during deposition. The temperature of undissolved WC particles is related only to the energy brought by the laser during deposition. The temperature of the liquid depends not only on the contact with the laser [24], but also on the temperature of the previously deposited material that acts as an apparent substrate. Thus, the increase in the peak temperature affects mainly the liquid part of the melt pool [15], but has no direct effect on the WC particles. The local thermal gradient increases since the temperature of the WC remains stable, while the temperature of the liquid is rising as deposition progresses [16,32].

The increase in the solidification rate (R) is indirectly related to the temperature rise during fabrication. It is usually accepted that R is linked to the transverse speed (V) of the laser [51]. Furthermore, it is supposed that the motion of the WC carbides due to the Marangoni flows also has an effect on the solidification rate [10,24]. Indeed, the nucleation rate and the solidification rate increase with the increase of the liquid in contact with the heterogeneous nucleation sites, and thus with the increase of the mixing in the melt pool [49,51].

#### **4.2. Macro-Hardness evolution**

316L stainless steel manufactured by AM is known to exhibit a cellular hierarchical structure (Fig. 1), resulting in improved mechanical properties in comparison with the microstructures of the classical wrought material. Higher yield strength and larger elongation are related to the refinement of the grain size and to the collective effect of a hierarchical heterogeneous microstructure [1,19,20,35]. Nevertheless, in metallic alloys not susceptible to phase transformations, the hardness and the mechanical properties tend to decrease with the progress of a DED deposition [1,33,38]. With the building parameters given in section 2.1, this tendency was observed for the 316L reference specimens. The decrease of the hardness (Fig. 7) is related to the heat accumulation during the deposition of previous layers and the consequent coarsening of the hierarchical structure [16,33]. Both grain and cell size increase because of heat build-up [11,15,34].

Unlike the pure 316L and other alloys fabricated by AM, the 316L+20%WC composite exhibits an increase and then a slight decrease of hardness with increasing height. Fig. 7 shows this evolution with a maximum of macro-hardness observed in Z2 (Fig. 2b). EBSD analyses on the three zones Z1, Z2 and Z3 revealed a significant decrease of the grain size from Z1 to Z2 and then an increase from Z2 up to Z3 (Fig. 6). When looking at the cells, on the other hand, image analysis revealed a constant increase in the cell size as previously observed in other works [16]. This indicates that only the grain size evolution can be linked to the observed variation of the macro-hardness value, in accordance with the classical Hall-Petch strengthening mechanism [16,20,35,41,50]. Local temperature variations and their

effect on the interactions between WC particles and molten metal allow to better understand this evolution as will be explained hereafter.

Fig. 12a shows the evolution of the temperature gradient between the deposited layer and its apparent substrate with the progress of the deposition. The two observed solidification modes are illustrated by arrows (Fig. 12b), while the respective cooling rates are represented by  $\varphi$  and  $\zeta$  angles (Fig. 12a). With this representation, the cooling rate decreases with the increase in the relative angles. The maximum temperature of the deposited layer rises with the progress of the deposition until a steady state is reached due to the increase in the heat loss at higher temperatures [16,17]. As consequence, the temperature of the apparent substrate follows the same trend [13,15,34], but with a different initial slope. This representation is in agreement with the results of numerical simulations based on a 2D FE thermal model that has been recently developed in order to better quantify these temperature variations [53].

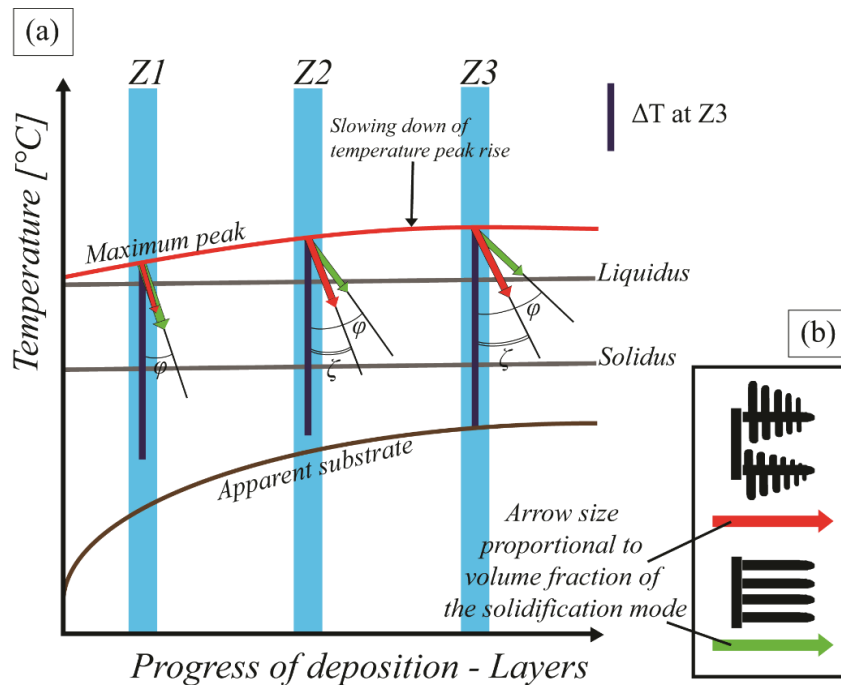


Fig. 12 : Representation of (a) the temperature evolutions of the maximum peak of the melt pool and the apparent substrate, and (b) the morphologies occurring with the progress of the deposition (colours referring to Fig. 11). The  $\Delta T$  at the top of the deposit (Z3) is placed in the two other zones (Z1 and Z2) in order to represent the decrease of the  $\Delta T$  between the melt pool and the apparent substrate during fabrication.

As explained in section 4.1, nanoindentation tests (Fig. 8) and chemical analyses (Fig. 5) in the first tracks (Fig. 10a) show that the liquid lifetime and the Marangoni flows are the lowest in the deposit due to the high temperature gradient between the first layer and the cold substrate [34]. Higher cooling rates are thus obtained in those layers [14]. With the progress of the deposition, the temperature gradient decreases leading to a continuous increase in dissolution rate, until the saturation of the liquid with W is reached. The W enrichment of the liquid (Fig. 5a) and the subsequent increase in the amount of solidification carbides lead to the increase in the hardness value (Fig. 7).

---

In zone Z1, WC carbides are locally observed to act as nucleation sites as a minor phenomenon due to the still low temperatures and the high cooling rates (small  $\varphi$ ) [15,24]. For this reason, in Fig. 12a the dendritic solidification is represented with a smaller arrow (Fig. 12b) and only the cellular solidification slope ( $\varphi$ ) is marked out. The modification of the 316L composition is the main reinforcing phenomenon leading to the formation of carbide structures (Fig. 8c) in a cellular reinforced microstructure [25–28].

As discussed in section 4.1.1, with the progress of deposition (Fig. 10b), the heat accumulation enhances the mixing in the melt pool and the liquid lifetime. As further discussed in section 4.1.2, these two conditions allow the saturation of the liquid with W and the stabilisation of the remaining WC particles as sites for heterogeneous nucleation. Where the saturation of the melt pool is reached (Fig. 11a), heterogeneous nucleation occurs on the remaining partially dissolved WC particles while these are moving in the melt pool [30,32,50]. Indeed, in zone Z2, the grain size (Fig. 6) decreases due to this refinement effect. At these heights, nanoindentation tests (Fig. 9a) and chemical analyses (Fig. 5b) showed a homogeneous microstructure with the formation of a finer rosette-like morphology mainly around the large WC reinforcements. In absence of WC particles, the saturated liquid solidifies into a reinforced cellular structure (Fig. 4a). As represented in Fig. 12a, the angle corresponding to the dendritic structure is smaller ( $\zeta$ ) than the cellular one ( $\varphi$ ) since the cooling rates of the rosette-like morphology lead to a finer microstructure (Fig. 4c and d) [15].

As deposition proceeds, the coarsening of the microstructure induced by the heat build-up overcomes the beneficial refining effect of the WC particles, thus leading to an increase in grain size (Fig. 6) and to a concomitant decrease of hardness (Fig. 7) [34,50]. As shown in Fig. 6, the cell size increases with increasing height, meaning that both cellular and dendritic morphologies were affected [20]. Consequently, the cooling rates associated with both solidification modes decrease with the progress of the deposition corresponding to the large angles in the representation of Fig. 12a.

## 5. Conclusions

- 316L+20%WC composite exhibits largely improved average macro-hardness (337 HV) in comparison to the reference SS 316L (197 HV), due to the presence of partially dissolved WC carbides and to a new reinforced matrix. The hardness of the thick deposit increases as a function of the height up to  $\pm 6$  mm from the substrate (360 HV) and then decrease slowly but constantly, reaching a value of 330 HV at the top of the deposit.
- Unlike SS 316L, heat accumulation during the DED of the composite may result in a favourable evolution of the local hardness by promoting an increase both in the dissolution of the WC particles until liquid saturation with W (9.5-10% wt.%) and in the homogenization of the melt pool through Marangoni convection. SEM observations and nano-indentation grids revealed the movements of the WC carbides in the melt pool through the WC comet-like tails. These carbide structures formed as a result of the interaction between the molten metal and the WC powders, while the WC particles are transported by Marangoni flow. With the progress of the deposition, the increase in the average temperature leads to an increase in the Marangoni effect and of the liquid lifetime.
- A cellular and a rosette-like morphologies are observed in the microstructure of the thick deposit. Detailed microstructural characterization reveals that undissolved WC particles act as sites for heterogeneous nucleation, leading to the formation of a finer rosette-like morphology. Based on previous works and on current microstructural observations, the two observed morphologies were located in the G-versus-R diagram.
- The variables affecting hardness were assumed and a scenario was determined considering three zones at different heights. In the bottom zone (Z1), the highest cooling rates in the deposit lead to the formation of a cellular heterogeneous reinforced microstructure. With the increase in the homogenization during deposition, the hardness increases due to the WC carbides acting as nucleation sites and thus promoting a finer rosette-like microstructure. In the middle zone (Z2), the hardness exhibits its maximum value. In the top zone (Z3), coarsening of the microstructure induced by the heat accumulation overcomes the beneficial refining effect of the WC particles, thus leading to an increase in grain size and to a concomitant decrease of hardness.

## Acknowledgements

This work has been supported by a subvention “Crédit classique” of the University of Liège, and by the European Fund for Regional Development and the Walloon Region under convention FEDER “Iawatha”. The authors acknowledge the CAREM of the ULiège for providing SEM/EDS/EBSDF facilities. They also wish to thank Sylvie Salieri for sample preparation, Samuel Rondia for the substrates preparation, Laura Zorzetto for helpful discussion, the Sirris Research Centre for access to the DED equipment and Hassan Bouzahzah for access to the Zeiss Sigma 300 SEM.

---

---

## References

- [1] T. DebRoy, H.L. Wei, J.S. Zuback, T. Mukherjee, J.W. Elmer, J.O. Milewski, A.M. Beese, A. Wilsonheid, A. De, W. Zhang, Additive manufacturing of metallic components – Process, structure and properties, *Prog. Mater. Sci.* 92 (2018) 112–224. doi:10.1016/j.pmatsci.2017.10.001.
- [2] D. Herzog, V. Seyda, E. Wycisk, C. Emmelmann, Additive manufacturing of metals, *Acta Mater.* 117 (2016) 371–392. doi:10.1016/j.actamat.2016.07.019.
- [3] A. Dass, A. Moridi, State of the art in directed energy deposition: From additive manufacturing to materials design, *Coatings*. 9 (2019) 1–26. doi:10.3390/COATINGS9070418.
- [4] S.M. Thompson, L. Bian, N. Shamsaei, A. Yadollahi, An overview of Direct Laser Deposition for additive manufacturing; Part I: Transport phenomena, modeling and diagnostics, *Addit. Manuf.* 8 (2015) 36–62. doi:10.1016/j.addma.2015.07.001.
- [5] W.J. Sames, F.A. List, S. Pannala, R.R. Dehoff, S.S. Babu, The metallurgy and processing science of metal additive manufacturing, *Int. Mater. Rev.* 61 (2016) 315–360. doi:10.1080/09506608.2015.1116649.
- [6] D.R. Feenstra, V. Cruz, X. Gao, A. Molotnikov, N. Birbilis, Effect of build height on the properties of large format stainless steel 316L fabricated via directed energy deposition, *Addit. Manuf.* 34 (2020) 101205. doi:10.1016/j.addma.2020.101205.
- [7] T. de Terris, O. Andreau, P. Peyre, F. Adamski, I. Koutiri, C. Gorny, C. Dupuy, Optimization and comparison of porosity rate measurement methods of Selective Laser Melted metallic parts, *Addit. Manuf.* 28 (2019) 802–813. doi:10.1016/j.addma.2019.05.035.
- [8] N. Ur Rahman, L. Capuano, A. van der Meer, M.B. de Rooij, D.T.A. Matthews, G. Walmag, M. Sinnavee, A. Garcia-Junceda, M. Castillo, G.R.B.E. Römer, Development and characterization of multilayer laser clad high speed steels, *Addit. Manuf.* 24 (2018) 76–85. doi:10.1016/j.addma.2018.09.009.
- [9] I. Todd, Metallurgy: Printing steels, *Nat. Mater.* 17 (2017) 13–14. doi:10.1038/nmat5042.
- [10] F. Wirth, S. Arpagaus, K. Wegener, Analysis of melt pool dynamics in laser cladding and direct metal deposition by automated high-speed camera image evaluation, *Addit. Manuf.* 21 (2018) 369–382. doi:10.1016/j.addma.2018.03.025.
- [11] A. Aversa, A. Saboori, E. Librera, M. de Chirico, S. Biamino, M. Lombardi, P. Fino, The role of Directed Energy Deposition atmosphere mode on the microstructure and mechanical properties of 316L samples, *Addit. Manuf.* 34 (2020) 101274. doi:10.1016/j.addma.2020.101274.
- [12] N. Hashemi, A. Mertens, H.M. Montrieux, J.T. Tchuindjang, O. Dedry, R. Carrus, J. Lecomte-Beckers, Oxidative wear behaviour of laser clad High Speed Steel thick deposits: Influence of sliding speed, carbide type and morphology, *Surf. Coatings Technol.* 315 (2017) 519–529. doi:10.1016/j.surfcoat.2017.02.071.
- [13] H.S. Tran, J.T. Tchuindjang, H. Paydas, A. Mertens, R.T. Jardin, L. Duchêne, R. Carrus, J. Lecomte-Beckers, A.M. Habraken, 3D thermal finite element analysis of laser cladding processed Ti-6Al-4V part with microstructural correlations, *Mater. Des.* 128 (2017) 130–142. doi:10.1016/j.matdes.2017.04.092.
- [14] R.T. Jardin, J.T. Tchuindjang, L. Duchêne, H.S. Tran, N. Hashemi, R. Carrus, A. Mertens, A.M. Habraken, Thermal histories and microstructures in Direct Energy Deposition of a High Speed Steel thick deposit, *Mater. Lett.* 236 (2019) 42–45. doi:10.1016/j.matlet.2018.09.157.
- [15] Y. Liu, J. Zhang, Z. Pang, Numerical and experimental investigation into the subsequent thermal cycling during selective laser melting of multi-layer 316L stainless steel, *Opt. Laser Technol.* 98 (2018) 23–32. doi:10.1016/j.optlastec.2017.07.034.
- [16] V. Manvatkar, A. De, T. Debroy, Heat transfer and material flow during laser assisted multi-layer additive manufacturing, *J. Appl. Phys.* 116 (2014). doi:10.1063/1.4896751.
- [17] Z. Xia, J. Xu, J. Shi, T. Shi, C. Sun, D. Qiu, Microstructure evolution and mechanical properties of reduced activation steel manufactured through laser directed energy deposition, *Addit. Manuf.* 33 (2020) 101114. doi:10.1016/j.addma.2020.101114.

- [18] G.L. Knapp, T. Mukherjee, J.S. Zuback, H.L. Wei, T.A. Palmer, A. De, T. DebRoy, Building blocks for a digital twin of additive manufacturing, *Acta Mater.* 135 (2017) 390–399. doi:10.1016/j.actamat.2017.06.039.
- [19] Y.M. Wang, T. Voisin, J.T. McKeown, J. Ye, N.P. Calta, Z. Li, Z. Zeng, Y. Zhang, W. Chen, T.T. Roehling, R.T. Ott, M.K. Santala, P.J. Depond, M.J. Matthews, A. V. Hamza, T. Zhu, Additively manufactured hierarchical stainless steels with high strength and ductility, *Nat. Mater.* 17 (2018) 63–70. doi:10.1038/NMAT5021.
- [20] L. Liu, Q. Ding, Y. Zhong, J. Zou, J. Wu, Y.L. Chiu, J. Li, Z. Zhang, Q. Yu, Z. Shen, Dislocation network in additive manufactured steel breaks strength–ductility trade-off, *Mater. Today.* 21 (2018) 354–361. doi:10.1016/j.mattod.2017.11.004.
- [21] M.R. Fernández, A. García, J.M. Cuetos, R. González, A. Noriega, M. Cadenas, Effect of actual WC content on the reciprocating wear of a laser cladding NiCrBSi alloy reinforced with WC, *Wear.* 324–325 (2015) 80–89. doi:10.1016/j.wear.2014.12.021.
- [22] D. Deschuyteneer, F. Petit, M. Gonon, F. Cambier, Processing and characterization of laser clad NiCrBSi/WC composite coatings - Influence of microstructure on hardness and wear, *Surf. Coatings Technol.* 283 (2015) 162–171. doi:10.1016/j.surfcoat.2015.10.055.
- [23] J. Wang, L. Li, W. Tao, Crack initiation and propagation behavior of WC particles reinforced Fe-based metal matrix composite produced by laser melting deposition, *Opt. Laser Technol.* 82 (2016) 170–182. doi:10.1016/j.optlastec.2016.03.008.
- [24] B. AlMangour, D. Grzesiak, J. Cheng, Y. Ertas, Thermal behavior of the molten pool, microstructural evolution, and tribological performance during selective laser melting of TiC/316L stainless steel nanocomposites: Experimental and simulation methods, *J. Mater. Process. Technol.* 257 (2018) 288–301. doi:10.1016/j.jmatprotec.2018.01.028.
- [25] T. Maurizi Enrici, O. Dedry, F. Boschini, J.T. Tchuindjang, A. Mertens, Microstructural and Thermal Characterization of 316L+WC Composite Coatings obtained by Laser Cladding, *Adv. Eng. Mater.* 13 (2020) 1–12. doi:10.1002/adem.202000291.
- [26] A.I. Mertens, J. Lecomte-Beckers, On the Role of Interfacial Reactions , Dissolution and Secondary Precipitation During the Laser Additive Manufacturing of Metal Matrix Composites : A Review, in: I. V Shishkovsky (Ed.), *New Trends 3D Print., I.V., InTech, Rijeka, Croatia, 2016*: pp. 187–213. doi:10.5772/63045.
- [27] X. Tong, F.H. Li, M. Kuang, W.Y. Ma, X.C. Chen, M. Liu, Effects of WC particle size on the wear resistance of laser surface alloyed medium carbon steel, *Appl. Surf. Sci.* 258 (2012) 3214–3220. doi:10.1016/j.apsusc.2011.11.066.
- [28] A. Mertens, T. L’Hoest, J. Magnien, R. Carrus, J. Lecomte-Beckers, On the Elaboration of Metal-Ceramic Composite Coatings by Laser Cladding, *Mater. Sci. Forum.* 879 (2017) 1288–1293. doi:10.4028/www.scientific.net/MSF.879.1288.
- [29] L. Song, G. Zeng, H. Xiao, X. Xiao, S. Li, Repair of 304 stainless steel by laser cladding with 316L stainless steel powders followed by laser surface alloying with WC powders, *J. Manuf. Process.* 24 (2016) 116–124. doi:10.1016/j.jmapro.2016.08.004.
- [30] I.T. Ho, Y.T. Chen, A.C. Yeh, C.P. Chen, K.K. Jen, Microstructure evolution induced by inoculants during the selective laser melting of IN718, *Addit. Manuf.* 21 (2018) 465–471. doi:10.1016/j.addma.2018.02.018.
- [31] H. Chen, D. Gu, K. Kosiba, T. Lu, L. Deng, L. Xi, U. Kühn, Achieving high strength and high ductility in WC-reinforced iron-based composites by laser additive manufacturing, *Addit. Manuf.* 35 (2020) 101195. doi:10.1016/j.addma.2020.101195.
- [32] M.A. Easton, M. Qian, A. Prasad, D.H. StJohn, Recent advances in grain refinement of light metals and alloys, *Curr. Opin. Solid State Mater. Sci.* 20 (2016) 13–24. doi:10.1016/j.cossms.2015.10.001.
- [33] J.S. Zuback, T. DebRoy, The hardness of additively manufactured alloys, *Materials (Basel).* 11 (2018). doi:10.3390/ma11112070.
- [34] P. Köhnen, M. Létang, M. Voshage, J.H. Schleifenbaum, C. Haase, Understanding the process-microstructure correlations for tailoring the mechanical properties of L-PBF produced austenitic advanced high strength steel, *Addit. Manuf.* 30 (2019) 100914. doi:10.1016/j.addma.2019.100914.

- [35] Z. Wang, T.A. Palmer, A.M. Beese, Effect of processing parameters on microstructure and tensile properties of austenitic stainless steel 304L made by directed energy deposition additive manufacturing, *Acta Mater.* 110 (2016) 226–235. doi:10.1016/j.actamat.2016.03.019.
- [36] A. Yadollahi, N. Shamsaei, S.M. Thompson, D.W. Seely, Effects of process time interval and heat treatment on the mechanical and microstructural properties of direct laser deposited 316L stainless steel, *Mater. Sci. Eng. A.* 644 (2015) 171–183. doi:10.1016/j.msea.2015.07.056.
- [37] H. Paydas, A. Mertens, R. Carrus, J. Lecomte-Beckers, J.T. Tchuindjang, Laser cladding as repair technology for Ti-6Al-4V alloy: Influence of building strategy on microstructure and hardness, *Mater. Des.* 85 (2015) 497–510. doi:10.1016/j.matdes.2015.07.035.
- [38] K. Li, D. Li, D. Liu, G. Pei, L. Sun, Microstructure evolution and mechanical properties of multiple-layer laser cladding coating of 308L stainless steel, *Appl. Surf. Sci.* 340 (2015) 143–150. doi:10.1016/j.apsusc.2015.02.171.
- [39] I. Yadroitsev, P. Krakhmalev, I. Yadroitsava, S. Johansson, I. Smurov, Energy input effect on morphology and microstructure of selective laser melting single track from metallic powder, *J. Mater. Process. Technol.* 213 (2013) 606–613. doi:10.1016/j.jmatprotec.2012.11.014.
- [40] Y. Lee, M. Nordin, S.S. Babu, D.F. Farson, Effect of fluid convection on dendrite arm spacing in laser deposition, *Metall. Mater. Trans. B Process Metall. Mater. Process. Sci.* 45 (2014) 1520–1529. doi:10.1007/s11663-014-0054-7.
- [41] P. Lehto, H. Remes, T. Saukkonen, H. Hänninen, J. Romanoff, Influence of grain size distribution on the Hall-Petch relationship of welded structural steel, *Mater. Sci. Eng. A.* 592 (2014) 28–39. doi:10.1016/j.msea.2013.10.094.
- [42] P. Lehto, J. Romanoff, H. Remes, T. Sarikka, Characterisation of local grain size variation of welded structural steel, *Weld. World.* 60 (2016) 673–688. doi:10.1007/s40194-016-0318-8.
- [43] B.B. Jung, H.K. Lee, H.C. Park, Effect of grain size on the indentation hardness for polycrystalline materials by the modified strain gradient theory, *Int. J. Solids Struct.* 50 (2013) 2719–2724. doi:10.1016/j.ijsolstr.2013.05.002.
- [44] O.K. Mahabadi, N.X. Randall, Z. Zong, G. Grasselli, A novel approach for micro-scale characterization and modeling of geomaterials incorporating actual material heterogeneity, *Geophys. Res. Lett.* 39 (2012). doi:10.1029/2011GL050411.
- [45] W. Tillmann, L. Hagen, D. Kokalj, Embedment of eutectic tungsten carbides in arc sprayed steel coatings, *Surf. Coatings Technol.* 331 (2017) 153–162. doi:10.1016/j.surfcoat.2017.10.044.
- [46] D. Deschuyteneer, F. Petit, M. Gonon, F. Cambier, Influence of large particle size – up to 1.2 mm – and morphology on wear resistance in NiCrBSi/WC laser clad composite coatings, *Surf. Coatings Technol.* 311 (2017) 365–373. doi:10.1016/j.surfcoat.2016.12.110.
- [47] D.M. Stefanescu, A. Moitra, A.S. Kacar, B.K. Dhindaw, The influence of buoyant forces and volume fraction of particles on the particle pushing/entrapment transition during directional solidification of Al/SiC and Al/graphite composites, *Metall. Trans. A.* 21 (1990) 231–239. doi:10.1007/BF02656440.
- [48] B. Amin-Ahmadi, H. Aashuri, Semisolid structure for M2 high speed steel prepared by cooling slope, *J. Mater. Process. Technol.* 210 (2010) 1632–1635. doi:10.1016/j.jmatprotec.2010.05.011.
- [49] T. Lienert, T.A. Siewert, S.S. Babu, V.L. Acoff, *Welding Fundamentals and Processes*, vol. 6A, in: S.W.P. Specif. ASM Int., Materials Park, OH, 2011: pp. 89–114.
- [50] T.E. Quested, A.L. Greer, The effect of the size distribution of inoculant particles on as-cast grain size in aluminium alloys, *Acta Mater.* 52 (2004) 3859–3868. doi:10.1016/j.actamat.2004.04.035.
- [51] Z. Zhang, P. Farahmand, R. Kovacevic, Laser cladding of 420 stainless steel with molybdenum on mild steel A36 by a high power direct diode laser, *Mater. Des.* 109 (2016) 686–699. doi:10.1016/j.matdes.2016.07.114.
- [52] P. Liu, Z. Wang, Y. Xiao, M.F. Horstemeyer, X. Cui, L. Chen, Insight into the mechanisms of columnar to equiaxed grain transition during metallic additive manufacturing, *Addit. Manuf.* 26 (2019) 22–29. doi:10.1016/j.addma.2018.12.019.

[53] S. Fetni, T. Maurizi Enrici, T. Niccolini, H. Tran, O. Dedry, L. Duchêne, A. Mertens, A.M. Habraken, Thermal model for the directed energy deposition of composite coatings in 316 L stainless steel enriched with tungsten carbides, *Mater. Des.* (2021) 109661. doi:10.1016/j.matdes.2021.109661.

---

---

## *Wear behaviour of laser clad 316L + WC composite against alumina*

*Tommaso Maurizi Enrici, Daniele Mario, Olivier Dedry, Sylvie Castagne, Anne Mertens, Jérôme Tchoufang Tchuindjang*

### **Abstract**

The wear behaviour of a laser clad 316L+WC composite sliding against alumina was investigated. The addition of 20% (in volume) of tungsten carbide (WC) reinforces the 316L microstructure and improves its wear resistance. The new austenitic microstructure is reinforced by partially dissolved WC and by a network of new solidification carbides. The novel approach of the interrupted tests was applied, where a test campaign is run under the same conditions and strategically stopped at times corresponding to specific variations of both the friction coefficient and penetration depth. The wear tracks were analysed through scanning electron microscopy and profilometer at the different stages. This approach allows to observe the evolution of the wear rate with the increase of the test length, to identify the evolution of the wear mechanisms with the progress of the test and to elucidate the complex wear sequence of the composite. WC reinforcements protect the matrix from being cut by the counterbody and contribute to the formation of a tribolayer by a mechanism that involves adhesive and abrasive wear. Moreover, the interrupted tests approach highlights that after a short run-in period, a cyclical regime follows, characterized by mild wear involving the repeated compaction, breakdown and reformation of a protective tribolayer.

**Keywords:** Metal matrix composite, Directed Energy Deposition, Interrupted tests, surface analysis, tribological properties, dry sliding

### **1. Introduction**

Austenitic stainless steels have widespread applications in aerospace, biomedical and chemical industry due to their excellent corrosion resistance and suitably high ductility. Among these alloys, 316L stainless steel (SS316L) has attracted particular attention for its good plasticity, toughness, weldability and excellent corrosion resistance in oxidizing and reducing media [1–3]. Consequently, this attention has been translated into a large number of publications, including applications of SS316L in the growing additive manufacturing (AM) field [4–7]. Indeed, AM is gaining wide acceptance in diverse industries for the manufacturing of metallic components due to the potential decrease of the wastes and to the improvement of the mechanical properties by the kinetics specific to AM [8–10]. Furthermore, in AM, metallic materials can be improved combining different feedstock during fabrication in order to enlarge their range of application with the formation of novel alloys and composites [11–15].

316L exhibits good potentialities for this purpose since its relatively low strength and poor abrasion performance have prevented its application in harsh tribological environments. The enhancement of its wear resistance can be achieved by the introduction of hard reinforcements such as ceramics during fabrication by AM techniques, thus creating metal matrix composites (MMCs) with improved

tribological and mechanical properties [13,16]. Among AM techniques, Directed Energy Deposition (DED) is particularly suitable for the manufacturing of metal coatings or thick deposits, allowing for a large variability in raw materials [9,14,17–19]. During DED process, extremely high cooling rates and the interactions between molten metal and reinforcements lead to complex hierarchical microstructures [11,17,20].

In recent years, various investigations have used tungsten carbide (WC) as possible reinforcement for both austenitic stainless steels and Ni-based alloys, due to the high hardness and good wettability of WC with both alloys [12,18]. Depending on the volume percentage, WC addition modifies the solidification route of these alloys, leading to new microstructures composed of partially dissolved WC particles and a matrix reinforced by new solidification carbides [17,18,20,21]. Where the wear resistance of these alloys was investigated [21–26], the attention was often given to the variation of the wear resistance as function of the test parameters, i.e. temperature, load, sliding speed. This approach is consistent to simulate industrial operating conditions when the testing parameters and setup of the test are close to the actual application conditions [25,27], but otherwise, it is limited in the understanding of the wear sequence by considering only post-mortem observations after relatively long tests. Therefore, variations of the wear mechanisms or of their relative amplitude with the progress of the test are difficult to detect since observable tribological features (i.e. grooves, oxides, adhered material) are either mixed or hidden by the last main wear mechanism [28–30]. Furthermore, for MMC, the understanding of the respective contribution of the large reinforcements and of the reinforced matrix on the wear resistance [13,17,19] is of great interest in order to tailor the microstructures, e.g. by controlling the characteristics of the initial reinforcement particles prior to fabrication [14,18,24,28].

Only few works have focused on elucidating the dynamics during the wear tests on complex materials [31–35]. Indeed, during long tests, the wear behaviour of multiphase materials often exhibits a succession of different wear mechanisms [19,23,27–29,34,36]. Depending on the test setup and on the characteristics of the constitutive phases (i.e. morphology, nature and thermal stability), evolving mechanical and chemical interactions between the phases of the tested material on the one hand, and counterbody and wear debris, on the other hand, result in increased complexity of the wear process [6,31,32,34,37].

This study considers a MMC based on SS316L and 20% (in volume) of WC fabricated by DED [18]. The wear behaviour using alumina as counterbody is investigated via a series of interrupted pin-on-disc tests, an approach that has rarely and only partially been explored to date [36]. These tests were performed under the same conditions and strategically stopped at times corresponding to specific variations of the friction coefficient (CoF) and penetration depth (PDe). This approach helps differentiating the respective contribution of the reinforcements and of the reinforced matrix on the wear behaviour as the wear test progresses, clarifying the evolution of the wear mechanisms and the

causes of eventual variations. In order to associate the CoD and PDe variations to wear mechanisms and to locate them in the general wear sequence, post-mortem observations of the specimens and counterbody were performed for each of the interrupted tests. Based on the comparison of these results with observations of the wear behaviour of reference DED SS316L without reinforcement, the role of the complex hierarchical reinforced microstructure of the SS316L + WC composite on its improved wear resistance is assessed.

## 2. Materials and Methods

### 2.1. Fabrication and sample preparation

This work considers a metal matrix composite coating composed of SS316L and reinforcements of WC particles (20% in volume). It has been deposited on a SS316L substrate using a 5-axis Irepa DED system with a Nd-YAG laser source. The two powders used for the production of the parts were stainless steel 316L and WC powders with a granulometry between 50 and 200  $\mu\text{m}$ , having a spherical shape [18]. The final dimensions of the three MMC deposits used in this study were 35  $\times$  35 mm side length and 14 mm height [18]. Furthermore, thick stainless steel 316L deposits were fabricated as reference with the same parameters. Full details of the manufacturing conditions can be found in a previous work [18].

After deposition, the cross-section (Fig. 1a) was obtained from the first deposit by electro-discharge machining (AgieCharmilles CUT E 600) and used for microscopic inspection by scanning electron microscopy (SEM), after being ground flat to obtain smooth surfaces and polished with diamond paste. The other two deposits were used for the production of the wear samples. Two 5 mm thick wear specimens per deposit (Fig. 1a) were obtained by electro-discharge machining. As shown in Fig. 1b, the deposits were cut at 11.3, 6.3 and 1.3 mm of distance to the substrate. These surfaces, perpendicular to the deposition direction, were ground to reach a  $R_a < 0.2 \mu\text{m}$ . The same procedure was applied to the 316L reference.

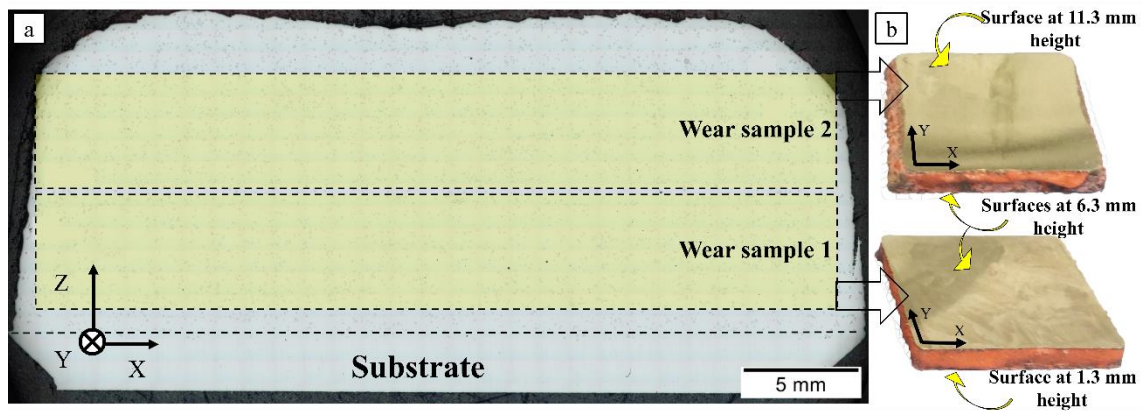


Fig. 1 : The two wear specimens located on the cross-section (a) with the respective surfaces (b).

### 2.2. Wear tests

Tribological experiments were performed at room temperature in dry conditions on a CSM high-temperature pin-on-disc tribometer [37]. The composite material was used as disc and an alumina ball ( $\text{Al}_2\text{O}_3$ ) of 6 mm diameter was used as pin. Alumina was chosen as counter-material because it possesses a hardness of 1800HV, which is harder than the test specimen i.e. 350-500 HV [2,5,31,38]. The whole test campaign was performed on surfaces at 6.3 mm of distance to the substrate (Fig. 1b), under a constant load of 10 N and sliding speed of 10 cm/s. This set of parameter was chosen in accordance with previous tribological studies on 316L and with ASTM G133-95 [1,7,26,39]. The height at 6.3 mm from the substrate has been chosen in order to have two surfaces (referred to as 6.3 surfaces)

corresponding to the same position from two different wear samples (Fig. 1b) and to avoid microstructural variations due to the heat accumulation [9,38,40]. CoF and PDe were measured by the tangential or vertical deviation of the pin-on-disc arm sensors, respectively. Moreover, the tests were recorded by a HERO7 Action camera in order to detect variations in acoustic emission [41–43]. Two tests with the same conditions and with a constant test length of 22000 laps (named test0 – 1313 m) were carried out on one 6.3 surface of the second deposit in order to check the repeatability of the results and to set the position of the interrupted tests. Then, four interrupted tests were carried out on the two 6.3 surfaces of the third deposit. The lengths of these interrupted tests were set respectively to 750 (test1 - 37.7 m), 9300 (test2 – 642.8 m), 11700 (test3 – 809.3 m) and 15000 laps (test4 – 754.3 m). Furthermore, a 22000 laps test was carried out on the reference clad 316L under the same conditions for comparison purposes.

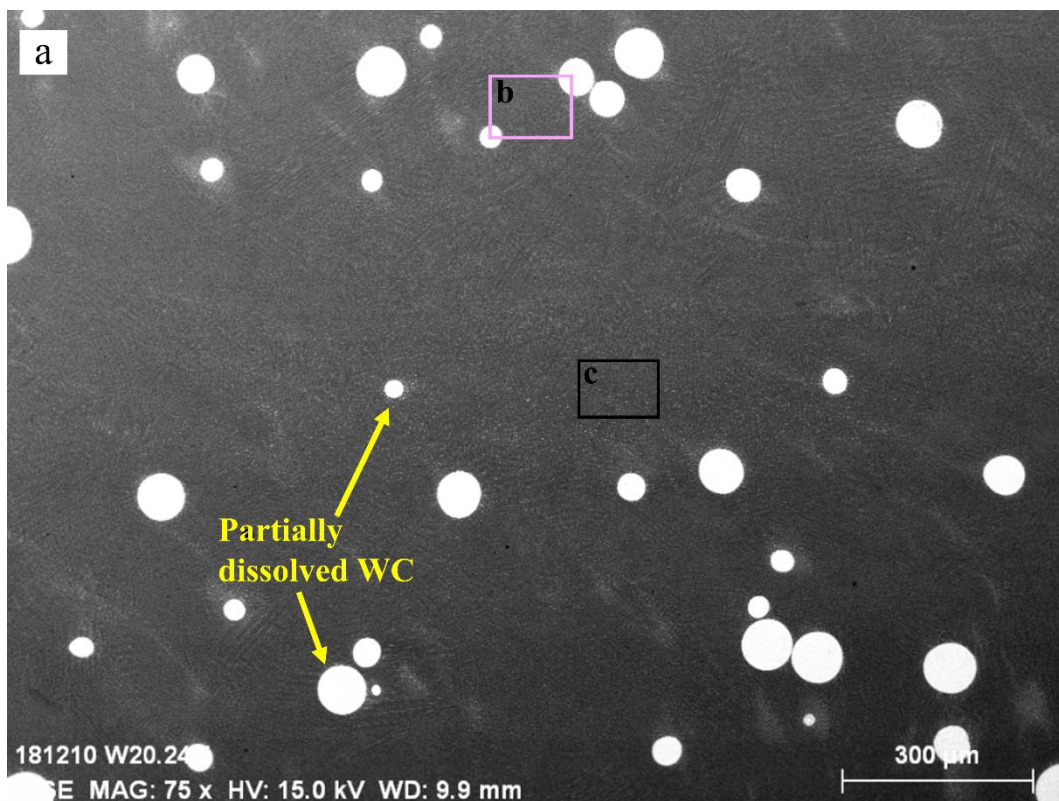
### **2.3. Characterization methods**

The volume loss of the samples was estimated by measuring the wear track profile using an Alicona Infinite Focus G5 optical profilometer, which allows to consider all surface features having sizes greater than the chosen resolution. In addition, the spherical cap of the alumina ball and the corresponding worn volumes were calculated by measuring the diameter and height on the topographies. The images were taken with the ring-light option. The vertical resolution was set at < 410 nm and the horizontal resolution at 7.83  $\mu\text{m}$ . Furthermore, the wear rates were calculated by dividing the worn volume by the sliding distance (m). After the tribological test, top views of the worn surfaces, cross-sections of the wear tracks and debris collected using a carbon sticker were analysed by SEM using both BSE and SE detectors [28].

### 3. Results

#### 3.1. Microstructure of the 316L+WC composite

In the microstructure of the metal matrix composite, partially dissolved WC reinforcements are well distributed in an austenitic matrix (Fig. 2a) reinforced by a bright network of solidification carbides (Fig. 2b). In a previous work by the present authors [18], an in-depth microstructural characterization has shown that these solidification carbides are of  $(W, Cr)_x C_y$  type, and that they result from the partial dissolution of the original WC powders within the metal matrix. In particular, metastable  $M_4C$  carbides are observed in the melt pool (Fig. 2c), while  $M_6C$  and  $M_{23}C_6$  carbides are found in the Heat Affected Zone (HAZ) formed due to the reheating of previously solidified material upon the deposition of a new layer (Fig. 2c), and in the immediate vicinity of the reinforcements (Fig. 2b) [11,18]. These solidification carbides are observed together with a crown of  $\gamma$ - $WC_{1-x}$  carbide and pure tungsten around the WC cores, forming a connection layer between the reinforcements and the matrix (Fig. 2b). On the other hand, reference 316L exhibits a cellular austenitic microstructure (Fig. S1, supplementary material), where both cells and cell boundaries are austenite [14,16].



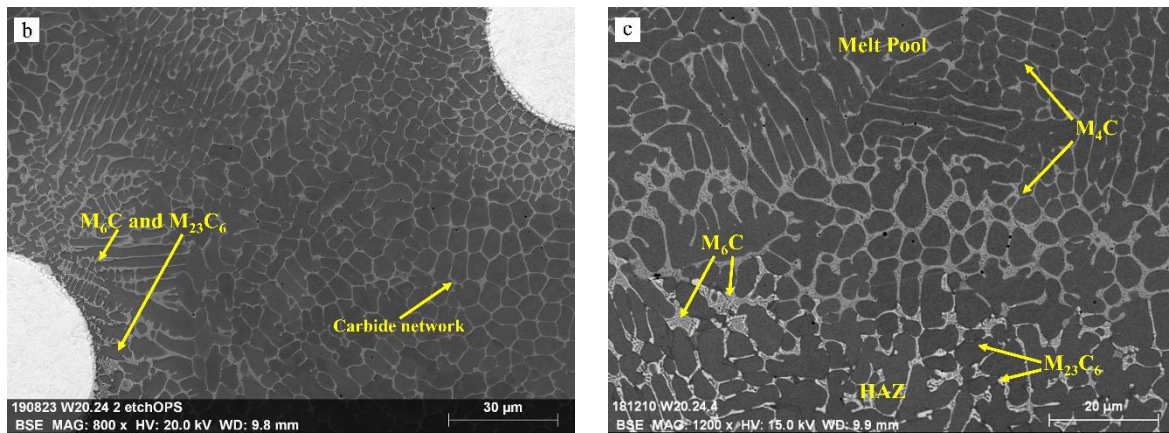


Fig. 2: (a) SEM micrograph of the 316L+20%WC composite. Partially dissolved WC carbides (bright circles) are homogeneously dispersed in a reinforced matrix. (b) Close-up view of (a) showing the immediate vicinity of the partially dissolved WC carbide (light grey) and the network composed of solidification carbides. (c) Another close-up view of (a) focused on the transition between melt pool and HAZ with their respective solidification carbides.

### 3.2. Wear tests

Fig. 3 presents the variations of CoF and PDe under sliding contact, indicating that the CoF continuously changed with the running length. Good test repeatability is achieved among the three tested 6.3 surfaces. Fig. 3a (test0) is considered as reference for the values of CoF and PDe in the following description. As shown in Fig. 3a, the CoF has a relatively short run-in period [29,30,44] and then enters a cyclical regime formed by repeated segments. A segment of the cyclical regime begins when the PDe reaches a steady value and it finishes when the CoF reaches values of 0.7-0.75 and then sharply drops to 0.6-0.65 (~12000 and ~17800 laps in Fig. 3a). All uninterrupted tests (test0) end during the third segment of the cyclical regime (Fig. 3a). For comparison purposes, the 22000 laps test of the reference 316L is given in the supplementary material (Fig. S2).

The run-in period and the first segment of the cyclical regime in test0 (Fig. 3a) can be divided into six stages, which are related to specific variations of the CoF and the PDe. A further seventh stage corresponds to the beginning of the second segment. This division will be used in section 4.2 for the elucidation of the wear sequence considering the observations of section 3.3.

The run-in period is characterized by a sharp increase of the CoF (Fig. 3b and c), followed by a stage characterized by small fluctuations around a CoF of 0.65-0.7. Simultaneously, the PDe exhibits an initial short plateau (stage1) and then a continuous rise (stage2). The run-in period ends after 2200 laps with a sharp increase of CoF up to 0.7-0.75 followed immediately by a sharp decrease to 0.6-0.65 (Fig. 3a and c), while the PDe levels off at 0.3 mm (stage3).

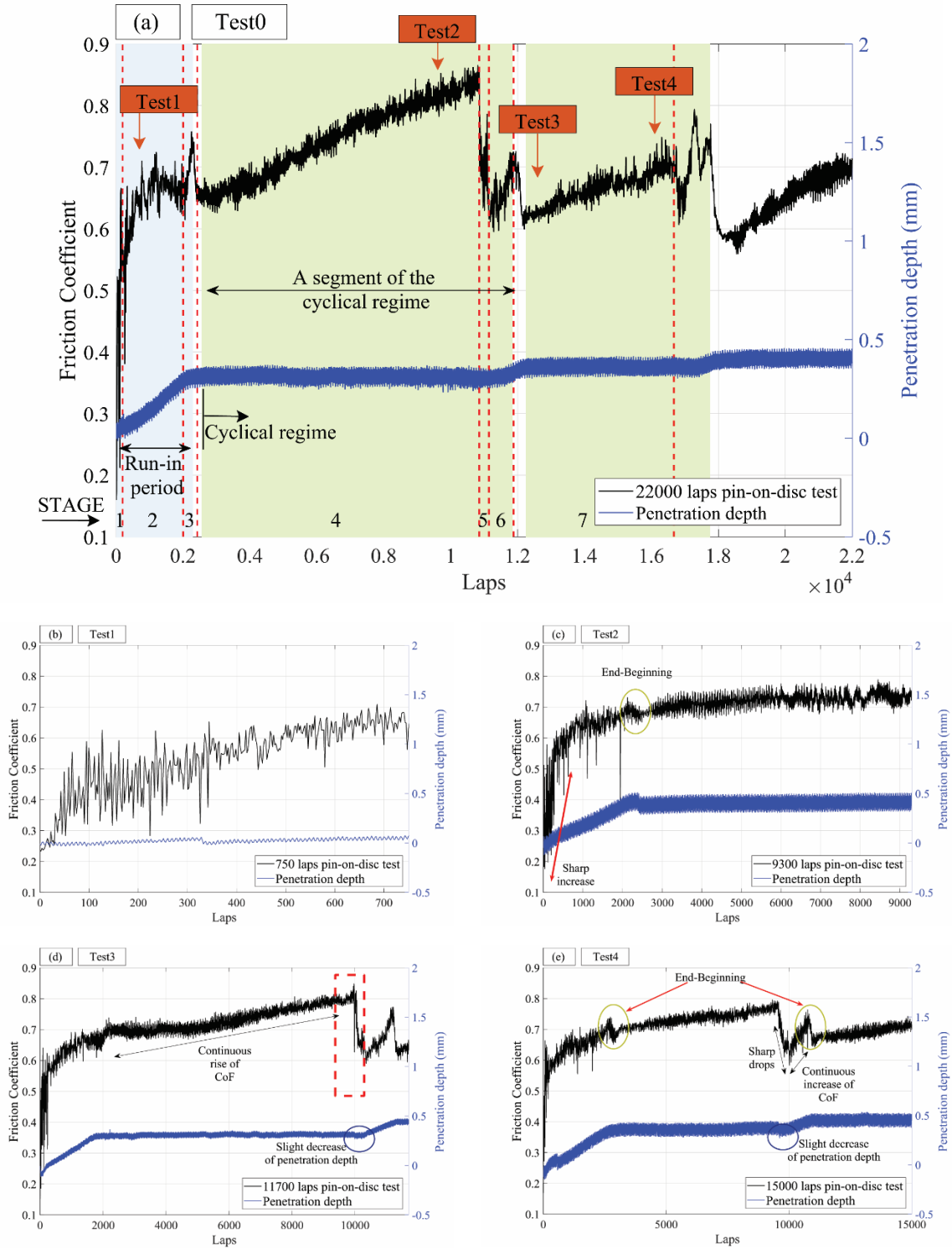


Fig. 3 : Measured friction coefficient (CoF) and penetration depth (PDe) during pin-on-disc tests, at (a) 22000, (b) 750, (c) 9300, (d) 11700 and (e) 15000 laps. In the supplementary materials, available online, a video exhibits the variation of the sound corresponding to the red rectangle of Fig. 3d.

The cyclical regime (Fig. 3d) is characterized by a continuous rise of the CoF, followed by one or two sharp drops (Fig. 3e), another increase under a steeper slope and a final decrease (Fig. 3e). The PDe exhibits a steady value at 0.3 mm while the CoF increases continuously (stage4). In contrast, as highlighted in Fig. 3d and e, while the CoF collapses, the PDe shows a slight decrease, followed by a

short plateau (stage5). Transitions between the continuous rise and collapse of the CoF (dotted red rectangle in Fig. 3d) can also be characterized by noise, with grinding squeals (Fig. S3 and video, supplementary material). During sliding, part of the kinetic energy produces waves and oscillations in the bodies, and part of this energy leads to plastic and anelastic deformation of the asperities [42,43]. Energy expends mainly through viscous dissipation, and a combination of adhesion, fracture and chemical reaction. The distribution of energy conversion varies for different applications. Each of these processes provides a mechanism for converting the original kinetic energy to an interim one in the form of vibration and sound, deformation energy, surface energy, tribo-chemical energy and other tribo-emissions [41]. Interestingly, an absence of acoustic emissions occurs as the CoF drops due to an evident decrease of friction and of the kinetic energy produced by the sliding contact. After this transition, both CoF and PDe increase (stage6). When this last increase of CoF reaches 0.7-0.75 and then sharply drops to 0.6-0.65 (as observed in the transition between the run-in period and the beginning of the cyclical regime), the first segment of the cyclical regime finishes and the second segment begins (stage7), restarting the cycle in a loop.

### 3.3. Post-mortem observations

#### 3.3.1. Profilometer measurements

The volume losses of the clad 316L+20% WC composite and of the alumina ball during the pin-on-disc tests are shown in Fig. 4. The wear track of the composite is homogeneous (Fig. 4a) and its volume loss after 22000 laps (1313 m) is  $0.581 \text{ mm}^3$ . For comparison, the volume loss of a clad SS316L produced with the same fabrication parameters and tested under the same conditions is 11 times higher ( $6.534 \text{ mm}^3$ ). As shown in Fig. 4b, the worn volume of the track shows an almost linear increase with respect to the number of laps. Moreover, as also observed in [36,45], the wear rate of the specimen first decreases, and then remains stable with prolonged sliding time. This is attributed to the formation of a protective tribolayer. Indeed, for short sliding time, wear debris is generated between the mating surfaces and the surface roughness increases, leading to higher wear rates. With increasing sliding time, an oxide film can be formed, effectively protecting the sliding surface. Furthermore, a worn cap [19,29,31] was observed in every alumina ball after the tests (Fig. 4c), and its size increases with the increase of the sliding distance for the four interrupted tests. In contrast, the worn cap of the alumina balls used for the two test0 deviate slightly from this tendency. This can be attributed to the fact that these two tests were carried out on a different 6.3 surface, as will be discussed in section 4.2.2. The wear rate of the alumina ball decreases linearly with the increase in the distance.

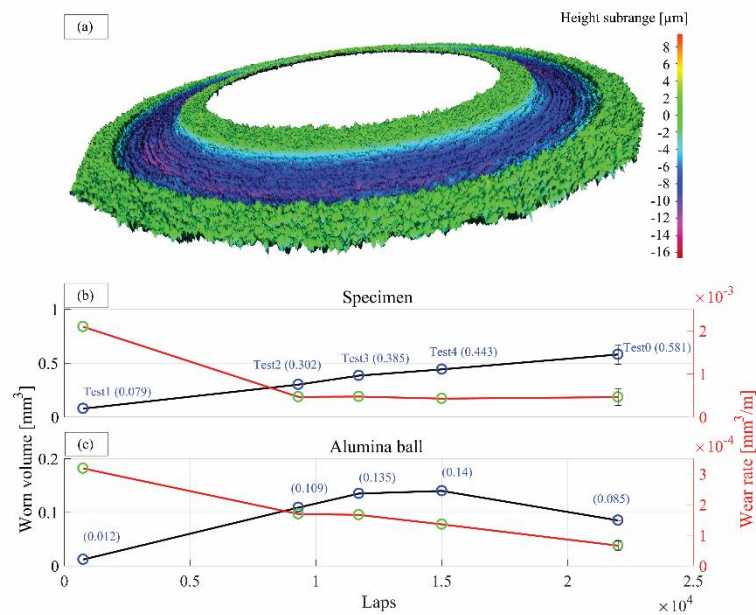
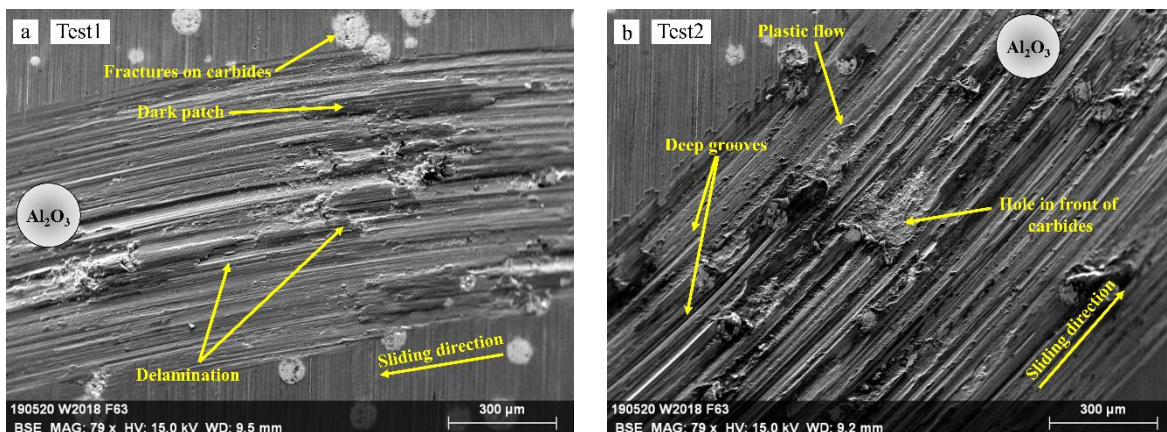


Fig. 4 : (a) 3D topography of the wear surface after 22000 laps pin-on-disc test. Measured worn volumes ((b) wear track and (c) alumina cap) of the five different tests vs the number of laps.

### 3.3.2. Wear tracks

#### 3.3.2.1. General overview

Fig. 5 shows the typical overview of the worn surfaces for the four interrupted pin-on-disc tests and for the complete test, ordered according to the number of laps. As shown in Fig. 5a, the surface away from the tracks is in ground conditions. It is homogeneous with a few crystals of the WC carbides [18] that have been pulled out during preparation leaving small fractures or cracks. Depending on the length of the test run, the track surfaces exhibit different features, such as delaminated material [3,16,44] (Fig. 5a and b), dark patches of various shapes [31,46] (Fig. 5a, c and d), grooves [26,30,31] (Fig. 5a, b and d), plastic flow [4,16,24,30] (Fig. 5b and d) and adhered material [24,32] (Fig. 5c, d and e). Test2 (Fig. 3c and Fig. 5b) and test4 (Fig. 3e and Fig. 5d) exhibit very similar features of the track surface and are thus considered as pertaining to the same wear mechanism.



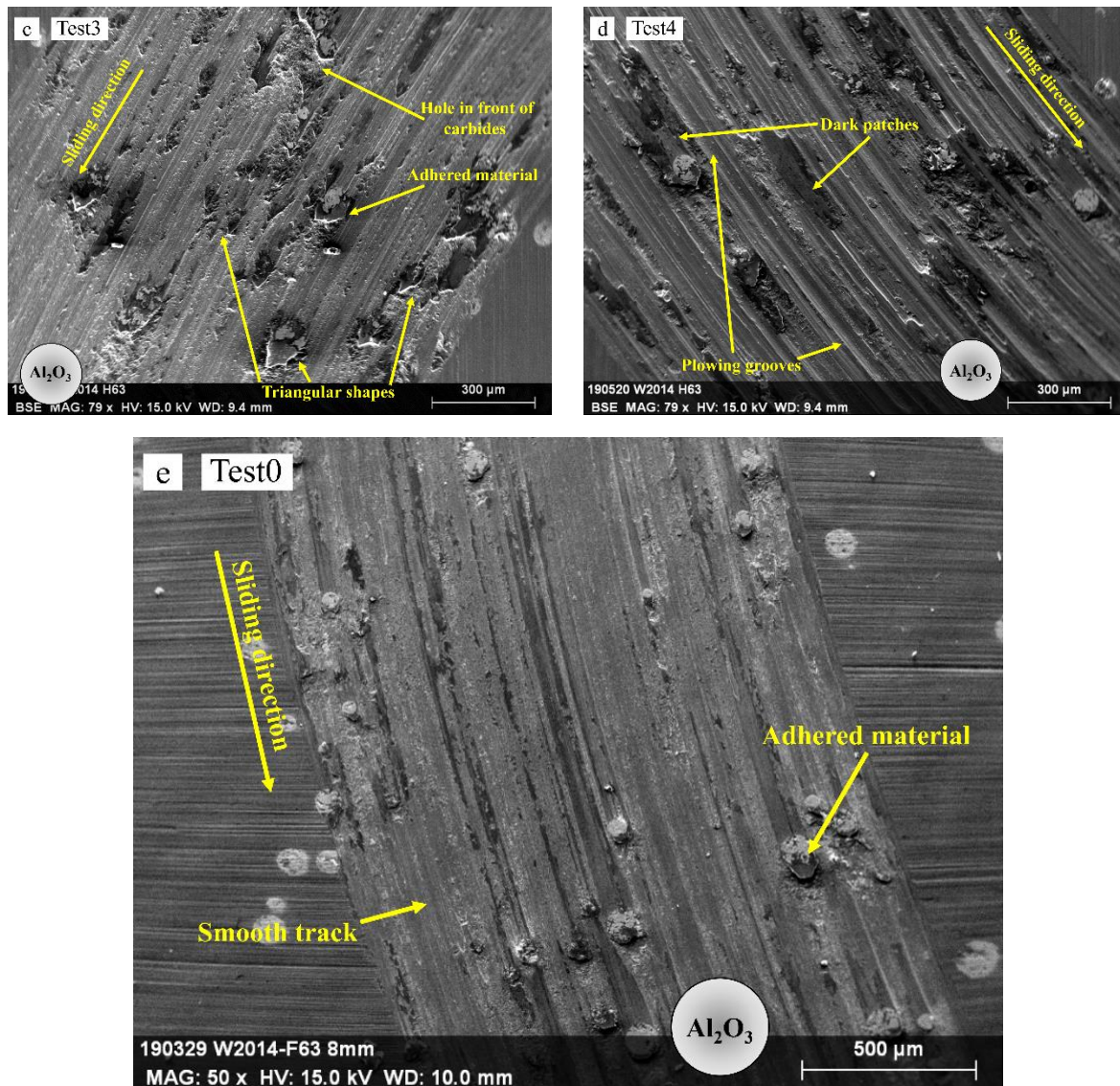


Fig. 5 : The worn tracks (SE mode) after (a) 750, (b) 9300, (c) 11700, (d) 15000 and (e) 22000 laps pin-on-disc test. A sphere represents the alumina ball position while the sample is turning anticlockwise.

### 3.3.2.2. Run-in period

The track overview of test1 corresponding to the run-in period (Fig. 3b) is characterized by the presence of delamination of material, few grooves and dark patches (Fig. 5a). In Fig. 6a, fragile failures are observed after the material delamination [30]. Moreover, the dark layer exhibits the same shape as the gap left by the fragile failure. The dark layer (Fig. 6b) is either well compacted or composed of small debris (Fig. 6a), including small bright WC debris (Fig. 6b). The dark patches cover both the matrix and the WC carbides (Fig. 6c), filling the fractures of the carbides and the cavities in the track. This adhered material is a mixture of Cr, Fe and Al oxide (Fig. 6e) and the presence of Al increases on the WC carbides (Fig. 6d). Cr and Fe oxide (Fig. 6g and h) is also observed on the matrix away from the patches.

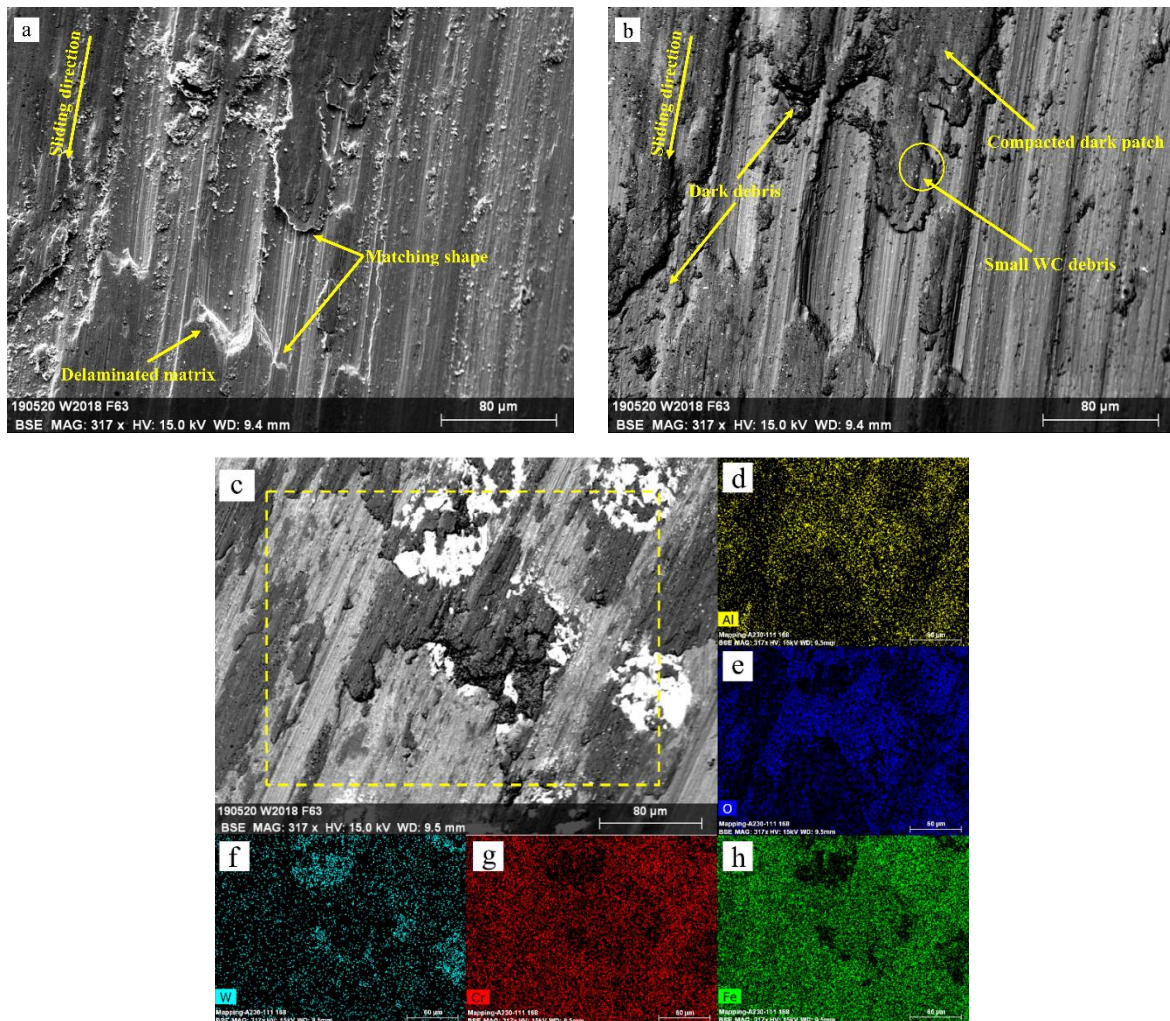


Fig. 6 : (a) SE and (b) BSE micrographs of the typical worn surface of test1 at 750 laps, as observed away from the WC carbides. (c) BSE micrograph of dark patches on the wear track and specifically on the WC carbides with the corresponding EDS analysis (d to h) after test1 at 750 laps).

### 3.3.2.3. Cyclical regime: first segment

When increasing the test length up to 9300 laps (Fig. 3c), the track exhibits increased grooving and plastic flow (Fig. 5b). Moreover, in addition to the adhered material on the WC carbides (Fig. 6c and Fig. 7a), cavities are observed during the cyclical regime in front of the WC carbides according to the sliding direction (Fig. 7c and e). The adhered material on the WC carbides corresponds to alumina (Rectangles 2 and 5 in Table 1, Fig. 7d and f), while some debris can be observed inside the cavity, corresponding to a mixture of Al, Cr, Fe and W oxides (Rectangles 3, 6 and 7 in Table 1, Fig. 7d and f). In this respect, it is worth noting that the contribution from the neighbour phases to the interaction volume may be high in the case of the isolated debris due to their small size compared to the matrix or the partially dissolved WC.

As shown in Fig. 7c and e, the matrix located behind the WC carbides according to the sliding direction (Rectangle 1 in Table 1 and Fig. 7d) does not exhibit grooves or plastic flow [4,20,24], while the matrix in front of the cavity is often severely worn (Fig. 7e). In addition, the oxidation of the matrix in this

severely worn area is more pronounced than in the protected zone behind the WC particle (Rectangle 1 and 4 in Table 1 and Fig. 7d). Fractured or partially pulled out carbides (Fig. 7c) and cracked oxide patches (Fig. 8a) may also be observed [24,25]. As shown in Fig. 7b, oxide patches exhibit different contrast depending on the element present in the oxide mixture. In particular, in the cyclical regime, cracked oxide patches exhibit a bright contrast with a composition rich in heavy metals (Rectangle 8 in Table 1 and Fig. 8b). Interestingly, the matrix in the vicinities of cracked patches is not oxidized (Rectangle 9 in Table 1 and Fig. 8b).

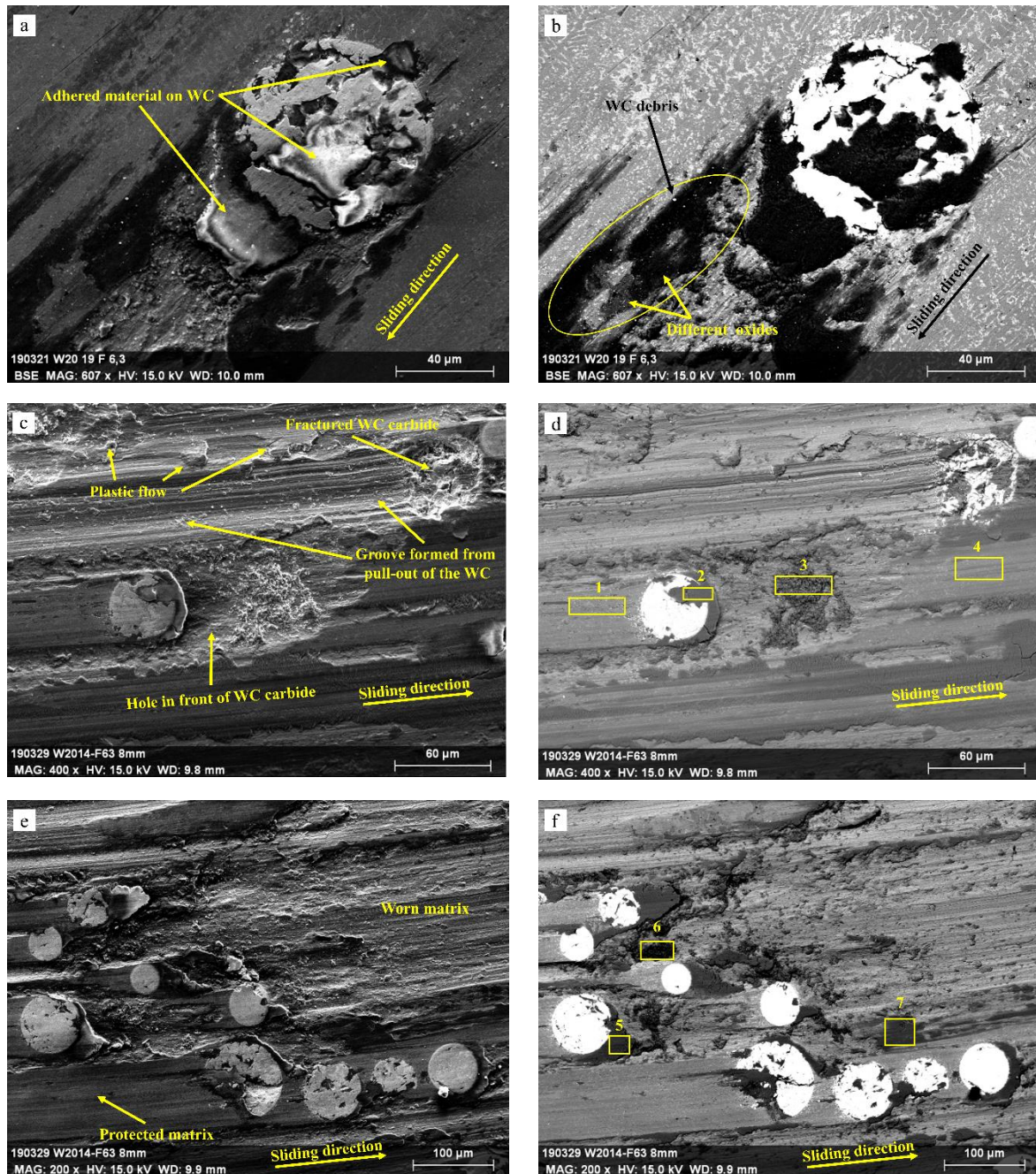


Fig. 7: SE and BSE micrographs of the typical worn surface for the first segment of the cyclical regime in the vicinities of the WC carbides, exhibiting (a and b) adhered material and different oxides, (c and d) holes, grooves and plastic flow and (e and f) the protection given by the WC carbides to the matrix.

Table 1: Chemical composition as measured by EDS for the rectangles in Fig. 8b, Fig. 7d and f after pin-on-disc tests.

% At.	C	O	Cr	Fe	Al	W	Ni	Mo
Point	Features in the vicinity of WC							
1	5.7	21.6	12.9	46.6	1.2	2.6	8.2	0.9
2	7.2	65.5	2.8	9.4	4.4	8.9	1.7	0.1
3	7.1	46.1	8.2	28.0	3.4	1.7	4.7	0.5
4	6.9	31.8	10.3	38.9	1.5	2.6	7.1	0.6
5	6.3	68.1	3.6	13.2	3.1	3.1	2.4	0.2
6	8.0	60.3	3.6	13.9	9.6	2.1	2.3	0.2
7	6.3	53.3	6.5	23.8	2.9	2.6	4.3	0.4
	Features of the matrix							
8	2.2	27.0	8.6	31.8	3.4	16.8	5.4	0.9
9	1.8	2.5	14.3	54.8	0.3	7.5	10.2	2.0

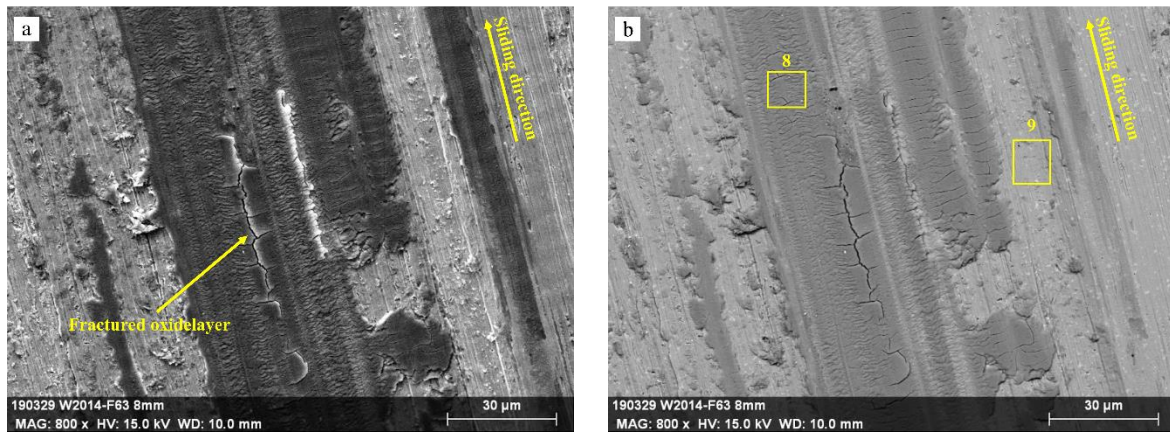


Fig. 8 : (a) SE and (b) BSE micrographs of fractured oxide patch observed after the 9300 laps test.

#### 3.3.2.4. Cyclical regime: second segment

After test3 (Fig. 3d), the surface of the wear track (Fig. 5c) appears smooth or with very narrow grooves that are observed far away from the WC carbides. In addition, triangular dark patches (Fig. 5c) are observed in front of the WC carbides, which correspond to pieces or compacted debris of alumina (Fig. 9b and c). Moreover, as shown in Fig. 9a, a large quantity of small debris is well distributed on the surface. Nevertheless, the matrix is less oxidized (Fig. 9c) in comparison to the other tests (Fig. 6e and Table 1).

Finally, the first test carried out up to 22000 cycles exhibit a worn track similar to test4 (Fig. 5d). The second test exhibits slight differences, i.e. the worn surface is smooth with traces of dark oxides and with adhered material on the WC carbides (Fig. 5e). This difference will be discussed in section 4.2.3.

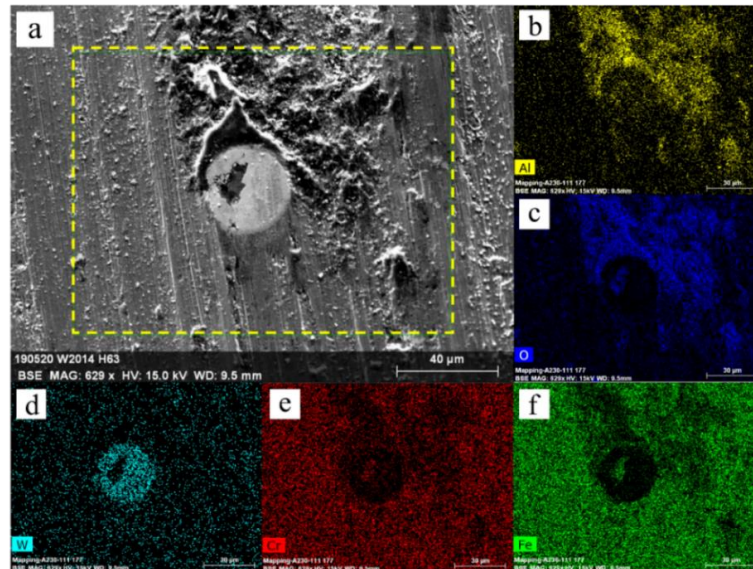
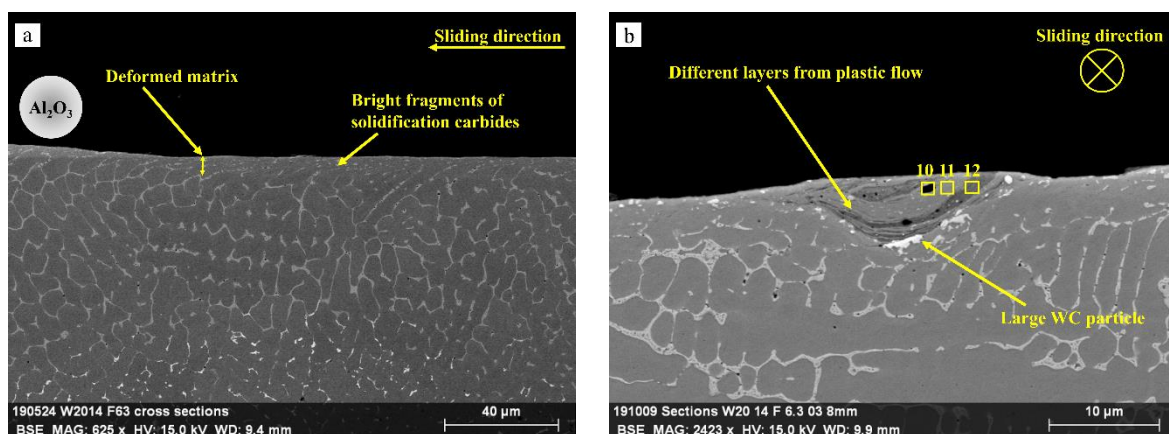


Fig. 9 : (a) SE micrograph of triangular dark patches on the wear track in front of the WC carbides, with the corresponding EDS analysis (b to f) after test4 at 11700 laps.

### 3.3.3. Cross-sections and debris

The two main observations on the cross-sections of worn samples are illustrated in Fig. 10. In Fig. 10a, a 5-10  $\mu\text{m}$  thick deformed layer is observed on the surface, with deformed grains oriented following the sliding direction [1,5,6,28], while the microstructure beneath the wear track is not perturbed [18]. The first 5  $\mu\text{m}$  of this deformed layer corresponds to a crack-free mechanical mixed layer (MML) [16,47], where the matrix is mixed with bright debris belonging to cracked WC carbides and to fragments of solidification carbides (Fig. 2b and Fig. 10b). In the remaining 5  $\mu\text{m}$  of the layer (i.e. in the subsurface) [16], solidification carbides are fragmented into small pieces due to the deformation of the matrix.



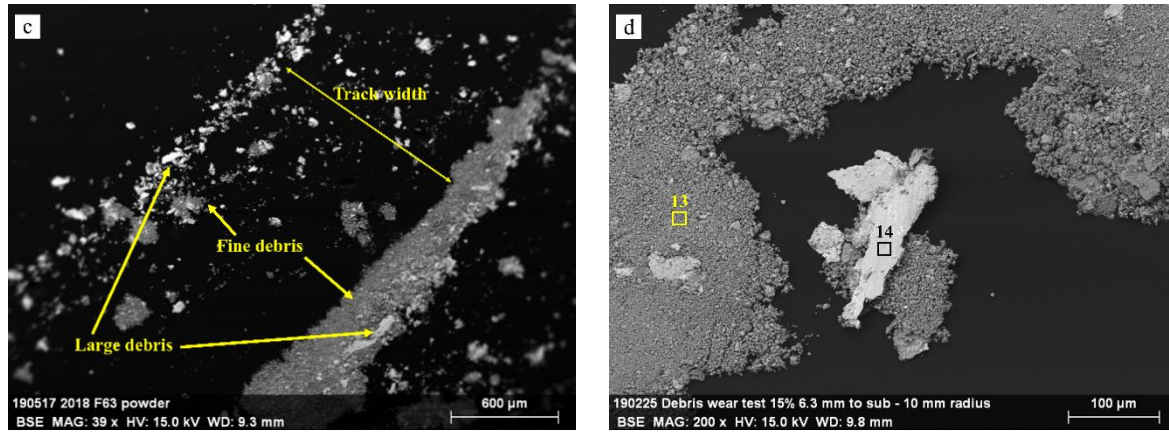


Fig. 10: Typical features of the cross-sections (a and b) and of the debris collected after the 22000 laps tests (c and d).

Furthermore, perpendicularly to the sliding direction, several cavities formed during the tests by pulled-out WC carbide (Fig. 7c) or delamination (Fig. 5b and c) are observed. These cavities are often filled with oxides through plastic flow (Fig. 10b) [35,48]. Three distinct oxide mixtures can be distinguished from the BSE contrast and from the compositions listed in Table 2. Indeed, as observed in [35,48], the MML is composed of six or seven layers of oxides, forming locally a stratified structure and corresponding to alumina (Rectangle 10), slightly oxidized matrix (Rectangle 11) or oxidized matrix + alumina (Rectangle 12).

Table 2: Chemical composition as measured by EDS for the rectangles in Fig. 10b and d.

% At.	C	O	Cr	Fe	Al	W	Ni	Mo
Point	Perpendicular cross-section							
10	5.9	49.4	3.1	9.5	29.9	0.5	1.2	0.3
11	12.2	7.0	13.4	52.7	0.1	2.4	9.3	0.9
12	9.4	40.3	8.0	31.1	1.9	2.0	5.5	0.6
	Debris							
13	6.2	14.2	11.3	45.2	4.6	11.1	7.5	/
14	25.0	8.5	10.5	44.6	0.4	1.4	9.4	0.9

The debris collected at the end of every test (Fig. 10c) is composed of a mixture of fine and large fragments [22,33]. Large flake-like debris exhibit a size range of 100-200  $\mu\text{m}$  (Fig. 10d) and correspond to the matrix that has been slightly oxidized (Table 1) [33]. On the other hand, much finer debris (Fig. 10d) tend to concentrate on the external edge of the wear track and are constituted of a mixture of oxides (Rectangle 13 in Table 2), including alumina.

## 4. Discussion

### 4.1 Influence of the original reinforcements and of the solidification carbides on the wear behaviour

Section 3 shows that the wear properties of the 316L+20%WC composite are higher than for the reference 316L. This is due to the combined effect of the original WC reinforcements and of the new solidification carbides present within the austenitic matrix (Fig. 2b). As also shown by [20,23], WC carbides protect the softer metal matrix (Fig. 7c and e) from being cut by the counterbody and restrain abrasive wear. This protective mechanism will be further discussed in section 4.2.1. In addition, wear damages typically observed on the 316L matrix [1,3,5,6,16], such as delamination, pit, groove and material removal are observed in the composite matrix (Fig. 6a and Fig. 7c). Adhesive wear on the matrix is also observed in the form of plastic flow (Fig. 7c and Fig. 10b). However, the presence of the solidification carbides in the matrix of the composite results in an increase of abrasive wear at the expense of a decrease of adhesive wear when compared to the reference 316L [5,23,24]. Indeed, as observed in [5,46], the toughness of the matrix rises due to the presence of a supersaturated solid solution and of the solidification carbides, thus leading to the formation of a thin deformed layer that follows the sliding direction (Fig. 10a). Solidification carbides are fragmented during this deformation and their fragments enrich the MML. As demonstrated by [6,16,21,47], the presence of these fragments or particles (Fig. 10b) significantly improves the work hardening ability of the matrix since they form an efficient barrier for dislocation glide. Dislocations pile-up due to plastic deformation may eventually lead to the development of a strain gradient, and consequently to micro-cracks and delamination [16,22]. Indeed, few large flake-like debris is observed after every test (Fig. 10d). The high amount of fine debris observed on the worn surfaces (Fig. 5), together with the large flakes (Fig. 10c), indicates a complex wear scenario with abrasive wear and oxidative wear as dominant wear mechanisms [16,22,33].

### 4.2 Elucidation of the wear sequence

The wear behaviour of complex alloys or composites often corresponds to a combination of different wear mechanisms [31–35]. Indeed, in this work, pin-on-disc tests show good repeatability while pointing towards a complex wear behaviour of the 316L+20%WC. Based on the results of the present paper, on the wear behaviour reported for the 316L without reinforcement [1,2,4–7,16] and on other studies of complex composite materials [19,23,29,31,32], the wear mechanisms for each of the respective stages are indicated hereafter.

#### 4.2.1. Run-in period

At the beginning of the run-in period (stage1), the surface roughness of the specimen is still relatively high. As a result, the actual contact area with the alumina ball – that is still intact at this stage – is at its smallest [32], thus leading to the highest contact stresses. Plastic deformation (Fig. 5a and Fig. 10a) and

adhesive wear take place for both the matrix (Fig. 6a) and the WC (Fig. 6c), as the initial contact of the alumina ball with the specimen causes bonding with the asperities of the composite surface. These high contact stresses deform the surface and initiate the formation of the MML (Fig. 10a). Simultaneously, the alumina ball is slightly worn by adhesive wear [16] or by mechanical locking on the WC carbides of the composite surface (Fig. 4c and Fig. 7a), leading ultimately to a progressive increase of the contact area and to a decrease of the contact stresses. This first stage, corresponding to mild wear, is short and the PDe remains almost stable during this time (Fig. 3a).

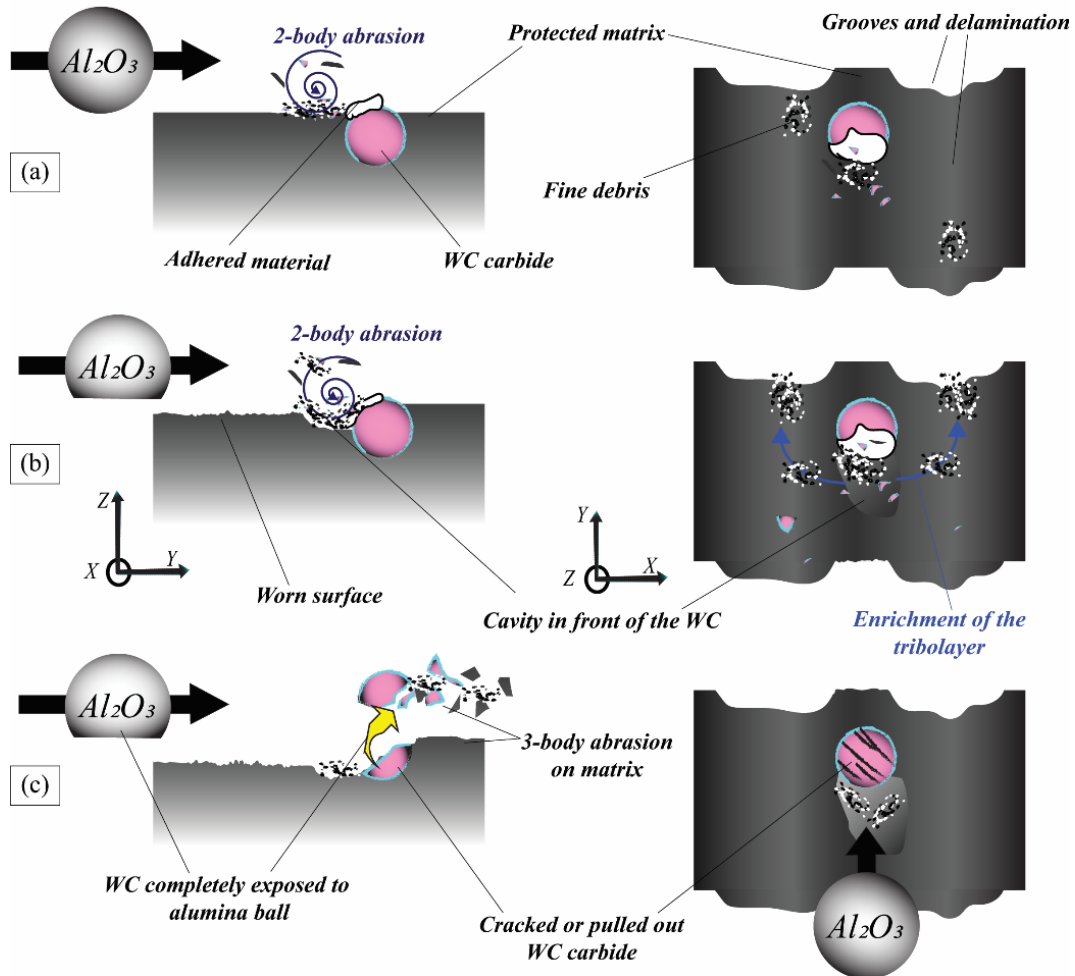


Fig. 11: Schematic of the abrasion phenomenon in front of WC carbides. (a) Beginning of the 2-body abrasion in front of the WC carbides. The ball is represented without damage (initial condition) This occurs mainly at the beginning of the test. (b) Enrichment of the tribolayer. (c) Delamination, cracking or pulling out of the WC carbides due to the high exposure to the alumina ball. In (b) and (c) the ball has been largely damaged during (a), by mechanical locking with the WC reinforcements.

Stage2 begins when the PDe starts rising (Fig. 3c) due to an increase of the delamination (Fig. 5a and Fig. 6a) and to the damages caused on both the composite matrix and the alumina ball by 2-body abrasive wear. Indeed, the strong plastic flow and deformation of stage1 have led to the development of a strain gradient. As already shown in previous works [4,16] and explained in section 4.1, the strain gradient then causes micro-cracks and delamination of the MML in stage2, in good agreement with the

presence of large debris after each test (Fig. 10c). Nevertheless, the MML is restored after delamination by continued contact with the alumina ball. As observed in [5,29,37], the delaminated debris can oxidise and wear the softer matrix underneath, leaving grooves. The combination of these different wear mechanisms leads to a high wear rate (Fig. 4b). In addition, the increase of the delamination may expose the WC carbides, thus increasing the adhesive wear of the alumina ball in contact with the hard reinforcements (Fig. 7c). On the other hand, some WC fragments (Fig. 7b) or even entire WC carbides can be pulled out (Fig. 7c) due to their enhanced exposure to the ball. The resulting large quantity of coarse hard debris, from the WC carbides or the matrix, are ground and refined (Fig. 7d) during abrasive wear (Fig. 5a), forming a first tribolayer [45,48]. As shown in Fig. 6e, oxygen is found all over the surface, confirming the existence of such an oxidized tribolayer.

In addition, similarly to [20,26], WC carbides exhibit a peculiar mechanism, schematized in Fig. 11. As shown in Fig. 11a, the adhered alumina (Fig. 6c and Fig. 7b) prevents further damage to the alumina ball and acts as a barrier for debris (Fig. 7e). With the progress of the test, debris accumulates in front of the WC carbides and abrade punctually the matrix, forming a hole (Fig. 11a and Fig. 7c). This cavity increases the quantity of debris that can accumulate in this position and thus the speed of the abrasion. This debris is composed of alumina with different oxides (Fig. 7f and Table 1). Moreover, during the abrasion, some fine debris in excess can move on the WC sides (Fig. 11b, Fig. 7d and f), enriching the tribolayer [26]. It is also assumed that WC carbides can fracture more easily or get pulled out if the depth of this hole increases up to more than half of the WC diameter (Fig. 5, Fig. 7a and d), increasing the exposure to the ball load (Fig. 11c). This phenomenon can be initiated whenever a WC particle is exposed on the surface and provided a tribolayer does not protect the track (Fig. 6c), independently of the current wear stage.

When the tribolayer (Fig. 7d) is homogeneously distributed on the whole track (Fig. 4 and Fig. 8b), it acts as a protective layer for both track and alumina ball [1,16,48]. The peak of stage3 is considered to correspond to the beginning of the compaction and the stabilisation [45] of the tribolayer. Indeed, the PDe exhibits a plateau starting from this moment of the test (Fig. 3e). It is worth noting that this steady-state stage does not occur when the 316L alone is tested (Fig. S2, supplementary material).

#### **4.2.2. Cyclical regime**

After the peak of the CoF at 2200 laps (Fig. 3a), a continuous increase of the CoF marks the beginning of the cyclical regime of the wear sequence. The rise of CoF and the steady PDe correspond to a mild oxidative wear mechanism (Fig. 12) and more specifically, to the compaction of the tribolayer with the progress of the test [49,50]. As shown in Fig. 4b, during the continuous rise of CoF (Fig. 3a), limited damages occur between test3 (Fig. 3d) and test4 (Fig. 3e). Indeed, within stage4, the tribolayer increases its thickness with material removed from the track and the debris formed in the precedent stages are refined and oxidized [49,50]. The continuous increase of the CoF corresponds to the increase in the

strain of the tribolayer. When the strain is too high to behold and the thickness of the tribolayer reaches the critical limit, compacted oxide patches crack (Fig. 8a) and the tribolayer breaks [36,49,50]. The length of this period depends on the mix of oxides that form the tribolayer, and especially on their hardness and tendency to compact [4,6,45,48]. Indeed, the mix of oxides formed during pin-on-disc tests on the reference 316L does not form a protective layer due to their different nature, as confirmed by the continuous increase of the PDe during sliding (Fig. S2, supplementary material).

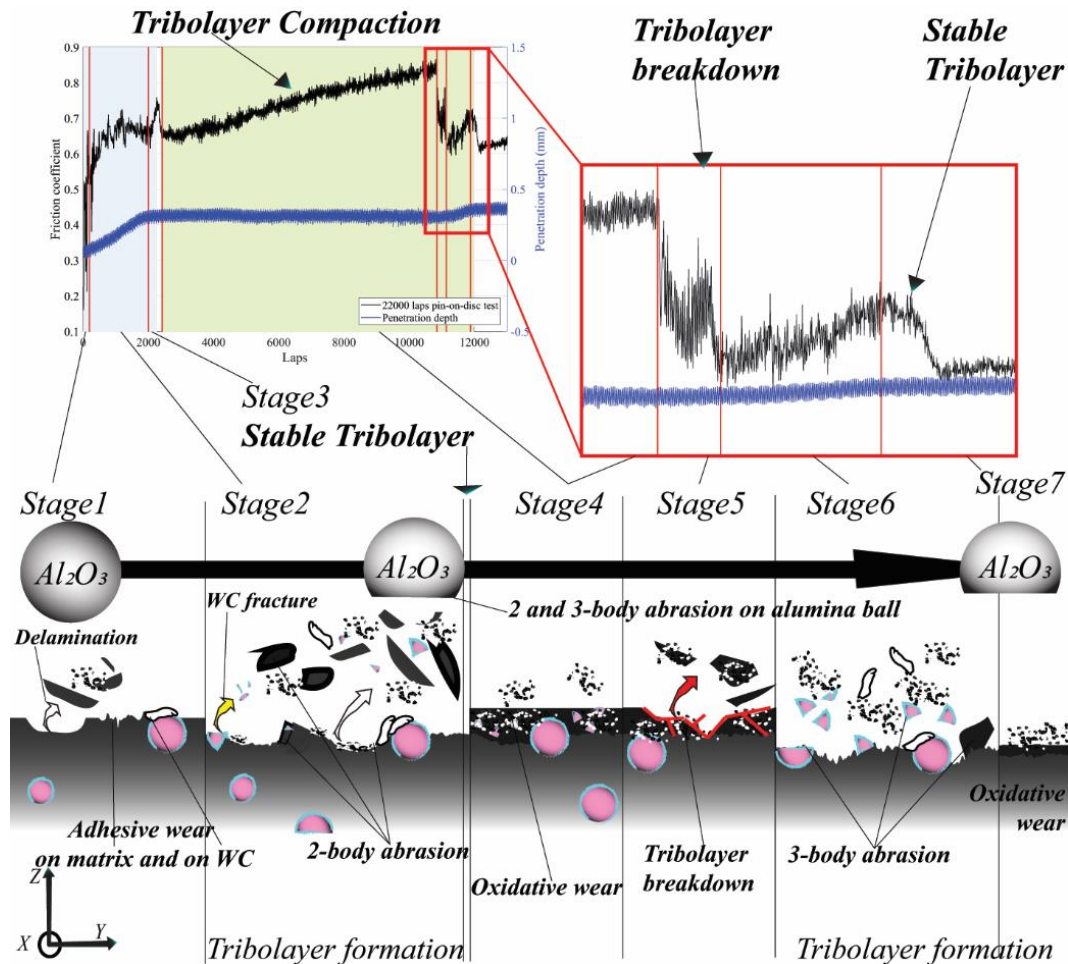


Fig. 12: Wear sequence of the 316L+20%WC composite. Each stage is associated with a part of the pin-on-disc test based on the specific variations of the CoF and the PDe. The main wear mechanisms for each stage are represented. In order to represent the wear of the track and the alumina ball, the height of the sample surface and the diameter of the ball decrease with the progress of the test.

At the main drop of CoF (transition between stage4 and stage5 in Fig. 12), acoustic emissions stop momentarily from being produced by the friction between the ball and the specimen (Fig. S3 and video, supplementary material). This sharp drop of CoF corresponds to the maximum compaction of the tribolayer, thus decreasing the friction between ball and specimen (or tribolayer). The absence of acoustic emissions corresponds to a minimum of the dissipation of kinetic energy as friction sounds or vibrations [41–43].

With the progress of the test, in stage5, the tribolayer breaks and reforms again several times since the debris can be replaced and moved along the track. However, this tribolayer is unstable since it is formed

by already compacted debris. During this process, a large number of compacted debris is evacuated out of the track by centrifugal forces. The small decrease of the PDe and the high variability of the CoF represent this phenomenon (Fig. 3d and e), where large and compacted debris is distributed heterogeneously on the track, increasing the distance between ball and surface.

When both CoF and PDe increase (Fig. 3d), large portion of the track surface is debris-free and the process to form a stable tribolayer restarts (Fig. 12). The main difference in comparison to the end of the run-in period (stage2) is the initial condition of the track surface. Indeed, in stage6 the MML is already formed and the punctual pressure of the ball is lower since the contact area is increased with the progress of the test (Fig. 4c). 2-body and 3-body abrasion on the alumina ball leads to increase in the contact area [32]. As a consequence, a lower contact pressure decreases the occurrence of delamination (Fig. 10a) by limiting the development of a strain gradient. The increase of the contact area during the test depends on the length of the oxidative stage (protecting both ball and specimen) and on the amount of WC exposed on the given surface (that controls the extent of the mechanical locking). Indeed, the worn caps of the alumina balls (Fig. 4c) for the two test0 exhibit lower sizes in comparison to the worn caps for the interrupted tests due to a slightly lower quantity of WC carbide in the specific 6.3 surfaces used for the test0 (see section 2.2). Furthermore, the condition of the track is also influenced by the evacuation of the tribolayer, which leaves the WC carbides more exposed to the alumina ball (Fig. 11c). Both the alumina ball and the WC carbides are worn by their contact through mechanical locking and fracture [25]. Large fragments from Alumina and WC, together with some finer debris from the first tribolayer, act as third body of the 3-body abrasion, restarting the formation of a new tribolayer [45].

#### ***4.2.3. Role of the tribolayer***

In Fig. 12, the stabilisation of the first tribolayer (stage3) corresponds to a complete peak in the CoF since the PDe is stable on both sides of this peak (Fig. 3a). On the other hand, as discussed in section 4.2.2, during the shorter formation (Fig. 3d) of the second tribolayer (stage6) the PDe exhibits an increase corresponding to the left part of the peak of the CoF. This variation is probably due to the different combinations of wear mechanisms that lead to the formation of debris and thus of the tribolayer. Therefore, the stabilisation of the second tribolayer is considered as part of a stage7, corresponding to a steady PDe. Indeed, the formation of the second tribolayer (stage6) is faster (Fig. 3a) than for the first tribolayer (stage2) due to the presence of debris on the track coming from the previous stages and to a more regular surface (Fig. 5c) [45,48]. Test3 was stopped just after the complete stabilisation of the second tribolayer. Its worn track is oxygen-free and exhibits overall a smooth surface (Fig. 5c). Indeed, during stage6, the worn surface was levelled by the contact with the alumina ball and by the abrasion due to finer debris (Fig. 10d). Furthermore, as shown in Fig. 9, debris of different nature (Table 2) can fill in the gaps left by pulled out WC carbides (Fig. 10b) or the grooves in the matrix (Fig. 5b and Fig. 7c). In particular, the triangular dark shapes observed in Fig. 5c and Fig. 9 are compacted

oxides spread onto the surface (Fig. 9), filling the grooves or gaps left by previous wear stages (Fig. 11c). However, as shown by the comparison of the different surface conditions for test4 and test0 (that correspond both to stage7), the surface roughness depends on the nature of the debris formed during stage6 [37,45]. Large quantity of hard debris (from WC carbides and alumina) can increase 3-body abrasion, thus leading to a more irregular track with dark patches (Fig. 5d) [45], while intensifying the formation of the tribolayer [45,48]. In contrast, finer debris leads to an enhanced smoothing of the track (Fig. 5c and e) and to a more a homogeneous and well-spread tribolayer [48].

Stage6 and the first segment of the cyclical regime finish when the second tribolayer homogenise on the track. Then, a new segment of the cyclical regime begins (Fig. 3a). Stage7 corresponds to the compaction and stabilisation of the new tribolayer (Fig. 12). This proposed wear sequence of the MMC is schematized in Fig. 12. In order to represent the wear of the track and of the alumina ball (Fig. 4b and c), the height of the sample surface and the diameter of the ball are shown to decrease with the progress of the test. Furthermore, the main wear mechanisms for each stage are represented.

## 6. Conclusions

Under dry sliding conditions, the addition of WC particles by DED can significantly improve the wear resistance of the SS316L due to (partially dissolved) WC carbides and the formation of a reinforced matrix. In particular, WC carbides protect the matrix from direct contact with the ball and lead to an enrichment effect of the tribolayer during wear test. Furthermore, as also observed in the SS316L, after an initial plastic flow of the matrix, fragments of the new solidification carbides also enrich a MML and increase its strength, helping to improve the wear resistance.

The wear rate of the specimen decreases firstly and then presents no visible difference with increasing sliding time due to the formation of a protective tribolayer. The wear rate of the counterbody also decreases with the progress of the test. The wear of the counterbody depends on the length of the oxidative stage, which protects both ball and specimen, and on the amount of WC exposed on the given surface, which controls the extent of the mechanical locking of the ball. Moreover, results highlight that the nature of the counterbody and in particular, the nature of the debris (oxides mix) determines the tendency to form a stable tribolayer.

The interrupted tests approach has revealed important insights into the complex wear sequence of the 316L+20%WC composite. Indeed, SEM observations have shown different situations of the wear track depending on the sliding distance, corresponding to an evolution of the wear mechanisms. By considering the variations of both the CoF and the PDe, the wear rate evolution and the post-mortem observations of the wear tracks, the wear behaviour of the 316L+20%WC composite was elucidated and 7 different stages were distinguished.

- Two initial stages compose the initial run-in period, which is characterized by relatively severe wear of both specimen and counterbody due to delamination, adhesive wear and abrasive wear.
- Wear mechanisms of the run-in period lead to the formation of a large quantity of debris and then to the formation of the first tribolayer. A cyclical regime follows, characterized by mild wear involving the repeated compaction, breakdown and reformation of the protective tribolayer.

Supplementary data to this article can be found online at

## 7. Acknowledgements

This work has been supported by a subvention “Crédit classique” of the University of Liège, and by the European Fund for Regional Development and the Walloon Region under convention FEDER “Iawatha”. The authors acknowledge the CAREM of the ULiège for providing SEM/EDS/EBSDF facilities. They also wish to thank Sylvie Salieri, Jide Han and Benjamin Peeters for the sample preparation, Laura Zorzetto and Mattia Nordera for helpful discussion, Samuel Rondia for the substrates preparation and the Sirris Research Centre for providing access to the laser cladding equipment.

## References

- [1] L.J. O'Donnell, G.M. Michal, F. Ernst, H. Kahn, A.H. Heuer, Wear maps for low temperature carburised 316L austenitic stainless steel sliding against alumina, *Surf. Eng.* 26 (2010) 284–292. doi:10.1179/026708410X12550773057901.
- [2] P.A. Dearnley, G. Aldrich-Smith, Corrosion-wear mechanisms of hard coated austenitic 316L stainless steels, *Wear.* 256 (2004) 491–499. doi:10.1016/S0043-1648(03)00559-3.
- [3] D. Guan, X. He, R. Zhang, R. Li, X. Qu, Tribological and corrosion properties of PM 316L matrix composites reinforced by in situ polymer-derived ceramics, *Vacuum.* 148 (2018) 319–326. doi:10.1016/j.vacuum.2017.12.003.
- [4] H. Li, M. Ramezani, M. Li, C. Ma, J. Wang, Tribological performance of selective laser melted 316L stainless steel, *Tribol. Int.* 128 (2018) 121–129. doi:10.1016/j.triboint.2018.07.021.
- [5] L. Song, G. Zeng, H. Xiao, X. Xiao, S. Li, Repair of 304 stainless steel by laser cladding with 316L stainless steel powders followed by laser surface alloying with WC powders, *J. Manuf. Process.* 24 (2016) 116–124. doi:10.1016/j.jmapro.2016.08.004.
- [6] A. Lanzutti, E. Marin, K. Tamura, T. Morita, M. Magnan, E. Vaglio, F. Andreatta, M. Sortino, G. Totis, L. Fedrizzi, High temperature study of the evolution of the tribolayer in additively manufactured AISI 316L steel, *Addit. Manuf.* 34 (2020) 101258. doi:10.1016/j.addma.2020.101258.
- [7] Y. Sun, A. Moroz, K. Alrbaey, Sliding wear characteristics and corrosion behaviour of selective laser melted 316L stainless steel, *J. Mater. Eng. Perform.* 23 (2014) 518–526. doi:10.1007/s11665-013-0784-8.
- [8] S.M. Thompson, L. Bian, N. Shamsaei, A. Yadollahi, An overview of Direct Laser Deposition for additive manufacturing; Part I: Transport phenomena, modeling and diagnostics, *Addit. Manuf.* 8 (2015) 36–62. doi:10.1016/j.addma.2015.07.001.
- [9] H. Paydas, A. Mertens, R. Carrus, J. Lecomte-Beckers, J.T. Tchuindjang, Laser cladding as repair technology for Ti-6Al-4V alloy: Influence of building strategy on microstructure and hardness, *Mater. Des.* 85 (2015) 497–510. doi:10.1016/j.matdes.2015.07.035.
- [10] P. Köhnen, M. Létang, M. Voshage, J.H. Schleifenbaum, C. Haase, Understanding the process-microstructure correlations for tailoring the mechanical properties of L-PBF produced austenitic advanced high strength steel, *Addit. Manuf.* 30 (2019) 100914. doi:10.1016/j.addma.2019.100914.
- [11] H. Chen, D. Gu, K. Kosiba, T. Lu, L. Deng, L. Xi, U. Kühn, Achieving high strength and high ductility in WC-reinforced iron-based composites by laser additive manufacturing, *Addit. Manuf.* 35 (2020) 101195. doi:10.1016/j.addma.2020.101195.
- [12] I.T. Ho, Y.T. Chen, A.C. Yeh, C.P. Chen, K.K. Jen, Microstructure evolution induced by inoculants during the selective laser melting of IN718, *Addit. Manuf.* 21 (2018) 465–471. doi:10.1016/j.addma.2018.02.018.
- [13] A.I. Mertens, J. Lecomte-Beckers, On the Role of Interfacial Reactions, Dissolution and Secondary Precipitation During the Laser Additive Manufacturing of Metal Matrix Composites: A Review, in: I. V Shishkovsky (Ed.), *New Trends 3D Print., I.V., InTech, Rijeka, Croatia, 2016*: pp. 187–213. doi:10.5772/63045.
- [14] O. Ertugrul, T. Maurizi Enrici, H. Paydas, E. Saggionetto, F. Boschini, A. Mertens, Laser cladding of TiC reinforced 316L stainless steel composites: Feedstock powder preparation and microstructural evaluation, *Powder Technol.* 375 (2020) 384–396. doi:10.1016/j.powtec.2020.07.100.
- [15] Y.L. Zhang, J. Li, Y.Y. Zhang, D.N. Kang, Evolution in microstructure and high-temperature oxidation behaviors of the laser-cladding coatings with the Si addition contents, *J. Alloys Compd.* 827 (2020). doi:10.1016/j.jallcom.2020.154131.

- [16] J. Li, Z. Zhao, P. Bai, H. Qu, M. Liang, H. Liao, L. Wu, P. Huo, Tribological behavior of TiC particles reinforced 316Lss composite fabricated using selective laser melting, *Materials (Basel)*. 16 (2019). doi:10.3390/ma12060950.
- [17] D. Deschuyteneer, F. Petit, M. Gonon, F. Cambier, Processing and characterization of laser clad NiCrBSi/WC composite coatings - Influence of microstructure on hardness and wear, *Surf. Coatings Technol.* 283 (2015) 162–171. doi:10.1016/j.surfcoat.2015.10.055.
- [18] T. Maurizi Enrici, O. Dedry, F. Boschini, J.T. Tchuindjang, A. Mertens, Microstructural and Thermal Characterization of 316L+WC Composite Coatings obtained by Laser Cladding, *Adv. Eng. Mater.* 13 (2020) 1–12. doi:10.1002/adem.202000291.
- [19] H. Torres, T. Vuchkov, M. Rodríguez Ripoll, B. Prakash, Tribological behaviour of MoS<sub>2</sub>-based self-lubricating laser cladding for use in high temperature applications, *Tribol. Int.* 126 (2018) 153–165. doi:10.1016/j.triboint.2018.05.015.
- [20] J.Z. Lu, J. Cao, H.F. Lu, L.Y. Zhang, K.Y. Luo, Wear properties and microstructural analyses of Fe-based coatings with various WC contents on H13 die steel by laser cladding, *Surf. Coatings Technol.* 369 (2019) 228–237. doi:10.1016/j.surfcoat.2019.04.063.
- [21] X. Tong, F.H. Li, M. Kuang, W.Y. Ma, X.C. Chen, M. Liu, Effects of WC particle size on the wear resistance of laser surface alloyed medium carbon steel, *Appl. Surf. Sci.* 258 (2012) 3214–3220. doi:10.1016/j.apsusc.2011.11.066.
- [22] S. Zhou, X. Dai, H. Zheng, Microstructure and wear resistance of Fe-based WC coating by multi-track overlapping laser induction hybrid rapid cladding, *Opt. Laser Technol.* 44 (2012) 190–197. doi:10.1016/j.optlastec.2011.06.017.
- [23] Z. Weng, A. Wang, X. Wu, Y. Wang, Z. Yang, Wear resistance of diode laser-clad Ni/WC composite coatings at different temperatures, *Surf. Coatings Technol.* 304 (2016) 283–292. doi:10.1016/j.surfcoat.2016.06.081.
- [24] M.R. Fernández, A. García, J.M. Cuetos, R. González, A. Noriega, M. Cadenas, Effect of actual WC content on the reciprocating wear of a laser cladding NiCrBSi alloy reinforced with WC, *Wear*. 324–325 (2015) 80–89. doi:10.1016/j.wear.2014.12.021.
- [25] J. Domitner, M. Aigner, T. Stern, A. Paar, C. Sommitsch, L. Elizondo, Thermo-Mechanical Wear Testing of Metal Matrix Composite Cladding for Potential Application in Hot Rolling Mills, *Steel Res. Int.* 1900478 (2019). doi:10.1002/srin.201900478.
- [26] X. Yan, C. Chen, R. Zhao, W. Ma, R. Bolot, J. Wang, Z. Ren, H. Liao, M. Liu, Selective laser melting of WC reinforced maraging steel 300: Microstructure characterization and tribological performance, *Surf. Coatings Technol.* 371 (2019) 355–365. doi:10.1016/j.surfcoat.2018.11.033.
- [27] M. Pellizzari, D. Cescato, M.G. De Flora, Hot friction and wear behaviour of high speed steel and high chromium iron for rolls, *Wear*. 267 (2009) 467–475. doi:10.1016/j.wear.2009.01.049.
- [28] A.C.P. Rodrigues, T. Yonamine, A. Sinatora, C.R.F. Azevedo, Pin-on-disc tribotests with the addition of Cu particles as an interfacial media: Characterization of disc tribosurfaces using SEM-FIB techniques, *Tribol. Int.* 100 (2016) 351–359. doi:10.1016/j.triboint.2016.03.034.
- [29] C. Vergne, C. Boher, R. Gras, C. Levailant, Influence of oxides on friction in hot rolling: Experimental investigations and tribological modelling, *Wear*. 260 (2006) 957–975. doi:10.1016/j.wear.2005.06.005.
- [30] M. Łepicka, A. Ciszewski, K. Golak, M. Gradzka-Dahlke, A comparative study of friction and wear processes of model metallic biomaterials including registration of friction-induced temperature response of a tribological pair, *Materials (Basel)*. 12 (2019). doi:10.3390/ma1224163.
- [31] C.X. Li, J. Xia, H. Dong, Sliding wear of TiAl intermetallics against steel and ceramics of Al<sub>2</sub>O<sub>3</sub>, Si<sub>3</sub>N<sub>4</sub> and WC/Co, *Wear*. 261 (2006) 693–701. doi:10.1016/j.wear.2006.01.044.

- [32] C. Zhang, J. Song, L. Jiang, J. Gao, G. Liang, C. Lei, J. Xie, S. Wang, M. Lv, Fabrication and tribological properties of WC-TiB<sub>2</sub> composite cutting tool materials under dry sliding condition, *Tribol. Int.* 109 (2017) 97–103. doi:10.1016/j.triboint.2016.12.029.
- [33] A. Ayyagari, V. Hasannaemi, H.S. Grewal, H. Arora, S. Mukherjee, Corrosion, erosion and wear behavior of complex concentrated alloys: A review, 2018. doi:10.3390/met8080603.
- [34] X. Liang, Z. Liu, B. Wang, Physic-chemical analysis for high-temperature tribology of WC-6Co against Ti-6Al-4V by pin-on-disc method, *Tribol. Int.* 146 (2020) 106242. doi:10.1016/j.triboint.2020.106242.
- [35] N.F. Garza-Montes-de-Oca, W.M. Rainforth, Wear mechanisms experienced by a work roll grade high speed steel under different environmental conditions, *Wear.* 267 (2009) 441–448. doi:10.1016/j.wear.2009.01.048.
- [36] J. Dai, X. Zhang, Q. Yin, S. Ni, Z. Ba, Z. Wang, Friction and wear behaviors of biodegradable Mg-6Gd-0.5Zn-0.4Zr alloy under simulated body fluid condition, *J. Magnes. Alloy.* 5 (2017) 448–453. doi:10.1016/j.jma.2017.11.002.
- [37] N. Hashemi, A. Mertens, H.M. Montrieux, J.T. Tchuindjang, O. Dedry, R. Carrus, J. Lecomte-Beckers, Oxidative wear behaviour of laser clad High Speed Steel thick deposits: Influence of sliding speed, carbide type and morphology, *Surf. Coatings Technol.* 315 (2017) 519–529. doi:10.1016/j.surfcoat.2017.02.071.
- [38] J.S. Zuback, T. DebRoy, The hardness of additively manufactured alloys, *Materials (Basel)*. 11 (2018). doi:10.3390/ma11112070.
- [39] M. Fellah, M. Labaiz, O. Assala, a Iost, L. Dekhil, Tribological behaviour of AISI 316L stainless steel for biomedical applications, *Tribol. - Mater. Surfaces Interfaces.* 7 (2013) 135–149. doi:10.1179/1751584X13Y.0000000032.
- [40] D.R. Feenstra, V. Cruz, X. Gao, A. Molotnikov, N. Birbilis, Effect of build height on the properties of large format stainless steel 316L fabricated via directed energy deposition, *Addit. Manuf.* 34 (2020) 101205. doi:10.1016/j.addma.2020.101205.
- [41] A. Akay, Acoustics of friction, *J. Acoust. Soc. Am.* 111 (2002) 1525–1548. doi:10.1121/1.1456514.
- [42] J. Downey, P. O’Leary, R. Raghavendra, Comparison and analysis of audible sound energy emissions during single point machining of HSTS with PVD TiCN cutter insert across full tool life, *Wear.* 313 (2014) 53–62. doi:10.1016/j.wear.2014.02.004.
- [43] Z. Bing Cai, H. da Guan, Z. Qiang Chen, H. Qian, L. Chen Tang, Z. Rong Zhou, M. Hao Zhu, Impact fretting wear behavior of 304 stainless steel thin-walled tubes under low-velocity, *Tribol. Int.* 105 (2017) 219–228. doi:10.1016/j.triboint.2016.10.002.
- [44] C. Samuel, S. M. Arivarasu, T.R. Prabhu, High temperature dry sliding wear behaviour of laser powder bed fused Inconel 718, *Addit. Manuf.* 34 (2020) 101279. doi:10.1016/j.addma.2020.101279.
- [45] H.L. Costa, M.M. Oliveira Junior, J.D.B. de Mello, Effect of debris size on the reciprocating sliding wear of aluminium, *Wear.* 376–377 (2017) 1399–1410. doi:10.1016/j.wear.2016.10.025.
- [46] M. Kazemi, H. Saghafian, Application of response surface methodology in determining the optimal wear properties of the titanium carbide reinforced AISI H13 hot working tool steel fabricated by pulsed laser method, *Surf. Coatings Technol.* 404 (2020) 126478. doi:10.1016/j.surfcoat.2020.126478.
- [47] H. Arik, Y. Ozcatalbas, M. Turker, Dry sliding wear behavior of in situ Al-Al<sub>4</sub>C<sub>3</sub> metal matrix composite produced by mechanical alloying technique, *Mater. Des.* 27 (2006) 799–804. doi:10.1016/j.matdes.2005.01.024.
- [48] M. Varga, H. Rojacz, H. Winkelmann, H. Mayer, E. Badisch, Wear reducing effects and temperature dependence of tribolayer formation in harsh environment, *Tribol. Int.* 65 (2013) 190–199. doi:10.1016/j.triboint.2013.03.003.

[49] W. Gwidon, A.W.B. Stachowiak, *Engineering Tribology* 4th Ed., Elsevier B.V., 2014.  
doi:10.1017/CBO9781107415324.004.

[50] V. Brizmer, C. Matta, I. Nedelcu, G.E. Morales-Espejel, The Influence of Tribolayer Formation on Tribological Performance of Rolling/Sliding Contacts, *Tribol. Lett.* 65 (2017). doi:10.1007/s11249-017-0839-3.



---

## *On the microstructures and strengthening mechanisms of new high-silicon austenitic stainless steels obtained by Laser Cladding*

*Tommaso Maurizi Enrici, Enrico Saggionetto, Olivier Dedry, Onur Ertugrul, Frédéric Boschini, Jérôme Tchoufang Tchuidjang, Anne Mertens*

### **Abstract**

This work focuses on the fabrication and characterization of thick deposits fabricated by laser cladding, composed of 316L stainless steel and respectively 10% and 20% in volume of silicon carbides (SiC). SEM observations, XRD and DTA analyses were considered to set the most suitable time-saving powders preparation in order to eliminate the oxygen from SiC feedstock and to elucidate the solidification sequence. The total dissolution of the original SiC powders led to the formation of two distinct austenitic microstructures reinforced by solidification carbides with a hardness increase of respectively 61 HV and 151 HV for additions of 10 or 20 vol. % SiC. Moreover, the effect of the Si enrichment in the alloy composition was evaluated via nanoindentation measurements inside the austenitic cells. As observed in high-entropy steels, Si solid solution leads to a remarkable strengthening of the FCC crystal lattice and thus contributes significantly to the improved mechanical properties.

**Keywords:** Laser cladding; Nanoindentation; Metal matrix composite; Mechanical alloying; Solid solution

### **1. Introduction**

Additive manufacturing (AM), also known as three-dimensional (3D) printing, has experienced significant growth over the past 25 years in several areas, ranging from the conception of new machines to the number and complexity of parts produced [1–3]. As far as materials are concerned, only few alloys borrowed from the existing weldable alloys, -the most relevant being stainless steels, TiAl6V4, AlSi10Mg, Inconel 718 and CoCr-, can be reliably printed [2,4]. However, efforts to modify conventional alloys or to develop new alloys taking advantage of the metallurgical characteristics and particularly of the ultra-fast kinetics of AM processes remain relatively scarce [2,4–8]. Only a handful of new alloys for AM or by AM is currently being researched [3], but the so-called alloys-by-design approach [7,9] offers tremendous opportunities to develop new alloys combining multiple strengthening mechanisms for improved mechanical properties or exploiting specific element segregations to increase the corrosion resistance [6,7,10].

In line with these considerations, the present work aims to synthesize a new stainless steel alloy for the deposition of wear-resistant coating on the surface of stainless steel 316L parts by modifying the composition of 316L through the dissolution of specific reactants in the molten metal during fabrication [3,11–13]. The dissolution of the reactants enriches the composition of the host matrix and leads to new solidification routes depending on the vol.% of these secondary reactants [8,13,14]. Among AM technologies, Laser Cladding (LC), also known as Directed Metal Deposition, is particularly well-suited for this approach since it is capable to handle one or two different powders, which are fed into a focused laser beam while being scanned across a substrate, thus leaving behind a coating or object. Furthermore, this technology is particularly suitable for material development among AM technologies since the quantity of powders needed is small in comparison to powder-bed fusion (PBF) processes and since this process can quickly build deposit with a 100% dense, metallurgically bonded and tailored material [4,10,15–17].

Among the possible reactants, silicon carbide (SiC) appears as a very promising candidate since, upon its dissolution, Si is expected to increase both the strength of the matrix and the corrosion resistance of the alloy while C is observed to form hard carbides by combining with the other available alloying elements in stainless steel 316L [10,12]. Moreover, studies on the fabrication of steel + SiC composites generally report the total dissolution of SiC due to its high chemical affinity with Fe-based alloys [8,12,14,18–21] and only [18] claims to obtain a partial dissolution of the SiC powders, although without showing an overview of the microstructure.

As observed in [12,20,22,23], Si addition has a considerable impact on the mechanical properties of ferrous alloys. Its presence as a substitutional element in the Fe-lattice leads to a decrease of the lattice parameters and a significant increase of the hardness in  $\alpha$ -ferrite (BCC crystal order) [24–26]. Besides, only [27] has investigated the presence of Si in Fe-alloys fabricated by AM, where extremely high cooling rates result in non-equilibrium phase formation and into a disordered solid solution. In contrast, the presence of Si in the lattice of  $\gamma$ -austenite (FCC crystal order) was considered both theoretically [26] and experimentally [28,29], but only under equilibrium conditions, possibly due to the low solubility of Si in the  $\gamma$ -austenite lattice (maximum solubility of 3.8 wt. % at 1130°C according to the Fe-Si phase diagram) and to the tendency of Si to stabilize the BCC crystal order [30]. In particular, in [26], calculation of the local lattice strain around solute atom reveals that under equilibrium conditions the addition of elements in the iron FCC lattice leads to an expansion, independently

to the atom.  $\gamma$ -stabilizers (i.e. Mn, Co and Ni) lead to small lattice strains due to their similar crystal order. On the other hand,  $\alpha$ -stabilizers (i.e. Mo, V, W and Ti) lead to high lattice strains [26].

From a practical standpoint, the use of SiC powders has often been shown to result in porosity problems [19,20,23] due to the oxygen present as cavities or closed pores in the feedstock that is produced by a carbo-thermal reduction (Acheson process) followed by a post-processing step involving spray drying [31–33]. Indeed, this is verified in the present study as shown in the cross-section of the deposit composed of 316L and 20% in volume of SiC fabricated by handling the original 316L and SiC powders separately (Fig. 1).

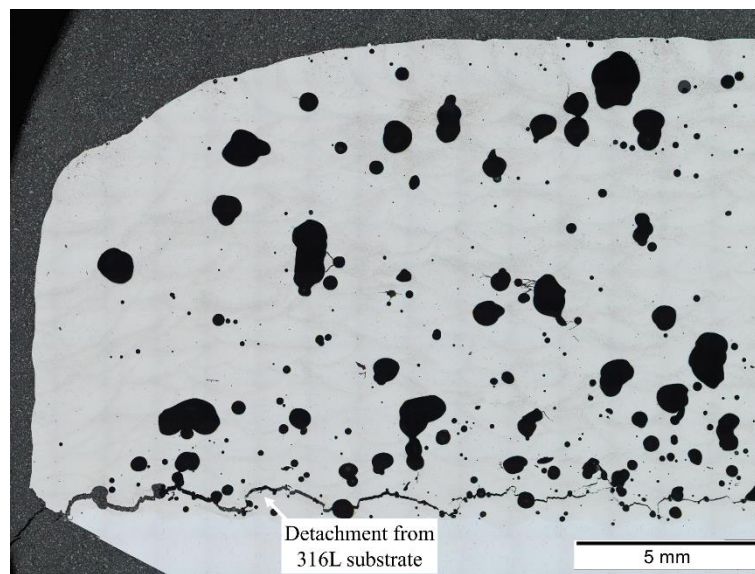


*Fig. 1: Overview of the deposit fabricated from a mixture of 316L + 20 vol. % SiC obtained by handling separately the two original powders.*

As also observed in [19,20,23], high quantities of porosities within the original SiC feedstock lead to the presence of large porosities after cladding and to the detachment of the deposit from the 316L substrate due to the build-up of residual stresses (Fig. 1). These defects can be ascribed at least in part to the uncompleted reduction from the silica to SiC and to the presence of remaining porosities after the production of spherical powders by spray drying. Indeed, it is generally established that spherical powders are more suitable than irregular morphologies for AM processes, so as to ensure good flowability and thus constant fabrication conditions [1,34,35]. Spray drying is used for the efficient production of large quantities of globular or spherical powders from smaller irregular particles [32,33]. In this process, a binder is needed at the beginning of the process, which is removed during a second step involving drying and

atomization [32]. For particles of large size, the outer shell may form faster due to local differences of temperature experienced during drying, leaving a hollow centre with trapped vapours, resulting in internal closed porosities in the final product [33].

In order to overcome this problem and extend the possible choice of feedstock for LC, mechanical alloying using ball milling has demonstrated a high versatility and good results have been obtained for the preparation of homogeneous powder mixtures [14,36]. The purpose of the mechanical alloying is to close the porosities and fracture the SiC particles. This diverges from the classical use of this procedure that aims at the attachment of the reinforcements to the host powders. Interestingly, [12,21] already applied this procedure, but without clarifying the purpose.

In this study, the attention is focused on the fabrication of thick deposits composed of 316L and respectively 10 and 20% in volume of SiC, the dissolution of the SiC in the melt pool and the characterization of the resulting microstructures. Since the used SiC powders exhibit a small oxygen content, they were modified via ball milling in order to eliminate the closed porosities and obtain a homogenous powder mixture in the shortest milling time. Differential thermal analysis (DTA) is considered in order to evaluate the evolution of the powder mixtures during ball milling as well as to elucidate the solidification sequence of the modified high-silicon stainless steels by means of a reverse analysis of the DTA heating curves [8,37]. Furthermore, the evolution of the microstructure with the increase of the vol.% of SiC and the corresponding strengthening mechanisms are investigated via SEM observations, nanoindentation and macrohardness measurements.

## 2. Materials and Methods

### 2.1. Powder preparation

Gas atomized AISI 316L stainless steel powder (Höganäs AB) with particle sizes in the range of 50-200  $\mu\text{m}$  (average particle size  $\sim 113 \mu\text{m}$ ) was used as matrix (Fig. 1a). SiC particles (H.C. Starck) with a size range of 20-200  $\mu\text{m}$  (average particle size  $\sim 65 \mu\text{m}$ ) were used as reactants (Fig. 1b). The compositions of both powders are given in Table 1. SiC exhibits a maximum oxygen content of 5 wt.% in the form of small quantities of unreacted silica and inside porosities (Fig. 1b) [31–33]. SiC particles are either spherical or “doughnut-like shape” with small satellites (Fig. 1b). In particular, as reported in [32], the doughnut-like shape may occur during spray drying due to the droplet-to-particle conversion.

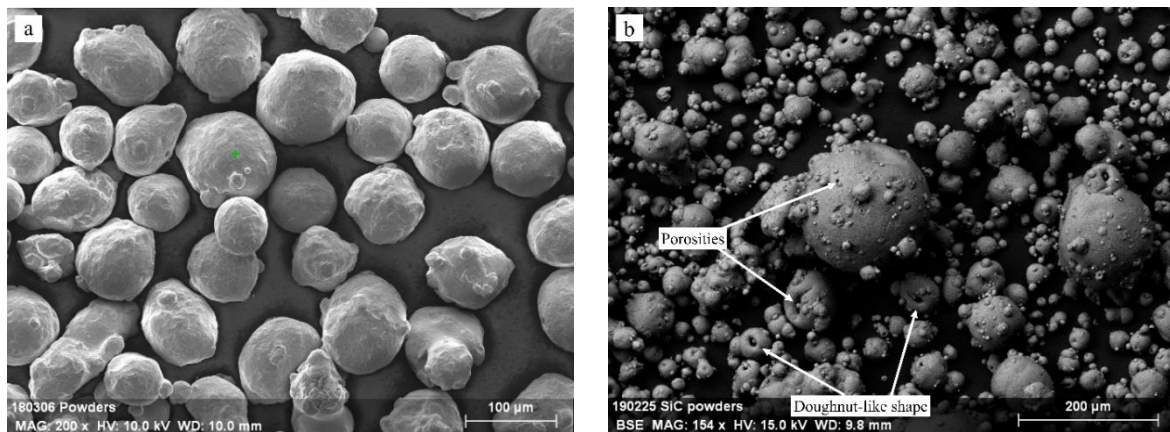


Fig. 2: SEM micrographs of 316L (SE mode) and SiC powders (BSE mode).

Table 1: Chemical composition of 316L and SiC powders from producers datasheets.

%wt.	C	Si	Cr	Mo	Mn	Ni	Fe	O
316L	0.015	0.7	16.9	2.5	1.5	12.6	Bal.	
SiC	32	Bal.						< 5

316L/SiC (10 and 20 vol.%) composite powders were prepared by high-energy ball-milling (mechanical alloying) of the powders using a Retsch planetary ball mill equipped with WC balls and vials [14]. The powders were milled for increasing milling times at a milling speed of 150 rpm and with a ball-to-powder mass ratio (BPR) of 1:5. No process control agent was used.

Table 2: Parameters of the ball milling procedures applied on the 316L+SiC mixture and SiC powders.

	Ball-to-powder ratio	Milling time (h)	Stage
316L+SiC	1:5	1	1
		2	2
		4	3
		6	4
SiC	1:5	1	1
	1:3	2	2
	1:1		

Four milling times were applied in order to close the porosities or break the SiC reactants while avoiding contamination from the WC ball and excessive deformation of the 316L powders (Table 2). Moreover, two milling times (1 or 2 hours) with three different BPR (1:5, 1:3 and 1:1) were applied on the SiC alone to evaluate the possibility of pre-treating the SiC powder before mixing with the 316L powders (Table 2). One set of powder mixtures was prepared by manual mixing for comparison purposes. The 20%SiC mixture was used as reference for the preparation of the powders due to the larger quantity of SiC powders to treat via ball milling. Therefore, the milling time chosen for the 20%SiC mixture was also applied to the 10%SiC mixture. After 30 min of milling, the rotation was stopped for 15 min in order to avoid excessive temperature rise inside the grinding bowl.

## 2.2. Sample fabrication

19 layers-thick stainless steel 316L – SiC deposits have been prepared on a SS316L substrate using a 5-axis Irepá DED system with a Nd-YAG laser source. The laser power (P) was varied between 260-400W for a corresponding traverse speed (V) of 250-270 mm/min, and the layer thickness was set equal to 600  $\mu\text{m}$ . A shift of a half-track width was applied every two layers to allow a good overlapping of the layers. The stream of powder was focused into the laser beam by an inert gas flow and directed towards the substrate at an angle of 38–45°. As feedstock, the mechanically alloyed mixtures mentioned in section 2.1 with respectively 10% (S10) and 20% (S20) in vol.% of SiC (Fig. 3b and c respectively) were used. The final dimensions of these deposits were 35 x 35 mm side length and 14 mm height Fig. 3b and c). For comparison purposes, one thick stainless steel 316L deposit (Fig. 3a) and one S20 deposit (Fig. 1) were fabricated with the same parameters, handling the powders separately as in [8].

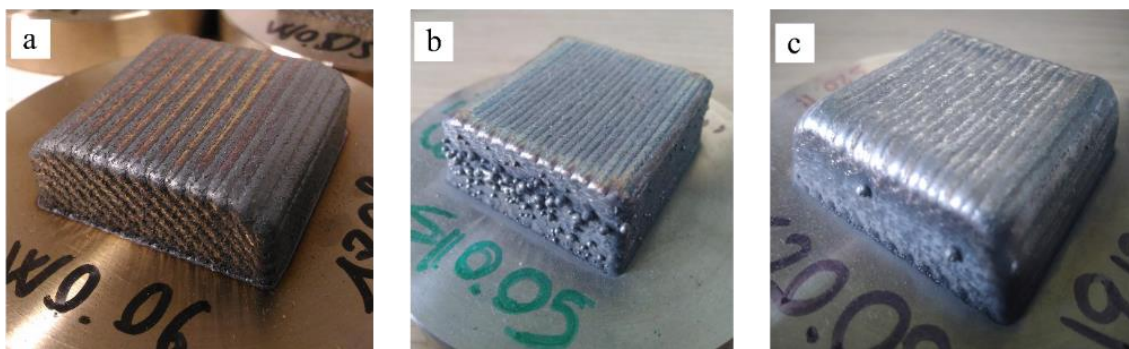


Fig. 3: (a) 316L, (b) 316L+10%SiC (S10) and (c) 316L+20%SiC (S20) deposits.

### 2.3. Microstructural characterization

Scanning electron microscopy (SEM) observations of the powder mixtures were carried out by using Philips XL30 FEG-ESEM microscope equipped with a 10 mm<sup>2</sup> Bruker SDD type EDS detector. Microstructural characterization of the clad microstructures was carried out with the same instrument after standard sample preparation [8]. In particular, the average chemical compositions of the phases were obtained from EDS chemical profiles [8,37]. Phase analysis of the powder mixtures and the clad samples was performed by X-ray diffraction (XRD) using a PANalytical X'Pert PRO D3290 model diffractometer with a Cu K $\alpha$  radiation. Particle size distribution of the powders was measured by laser diffraction granulometry (Malvern Instruments Ltd., Malvern, UK – Mastersizer 2000 Dry Dispersion); number of measurements,  $n = 3$ . In addition, DTA analyses of the mixtures were carried out on a NETZSCH 449C Jupiter apparatus in heating mode at constant scans of 5°C min<sup>-1</sup> up to 1500°C, so as to achieve a complete remelting of the original 316L powders, the of the 20%SiC mixtures with increasing milling time and of the clad deposits. DTA analysis was also carried out on the original SiC powder up to 1400°C. DTA remelting curves are considered here to evaluate the phase transformations of the powders with the increase of the temperature as well as to restore the solidification sequence of the three clad specimens by means of a reverse analysis, as in [8,37]. This approach has proven efficient to identify the phases in complex out-of-equilibrium microstructures obtained at high cooling rates and to gain insights into their formation. The first derivative of the DTA curve (DDTA) is computed using NETZSCH Proteus® Thermal Analysis software. This helps to identify individual peaks when overlapping occurs [8,37].

#### **2.4. Macro-Hardness test and nanoindentation measurements**

10 kg Vickers hardness tests were carried out on both the pure 316L and S10 and S20 deposits (in as polished state) using a universal hardness device equipped with an electronic cell force. A distance of 1 mm was set between test points (horizontally and vertically) to avoid interactions between adjacent indents [38].

Moreover, nano-indentations measurements inside the cells of all the deposits were carried out using a HYSITRON TI 950 TriboIndenter at controlled displacement equal to 100 nm using a Cube-corner indenter tip on a low load transducer, while the load was continuously monitored. A few erratic measurements involving pop-in and relaxation phenomena were deleted. Owing to the chosen displacement, a minimum distance of 1.5  $\mu\text{m}$  was maintained between the indents to avoid any overlapping of their affected volumes [39].

### 3. Results and Discussion

#### 3.1. Powder preparation

##### 3.1.1. Morphological evolution of ball-milled powders

Fig. 4 – 7 show the SEM micrographs describing the evolution of the particle morphology and of the interactions between the two initial powders. Powders mixed manually, stage 0 (Fig. 4a), exhibit a heterogeneous distribution of the two initial powders. In comparison to Fig. 2, few small SiC satellites are attached to the 316L particles in addition to the satellites already present on the SiC powders (Fig. 4b). The spherical or “doughnut-like” shape of the SiC is still observed (Fig. 4b).

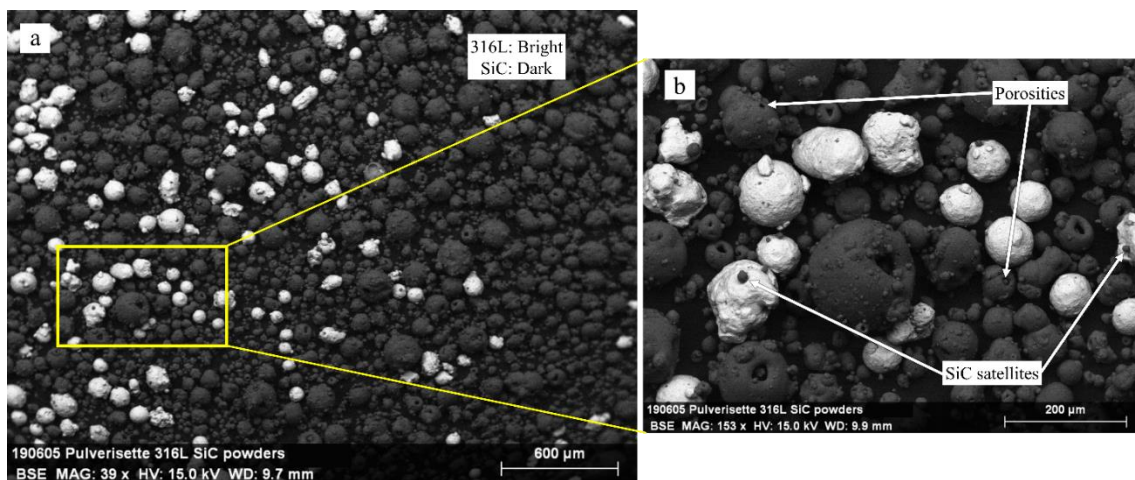
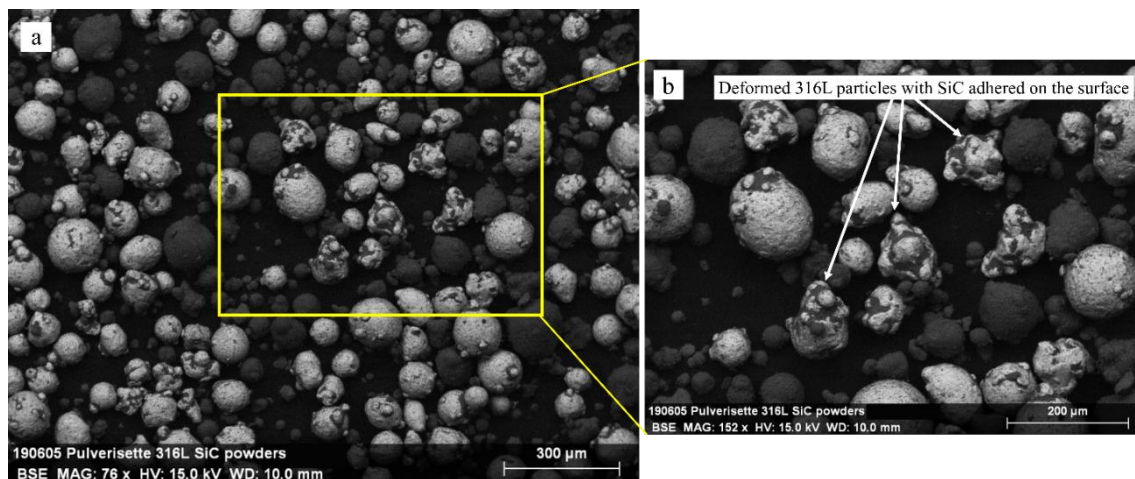


Fig. 4: Stage 0 – (a) Lower and (b) higher magnification of manual mixed powder mixture (BSE mode).

After 1-hour milling (stage 1), the mixing of the two powders is more homogeneous (Fig. 5a) and the morphologies remain similar to the manually mixed powders (Fig. 4b). 316L powders appear unperturbed. Nevertheless, some material from the SiC powder is adhered on the surface of deformed 316L particles due to the continuous friction between the powders during milling (Fig. 5b).



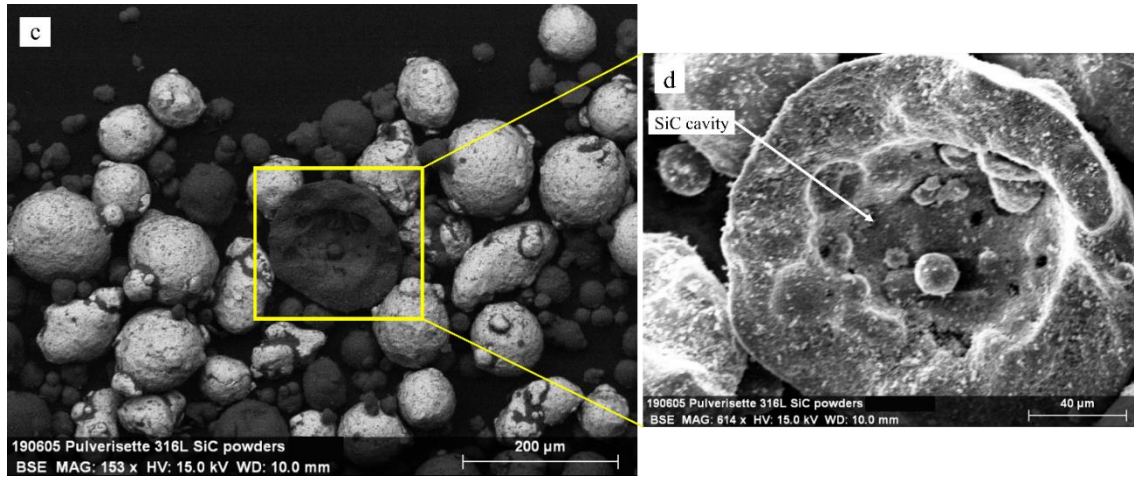
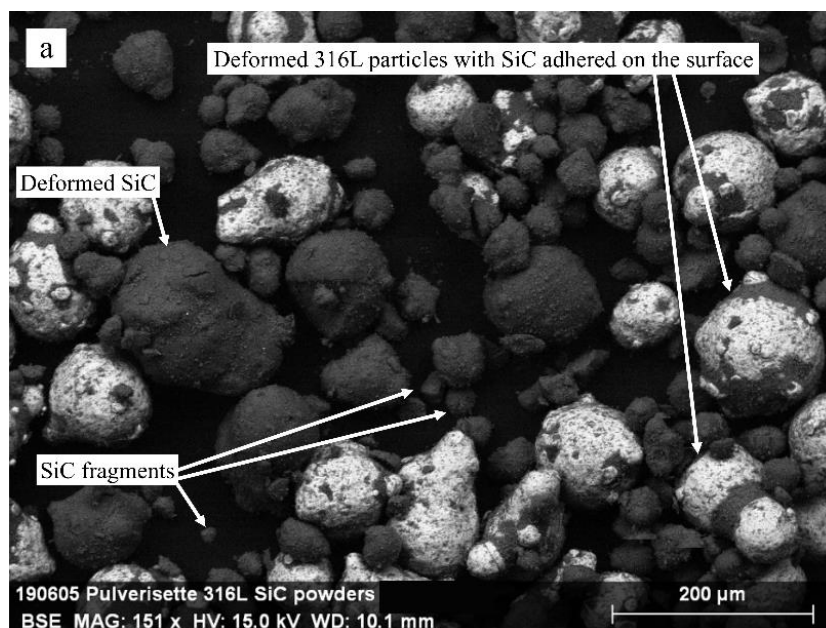


Fig. 5: Stage 1 (1-hour milling) - (a) Overview of the mixture. (b) Fractured SiC and adhered SiC on the deformed 316L and (c) are observed (BSE mode). (d) Zoom of a hollow SiC with porosities (SE mode).

SiC particles are deformed and the “doughnut-like” shape is not observed anymore. Moreover, most of the open pores on the SiC particles surfaces have disappeared due to the plastic deformation applied during milling. Indeed, many SiC particles are fractured (Fig. 5c) and some appear hollow with few internal porosities (Fig. 5d) due to the contact with the WC balls and with the 316L powders.

After 2-hours milling (stage 2), the 316L particles in the mixed powders exhibit an elongated or globular morphology due to plastic deformation and the adhesion of SiC particles increases (Fig. 6a). The quantity of SiC fragments also increases while their size decreases as SiC powders are fractured (Fig. 6b) or mashed (Fig. 6c). After 2 hours, open porosities are not visible anymore, but this change is achieved at the expense of the SiC morphology and size.



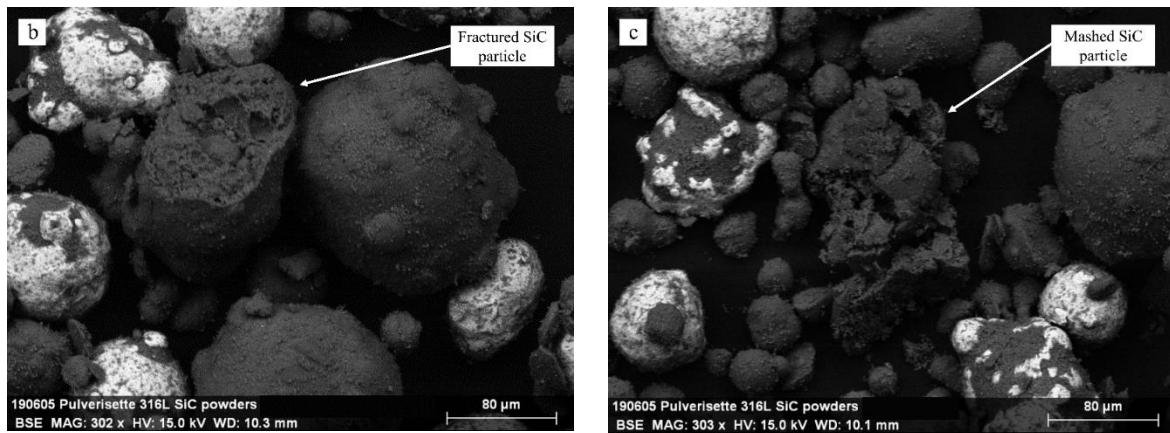
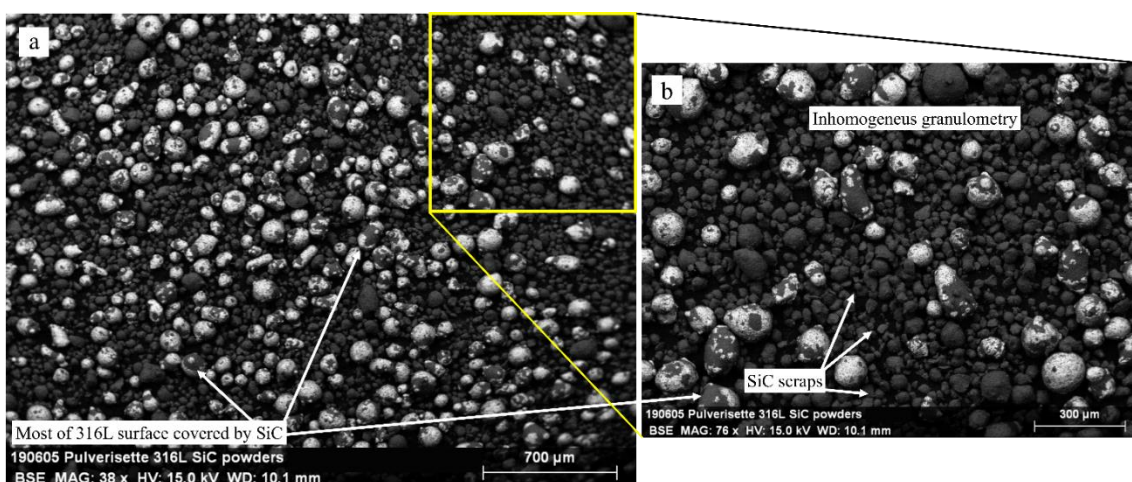


Fig. 6: Stage 2 (2-hours milling) - (a) Small fragments, deformed SiC and adhered SiC on the deformed 316L. Zooms of (b) fractured and (c) highly deformed SiC (BSE mode).

After 4 and 6-hours milling (stage 3 and 4 respectively), the mechanical alloying of the two powders begins to show deleterious effects. Indeed, with the progress of milling, the difference of size between 316L particles and SiC fragments increases (Fig. 7a). The amount of adhered SiC material further increases until it almost completely covers the 316L powders (Fig. 7b). As seen in Fig. 7c, some SiC scraps are smaller than  $20\ \mu\text{m}$  (Fig. 7c). These long milling times thus lead to a significant proportion of the powders being outside of the required particle size range of LC [14]. Indeed, while small SiC can be carried by the 316L powders during fabrication, excessive quantities of small fragments can lead to heterogeneities of the repartition of the two powders inside the mixture and as a result to the formation of locally heterogeneous microstructures in the deposit.



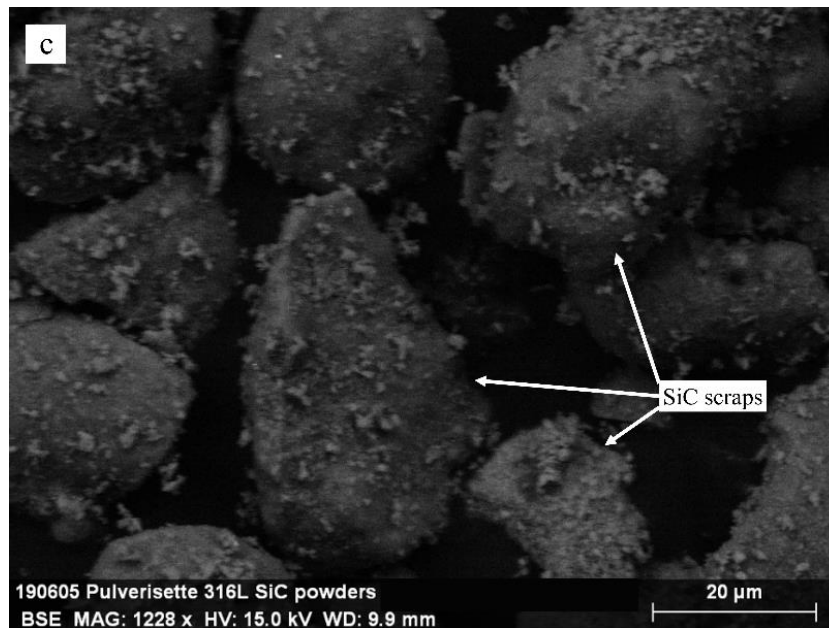


Fig. 7: Stage 3 and 4 (respectively 4 and 6-hours milling) - (a) Overview of Stage 3 shows an (b) large size distribution. (c) Zoom of SiC fragments with small satellites (BSE mode).

### 3.1.2. Evolution of the size distribution

The various powder mixtures obtained after 1-hour milling, together with the original and the manually mixed powders for comparison purposes, were further analysed via particle size analysis (Table 3) in order to confirm the SEM observations.

Both the manual mixture and the milled mixtures exhibit a lower average particle size (APS) in comparison to the original 316L powders due to the presence of the small SiC particles. The fragmentation of the SiC during ball milling remains limited, as shown by the APS values and the particle size ranges for the milled mixtures that are only slightly higher than the ones for the manual mixed state (Fig. 5). Indeed, as shown in Fig. 5c, the fragmentation concerns mainly large reactants ( $\sim 200 \mu\text{m}$ ), leading to an enrichment of the population of particles at  $\sim 100 \mu\text{m}$ . On the other hand, original SiC exhibits a slightly smaller particle size than the official size range announced by the powder producer, a variation that can be ascribed to the detachment of satellites during the measurements (Fig. 1b and Fig. 4). The milling process broadens the size distribution of the milled SiC powders in comparison to the original SiC.

Table 3: Particle size distribution of the original and milled powders.

Powders	Particle size distribution ( $\mu\text{m}$ )		
	d10	d50	d90
SiC	17	58	122
316L	76	113	168
Milled SiC (1:3 – 1h)	11	52	158
Manual mixture - 316L+20% SiC	54	87	132
Milled 316L+10% SiC (1:5 - 1h)	67	100	150
Milled 316L+20% SiC (1:5 - 1h)	54	93	150

### 3.1.3. X-ray analysis

XRD analysis was carried out on the milled mixed 316L + 20% SiC powder, the milled pure SiC powder and the original 316L powder, in order to verify for the possible occurrence of oxidation during mechanical alloying. Fig. 8 illustrates the measured XRD patterns. 316L (Fig. 8a) and  $\alpha$ -SiC (Fig. 8b) powders show the typical characteristic peaks as already given in the literature [14,40,41]. The XRD pattern of the powder mixture (Fig. 8c) is the combination of the two previous patterns. The patterns of the two milled powders do not exhibit peaks related to oxide formation during mechanical alloying.

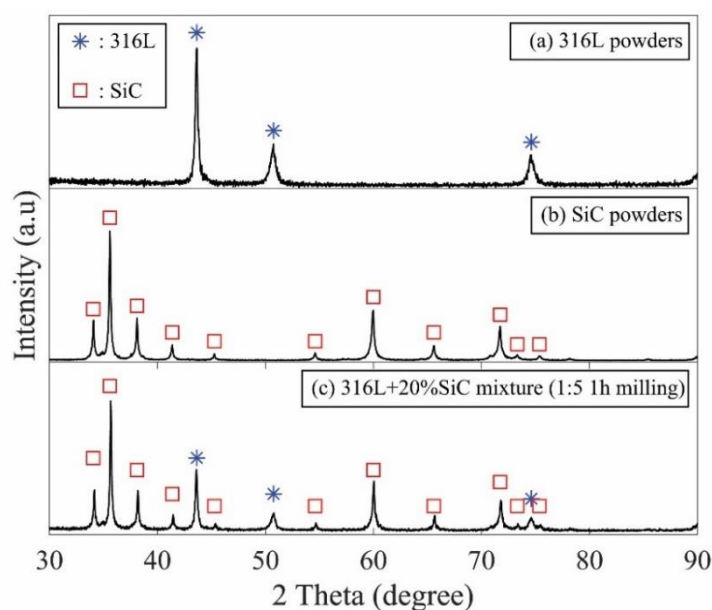
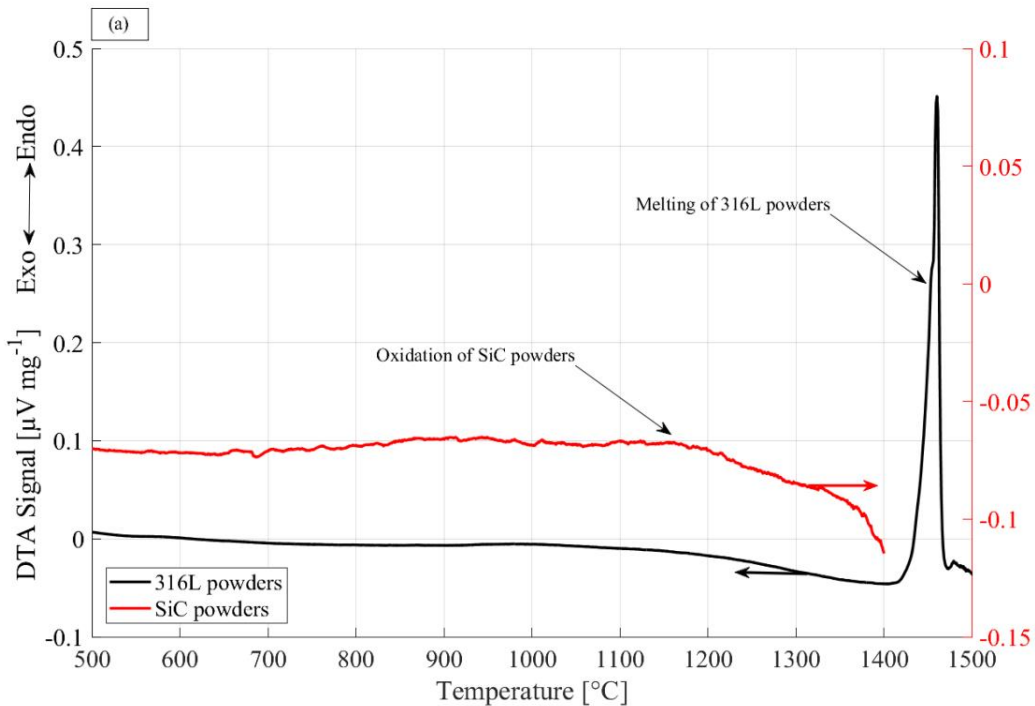


Fig. 8: XRD patterns of (a) original 316L, (b) milled SiC (1:3) and (c) milled 316L+20%SiC powders (1:5).

### 3.1.4. Thermal analysis – role of the carbo-thermal reduction

The DTA heating curves of the original powders and of the mixtures corresponding to the various milling time are illustrated in Fig. 9. The plots cover both the solid-state and remelting temperature ranges. Fig. 9a shows the heating curves of the two original powders. At 1450°C, the  $\gamma$ -austenite phase of the 316L powders reaches complete melting. SiC powders exhibit gradual oxidation from 1150°C as observed in [42,43]. Fig. 9b shows the heating curves of the various powder mixtures. The fusion peak appears wider than observed for the original 316L powders (Fig. 9a) and the fusion begins at 1120°C. The complete melting is then attained at 1250°C. The decrease of the melting temperature and the broadening of the peak can be explained by the progressive dissolution of SiC particles in the molten metal simultaneously with the melting of the 316L powder.



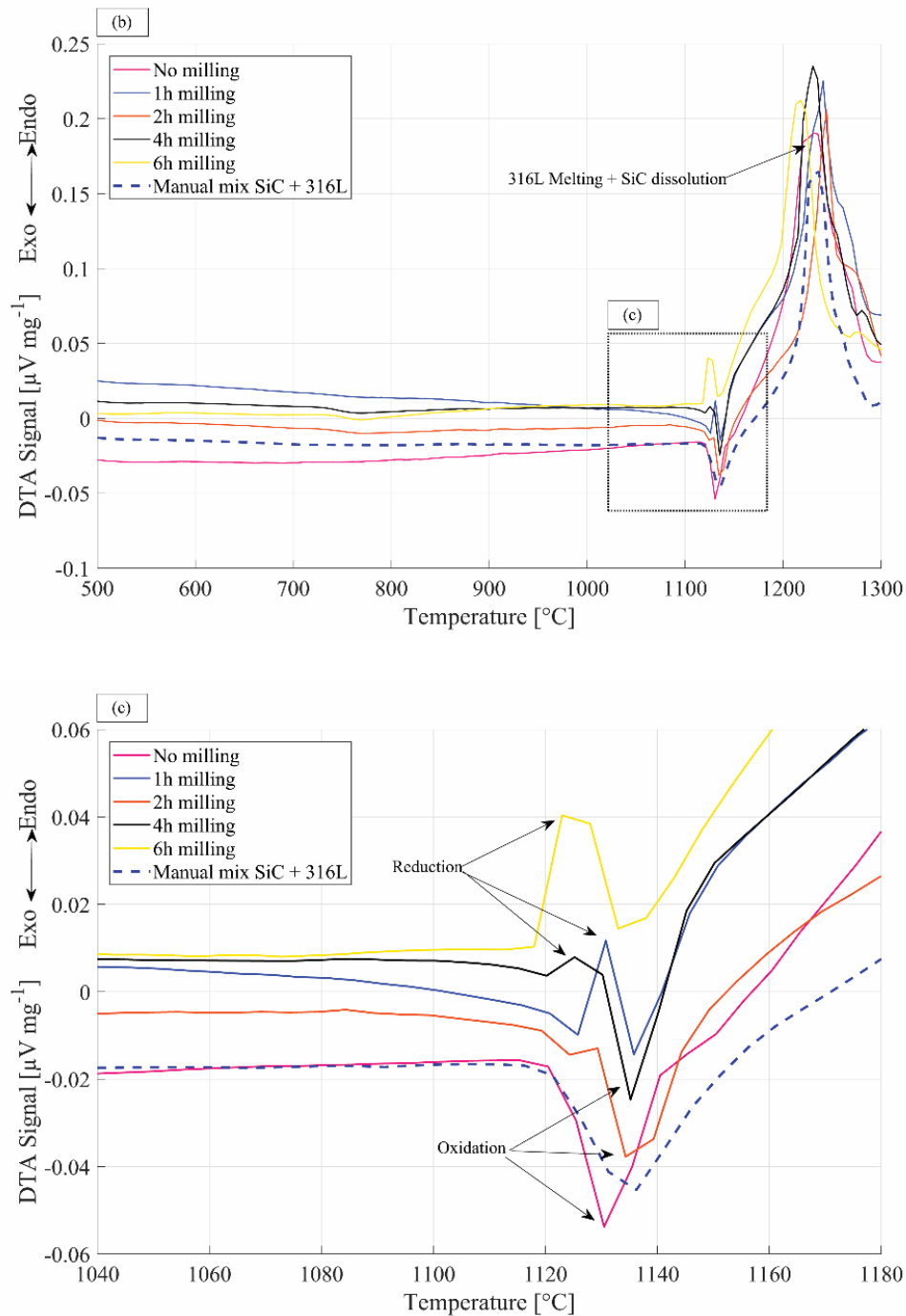


Fig. 9: DTA heating curves run at  $5^{\circ}\text{C min}^{-1}$  of the (a) original powders and (b) the powders mixtures with the five milling time. The original 316L powders and all the mixtures achieve the complete melting. (c) Zoom corresponding at the beginning of the 316L melting and the variation of the oxidation-reduction peak.

A peculiar evolution is observed among the various powders preparations, just prior to the onset of melting i.e. in the temperature range  $1120^{\circ}\text{C}$ - $1140^{\circ}\text{C}$  (Fig. 8c). In this temperature range, the manually mixed powders exhibit an exothermic peak associated with the catastrophic oxidation of the SiC in contact with the oxygen present within the feedstock. This reaction was reported in [42], where the onset of the melting was activating this strong exothermic reaction, speeding up the normal oxidation of the SiC powders (Fig. 9c). With increasing milling time,

the size of this exothermic peak decreases and another endothermic reaction occurs. This endothermic peak is associated with the carbo-thermal reaction between the chromium oxide in contact with the SiC or free C left from the Acheson process [31–33,43]. For a milling time of 6 hours, oxidation is not observed, leaving only the carbo-thermal reduction. For intermediate preparation times, both reactions are observed with some variations in intensity.

It is also worth noting that the ball milling applied on the SiC alone with three different BPR were not able to close efficiently the porosities of the SiC. When mixing manually these milled SiC powders with original 316L, the same oxidation peak was observed as the manual mix (Fig. 9b and c). Therefore, milling of the SiC alone was not considered further. In contrast, the milling procedure applied to the mixed 316L + SiC powders leads to the occurrence of the carbothermal reaction at the expense of the oxidation. As shown in section 3.1.1, the mechanical alloying of the two powders decreases the amount of porosity present in the SiC powders and thus the presence of oxygen in the feedstock, favouring the reduction reaction.

#### **3.1.5. Chosen preparation procedure**

Based on the SEM observations, on the evolution of the interaction between the two powders observed through DTA analyses and on the benefits of reduced preparation time, a milling time of 1 hour was chosen as the most suitable preparation time in order to produce the deposits. Indeed, milling for 1 hour results in fractured carbides (Fig. 5) and moderated plastic deformation, which was found favourable by decreasing the porosity and oxygen content, thus eliminating the oxidation peak during DTA test. Longer milling times are considered to be time-consuming without additional improvement and lead to an elevated fragmentation of the SiC. As mentioned in section 3.1.1, high quantities of small fragments may induce flowability issues during LC, leading ultimately to the formation of local heterogeneities within the deposit.

### 3.2. Materials characterization

#### 3.2.1. Macrostructure of the clad deposits

The cross-section of the S20 deposit fabricated from the mechanically alloyed powder mixture of 316L + 20 vol. % SiC is shown in Fig. 10b. In contrast to the deposit obtained from manually mixed 316L + SiC powders shown in Fig. 1, the S20 deposit fabricated using the mechanically alloyed powders exhibits a very small amount of porosities, whose presence can be ascribed to a few remaining porous SiC particles. It is also representative of the quality of the S10 deposit that does not exhibit porosities (Fig. 10a). Indeed, as discussed in section 3.1.4., the gradual replacement of the exothermic oxidation peak by the endothermic peak associated to a reduction reaction during the DTA test on the various powder mixtures (Fig. 9c) provides a sign of the decrease of the oxygen content in the mechanically alloyed feedstock thus allowing for the production of sound deposits.

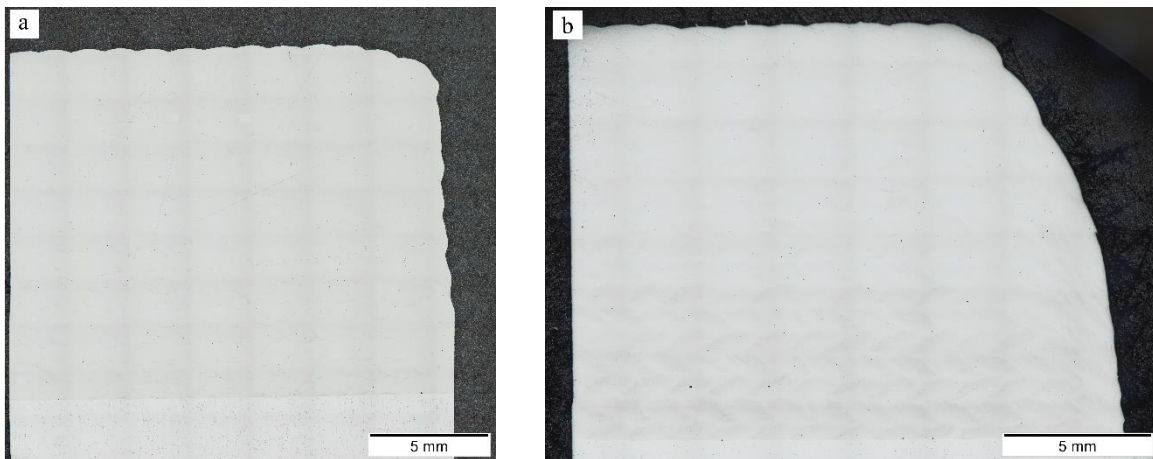


Fig. 10: Overview of the S10 and S20 deposits fabricated with mechanical alloying.

#### 3.2.2. Microstructure evolution as a function of SiC addition of the clad deposits

The microstructures of the three sound deposits (Fig. 3) are shown in Fig. 11. The microstructure of the 316L reference sample exhibits the well-known cellular morphology [45,46] with brighter cell boundaries (Fig. 11a). In both S10 and S20, the original SiC particles are nowhere to be seen (Fig. 11b and c). Unlike in [8,35,36], SiC reactants are completely dissolved in contact with the molten metal, thus forming two modified 316L stainless steels. The complete dissolution can be explained in view of the high affinity of Si with the Fe matrix and of the higher absorption of the 316L powders (Fig. 5b) after mechanical alloying [14]. Indeed, the adhesion of SiC fragments on the 316L powders increases the average absorption of the mixture since the absorption of carbides is higher [44].

The dissolution of the SiC and the subsequent enrichment of the modified alloys with Si and C have induced a change of the solidification route in comparison to the parent 316L [8,14]. As a result, the two modified S10 and S20 alloys exhibit two distinct cellular-dendritic reinforced microstructures. Small nodular Cr-carbides with an unusually high content of Si (Fig. 11b and Table 4) are observed at the cell boundaries of the S10. In the vicinities of the Cr-carbides and at the cell boundaries where carbides are not present, high content of Mo and Si is observed (Table 4), reminding the bright boundaries observed in the 316L microstructure (Fig. 11a) [45,46].

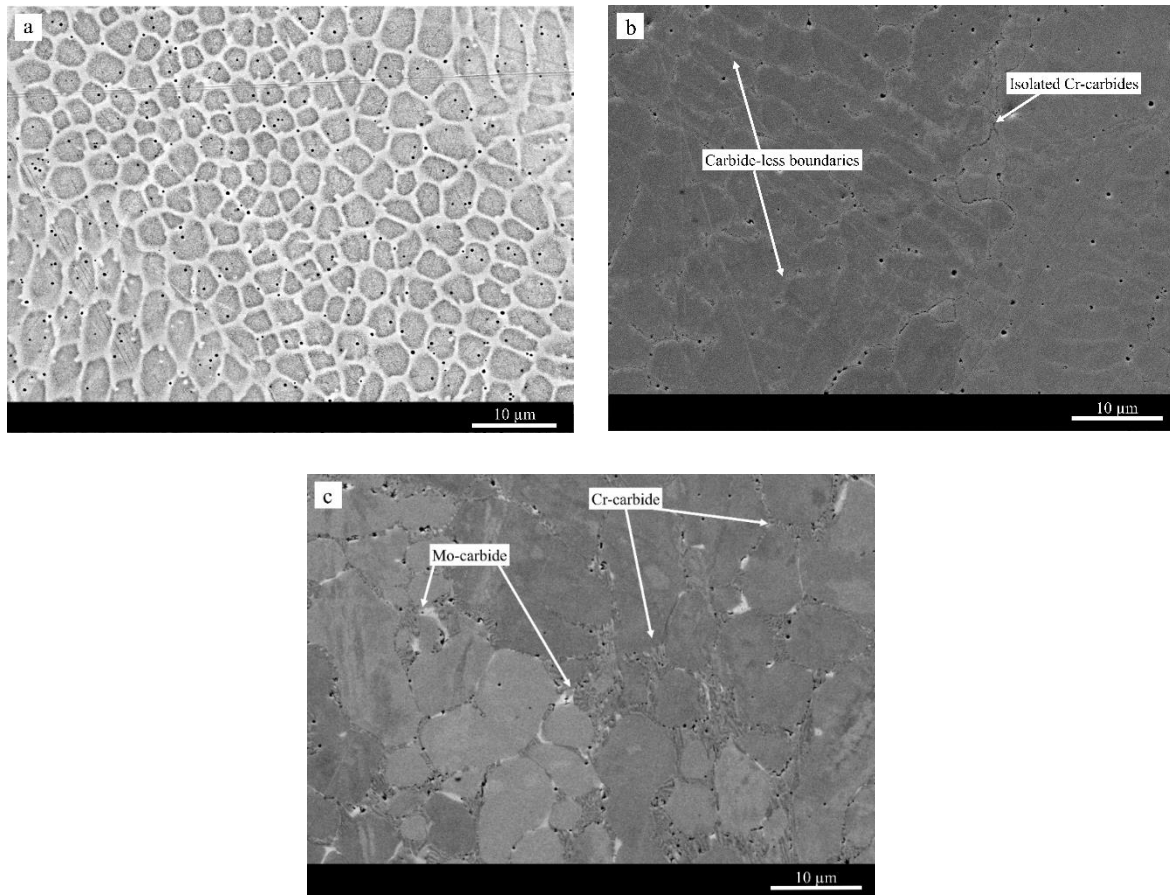


Fig. 11: Microstructure of (a) 316L (BSE mode), (b) S10 (SE mode) and (c) S20 (BSE mode), etched in aqua regia.

In contrast, the almost continuous carbide network of the S20 deposit is composed of grey nodular Cr-carbides and eutectic Mo-carbides (Table 4). The amount of Si in the matrix increases with the increasing SiC addition (Table 4). Interestingly, the Cr and Mo contents in the matrix follow an opposite trend. Indeed, when increasing the SiC addition, larger amounts of Cr and Mo are captured to form more carbides at the boundaries. Cr-carbides in S10 and S20 exhibit similar compositions (Table 4).

Table 4: Average chemical composition (atomic %) of the different phases observed in the 316L, S10 and S20 microstructure and relative standard deviations.

	Fe	Cr	Ni	Mo	Mn	Si	C
Cell composition (%at.)							
316L	60.00±2.55	15.96±1.57	10.71±1.6	1.16±0.43	1.14±0.45	1.13±0.44	9.90±3.27
S10	58.18±0.36	15.49±0.96	10.63±0.63	0.92±0.2	1.41±0.14	3.12±0.29	10.25±1.98
S20	56.6±3.34	13.96±2.01	10.35±0.73	0.86±0.37	2.31±0.75	5.72±0.55	10.2±1.89
<u>S10</u>							
Carbide-less							
boundaries	57,25±1.9	17,93±0.48	10,20±0.23	1,62±0.76	1,39±0.25	3,51±0.63	8,11±1.34
Cr-carbide	36,42±4.07	25,05±2.15	5,16±0.37	4,67±1.23	2,40±0.52	5,58±1.32	20,72±2.26
<u>S20</u>							
Cr-carbide	32,04±9.16	28,77±6.48	5,24±2.53	3,67±0.85	1,82±1.58	6,02±1.82	22,44±4.79
Mo-carbide	27,53±10.02	14,78±6.11	7,12±2.49	11,05±2.62	3,36±1.96	12,66±2.99	23,50±4.72

Fig. 12 shows the results of XRD analyses on the reference 316L and the S20. The matrix of both deposits is identified as  $\gamma$ -austenite. In good agreement with previous studies,  $M_7C_3$  carbide is identified [20,23,47] and associated with Cr-carbides observed in both the S20 and S10. Furthermore, in S20,  $M_{23}C_6$  carbides, seen as bright Mo-carbides in Fig. 12c, are also identified on the same two peaks as  $\gamma$  since both phases adopt the FCC crystal lattice [11,41,48,49]. By comparison with these XRD results, the small Cr-carbides present in the S10 deposits, with the same composition as the Cr-carbides of S20, are identified as  $M_7C_3$  carbides, and the matrix of S10 is also identified as austenite.

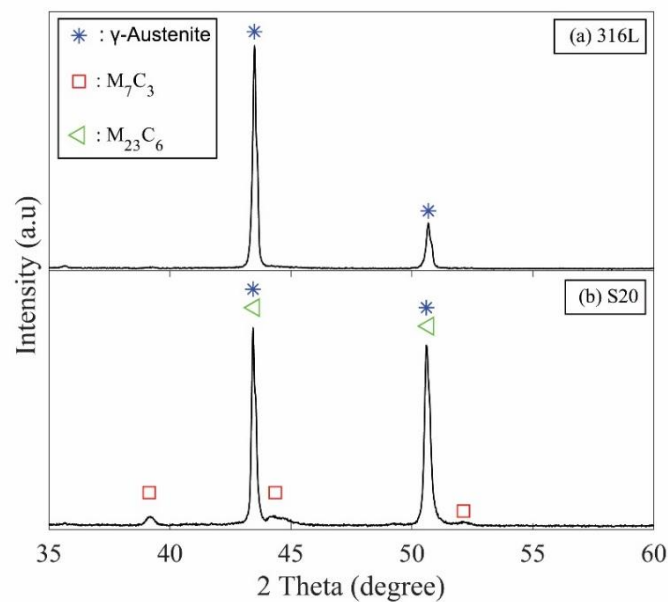


Fig. 12: XRD patterns of (a) 316L and (b) S20 deposits.

Thermodynamically, these results can be explained in reference to the ternary Fe-Cr-C system and quaternary Fe-Cr-C-Si system [37,50,51]. Indeed, it is well known that Si reduces the solubility of C in the  $\gamma$ -austenite matrix [29,50]. The dissolution of the SiC in the molten metal and thus the addition of C and Si modify the solidification route of the 316L in comparison to its typical structure where cells and cell boundaries are both  $\gamma$ -austenite (Fig. 12). More precisely, the solidification routes of the three deposits depend on the composition of the liquid as solidification proceeds. These solidification routes can be assumed from the reverse consideration of the remelting DTA curves (Fig. 13a) and from microscopy observations following the procedure proposed in [8,37].

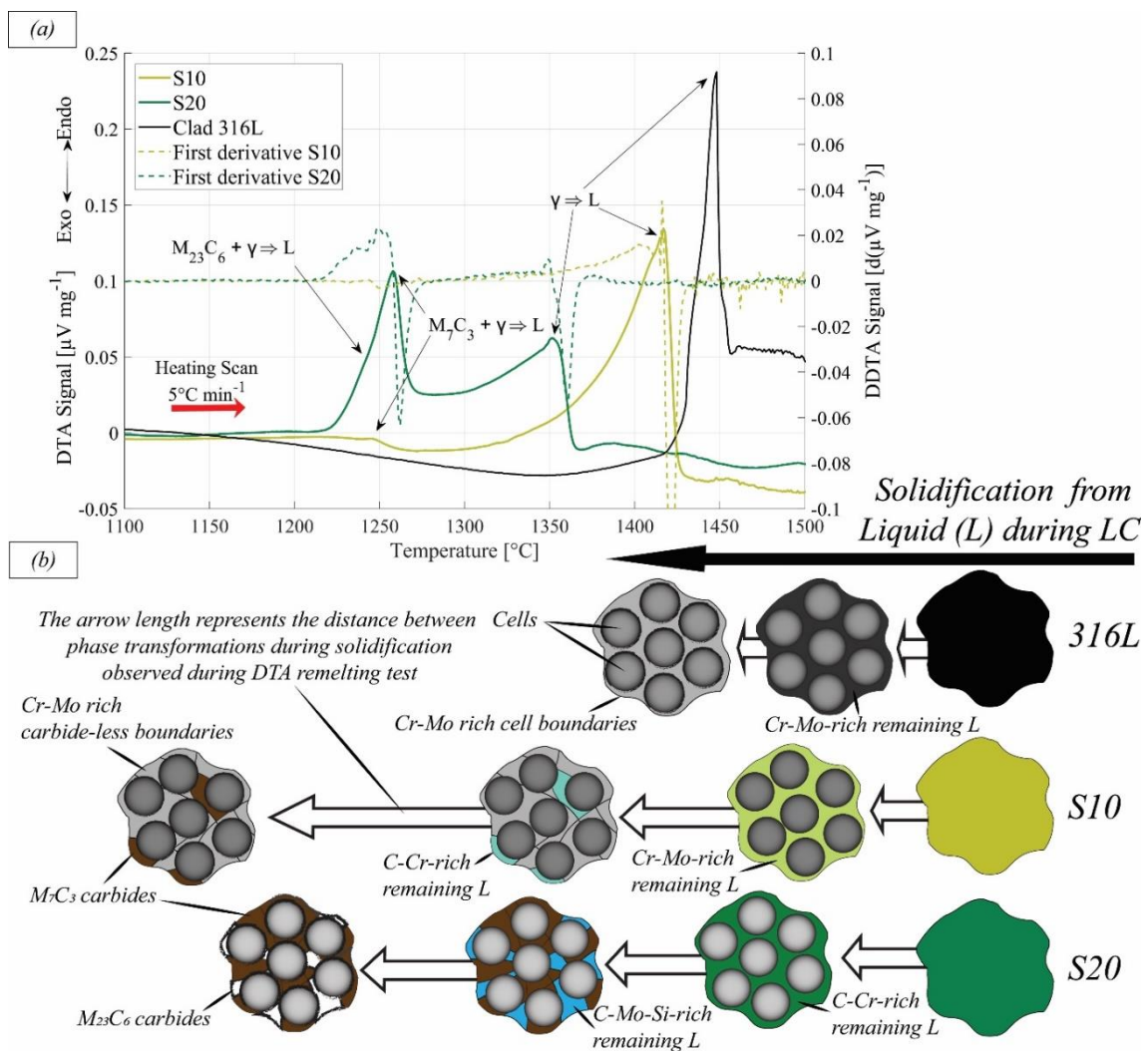


Fig. 13: (a) DTA heating curves run at  $5^{\circ}\text{C min}^{-1}$  up to complete remelting for the three deposits. This zoom corresponds to the DTA remelting temperature range where the first derivative curve helps to identify the different reaction peaks of the S10 and S20. (b) Scheme of the solidification routes of 316L, S10 and S20 during LC from the respective molten metal, based on the reverse consideration of the DTA remelting curves. The different colours represent the composition differences observed in Table 4.

---

The DTA curve for the pure 316L exhibits a single peak (Fig. 13a), which corresponds to a short solidification range, i.e. the formation of the austenitic cells and the cell boundaries (Fig. 11a). Mild segregations of Cr and Mo in the remaining liquid at the intercellular spaces lead to the formation of the bright austenitic boundaries (Fig. 13b).

The dissolution of the SiC in the molten pool of the S10 and S20 alloys during fabrication leads to a high degree of C super-saturation and this excess of C provides high driving forces for the formation of carbides [51]. In the S10 alloy, the amount of C in the liquid after the dissolution of the added 10% vol. of SiC is not enough to drive Cr towards the grain boundaries (Table 4). Indeed, the amount of Cr-carbides remains small and the matrix of the S10 and the pure 316L alloys exhibit only a small difference in Cr content. In this case, when the C content is still low and the Cr content in the matrix remains high, the Si is driven to the cell boundaries. The resulting large variation of the local composition of the  $\gamma$ -austenite (Table 4) corresponds to the large solidification range of S10 (Fig. 13b). Indeed, the first derivative of the S10 remelting curve reveals two individual peaks, corresponding to  $\gamma$ -austenite with different compositions. After solidification of the  $\gamma$ -austenite, a small quantity of  $M_7C_3$  carbides precipitates in the intercellular spaces from the remaining liquid that is enriched with C and Cr. This precipitation corresponds to a small peak at approximately 1250°C in the DTA remelting curve (Fig. 13a).

On the other hand, in the S20 alloy, the higher amount of Si in the matrix drives C towards the remaining liquid [29,50]. Moreover, the outward flows of C tend to drive carbide forming elements (e.g. Cr and Mo) also in the remaining liquid [51]. Therefore, after the formation of the  $\gamma$ -austenite that is enriched with Si compared to the matrix of the 316L and S10 alloys (Table 4), the high content of Cr leads to the formation of a large quantity of  $M_7C_3$  carbides (Fig. 13). Indeed, a high peak is observed in the DTA remelting curve of alloy S20 (Fig. 13a) in the same temperature range as for the precipitation of the Cr-rich  $M_7C_3$  carbides in the S10 alloy. After the formation of these Cr-carbide at the intercellular spaces, the remaining liquid is enriched with Si and Mo (Table 4) and, from this liquid, few Mo-rich  $M_{23}C_6$  carbides precipitate at the remaining cell boundaries (Fig. 13b). The first derivative reveals the presence of the corresponding peak, which is overlapped with the  $M_7C_3$  peak. As observed in [37,50], the low Si content in the Cr-carbides and the high amount of Si in the few Mo-rich carbides correspond to the higher supersaturation of Si in the matrix of alloy S20.

### 3.2.3. Nano-indentation and solid solution strengthening of the matrix

The consequences of the variation in composition of the matrix of the three alloys (Table 4) on its nanohardness are shown in Fig. 14. Nanoscans of the 316L (Fig. 14a) and S10 (Fig. 14b) microstructures highlight the austenitic cell and dendrite boundaries. In contrast, as observed in Fig. 11c, the cell boundaries of the S20 are composed mainly of solidification carbides (Fig. 14c).

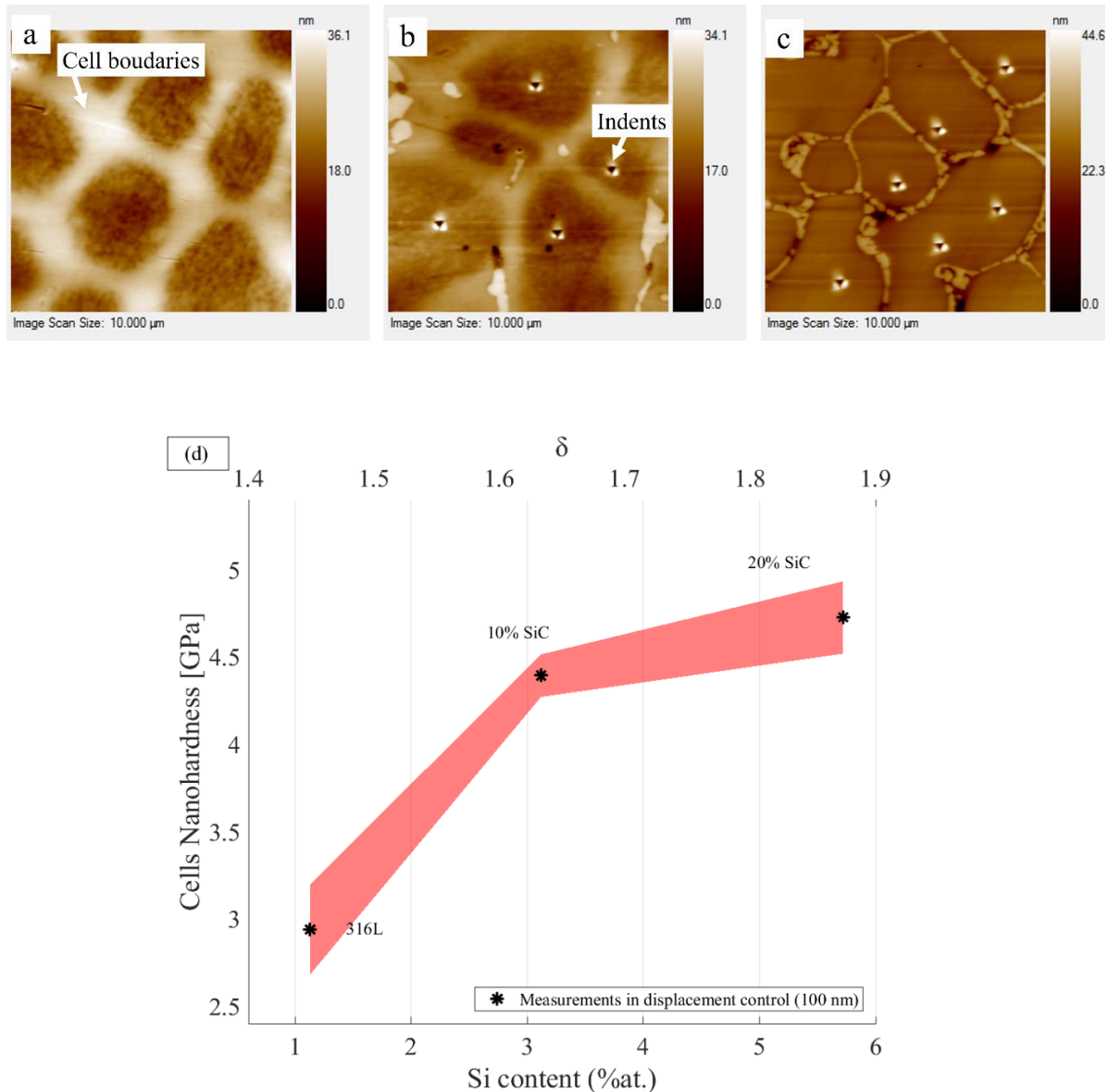


Fig. 14: Nanoscans of (a) 316L, (b) S10 and (c) S20 microstructure, etched with aqua regia. (d) Atom size difference parameter  $\delta$  vs. nanohardness value of the austenitic cells (FCC crystal order) as a function of Si enrichment of the matrix (Table 4).

Nanoindentation measurements on the matrix (Fig. 14d) show a remarkable increase of the nanohardness of the austenitic cells with the increase of the Si content (Table 4). The effect of Si additions in the BCC lattice of Fe-alloys is well known, leading to a lattice contraction and

to a remarkable increase of the macrohardness as observed both in equilibrium conditions and for supersaturated solutions [24–26,30]. On the other hand, fewer data are available regarding the addition of Si in FCC lattice, and these data are limited to equilibrium conditions. In FCC lattice, Si is known to lead to an expansion of the lattice and, its small size compared to the main element (Fe) also leads to an increase of the general atomic-size difference as illustrated by the evolution of the parameter (Fig.14d) [26,28]. In view of these elements, the nanohardness increase of the S10 alloy can be attributed to a remarkable increase of the lattice distortion and thus of the solid solution strengthening effect of Si in a supersaturated solution in the FCC lattice. Indeed, Si atom leads to higher lattice strains of the FCC crystal lattice than Cr, Ni and Mn [26]. Furthermore, the fast cooling rates of LC reduce the segregation, often leading to out-of-equilibrium and supersaturated microstructures [14,37]. Therefore, the solid solution strengthening effect is enhanced in comparison to the predictions under equilibrium conditions [27,30]. The nanohardness of the S10  $\gamma$ -austenite increases by 0.75 GPa for every 1 at. % of Si added to the matrix composition and this corresponds to an improvement of the nanohardness by 30% compared to the pure 316L.

An increase of the solid solution strengthening can also be held responsible for the further increase of the nanohardness values up to 5 GPa in the S20 alloy (Fig. 14d). However, in this case, the increase of the Si content must compensate for the loss of Cr and Mo to carbide precipitation. Indeed, the decrease of the Cr and Mo contents leads to a decrease of 1.75 GPa for each at. % lost. Since the addition of Si corresponds to an increase of nano-hardness of +0.75 GPa for every 1 at. % of Si, the total change of composition corresponds to an overall improvement of the nanohardness by 5% compared to the alloy S10.

#### **3.2.4. Influence of the carbide amount on the macrohardness**

Results of macro-hardness measurements on the deposits are shown in Fig. 15. The hardness line at the bottom is related to the 316L substrate. The average hardness of the pure 316L deposit is 197 HV, slightly lower than that of the substrate at 204 HV. The average hardness of the S10 and S20 alloys is respectively 258 HV and 348 HV, which shows the influence of the dissolution of SiC on the hardness. The hardness of the three deposits constantly decreases with increasing distance from the 316L substrate due to the coarsening of the microstructure induced by heat accumulation as deposition proceeds [2,52].

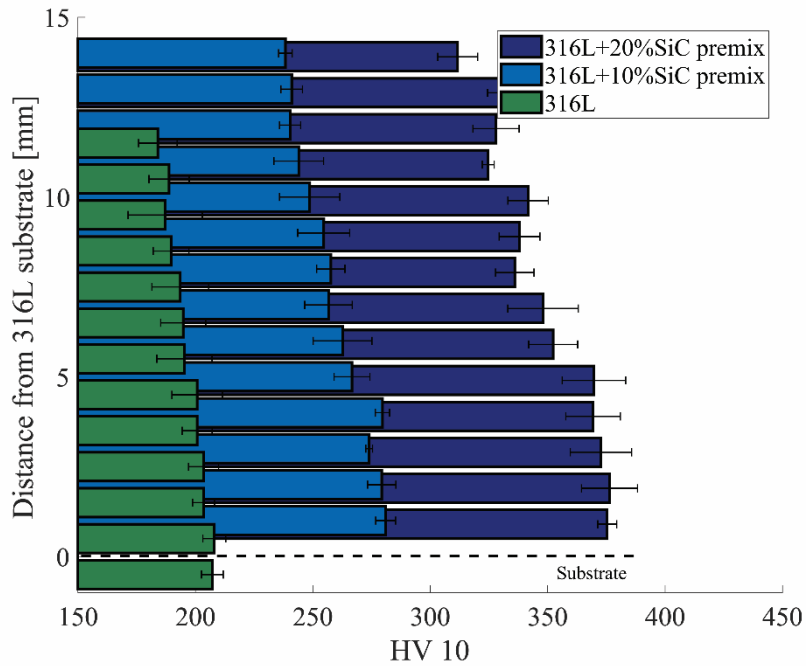


Fig. 15: Macro-hardness evolution of 316L, S10 and S20 fabricated with the same parameters, with the relative standard deviation for each measurement row.

The hardness increase in both S10 and S20 alloys can be ascribed to the combined effects of the Si solid solution strengthening effect of the matrix (Fig. 14d) (see section 3.2.3) and of the presence of solidification carbides in the intercellular spaces. In alloy S10, because of the very small amount of Cr-carbides (Fig. 11b and Fig. 14a), the solid solution strengthening effect of Si is the main strengthening mechanism and the remarkable increase of macrohardness (Fig. 15) directly corresponds to the nanohardness increase (Fig. 15). On the other hand, as mentioned in section 3.2.3, the nanohardness of alloy S20 exhibits only an improvement of 5% compared to the S10 alloy [52]. Therefore, to justify the remarkable macrohardness improvement of alloy S20 compared to alloy S10, precipitation strengthening by the quasi-continuous carbide network (Fig. 11c and Fig. 14c) is considered as the main strengthening mechanism whereas the solid solution strengthening due to the higher amount of Si in the  $\gamma$ -austenite plays only a secondary role (Table 4).

### 3.2.5. On the role of lattice distortion and the potential of modified high-silicon austenitic stainless steels

Recently, the solid solution strengthening mechanisms discussed in section 3.2.3 have been reported and exploited both in high-entropy steels (HESs) under equilibrium conditions [28,29] and in high-entropy alloys (HEAs) under out-of-equilibrium conditions [30,53,54]. In these alloys, the presence of atoms of different sizes distorts the crystal lattice, leading to a very

---

efficient reinforcement by solid solution strengthening [55]. Moreover, in HEAs fabricated by AM, the extremely high cooling rates favour even more the formation of metastable highly distorted lattices, with five or more elements in substitutional positions. The obtainment of a FCC instable matrix is of particular interest since it opens the prospect for deformation-induced-confined phase transformations such as martensite induced by deformation or twinning [28].

The empirical atomic size difference parameter  $\delta$  is generally accepted in order to describe the comprehensive effect of the atomic-size difference in multi-component alloys [41,53,55,56]. This value is equal to 0 for pure metals and, as proposed in [53,57], it was used in this work as an indication of the lattice modification considering the EDS analyses of the three alloys in Table 4 and the atomic radii from [58]. The obtained  $\delta$  values are plotted in Fig. 14d vs. the Si content and the respective nanohardness values. The results are in good agreement with previous works [53,55]. Pure 316L exhibits a  $\delta$  value of 1.45 due to its Mo content which leads to high local lattice strains [26]. As mentioned in section 3.2.3, with the increase of the Si content and decrease of Cr and Mo content (Table 4), the distortion of the lattice increase in alloy S10 and S20 (Fig. 14d) and the observed increase of the  $\delta$  values fits well with the improvement of the nanohardness.

In high entropy alloys, V, Ti, W and Mo atoms are often used as they are expected to lead to a high expansion of the FCC crystal order and thus to an improvement of the mechanical properties via solid solution strengthening [26]. Nevertheless, the tendency of these elements to form carbides and other fragile phases in Fe-based alloys, together with their low solubility in the FCC lattice [8,14] limit their use in alloys for AM [7]. Therefore, the addition of Si is very promising to improve the mechanical properties of alloys with FCC crystal order designed for AM (Fig. 14), while avoiding brittleness issues thanks to the suppression of phase ordering under extremely high cooling rates [27]. Furthermore, Si may promote the formation of improved oxide surface layers, providing protection against corrosive attack [21,28].

#### 4. Conclusions

- Mechanical alloying can be used as a method for powder preparation for using porous SiC powders (or other porous powders containing oxygen). DTA analyses allow to detect efficiently the carbo-thermal reduction or oxidation reactions and thus to estimate the remaining oxygen amount in the powders as a function of the milling time. However, milling on the original SiC powders alone (without the 316L powders) is not capable to eliminate the porosities
- SiC demonstrates a high affinity with the Fe-alloys and the complete dissolution of the powders is achieved systematically during the deposition for both modified alloys containing 10 or 20 vol. %. These results reveal that the nature of the reinforcement and their chemical affinity with the host powders are the predominant factors to maintain the original reinforcements, more than the powder size and powder morphology.
- SiC dissolution during deposition leads to an enrichment of the 316L composition and thus to the modification of its solidification route. The two modified stainless steels S10 and S20 exhibit a reinforced austenitic microstructure. With the increase of the SiC addition, the amount of carbides at the cell boundaries increases due to C enrichment in the liquid. Moreover, Si addition in the liquid composition leads to significant solid solution strengthening of the matrix after solidification. Nanohardness of the austenitic cells increases from 3 GPa for the 316L to a maximum of 5 GPa of the S20 alloy.
- The combined effect of the presence of carbides and the Si solid solution strengthening leads to an increase of the average macrohardness from a value of 197 HV in the pure 316L by 61 HV and 151 HV in the new S10 and S20 stainless steels respectively. Si addition thus appears particularly promising to improve the mechanical properties for AM austenitic stainless steels.

#### Acknowledgements

This work has been supported by the IAWATHA project. The authors acknowledge the CAREM of the ULiège for providing SEM/EDS/EBSD facilities. They also wish to thank Sylvie Salieri for the sample preparation, Samuel Rondia for the substrates preparation, Vincent Delaval for the powder characterization and Sirris Research Centre for the access to the DED machine.

---

---

## References

- [1] T. DebRoy, H.L. Wei, J.S. Zuback, T. Mukherjee, J.W. Elmer, J.O. Milewski, A.M. Beese, A. Wilsonheid, A. De, W. Zhang, Additive manufacturing of metallic components – Process, structure and properties, *Prog. Mater. Sci.* 92 (2018) 112–224. doi:10.1016/j.pmatsci.2017.10.001.
- [2] D. Herzog, V. Seyda, E. Wycisk, C. Emmelmann, Additive manufacturing of metals, *Acta Mater.* 117 (2016) 371–392. doi:10.1016/j.actamat.2016.07.019.
- [3] A. Dass, A. Moridi, State of the art in directed energy deposition: From additive manufacturing to materials design, *Coatings*. 9 (2019) 1–26. doi:10.3390/COATINGS9070418.
- [4] W.J. Sames, F.A. List, S. Pannala, R.R. Dehoff, S.S. Babu, The metallurgy and processing science of metal additive manufacturing, *Int. Mater. Rev.* 61 (2016) 315–360. doi:10.1080/09506608.2015.1116649.
- [5] I. Todd, Metallurgy: Printing steels, *Nat. Mater.* 17 (2017) 13–14. doi:10.1038/nmat5042.
- [6] Q. Jia, P. Rometsch, P. Kürnsteiner, Q. Chao, A. Huang, M. Weyland, L. Bourgeois, X. Wu, Selective laser melting of a high strength AlMnSc alloy: Alloy design and strengthening mechanisms, *Acta Mater.* 171 (2019) 108–118. doi:10.1016/j.actamat.2019.04.014.
- [7] Y.T. Tang, C. Panwisawas, J.N. Ghossoub, Y. Gong, J. Clark, A. Németh, D.G. McCartney, R.C. Reed, Alloys-By-Design: Application to New Superalloys for Additive Manufacturing, *Acta Mater.* 202 (2020) 417–436. doi:10.1016/j.actamat.2020.09.023.
- [8] T. Maurizi Enrici, O. Dedry, F. Boschini, J.T. Tchuindjang, A. Mertens, Microstructural and Thermal Characterization of 316L+WC Composite Coatings obtained by Laser Cladding, *Adv. Eng. Mater.* 13 (2020) 1–12. doi:10.1002/adem.202000291.
- [9] E. Alabort, D. Barba, M.R. Shagiev, M.A. Murzinova, R.M. Galeev, O.R. Valiakhmetov, A.F. Aletdinov, R.C. Reed, Alloys-by-design: Application to titanium alloys for optimal superplasticity, *Acta Mater.* 178 (2019) 275–287. doi:10.1016/j.actamat.2019.07.026.
- [10] Y.L. Zhang, J. Li, Y.Y. Zhang, D.N. Kang, Evolution in microstructure and high-temperature oxidation behaviors of the laser-cladding coatings with the Si addition contents, *J. Alloys Compd.* 827 (2020). doi:10.1016/j.jallcom.2020.154131.
- [11] J. Wang, L. Li, W. Tao, Crack initiation and propagation behavior of WC particles reinforced Fe-based metal matrix composite produced by laser melting deposition, *Opt. Laser Technol.* 82 (2016) 170–182. doi:10.1016/j.optlastec.2016.03.008.
- [12] G. Lian, C. Zhao, Y. Zhang, M. Feng, J. Jiang, Investigation into micro-hardness and wear resistance of 316L/SiC composite coating in laser cladding, *Appl. Sci.* 10 (2020). doi:10.3390/app10093167.
- [13] D. Deschuyteneer, F. Petit, M. Gonon, F. Cambier, Processing and characterization of laser clad NiCrBSi/WC composite coatings - Influence of microstructure on hardness and wear, *Surf. Coatings Technol.* 283 (2015) 162–171. doi:10.1016/j.surfcoat.2015.10.055.
- [14] O. Ertugrul, T. Maurizi Enrici, H. Paydas, E. Saggionetto, F. Boschini, A. Mertens, Laser cladding of TiC reinforced 316L stainless steel composites: Feedstock powder preparation and microstructural evaluation, *Powder Technol.* 375 (2020) 384–396. doi:10.1016/j.powtec.2020.07.100.
- [15] N. Li, S. Huang, G. Zhang, R. Qin, W. Liu, H. Xiong, G. Shi, J. Blackburn, Progress in additive manufacturing on new materials: A review, *J. Mater. Sci. Technol.* 35 (2019) 242–269. doi:10.1016/j.jmst.2018.09.002.
- [16] N.T. Aboulkhair, M. Simonelli, L. Parry, I. Ashcroft, C. Tuck, R. Hague, 3D printing of Aluminium alloys: Additive Manufacturing of Aluminium alloys using selective laser melting, *Prog. Mater. Sci.* 106 (2019) 100578. doi:10.1016/j.pmatsci.2019.100578.

- [17] M. Lang, From aerospace engineering to AM: Melanie Lang on FormAlloy and the future of Directed Energy Deposition (DED), *Met. Addit. Manuf.* 6 (2020) 145–152.
- [18] J. Dutta Majumdar, A. Kumar, L. Li, Direct laser cladding of SiC dispersed AISI 316L stainless steel, *Tribol. Int.* 42 (2009) 750–753. doi:10.1016/j.triboint.2008.10.016.
- [19] M.W. Yip, S. Barnes, A.A.D.M. Sarhan, Deposition of a silicon carbide reinforced metal matrix composite (P25) layer using CO<sub>2</sub> laser, *J. Manuf. Sci. Eng. Trans. ASME.* 137 (2015) 1–8. doi:10.1115/1.4029831.
- [20] Z. Brytan, L. a Dobrzański, W. Pakieła, Laser surface alloying of sintered stainless steels with SiC powder, *J. Achiev. Mater. Manuf. Eng.* 47 (2011) 42–56.
- [21] C.L. Wu, S. Zhang, C.H. Zhang, J.B. Zhang, Y. Liu, J. Chen, Effects of SiC content on phase evolution and corrosion behavior of SiC-reinforced 316L stainless steel matrix composites by laser melting deposition, *Opt. Laser Technol.* 115 (2019) 134–139. doi:10.1016/j.optlastec.2019.02.029.
- [22] C.A. Stickels, *Steel and its Heat Treatment*, Second Edition, *J. Heat Treat.* 3 (1984) 356–356. doi:10.1007/bf02833130.
- [23] S. Buytoz, Microstructural properties of SiC based hardfacing on low alloy steel, *Surf. Coatings Technol.* 200 (2006) 3734–3742. doi:10.1016/j.surfcoat.2005.01.106.
- [24] F. Huyan, R. Larker, P. Rubin, P. Hedström, Effect of solute silicon on the lattice parameter of ferrite in ductile irons, *ISIJ Int.* 54 (2014) 248–250. doi:10.2355/isijinternational.54.248.
- [25] Y. You, M.F. Yan, Behaviors and interactions of Ia atom with other foreign substitutional atoms (Al, Si, Ti, V, Cr, Mn, Co, Ni, Cu, Nb or Mo) in iron based solid solution from first principles, *Comput. Mater. Sci.* 73 (2013) 120–127. doi:10.1016/j.commatsci.2013.02.028.
- [26] M. Morinaga, *Local Lattice Strains Around Alloying Elements in Metals*, 2019. doi:10.1016/b978-0-12-814706-1.00011-x.
- [27] M. Garibaldi, I. Ashcroft, M. Simonelli, R. Hague, Metallurgy of high-silicon steel parts produced using Selective Laser Melting, *Acta Mater.* 110 (2016) 207–216. doi:10.1016/j.actamat.2016.03.037.
- [28] D. Raabe, C.C. Tasan, H. Springer, M. Bausch, From high-entropy alloys to high-entropy steels, *Steel Res. Int.* 86 (2015) 1127–1138. doi:10.1002/srin.201500133.
- [29] Z. Wang, W. Lu, H. Zhao, J. He, K. Wang, B. Zhou, D. Ponge, D. Raabe, Z. Li, Formation mechanism of  $\kappa$ -carbides and deformation behavior in Si-alloyed FeMnAlC lightweight steels, *Acta Mater.* 198 (2020) 258–270. doi:10.1016/j.actamat.2020.08.003.
- [30] C.C. Yang, J.L. Hang Chau, C.J. Weng, C.S. Chen, Y.H. Chou, Preparation of high-entropy AlCoCrCuFeNiSi alloy powders by gas atomization process, *Mater. Chem. Phys.* 202 (2017) 151–158. doi:10.1016/j.matchemphys.2017.09.014.
- [31] I. Polozov, N. Razumov, D. Masaylo, A. Silin, Y. Lebedeva, A. Popovich, Fabrication of silicon carbide fiber-reinforced silicon carbide matrix composites using binder jetting additive manufacturing from irregularly-shaped and spherical powders, *Materials (Basel)*. 13 (2020). doi:10.3390/MA13071766.
- [32] A.B.D. Nandiyanto, T. Ogi, W.N. Wang, L. Gradon, K. Okuyama, Template-assisted spray-drying method for the fabrication of porous particles with tunable structures, *Adv. Powder Technol.* 30 (2019) 2908–2924. doi:10.1016/j.apt.2019.08.037.
- [33] A.W. Weimer, *Carbide, nitride and boride materials synthesis and processing*, Springer Science & Business Media, Berlin, 2012.
- [34] A.I. Mertens, J. Lecomte-Beckers, On the Role of Interfacial Reactions , Dissolution and Secondary Precipitation During the Laser Additive Manufacturing of Metal Matrix Composites : A Review, in: I. V Shishkovsky (Ed.), *New Trends 3D Print., I.V., InTech, Rijeka, Croatia*, 2016: pp. 187–213. doi:10.5772/63045.

- [35] D. Deschuyteneer, F. Petit, M. Gonon, F. Cambier, Influence of large particle size – up to 1.2 mm – and morphology on wear resistance in NiCrBSi/WC laser cladded composite coatings, *Surf. Coatings Technol.* 311 (2017) 365–373. doi:10.1016/j.surfcoat.2016.12.110.
- [36] M. Sheikhzadeh, S. Sanjabi, Structural characterization of stainless steel/TiC nanocomposites produced by high-energy ball-milling method at different milling times, *Mater. Des.* 39 (2012) 366–372. doi:10.1016/j.matdes.2012.02.011.
- [37] T. Maurizi Enrici, A. Mertens, M. Sinnaeve, J.T. Tchuindjang, Elucidation of the solidification sequence of a complex graphitic HSS alloy under a combined approach of DTA and EBSD analyses, *J. Therm. Anal. Calorim.* (2019) 1–15. doi:10.1007/s10973-019-09093-9.
- [38] H. Paydas, A. Mertens, R. Carrus, J. Lecomte-Beckers, J.T. Tchuindjang, Laser cladding as repair technology for Ti-6Al-4V alloy: Influence of building strategy on microstructure and hardness, *Mater. Des.* 85 (2015) 497–510. doi:10.1016/j.matdes.2015.07.035.
- [39] S. Sartori, L. Pezzato, M. Dabalà, T. Maurizi Enrici, A. Mertens, A. Ghiotti, S. Bruschi, Surface Integrity Analysis of Ti6Al4V After Semi-finishing Turning Under Different Low-Temperature Cooling Strategies, *J. Mater. Eng. Perform.* 27 (2018) 4810–4818. doi:10.1007/s11665-018-3598-x.
- [40] D. Zhu, M. Gao, H. Pan, Y. Pan, Y. Liu, S. Li, H. Ge, N. Fang, Fabrication and Mechanical Properties of SiCw(p)/SiC-Si Composites by Liquid Si Infiltration using Pyrolysed Rice Husks and SiC Powders as Precursors, *BioResources.* 9 (2014). doi:10.15376/biores.9.2.2572-2583.
- [41] H. Jain, Y. Shadangi, V. Shivam, D. Chakravarty, N.K. Mukhopadhyay, D. Kumar, Phase evolution and mechanical properties of non-equiatomic Fe–Mn–Ni–Cr–Al–Si–C high entropy steel, *J. Alloys Compd.* 834 (2020) 155013. doi:10.1016/j.jallcom.2020.155013.
- [42] D. O’Sullivan, M.J. Pomeroy, S. Hampshire, M.J. Murtagh, Degradation resistance of silicon carbide diesel particulate filters to diesel fuel ash deposits, *J. Mater. Res.* 19 (2004) 2913–2921. doi:10.1557/JMR.2004.0373.
- [43] Y. Hijikata, S. Yagi, H. Yaguchi, Y. Sadafumi, Thermal Oxidation Mechanism of Silicon Carbide, in: Y. Hijikata (Ed.), *Phys. Technol. Silicon Carbide Devices*, InTech, 2013: p. 181. doi:http://dx.doi.org/10.5772/50748.
- [44] N.K. Tolochko, T. Laoui, Y. V. Khlopkov, S.E. Mozzharov, V.I. Titov, M.B. Ignatiev, Absorptance of powder materials suitable for laser sintering, *Rapid Prototyp. J.* 6 (2000) 155–160. doi:10.1109/CCNC.2017.7983268.
- [45] Y.M. Wang, T. Voisin, J.T. McKeown, J. Ye, N.P. Calta, Z. Li, Z. Zeng, Y. Zhang, W. Chen, T.T. Roehling, R.T. Ott, M.K. Santala, P.J. Depond, M.J. Matthews, A. V. Hamza, T. Zhu, Additively manufactured hierarchical stainless steels with high strength and ductility, *Nat. Mater.* 17 (2018) 63–70. doi:10.1038/NMAT5021.
- [46] L. Liu, Q. Ding, Y. Zhong, J. Zou, J. Wu, Y.L. Chiu, J. Li, Z. Zhang, Q. Yu, Z. Shen, Dislocation network in additive manufactured steel breaks strength–ductility trade-off, *Mater. Today.* 21 (2018) 354–361. doi:10.1016/j.mattod.2017.11.004.
- [47] S. Buytoz, Microstructural properties of  $M_7C_3$  eutectic carbides in a Fe – Cr – C alloy, *60* (2006) 605–608. doi:10.1016/j.matlet.2005.09.046.
- [48] K. Wiecezrak, P. Bala, M. Stepień, G. Cios, T. Koziel, Formation of eutectic carbides in Fe-Cr-Mo-alloy during non-equilibrium crystallization, *Mater. Des.* 94 (2016) 61–68. doi:10.1016/j.matdes.2016.01.028.
- [49] K. Wiecezrak, P. Bala, R. Dziurka, T. Tokarski, G. Cios, T. Koziel, L. Gondek, The effect of temperature on the evolution of eutectic carbides and  $M_7C_3 \rightarrow M_{23}C_6$  carbides reaction in the rapidly solidified Fe-Cr-C alloy, *J. Alloys Compd.* 698 (2017) 673–684. doi:10.1016/j.jallcom.2016.12.252.
- [50] G. Laird, G.L.F. Powell, Solidification and solid-state transformation mechanisms in Si alloyed high-chromium white cast irons, *Metall. Trans. A.* 24 (1993) 981–988. doi:10.1007/BF02656520.

- [51] C. Qiu, H.S. Zurob, C.R. Hutchinson, The coupled solute drag effect during ferrite growth in Fe-C-Mn-Si alloys using controlled decarburization, *Acta Mater.* 100 (2015) 333–343. doi:10.1016/j.actamat.2015.08.065.
- [52] J.S. Zuback, T. DebRoy, The hardness of additively manufactured alloys, *Materials (Basel)*. 11 (2018). doi:10.3390/ma11112070.
- [53] C.C. Yen, G.R. Huang, Y.C. Tan, H.W. Yeh, D.J. Luo, K.T. Hsieh, E.W. Huang, J.W. Yeh, S.J. Lin, C.C. Wang, C.L. Kuo, S.Y. Chang, Y.C. Lo, Lattice distortion effect on elastic anisotropy of high entropy alloys, *J. Alloys Compd.* 818 (2020) 152876. doi:10.1016/j.jallcom.2019.152876.
- [54] Z. Li, S. Zhao, R.O. Ritchie, M.A. Meyers, Mechanical properties of high-entropy alloys with emphasis on face-centered cubic alloys, *Prog. Mater. Sci.* 102 (2019) 296–345. doi:10.1016/j.pmatsci.2018.12.003.
- [55] Y.F. Ye, Y.H. Zhang, Q.F. He, Y. Zhuang, S. Wang, S.Q. Shi, A. Hu, J. Fan, Y. Yang, Atomic-scale distorted lattice in chemically disordered equimolar complex alloys, *Acta Mater.* 150 (2018) 182–194. doi:10.1016/j.actamat.2018.03.008.
- [56] Q. He, Y. Yang, On lattice distortion in high entropy alloys, *Front. Mater.* 5 (2018) 1–8. doi:10.3389/fmats.2018.00042.
- [57] Y. Brif, M. Thomas, I. Todd, The use of high-entropy alloys in additive manufacturing, *Scr. Mater.* 99 (2015) 93–96. doi:10.1016/j.scriptamat.2014.11.037.
- [58] L.J. Challis, *Modern Crystallography II. Structure of Crystals*, 1982. doi:10.1080/716099587.

---

---

## Curriculum Vitae

Tommaso Maurizi Enrici

Born November 26<sup>th</sup>, 1990, Treviso, Italy

### **Work Experience**

**Business Line Specialist | Abra Iride S.p.A., Italy**

SEPTEMBER 2021 – Present

**Additive Manufacturing Engineer | MBN Nanomaterialia, Italy**

MARCH 2021 – SEPTEMBER 2021

### **Education**

**PhD in Engineering Science | University of Liège, Belgium**

JUNE 2016 –

Supervisor: Prof. Anne Mertens and Dr. Jérôme Tchoufang Tchuindjang

**Master of Science in Materials Engineering | Università degli studi di Padova, Italy**

OCTOBER 2013 – DECEMBER 2015

Supervisor: Prof. Irene Calliari, Prof. Jacqueline Lecomte-Beckers and Dr. Jérôme Tchoufang Tchuindjang

**Bachelor of Science in Industrial Process and Materials Engineering | Università degli studi di Padova, Italy**

OCTOBER 2009 – JUNE 2013

Supervisor: Prof. Massimo Guglielmi

### **Awards**

Award for the best PhD research and presentation at the 2019 Benelux student contest of Society for the Advancement of Material and Process Engineering (SAMPE). Presentation title: “Fabrication and improvement of 316L+WC composite coatings processed by Laser Cladding”

---

---

## ***Publications (last update: 08/06/2021)***

### ***Articles in Peer-Reviewed Journals***

9. Maurizi Enrici, T., Saggionetto, E., Dedry, O., Ertugrul, O., Boschini, F., Tchuindjang, J. T. & Mertens, A. (n.d.). “On the microstructures and strengthening mechanisms of new high-silicon austenitic stainless steels obtained by Laser Cladding” [In preparation]
8. Maurizi Enrici, T., Mario, D., Dedry, O., Castagne, S., Tchuindjang, J. T. & Mertens, A. (n.d.). “Wear behaviour of laser clad 316L + WC composite against alumina.” Submitted to Additive Manufacturing.
7. Maurizi Enrici, T., Dedry, O., Mario, D., Paydas, H., Tchuindjang, J. T. & Mertens, A. (n.d.). “Heat accumulation in multiple layers 316L + WC composite fabricated by DED: influence on local microstructure and hardness” Submitted to Additive Manufacturing.
6. Fetni, S., Maurizi Enrici, T., Niccolini, T., Tran, H., Dedry, O., Duchêne, L., ... Habraken, A. M. (2021). “Thermal model for the directed energy deposition of composite coatings in 316 L stainless steel enriched with tungsten carbides.” *Materials & Design*, 109661. <https://doi.org/10.1016/j.matdes.2021.109661>
5. Fetni, S., Maurizi Enrici, T., Niccolini, T., Tran, S. H., Dedry, O., Jardin, R., ... Habraken, A. M. (2020). “2D thermal finite element analysis of laser cladding of 316L+WC Composite coatings.” *Procedia Manufacturing*, 50, 86–92. <https://doi.org/10.1016/j.promfg.2020.08.016>
4. Ertugrul, O., Maurizi Enrici, T., Paydas, H., Saggionetto, E., Boschini, F. & Mertens, A. (2020). “Laser cladding of TiC reinforced 316L stainless steel composites: Feedstock powder preparation and microstructural evaluation.” *Powder Technology*, 375, 384–396. <https://doi.org/10.1016/j.powtec.2020.07.100>
3. Maurizi Enrici, T., Dedry, O., Boschini, F., Tchuindjang, J. T. & Mertens, A. (2020). “Microstructural and Thermal Characterization of 316L+WC Composite Coatings obtained by Laser Cladding.” *Advanced Engineering Materials*, 13, 1–12. <https://doi.org/10.1002/adem.202000291>
2. Maurizi Enrici, T., Mertens, A., Sinnaeve, M. & Tchuindjang, J. T. (2019). “Elucidation of the solidification sequence of a complex graphitic HSS alloy under a combined approach of DTA and EBSD analyses.” *Journal of Thermal Analysis and Calorimetry*, 1–15. <https://doi.org/10.1007/s10973-019-09093-9>
1. Sartori, S., Pezzato, L., Dabalà, M., Maurizi Enrici, T., Mertens, A., Ghiotti, A. & Bruschi, S. (2018). “Surface Integrity Analysis of Ti6Al4V After Semi-finishing Turning Under Different Low-Temperature Cooling Strategies.” *Journal of Materials Engineering and Performance*, 27(9), 4810–4818. <https://doi.org/10.1007/s11665-018-3598-x>

### ***Oral and poster presentation at international conferences***

8. Saggionetto, E., Maurizi Enrici, T., Dedry, O., Mario, D., Serrano Martin, I., Tchuindjang, J. T. & Mertens, A. (26-29 April 2021). “*The role of the Counterbody Material on Tribological Properties of 316L+WC Composite Coatings processed by Laser Cladding*” **Poster Presentation** at 23rd International Conference on Wear of Materials – WOM 2021 (Online event)
7. Maurizi Enrici, T., Mario, D., Mancini, E., Dedry, O., Tchuindjang, J. T. & Mertens, A. (1-5 September 2019). “*Stainless steel 316L + WC composite coating produced by laser cladding: on the role of particles dissolution and interfacial reactions*” **Oral Presentation** at 16th European Congress and Exhibition on Advanced Materials and Processes – EUROMAT 2019 (Stockholm - Sweden)
6. Maurizi Enrici, T., J., Mario, D., Dedry, O., Tchuindjang, J. T. & Mertens, A. (27-28 May 2019). “*Recent advances on 316L+WC Composite Coatings Processed by Laser Cladding*” **Oral Presentation** at 4<sup>th</sup> Workshop on Metal Additive Manufacturing (Leuven - Belgium)
5. Maurizi Enrici, T., Tchuindjang, J. T., Dedry, O., Mario, D. & Mertens, A. (9-10 April 2019 / 1-5 September 2019). “*Fabrication and improvement of 316L+WC composite coatings processed by Laser*

---

*Cladding*” **Oral Presentation** at SAMPE Benelux 2019 / SAMPE Europe 2019 (Marknesse – Netherlands / Nantes – France)

4. Maurizi Enrici, T., Tchuindjang, J. T. & Mertens, A. (11-14 September 2018). “*Segregation network structure investigation on 316L stainless steel processed by Laser Cladding*” **Oral Presentation** at INDENTATION2018 (Liège - Belgium)
3. Maurizi Enrici, T., Tchuindjang, J. T. & Mertens, A. (28-29 May 2018). “*Microstructural and Thermal Characterization of 316L+WC Composite Coatings by Laser Cladding*” **Poster Presentation** at 3<sup>rd</sup> Workshop on Metal Additive Manufacturing (Liège - Belgium)
2. Maurizi Enrici, T., Mancini, E., Magnien, Tchuindjang, J. T. & Mertens, A. (26-28 March 2018). “*Microstructure and Nano-Hardness in 316L+WC Composite Coatings Processed by Laser Cladding*” **Oral Presentation** at 16th European Mechanics of Materials Conference – EMMC16 (Nantes - France)
1. Maurizi Enrici, T., Dedry, O., Sinnaeve, M., Lecomte-Beckers, J. & Tchuindjang, J. T. (25-28 August 2017). “*New Insights on the in-situ Destabilization of the  $M_2C$  Eutectic Carbides under Thermal Treatment in a Multicomponent Cast Iron Grade*” **Oral Presentation** at 6th International Conference on Abrasion Wear Resistant Alloyed White Cast Iron for Rolling and Pulverizing Mills - ABRASION 2017 (Osaka - Japan)

